Low-Order Modeling, Controller Design and Optimization of Floating Offshore Wind Turbines

A thesis accepted by the Faculty of Aerospace Engineering and Geodesy of the University of Stuttgart in partial fulfillment of the requirements for the degree of Doctor of Engineering Sciences (Dr.-Ing.)

by

Frank Lemmer (né Sandner)

born in Ostfildern-Ruit, Germany

Main referee: Prof. Dr. Po Wen Cheng

Co-referee: Prof. Dr. Carlo L. Bottasso

Date of defense: 2.07.2018

Institute of Aircraft Design

University of Stuttgart

2018

Acknowledgements

Contents

Abbreviations

1p	Once-Per-Revolution
3p	Three-Times-Per-Revolution
AFOSP	Alternative Floating Platform Designs for Offshore Wind Turbines using Low Cost Materials
ASME	American Society of Mechanical Engineers
BEM	Blade Element Momentum
CAD	Computer-Aided Design
CB	Center of Buoyancy
CDF	Cumulated Distribution Function
CENER	National Renewable Energy Centre of Spain
CF	Center of Flotation
CFD	Computational Fluid Dynamics
CL	Closed Loop
CM	Center of Mass
CPC	Collective Pitch Control
DAC	Disturbance Accomodating Controller
DAE	Differential Algebraic Equation
DEL	Damage-Equivalent Load
DFT	Discrete Fourier Transform
DHI	Danish Hydraulic Institute
DLC	Design Load Case
DNV-GL	Det Norske Veritas - Germanischer Lloyd
DoF	Degree of Freedom
DP	Dynamic Positioning
DTU	Technical University of Denmark
EAWE	European Academy of Wind Energy
ECN	Energy Research Center of the Netherlands
ECN	Ecole Centrale de Nantes, France
EOG	Extreme Operating Gust
EQM	Equation of Motion

FE	Finite Element
FLS	Fatigue Limit State
FOWT	Floating Offshore Wind Turbine
GA	Genetic Algorithm
GDW	Generalized Dynamic Wake
GM	Gain Margin
HAWT	Horizontal-Axis Wind Turbine
HIL	Hardware-in-the-Loop
IDFT	Inverse Discrete Fourier Transform
IEA	International Energy Agency
IEC	International Electrotechnical Commission
IFE	Institute for Energy Technology, Norway
IP	In-Plane
IPC	Individual Pitch Control
LC	Load Case
LCOE	Levelized Cost of Energy
LHEEA	Research Laboratory in Hydrodynamics, Energetics & Atmospheric Environment, Nantes, France
LiDAR	Light Detection And Ranging
LQR	Linear Quadratic Regulator
LTI	Linear Time-Invariant
MARIN	Marine Research Institute Netherlands
MBS	Multibody System
MDO	Multidisciplinary Design Optimization
MIMO	Multi-Input-Multi-Output
MIT	Massachussetts Institute of Technology
MOR	Model Order Reduction
MPC	Linear Model-Predictive Control
NASA	National Aeronautics and Space Administration, USA
NMPC	Nonlinear Model-Predictive Control
NREL	National Renewable Energy Laboratory, Boulder, USA
NTM	Normal Turbulence Model
NTNU	Norwegian University of Science and Technology
NTUA	National Technical University of Athens
OC3	Offshore Code Comparison Collaboration

OC4	Offshore Code Comparison Collaboration, Continued
OC5	Offshore Code Comparison Continuation, Continued, with Correlation
ODE	Ordinary Differential Equation
OL	Open Loop
OoP	Out-of-Plane
PDE	Partial Differential Equation
PDF	Probability Density Function
PI	Proportional-Integral
PM	Phase Margin
PSD	Power Spectral Density
PSO	Particle-Swarm Optimization
QTF	Quadratic Transfer Function
RAO	Response Amplitude Operator
RGA	Relative Gain Array
RHPZ	Right Half-Plane Zero
RMS	Root Mean Square
RNA	Rotor-Nacelle Assembly
RWT	Reference Wind Turbine
SID	Standard Input Data
SISO	Single-Input-Single-Output
SLOW	Simplified Low-Order Wind turbine
SQP	Sequential Quadratic Programming
STD	Standard Deviation
SVD	Singular Value Decomposition
SWE	Stuttgart Wind Energy
SWL	Still Water Level
TF	Transfer Function
TLP	Tension Leg Platform
TMD	Tuned Mass Damper
TRL	Technology Readiness Level
TSR	Tip Speed Ratio
ULS	Ultimate Limit State
VAWT	Vertical-Axis Wind Turbine
ZOH	Zero-Order Hold

Symbols

Greek letters

$\boldsymbol{\alpha}_i$	Angular acceleration of body i, $\boldsymbol{\alpha}_i \in \mathbb{R}^{(3 \times 1)}$
β_p	Platform pitch angular displacement (DoF)
$\boldsymbol{\epsilon}$	Strain vector for body i, $\boldsymbol{\epsilon}_i \in \mathbb{R}^{(6 \times 1)}$
$\hat{\zeta}$	Wave height amplitude, $2\hat{\zeta} = H$
$\zeta_0(\omega)$	Wave height complex amplitude spectrum at CF
$\zeta_0(t)$	Incident wave height at CF
η	Efficiency
θ	Blade pitch angle (commanded)
θ_1	Blade pitch angle (measured, DoF)
λ	Wavelength (hydrodynamics)
λ	Scaling ratio (experimental testing)
λ	Tip Speed Ratio (TSR)
ξ_k	Flexible body structural damping ratio for mode k
ν	Kinematic viscosity
$\boldsymbol{\xi}(\omega)$	Response amplitude spectrum of generalized platform DoFs, $\boldsymbol{\xi} \in \mathbb{R}^{(6 \times 1)}$
ξ	Damping ratio
$\boldsymbol{\rho}_i^k$	Flexible body i nodal reference coordinates in inertial frame, $\boldsymbol{\rho}_i^k \in \mathbb{R}^{(3 \times 1)}$
ρ_a	Air density
ρ_w	Water density
σ_b	Bending stress
σ	Standard Deviation (STD)
$\overline{\sigma}$	Maximum singular value
$\underline{\sigma}$	Minimum singular value
τ	Time constant (for real, overcritically damped poles)
∇	Submerged volume of floating body
$\boldsymbol{\xi}$	Platform rigid-body generalized coordinates, $\boldsymbol{\xi} \in \mathbb{R}^{(6 \times 1)}$
φ	Rotor azimuth angle (DoF)
$\boldsymbol{\Phi}_i$	Flexible body i shape function for translation, $\boldsymbol{\Phi}_i \in \mathbb{R}^{(3 \times f_{e,i})}$
$\boldsymbol{\vartheta}_i$	Flexible body i shape function for rotation, $\boldsymbol{\vartheta}_i \in \mathbb{R}^{(3 \times f_{e,i})}$
ω	Angular frequency
φ	Phase angle
ω_0	Undamped natural frequency, $\omega_0 = 2\pi f_0$
ω_d	Damped natural frequency (for undercritically damped poles), $\omega_d = 2\pi f_d$
Ω	Rotor angular velocity (DoF) (low-speed shaft)
Ω_g	Generator angular velocity (high-speed shaft)
$\boldsymbol{\omega}_i$	Angular velocity of body i, $\boldsymbol{\omega}_i \in \mathbb{R}^{(3 \times 1)}$
Ω_{ref}	Commanded rotor angular velocity, equal to rated value for above-rated winds

Roman letters

$\boldsymbol{A}$	Added mass coefficient, $\boldsymbol{A} \in \mathbb{R}^{(6 \times 6)}$
$\boldsymbol{A}$	System matrix of dynamic system, $\boldsymbol{A} \in \mathbb{R}^{(2f \times 2f)}$
$\boldsymbol{a}_i$	Translational acceleration of body i, $\boldsymbol{a}_i \in \mathbb{R}^{(3 \times 1)}$
a_i	Wave particle acceleration in direction i
$\boldsymbol{A}_\infty$	Infinite-frequency limit of added mass coefficient, $\boldsymbol{A}_\infty \in \mathbb{R}^{(6 \times 6)}$
$a_{w,ik}$	Water acceleration in coordinate i of inertial system at body node k
A_{wp}	Waterplane area of floating body
$\boldsymbol{B}$	Input matrix of dynamic system, $\boldsymbol{B} \in \mathbb{R}^{(2f \times n_u)}$
$\boldsymbol{B}$	Radiation damping coefficient (hydrodynamics), $\boldsymbol{B} \in \mathbb{R}^{(6 \times 6)}$
$\boldsymbol{B}_{L,i}$	Strain vector jacobian, linear component, $\boldsymbol{B}_{L,i} \in \mathbb{R}^{(6 \times f_{e,i})}$
$\boldsymbol{c}_i$	Flexible body i CM in floating frame of reference, $\boldsymbol{c}_i \in \mathbb{R}^{(3 \times 1)}$
$C_{D,ik}$	Quadratic Morison drag coefficient in coordinate i of inertial system at body node k
$C_{M,ik}$	Morison inertia coefficient in coordinate i of inertial system at body node k
$C_{A,ik}$	Morison added mass coefficient in coordinate i of inertial system at body node k
$C_{A,ik}^*$	Modified Morison added mass coefficient in coordinate i of inertial system at body node k
$C_{D,ik}^*$	Modified Morison drag coefficient in coordinate i of inertial system at body node k
$\bar{C}_{D,ik}^{b*}$	Linearized modified Morison drag coefficient for damping in coordinate i of inertial system at body node k
$\bar{C}_{D,ik}^{w*}$	Linearized modified Morison drag coefficient for drag excitation in coordinate i of inertial system at body node k
C_D	Morison drag coefficient (horizontal directions) for columns (with circular cross-section)
$C_{D,hp}$	Morison drag coefficient (vertical direction) for heave plates
$\boldsymbol{C}$	Output matrix of dynamic system
$\boldsymbol{C}$	Hydrostatic stiffness matrix, defined about CF, $\boldsymbol{C} \in \mathbb{R}^{(6 \times 6)}$
$\boldsymbol{C}_{moor}$	Mooring system overall generalized stiffness about CF, $\boldsymbol{C}_{moor} \in \mathbb{R}^{(6 \times 6)}$
c_p	Rotor power coefficient
$\boldsymbol{C}_{r,i}$	Flexible body i inertial coupling between reference rotations and deformation, $\boldsymbol{C}_{r,i} \in \mathbb{R}^{(f_{e,i} \times 3)}$
c_t	Rotor thrust coefficient
$\boldsymbol{C}_{t,i}$	Flexible body i inertial coupling between reference translations and deformation, $\boldsymbol{C}_{t,i} \in \mathbb{R}^{(f_{e,i} \times 3)}$
$\boldsymbol{d}$	Disturbance inputs to dynamic system
d	Platform column spacing, distance from tower centerline
$\boldsymbol{D}$	Feedthrough matrix of dynamic system
$\boldsymbol{D}$	Morison generalized damping matrix (w.r.t SWL), $\boldsymbol{D} \in \mathbb{R}^{(6 \times 6)}$
$\boldsymbol{D}_{e,i}$	Flexible body i modal damping matrix, $\boldsymbol{D}_{e,i} \in \mathbb{R}^{(f_{e,i} \times f_{e,i})}$
D	Body diameter
dt	Timestep, $dt = 1/f_s = 1/2/f_{nyquist}$
$\boldsymbol{E}$	Identity matrix
E	Young's modulus, modulus of elasticity
f	Number of MBS DoFs

F_{aero}	Aerodynamic thrust force in shaft direction
f_e	Total number of generalized elastic coordinates $f_e = \sum_i f_{e,i}$
$f_{e,i}$	Number of generalized elastic coordinates of body i
$\boldsymbol{F}_i$	Forces acting on body i, $\boldsymbol{F}_i \in \mathbb{R}^{(3 \times 1)}$
$\boldsymbol{F}_{Mor}$	Generalized wave forces on floating body from Morison's equation, $\boldsymbol{F}_{Mor} \in \mathbb{R}^{(6 \times 1)}$
Fr	Froude number $Fr = v/\sqrt{gD}$
f_s	Sampling frequency, $f_s = 2f_{nyquist}$
$\boldsymbol{F}^{(1)}$	Generalized wave forces (1$^\text{st}$ order) on floating body, $\boldsymbol{F}^{(1)} \in \mathbb{R}^{(6 \times 1)}$
$\boldsymbol{F}^{(2)}$	Generalized wave forces (2$^\text{nd}$ order, slow-drift component) on floating body, $\boldsymbol{F}^{(2)} \in \mathbb{R}^{(6 \times 1)}$
g	Gravity constant
$\boldsymbol{G}_i$	Green-Lagrange strain tensor for body i, $\boldsymbol{G}_i \in \mathbb{R}^{(3 \times 3)}$
$G_{v \to F}$	Transfer function from rotor-effective wind speed v_0 to thrust force F_{aero}
$\boldsymbol{G}_F$	see $\boldsymbol{G}_{\zeta \to F}$
$\boldsymbol{G}_{Fmor}$	Transfer function for linearized Morison equation from incident wave elevation ζ_0 to the six generalized excitation forces on the floating body, $\boldsymbol{G}_{Fmor} \in \mathbb{R}^{(6 \times 1)}$
$\boldsymbol{G}_{\zeta \to F}$	Force-RAO: Transfer function from incident wave elevation ζ_0 to generalized forces on floating body $\boldsymbol{F}_{wave} = \boldsymbol{X}$, $\boldsymbol{G}_{\zeta \to F} \in \mathbb{R}^{(6 \times 1)}$
$G_{v \to \Omega}$	Transfer function from rotor-effective wind speed v_0 to rotor speed Ω
$\boldsymbol{G}_{\zeta \to \xi}$	RAO: Transfer function from incident wave elevation ζ_0 to rigid body generalized coordinates $\boldsymbol{\xi}$, $\boldsymbol{G}_{\zeta \to \xi} \in \mathbb{R}^{(6 \times 1)}$
$\hat{\boldsymbol{G}}$	Transfer function matrix, scaled.
$\boldsymbol{G}_x$	see $\boldsymbol{G}_{\zeta \to x}$
h	Water depth
$\boldsymbol{H}$	System transformation matrix, $\boldsymbol{H} \in \mathbb{R}^{(6 \times 6)}$
H	Wave height from trough to crest, $H = 2\hat{\zeta}$
$\boldsymbol{h}_{d,i}$	Flexible body i discrete applied force vector, $\boldsymbol{h}_{d,i} \in \mathbb{R}^{(6p+f_e \times f)}$
$\boldsymbol{h}_{e,i}$	Flexible body i inner elastic force vector, $\boldsymbol{h}_{e,i} \in \mathbb{R}^{(6p+f_e \times f)}$
$\boldsymbol{h}_{g,i}$	Flexible body i gravitational force vector, $\boldsymbol{h}_g \in \mathbb{R}^{(6p+f_e \times f)}$
h_{hp}	Platform heave plate thickness
h_{hub}	Hub height (from SWL)
$\boldsymbol{h}_{\omega,i}$	Flexible body i quadratic velocity vector, $\boldsymbol{h}_{\omega,i} \in \mathbb{R}^{(6p+f_e \times f)}$
$\boldsymbol{h}_{r,i}$	Flexible body i reaction force vector, $\boldsymbol{h}_{r,i} \in \mathbb{R}^{(6p+f_e \times f)}$
H_s	Significant wave height
$\boldsymbol{I}_i$	Inertia tensor of body i, $\boldsymbol{I}_i \in \mathbb{I}^{3 \times 3}$
$\boldsymbol{I}_{wp}$	Second moment of waterplane area, $\boldsymbol{I}_{wp} \in \mathbb{R}^{(2 \times 2)}$
j	Imaginary unit
$\boldsymbol{J}$	Global Jacobi matrix for system-EQM, $\boldsymbol{J} \in \mathbb{R}^{(6p + \sum_i f_{e,i} \times f)}$
J	Second moment of area
$\boldsymbol{J}_{e,i}$	Elastic body Jacobi (or selection-) matrix of body i, $\boldsymbol{J}_{e,i} \in \mathbb{R}^{(f_{e,i} \times f_{e,i})}$
$\boldsymbol{J}_{r,i}$	Rotational Jacobi matrix of body i, $\boldsymbol{J}_{r,i} \in \mathbb{R}^{(3 \times f)}$
$\boldsymbol{J}_{t,i}$	Translational Jacobi matrix of body i, $\boldsymbol{J}_{t,i} \in \mathbb{R}^{(3 \times f)}$
$\boldsymbol{k}$	Vector of generalized Coriolis, centrifugal and gyroscopic forces, $\boldsymbol{q} \in \mathbb{R}^{(f \times 1)}$
k	Wavenumber ($k = 2\pi/\lambda$)
$\boldsymbol{K}$	Potential flow retardation function, $\boldsymbol{K} \in \mathbb{R}^{(6 \times 1)}$
ka	Diffraction parameter

KC Keulegan-Carpenter number $KC = vT/D$

k_D Morison damping factor (for uniform cylinders), $k_D = 1/2\rho C_D D$

$\boldsymbol{K}_{eL,i}$ Flexible body i linear modal stiffness matrix, $\boldsymbol{K}_{eL,i} \in \mathbb{R}^{(f_{e,i} \times f_{e,i})}$

k_M Morison inertia factor (for uniform cylinders), $k_M = C_M \rho \pi D^2/4$

k_p Proportional gain (PI-controller)

$\boldsymbol{L}_i$ Torques acting on body i, $\boldsymbol{L}_i \in \mathbb{R}^{(3 \times 1)}$

m Inverse slope of S/N or Wöhler curve (logarithmic x)

m Body mass

$\boldsymbol{M}$ Global mass matrix for system-EQM, $\boldsymbol{M} \in \mathbb{R}^{(f \times f)}$

M_{aero} Aerodynamic torque about shaft axis

$\boldsymbol{M}_{e,i}$ Flexible body i modal mass matrix, $\boldsymbol{M}_{e,i} \in \mathbb{R}^{(f_{e,i} \times f_{e,i})}$

m_i Spectral moment of ith order

M_{yt} Tower-base fore-aft bending moment

$\boldsymbol{N}$ LQR weights on input-state coupling, $\boldsymbol{N} \in \mathbb{R}^{(2f \times n_u)}$

N_r Reference number of cycles for DEL calculation

n_u Number of dynamic system inputs

$\boldsymbol{p}$ Vector of generalized applied forces, $\boldsymbol{p} \in \mathbb{R}^{(f \times 1)}$

p Number of bodies in MBS

$\boldsymbol{P}$ Generalized damping matrix (velocity-dependent applied forces), $\boldsymbol{P} \in \mathbb{R}^{(f \times f)}$

P Electrical power

$\boldsymbol{q}$ Vector of generalized coordinates, containing the system DoFs, $\boldsymbol{q} \in \mathbb{R}^{(f \times 1)}$

$\boldsymbol{Q}$ Generalized stiffness matrix (position-dependent applied forces), $\boldsymbol{Q} \in \mathbb{R}^{(f \times f)}$

$\boldsymbol{Q}$ LQR weights on states, $\boldsymbol{Q} \in \mathbb{R}^{(2f \times 2f)}$

r Platform column radius

R Rotor radius

$\boldsymbol{R}_i^k$ Flexible body node k reference coordinates in floating frame of reference, $\boldsymbol{R}_i^k \in \mathbb{R}^{(3 \times 1)}$

$\boldsymbol{R}$ LQR weights on inputs, $\boldsymbol{R} \in \mathbb{R}^{(n_u \times n_u)}$

Re Reynolds number $Re = vD/\nu$

r_{hp} Platform heave plate radius

$\boldsymbol{r}_i$ Position vector of body i, $\boldsymbol{r}_i \in \mathbb{R}^{(3 \times 1)}$

s Laplace variable

S Load range (S/N curve)

$\tilde{\boldsymbol{S}}$ Cross product operator $\tilde{\boldsymbol{S}}(\cdot)$, $\boldsymbol{\lambda} \times \boldsymbol{a} = \tilde{\boldsymbol{S}}(\boldsymbol{\lambda})\boldsymbol{a}$

S_{vv} Spectrum of rotor-effective wind speed, including rotational sampling of turbulence

$\boldsymbol{S}_{dd}$ Spectrum of disturbance inputs to dynamic system

$\boldsymbol{S}_{FF}^{(1)}$ Force spectrum of generalized first order wave forces, $\boldsymbol{S}_{FF}^{(1)} \in \mathbb{R}^{(6 \times 6)}$

$\boldsymbol{S}_{FF}^{(2)}$ Force spectrum of generalized second order wave forces, $\boldsymbol{S}_{FF}^{(2)} \in \mathbb{R}^{(6 \times 6)}$

$\boldsymbol{S}_i$ Rotation tensor of body i, $\boldsymbol{S}_i \in \mathbb{R}^{(3 \times 3)}$

$\boldsymbol{S}_{yy}$ Spectrum of response of dynamic system

$S_{\zeta\zeta}$ Spectrum of incident wave height at the CF

t Platform draft

$\boldsymbol{T}$ Quadratic Transfer Function (QTF), $\boldsymbol{T} \in \mathbb{R}^{(6 \times 1)}$

T Complementary sensitivity function $T = GK/(1+GK)$

T_{2r} Zero-upcrossing period of response

T_i	Integrator time constant (PI-controller)
T_{life}	System design lifetime
T_p	Peak spectral period
$\boldsymbol{u}_i$	Deformation field for nodes k of body i, relative to undisplaced position, $\boldsymbol{u}_i^k \in \mathbb{R}^{(3 \times 1)}$
$\boldsymbol{u}$	Control inputs to dynamic system, $\boldsymbol{u} \in \mathbb{R}^{(n_u \times 1)}$
$\boldsymbol{U}$	Matrix of output directions of SVD
$\boldsymbol{u}_0$	Dynamic model input operating point at system steady state, $\boldsymbol{u} \in \mathbb{R}^{(n_u \times 1)}$
$\Delta\boldsymbol{u}$	Dynamic model inputs, linearized about $\boldsymbol{u}_0 \in \mathbb{R}^{(n_u \times 1)}$
$\boldsymbol{V}$	Matrix of input directions of SVD
v_0	Rotor-effective wind speed, wind disturbance input operating point
$v_{b,ik}$	Body velocity in coordinate i of inertial system at body node k
$\bar{v}_{hub}$	Mean wind speed at hub height
$\boldsymbol{v}_i$	Translational velocity of body i, $\boldsymbol{v}_i \in \mathbb{R}^{(3 \times 1)}$
v_i	Wave particle velocity in direction i
v_{rel}	Relative rotor-effective wind speed
v_{rated}	Rated wind speed
$v_{w,ik}$	Water velocity in coordinate i of inertial system at body node k
$\boldsymbol{W}_i$	Elastic beam shape function vector, $\boldsymbol{W}_i \in \mathbb{R}^{(3 \times f_{e,i})}$
$\boldsymbol{x}$	Dynamic model states $\boldsymbol{x} = [\boldsymbol{q},\ \dot{\boldsymbol{q}}]^T \in \mathbb{R}^{(2f \times 1)}$
$\Delta\boldsymbol{x}$	Dynamic model states, linearized about $\boldsymbol{x}_0 \in \mathbb{R}^{(2f \times 1)}$
$\boldsymbol{X}$	Wave excitation force coefficient or force- RAO, $\boldsymbol{X} \in \mathbb{R}^{(6 \times 1)}$
$\boldsymbol{x}_0$	Dynamic model states operating point at system steady state, $\boldsymbol{x}_0 \in \mathbb{R}^{(2f \times 1)}$
x_p	Platform surge displacement (DoF)
x_t	Tower-top fore-aft deflection w.r.t. tower-base (DoF)
$\boldsymbol{y}$	Outputs of dynamic system
$\boldsymbol{z}_{II,i}$	Kinematic function for velocity of flexible body i including translation and rotation of reference frame as well as elastic deformation in floating frame of reference, $\boldsymbol{z}_{II,i} \in \mathbb{R}^{(6p+f_e \times f)}$
$\boldsymbol{z}_{III,i}$	Kinematic function for acceleration of flexible body i including translation and rotation of reference frame as well as elastic deformation in floating frame of reference, $\boldsymbol{z}_{III,i} \in \mathbb{R}^{(6p+f_e \times f)}$
z_{cb}	Distance of center of buoyancy of floating body below SWL, positive downwards
z_{cm}	Distance of center of mass of floating body below SWL, positive downwards
z_p	Platform heave displacement (DoF)

Abstract

Various existing prototypes of Floating Offshore Wind Turbines (FOWTs) demonstrate the feasibility of placing offshore wind turbines on floating foundations, held in place by anchor lines. The motivation of this thesis is to improve the understanding of how wind and waves impact the dynamic behavior of semi-submersible-type platforms. The understanding of the multi-disciplinary system shall be used to optimize the shape of the floating platforms to show the same stable dynamics as fixed-bottom ones with a resource-efficient foundation.

The thesis addresses first the development of a dynamic simulation model with not more than the necessary physical details. It shall bridge the existing gap between spreadsheet design calculations and dynamic simulation models, which are used until the final design stage and for certification. The structural equations of motion result from an elastic multi-body system for a reduced set of degrees of freedom. The mathematical model shall represent the overall system dynamics without resolving the component loads. Therefore, the response is only calculated in a two-dimensional plane, in which the aligned wind and wave forces act. Additional force models for wind and wave forcing, as well as the mooring line forces, complete the mathematical description. From the nonlinear system of equations a linearized model is derived. First, to be used for controller design and second, for an efficient calculation of the response to stochastic load spectra in the frequency-domain. A verification through a comparison against a higher-fidelity model shows that the model is able to reproduce the response magnitude at the system eigenfrequencies as well as the forced response magnitude to wind and wave excitations. The computational efficiency proves to be high with one-hour simulations completing in about 25 seconds and even less in the case of the frequency-domain model.

Through a comparison to experimental measurements in a combined wind and wave basin at a scale of 1:60, the model validity could be confirmed. The tested concept is the TripleSpar, a deep-drafted semi-submersible, designed as a reference in this thesis. A lesson from the experiments is that a correct modeling of the hydrodynamic drag, as well as the wave forcing, is important because these loads dominate the system response of floating wind turbines. The coupled system stability shows to be driven by the gains of the blade-pitch controller in connection with the aerodynamic and the hydrodynamic damping. Controlling the rotor speed can destabilize the rotor fore-aft motion, while a large damping in fore-aft direction can mitigate the problem and increase system stability.

As a result of the findings from the experiments, the force models of the developed simulation

model include a rather detailed hydrodynamic model and a simplified, efficient aerodynamic model. The aerodynamic model computes the quasi-steady integral rotor forces as function of the tip speed ratio and the blade pitch angle. The hydrodynamic model combines the first-order potential flow coefficients and the viscous Morison drag, which is linearized for both, the wave excitation and the damping forces from drag. Vertical drag at the heave plates, identified from the measurements, compares well with data from the literature. To generally model the drag as realistically as possible, the literature data was parameterized and used for iteratively solving for response magnitude-dependent drag coefficients. The wave radiation model is simplified using a constant added mass, independent of the frequency. Second-order wave forces through Newman's approximation allow a prediction of the low-frequency platform resonances. From the frequency and time-domain models the response standard deviation, the fatigue damage and short-term extremes are calculated.

With the obtained tailored simulation model, two parametric controllers were designed: A new, robust proportional-integral-control design procedure results in a gain scheduling, specific to FOWTs. It takes the stability margins at each operating point into account and thus allows larger gains where the floating system is better damped. The controller design can be automated and is highly independent of the platform shape as it only feeds back the rotor speed error. For comparison, an optimal model-based state-feedback controller was designed to show the prospect of a multi-input-multi-output controller. Results show that this controller is less robust but improves the system fore-aft damping and allows, again, higher gains for the rotor speed control loop.

Finally, the previously developed simulation model and the parametric controllers were applied in a brute-force optimization with parameterized design routines for the floating platform. The optimum hull shape yields a reduction of more than 30% of the lifetime-weighted fatigue damage at a reasonable material cost. It is known that a good hull design can result in a cancellation of the first-order wave loads. However, a coupled effect could be observed for the optimal shape: It responds to sinusoidal waves with a translation in surge and a pitching, out-of-phase to the surge response. This means that the FOWT rotates about a point close to the rotor hub. Consequently, the rotor fore-aft motion is almost unaffected by the wave excitation. A final code-to-code comparison with the higher-fidelity model over the entire design space was successful, yielding the same optimum as the developed reduced-order model. In order to transfer this optimal response behavior to state-of-the-art design practices, a design indicator was developed, which can successfully predict the optimal shape. These results show that it is possible to design FOWTs with a very stable operational behavior. The power production and the tower-top motion and loads are comparable to onshore wind turbines, while keeping the size and mass of the foundation reasonably small.

Kurzfassung

Die Machbarkeit schwimmender, nur durch Ankerleinen fixierter Windkraftanlagen, wurde in den letzten Jahren durch mehrere Prototypen bestätigt. Die Motivation der vorliegenden Arbeit ist, das physikalische Verständnis, wie Wind und Wellen die Dynamik von Anlagen mit Halbtaucherplattformen beeinflussen, zu verbessern. Mit dem erlangten Verständnis des multidisziplinären Systems soll die Hüllform des Schwimmkörpers optimiert werden, um das Schwingungsverhalten auf das Niveau von am Boden verankerten Offshore-Anlagen zu bringen. Dabei sollen die Schwimmkörper möglichst ressourceneffizient aufgebaut sein.

Die Arbeit beginnt mit dem Entwurf eines dynamischen Simulationsmodells, das nicht mehr als die notwendigen physikalischen Effekte abbildet. Hiermit soll die Lücke zwischen einfachen Tabellenkalkulationsprogrammen und komplexen dynamischen Simulationsmodellen, die bis hin zur Zertifizierung angewendet werden, geschlossen werden. Das strukturdynamische Modell basiert auf einem elastischen Mehrkörpersystem mit wenigen Freiheitsgraden. Es soll die globale Systemdynamik korrekt abbilden, ohne detaillierte Schnittlasten einzelner Komponenten aufzulösen. Aus diesem Grund ist die modellierte Systembewegung auf die Ebene beschränkt, in der Wind und Wellenkräfte wirken. Zusätzliche Untermodelle für die Berechnung der externen Kräfte aus Wind- und Wellenanregung, sowie der Ankerleinen vervollständigen die mathematische Beschreibung des Gesamtsystems. Eine Linearisierung erlaubt zum einen die Anwendung linearer Reglerentwurfsmethoden und zum anderen effiziente Berechnungen der Systemantwort auf stochastische Anregungen im Frequenzbereich. Der Vergleich mit einem detaillierteren Modell hat gezeigt, dass das entwickelte Modell sowohl die Eigenschwingungen, als auch die Anregungen durch Wind- und Wellenkräfte korrekt abbilden kann. Die Recheneffizienz ist beachtlich, mit Simulationsdauern von nur 25 Sekunden für die Berechnung einer einstündigen Zeitreihe und noch kürzeren Rechenzeiten im Freqzenzbereich.

Die Gültigkeit des Modells konnte durch einen Vergleich mit experimentellen Messdaten in einer Skala von 1:60 gezeigt werden. Das im Test verwendete Plattform-Konzept ist der Triple-Spar, eine Halbtaucherplattform mit großem Tiefgang, die im Rahmen dieser Forschungsarbeit als Referenzmodell entwickelt wurde. Die Experimente zeigen, dass eine korrekte Modellierung des hydrodynamischen Widerstands, sowie der Wellenkräfte unerlässlich ist, da diese die Antwort dominieren. Die Stabilität des schwimmenden Systems wird hauptsächlich durch die Reglerkoeffizienten, in Verbindung mit der hydrodynamischen und aerodynamischen Dämpfung, bestimmt. Die Drehzahlregelung neigt dazu, die Bewegung der Gondel in Längsrichtung (in

Windrichtung) zu destabilisieren. Andererseits, kann eine größere Dämpfung in dieser Richtung die Stabilität erhöhen.

Auf Basis der Erkenntnisse aus den Experimenten wurde das Hydrodynamikmodell mit einer großen Detailtiefe aufgebaut, während sich ein einfaches Aerodynamikmodell als ausreichend erwiesen hat. Die globalen aerodynamischen Rotorkräfte sind eine Funktion der Schnelllaufzahl und des Blattverstellwinkels. Das hydrodynamische Modell kombiniert die Koeffizienten des Potenzialströmungs-Ansatzes mit dem Widerstandsterm der Morison-Gleichung. Der viskose Widerstandsterm wird linearisiert für die Anregung und ebenso für die Dämpfung, die aus dem Strömungswiderstand resultiert. Für eine allgemein realistischere Abbildung des Widerstands an den Tauchplatten, wurden Daten aus der Literatur parametrisiert. Das bedeutet, dass die Widerstandskoeffizienten eine Funktion der Antwortamplitude sind. Das Wellenabstrahlungsproblem (Radiation) wurde vereinfacht durch die Verwendung einer frequenzunabhängigen hydrodynamischen Zusatzmasse. Wellenkräfte zweiter Ordnung sind durch die Annäherung nach Newman modelliert und erlauben damit eine Abbildung der niederfrequenten Plattformresonanzen. Aus den Frequenz- und Zeitbereichsergebnissen werden die Standardabweichung, die Schädigungslasten, sowie die Kurzzeit-Extrema berechnet.

Mit dem erstellten Simulationsmodell wurden zwei parametrisierte Regler entworfen. Ein neues Verfahren zum Entwurf eines robusten PI-Reglers erlaubt eine neue Verstärkungsplanung, die die arbeitspunktabhängige Stabilität der schwimmenden Plattform berücksichtigt. Höhere Verstärkungsfaktoren sind hier möglich bei besseren Dämpfungseigenschaften. Das Entwurfsverfahren kann automatisiert und unabhängig von der Plattform angewendet werden, da es lediglich die Rotordrehzahl zurückführt. Neben diesem wurde ein optimaler Regler mit Zustandsrückführung entworfen, um die Vorteile eines Mehrgrößenreglers zu zeigen. Die Robustheit des Reglers ist eingeschränkt, allerdings erhöht er deutlich die Dämpfung in Längsrichtung.

Am Ende der Arbeit steht eine integrierte Optimierung des Schwimmkörpers unter Zuhilfenahme des vorab entwickelten Modells und der beiden Regler mit parametrisierten Entwurfsroutinen. Das Optimum zeigt eine Reduktion der gewichteten Ermüdungslasten um bis zu 30 %, ohne Erhöhung der Materialkosten. Für Halbtaucher ist bekannt, dass die Hüllform eine Eliminierung der Wellenkräfte erster Ordnung begünstigen kann. Zusätzlich wurde für die optimale Plattform ein gekoppelter Effekt entdeckt: Das System antwortet auf harmonische Wellenanregung mit einer Translation in Längsrichtung und einer gegenphasigen Stampfbewegung. Das bedeutet, dass das System um einen Punkt in der Nähe der Rotornabe rotiert und damit der Einfluss der Wellenkräfte auf den Rotor auf ein Minimum beschränkt wird. Eine Verifikation der Optimierungsergebnisse mit einem detaillierteren Modell über den gesamten Parameterraum konnte das gefundene Optimum reproduzieren. Um die erreichte günstige Antwortdynamik im gewöhnlichen Auslegungsprozess zu berücksichtigen, wurde ein passender Indikator entworfen. Diese Ergebnisse zeigen, dass es möglich ist, Schwimmplattformen mit ruhigem Verhalten und geringen Gondelbewegungen bei verhältnismäßigem Materialaufwand zu entwerfen.

1 Introduction

Placing offshore wind turbines on floating foundations instead of bottom-fixed ones has the prospect of increasing the applicable range to sites with intermediate to deep waters, beyond 45 m. The idea is not new but only in recent years large-scale prototypes have been built in a realistic environment. This shows that from a technical and logistic point of view the concept is realizable. The technology of Floating Offshore Wind Turbines (FOWTs) is currently passing the state of being "validated in relevant environment", see [1, p. 139]. However, the free-floating foundation adds complexity to the dynamics of Horizontal-Axis Wind Turbines (HAWTs) of a size currently approaching 10 MW, which are already the largest existing rotor-dynamic systems.

This chapter gives a concise summary of the state-of-the art and the motivation of this work, with a review of the most important previous works. The last section of this chapter introduces the research methodology of the present thesis. A thorough introduction to the topic with the relevant theoretical background will then be given in Chapter 2.

1.1 Motivation

Currently, the common design practice of FOWTs builds on the established methodologies for wind turbines on the one side and the ones from offshore structures on the other side. The current design process for fixed-bottom offshore turbines was compared to floating turbines in the paper [2] and the related project report [3]. The paper illustrates how the substructure and the wind turbine are designed, based only on a limited exchange of parameters among the two designers.

The consequence is a separated, component-oriented design, where the loads at the interface are calculated using approximate models, delivered by the designer of the respective counterpart. On the one side this means that the structural dimensioning of FOWTs follows proven and certified procedures and the systems do satisfy all design requirements. On the other side however, the restrictive exchange of data impedes full-system optimizations. Especially for a novel technology as FOWTs, it is important to save costs at early design stages, because a large portion of the upcoming lifecycle costs is being determined at the beginning of the design process already, see [1, p. 44]. The first out of three design stages declared by [3] includes

mainly so-called spreadsheet calculations but no coupled simulations of the entire FOWT system. Hence, many decisions are taken and the design is being frozen, before the full, coupled system dynamics are considered. Therefore, new design tools of low and medium fidelity are necessary to make early-stage full-system studies possible. These tools, based on simplified dynamic models, have the advantage that they require a less detailed set of design parameters, such that the exchange of data between two designers is less critical. The review on the FOWT technology and markets of [1] highlights the obstacles of development due to intellectual property and stresses the need for collaborative research. They predict a large potential for cost reduction through technology enhancements [1, p. 143].

The goal of this work is to improve the engineering methodology for FOWT designs, which are optimized to reject structural loads induced by wind and waves and thus, enable a smooth and stable operation in the offshore environment. For this end, fully integrated but computationally efficient mathematical models shall be used and the findings will be compared to conventional methods. The focus of this work is semi-submersible-type FOWTs and the design parameters of interest within the integrated analysis are the floating platform hull shape and the wind turbine controller. Since the wind turbine is usually not re-designed for the floating foundation, the platform shape and the wind turbine controller are the components, which firstly vary most between ongoing projects and secondly impact substantially the dynamic behavior. As a result, the physical understanding of the dynamics of the FOWT system shall be improved and the findings shall be processed to be incorporated in the state-of-the-art design process.

In summary, the main research questions are:

- Numerical modeling:
    - Is a "medium-fidelity" simulation tool realizable to bridge the gap between spreadsheet calculations and tools for certification?
    - Which are the relevant physical effects in the concept design phase?
- Design:
    - How to design a FOWT platform with a minimum response to wind and waves?
    - How much fatigue load reduction is possible through
        ◦ hull shape optimization?
        ◦ controller optimization?
    - Is an integrated FOWT system optimization necessary instead of a sequential one?
    - Are there new design indicators which outperform conventional ones?

Design indicators refer to quantities, which can be used as cost functionals for conceptual design calculations. They are expected to indicate optimal system properties before detailed design calculations are conducted.

After the review of related research in the next section, the specific goals, the methodology and the scope of the present study will be outlined.

1.2 Related Work

Several works were performed before the research on this thesis started in 2013 on reduced-order modeling, control design and integrated optimization. With the first conceptual designs of FOWT platforms, studies were made already on the differences of the dynamic behavior with the goal of gaining more insight into the driving physics. First approaches for numerical simulations and an evaluation of different concepts was made as early as 2000 in the thesis by Henderson [4]. The first generic concepts were developed at Massachussetts Institute of Technology (MIT) in 2006 with a comparison between concepts with taut versus catenary mooring lines under supervision of Sclavounos [5]. Around 2010, a thorough numerical analysis comparing three types of floating platforms was carried out at National Renewable Energy Laboratory, Boulder, USA (NREL) and the University of Stuttgart by Jonkman and Matha, see [6]. Several studies applying optimization algorithms to FOWT platforms were done afterwards for spar-type platforms [7], for Tension Leg Platforms (TLPs) [8] and for a design space spanning different types [9].

The critical influence of the blade pitch controller for the FOWT dynamics was reported first in [10] with further studies in [11] and [12]. The first parametric design study including the wind turbine controller was done in [8] on TLPs. The distinct influence of the controller in the design process, however, has not yet been analyzed.

Reduced-order numerical FOWT models, necessary for system analysis and optimization, have been developed in 2011 by [13] for spar-type platforms including aerodynamic loads and a bit later by [14] for the same type but specifically for control design purposes. The basis for state-of-the-art numerical FOWT modeling, however, with a clear preparation of the hydrodynamic time-domain modeling techniques, adopted from offshore engineering, and wind turbine aero-servo-elasticity was provided by Jonkman [15].

The thesis by Lupton [16] of the University of Cambridge, UK, focuses in detail on linearization approaches for FOWT modeling, which enables fast spectral methods for load calculations. As in this work, a numerical model was developed using Lagrange's equation for the multibody system description. The subsystems of aerodynamic, hydrodynamic and mooring line forces and the controller were linearized separately applying two different methods. Additionally, an approximation of the second-order hydrodynamic forces was investigated. The work showed in a comprehensive way how linearization techniques can be applied to a system as complex as a FOWT, where nonlinear effects play a non-negligible role for various load cases. In summary, the work has provided a good understanding of the potential of linearized formulations of the different submodels. Also, the coupled FOWT response was investigated in realistic environmental conditions but it is stated that further work is needed for a practical application of the code due to limitations in the operating range of the wind turbine, the description of the environmental conditions (deterministic vs. stochastic), the platform type and the compu-

tational efficiency. Several findings and derivations of [16] strengthen the present work, such as the frequency-domain calculations and the linearization of the hydrodynamic drag. The work provides important findings for the present simulation model, especially regarding the frequency-domain hydrodynamics.

The thesis by Bachynski [8] of the Norwegian University of Science and Technology (NTNU) has a comparable structure as the present one as it extends existing simulation models for the dynamic analysis of various TLP-type floating wind turbines. For the different developed TLP platforms, in-depth numerical analyses were performed with realistic load cases, used for certification, including controller fault cases. A large part of the work addresses second-order and third-order hydrodynamic forcing with an assessment of the importance of such forces for the considered TLPs. Nonetheless, a reduced-order model is also developed and compared to a state-of-the art aerodynamic model, coupled to a structural model. Although Bachynski focused on another FOWT-type than the present work, the numerical modeling approaches are comparable, including linear frequency-domain methods, the inclusion of the controller (although not platform-dependent) and higher-order hydrodynamic models.

1.3 Aim and Scope

The methodology and outline of this thesis is shown in Figure 1.1. On the modeling side, a new simulation model will be presented in Chapter 3, which is tailored to the specific research questions. The computational efficiency will allow for many load case simulations and extensive sensitivity studies. Only the main system dynamics shall be modeled without a representation of the component response. A linearization allows for linear system analyses, first of all for controller design but also to improve the understanding of the system behavior, which depends on the operating point and on the system parameters with and without the controller.

The developed model will be verified through experimental tests in a combined wind and wave basin, including the controller, in Chapter 4. With the measurement data the hydrodynamic drag will be identified and subsequently a validation of the assumptions taken for the model derivation is carried out.

Two model-based controllers will be developed for an automated controller design in Chapter 5. They are a baseline controller and an advanced controller, in order to assess their differences but also their effect on different platform hull shapes. The controllers will be applied in an integrated optimization study.

A design space of the platform hull shape will be defined in Chapter 6 with the goal of running an optimization and sensitivity studies. Design routines for the structural dimensioning as function of the hull shape will be developed. This leads to the integrated design load simulations of the fully parameterized system and linear system analyses to improve the understanding of

the previously obtained loads. The obtained optimum of this brute-force optimization will be verified with the reference model FAST.

In order to limit the scope, the system analyses in this work are carried out for operational cases with fatigue load assessments rather than extreme loads from extreme wind and wave conditions or fault conditions. In operational conditions, the applied simplified simulation models give surprisingly accurate results and provide useful lessons for a good, disturbance rejecting floater design. Thus, no detailed design is carried out but a conceptual design with a reduced set of load cases. The aim is to develop systems with good physical characteristics through system understanding with simple models, few optimization variables and simple cost functions, rather than a large and complex black-box optimization. Such approaches usually imply complex cost functions for Levelized Cost of Energy (LCOE) calculation. Here, the system dynamics are the focus, rather than the final LCOE.
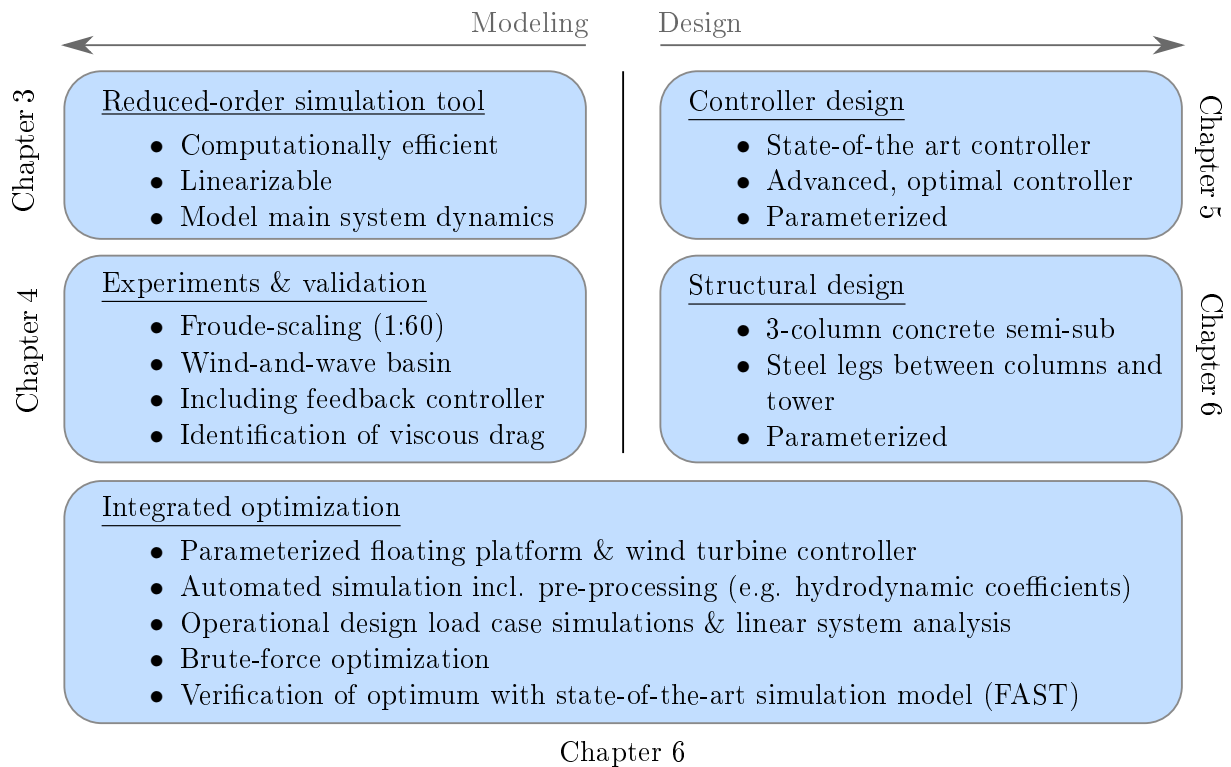
Figure 1.1: Thesis structure and methodology.

1.4 Notation

The notation is generally adapted as much as possible from standard literature. Bold symbols always denote vectors or matrices. The colored graphs have always lines with different brightnesses. The explanations in the captions are ordered such that the darkest line comes first, if not indicated otherwise.

2 Background

This chapter provides the necessary theory and a literature review on offshore wind energy and floating wind energy with a comparison of different FOWT platform types and integrated design approaches. Subsequently, the specific dynamics of FOWTs are discussed, followed by linear frequency-domain modeling techniques, the environmental conditions for load simulations and scaled experimental testing approaches, before an introduction into the wind turbine control system, especially for FOWTs, is presented. The chapter terminates with the specification of a reference floater for a 10 MW wind turbine, which is developed as a baseline for all of the following studies.

2.1 Offshore Wind Energy

The Paris Agreement of the United Nations on climate change, which entered into force in 2016, has marked a turning point in the goal of reducing global warming, it has been ratified by 184 states at the time of publication of this thesis. Societal efforts on a large scale favor sustainable traffic, industry and power production, triggering global trends such as the Divestment Movement, which attracts more and more global players to stop their investments in fossil power generation. Public policy regulates the market by introducing measures such as the European Emission Trading System or different subsidy systems by national governments. The multidisciplinary interconnectedness of the energy transition is a challenging project, especially when it comes to leaving behind traditional industries. The renewable electricity market shows complex dynamics, above all in the times of renewable energy exceeding the demand. Notwithstanding these challenges, with the Paris Agreement the transition to renewable energy was for the first time regarded by the media as having a potential of being economically profitable, which is a proof of the technological achievements in the renewable energy sector as well as the development of more efficient machinery. Nonetheless, the research of this thesis shall not be seen as a manifesto for high-tech solutions to the current challenges of humankind but rather as one piece of a manifold of necessary measures, with, above all, societal changes.

According to [17] more than 50 % of the installed power capacity in Europe can be attributed to wind energy. Wind energy overtook coal, which used to be the second largest form of power generation in 2016. The installed capacity is higher than that of hydroelectric power and

about 50 % larger than that of solar power. The outlook for 2030 by WindEurope (former EWEA) [18] predicts in its central scenario an installed capacity offshore of 66 GW compared to 12.4 GW in 2016 [17]. In terms of the energy mix, currently about 10 % of Europe's energy production stems from wind, of which about 12 % is produced offshore [17]. The International Energy Agency (IEA) predicts in its World Energy Outlook [19] a portion of 40 % of the total power generated worldwide to come from renewables by 2040. This shows the large potential of offshore wind as a technology but also as a mature and expanding industry. While in Germany, as the nation with the largest installed wind capacity in Europe (44 % [17]), the market growth will slow down for onshore wind, there is a large potential offshore. The overall installed capacity offshore in Europe grew between 2002 and 2012 from less than 100 MW to 1100 MW [20]. In 2012 about 75 % of offshore wind turbines were installed on fixed-bottom Monopile foundations but [20] predicts that the market of deeper waters is increasing exploring water depths of more than 200 m. In such depths, fixed-bottom foundations are no longer feasible. Floating platforms can be alternatives in these locations.

2.2 Floating Offshore Wind Energy

To date, the first prototype tests of FOWTs were successfully completed, such as Statoil's Hywind spar with a 2.3 MW turbine [21], Principle Power's WindFloat [22], with a 2 MW turbine and the Japanese project Kabashima with a 2 MW turbine on two different platform types. Currently, various demonstration projects are running and first commercial projects are under way such as the Hywind Scotland project, the Kincardine and Dounreay floating wind farms, also in Scotland, with a total of almost 100 MW. The WindFloat Atlantic off the coast of Portugal will comprise 25 MW and a French project of 100 MW is planned with four different floating platform concepts in two construction phases. Recently, a British and an Irish project were announced with 1.5 GW, each. An overview of technologies and current projects can be found in [23], [24] and [25].

Floating wind turbines can be distinguished from other offshore turbines through the criterion that no rigid structural connection to the sea floor exists as is the case for fixed-bottom foundations such as Monopiles, gravity foundations and jackets. The definition by [26] highlights the vertical force from buoyancy as unique feature of FOWTs.

2.3 Comparison of Platform Types

The technologies can be grouped into ballast-stabilized, buoyancy stabilized and mooring-stabilized systems. The first, called spar, feature a rather large draft with mostly a slender cylindric shape and a keel filled with ballast. Here, the large gravitational force, far below

the Still Water Level (SWL), ensures the static stability. For buoyancy-stabilized systems, called barge, a large volume at the water surface yields increased buoyancy forces where the volume displaces more water, which in turn results in static stability, see Figure 2.1a. This type of platform usually features a low draft with a large breadth. Currently, several concepts are being developed which are hybrids between a spar and a barge, meaning that they receive the static stability from both, buoyancy and gravity. These are called semi-submersibles, see Figure 2.1b, 2.1c. Most ongoing projects work with semi-submersible-type concepts, of which [27] provides a general overview.

The systems with taut moorings, called TLP, are stabilized by the mooring lines, pulling the platform body with excess buoyancy below the water surface such that a large pre-tension exists in the lines. Due to the taut lines and a little amount of ballast this type of platform is lighter than the other floaters and has higher eigenfrequencies of the substructure. It is therefore stiffer, in vertical direction almost comparable to fixed-bottom platforms, see [28]. Consequently, the system eigenfrequencies of the TLP substructure are usually above the wave frequency range. This is not the case for the types with slack lines, where the horizontal translation mode can be far below the peak spectral frequency of the waves.

In the literature, a number of comparative studies can be found on the different FOWT concepts. The previously mentioned early studies by Sclavounos are summarized in the overview paper [5]. The authors have shown that, based on frequency-domain hydrodynamic modeling and a simplified representation of the wind turbine, a small dynamic response can be achieved either with a shallow-drafted barge or a spar on the other hand. Matha and Jonkman [6], however, highlighted the large response of barges compared to semi-submersibles and TLPs, in line with the findings by Robertson [29]. However, the latter studies did not consider parameter variations of the hull shape, in contrast to [5]. The studies show that especially the section forces close to the sea surface, are higher for FOWTs than for onshore turbines, due to the wave loads.

The European research project LIFES50+[1] brings together four designers of different platform types (2 semi-submersibles, 1 barge, 1 TLP) with three universities and three research institutes in order to upscale the existing concepts and increase the Technology Readiness Level (TRL) to a value of 5, meaning that the technology development of the designs is completed, including experimental testing. This project fosters technology transfer from research to industry and provides an important platform for the exchange of knowledge of the different fields involved in offshore wind energy. The concepts with slack mooring lines are shown in Figure 2.1. This platform type is is the focus of this thesis and parts of the presented results were generated within LIFES50+.

---

[1]`http://lifes50plus.eu/`, accessed on January 22, 2018.

(a) Ideol barge   (b) Nautilus semi-submersible   (c) OlavOlsen OO-Star Wind Floater semi-submersible
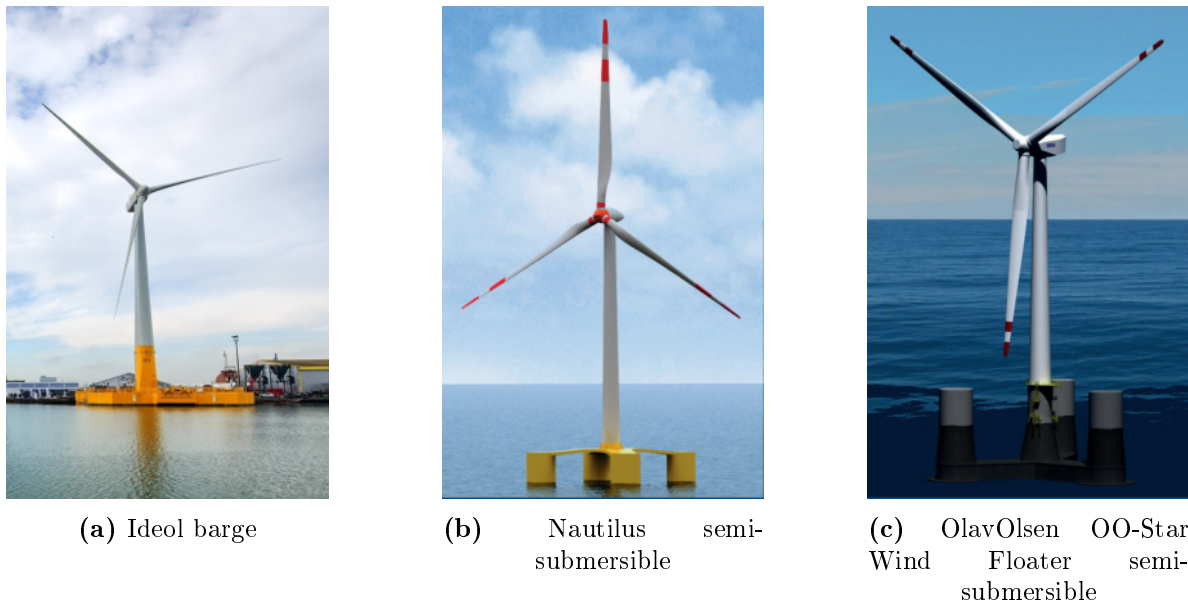
Figure 2.1: Ballast- and buoyancy-stabilized FOWT concepts of the project LIFES50+, photographs courtesy of the designers.

2.4 Optimization and Systems Engineering

Design optimization is a topic in engineering which has been addressed extensively in the literature, especially challenging are multi-disciplinary systems such as FOWTs. Currently, the concept of Systems Engineering is being introduced to wind turbine design (IEA task 37[2]), mainly focusing on the aero-elastic design, see [30, 31]. Both of these examples use a Sequential Quadratic Programming (SQP) algorithm. Systems Engineering has its origins at the National Aeronautics and Space Administration, USA (NASA) for aerospace applications and has the main objective of integrating a multidisciplinary design process. As a result, components are not designed independently but taking into account the coupling effects on the entire system. For a comprehensive realization of the Systems Engineering principles, integrated, multidisciplinary design tools are necessary, with various interfaces between the dedicated tools for a single discipline. The methodology is called Multidisciplinary Design Optimization (MDO). In this work, a multidisciplinary numerical model is used for a design optimization through a simultaneous variation of the parameters of the wind turbine controller and the platform dimensions. Whereas MDO studies usually aim at the reduction of the overall lifetime cost, in this work the cost function is reduced to fatigue loads and the power fluctuation. Hence, the main goal is to optimize the dynamic behavior.

Optimization algorithms were already applied to traditional offshore structures. An example for a parametric design model of oil and gas support structures subject to optimization for a reduced downtime through improved seakeeping is given in [32]. Here, a complex potential

---

[2]`http://windbench.net/iea37`, accessed on January 11, 2018.

flow model was parameterized, comparable to the present work. A first approach for integrated design of fixed-bottom offshore turbines was presented in 2004 in the thesis by Kühn [33]. Later, various studies were published, especially for jackets, where the lattice structure was optimized. Examples are [34], applying a Particle-Swarm Optimization (PSO) algorithm, [35] with a Genetic Algorithm (GA) and [36] using a gradient-based optimizer. With the latter it is especially important to ensure a continuous description of the cost function, which is not possible with complex functions and usually not feasible for MDO. For Monopiles, a recent risk-based optimization was presented in [37]. A summary of various optimization algorithms and an application to mechanical systems using multibody approaches and symbolic programming, as in the present work, can be found in the thesis [38].

For FOWTs several optimization studies were described already in Section 1.2. One study, resembling MDO techniques to the largest extent is published in [9]. It includes the hull shape and mooring line design across different platform types using a genetic algorithm. In that work, a frequency-domain model is derived from the code FAST v7 [39], with a linear representation of the hydrodynamic viscous damping but without representing the wind turbine controller. The genetic algorithm is applied for single- and multi-objective optimization. The results show different, rather unconventional, designs, which might indicate that a refinement of the cost function is necessary, according to the author. A first brute-force optimization with tailored blade-pitch controllers was performed in the course of the present research and was presented in [40].

2.5 Dynamics of Floating Wind Turbines

While for conventional offshore oil and gas structures the wave loads are dominant and the wind loads are only approximated by static forces [41], this approach is not possible for FOWTs: Dynamic simulations with a representation of the wind turbine aero-elasticity are necessary in order to capture the dynamic response correctly and to ensure that the structure does not show resonances leading to large loads and excursions. For FOWTs, structural elasticity is important due to the slenderness of the tower and the blades and needs to be considered for design calculations. The aerodynamic forces depend on the blade section local inflow angle of attack. Therefore, the integral rotor forces depend on the wind speed, the rotor speed and the blade pitch angle. Since the blade pitch angle is an actuated variable of the wind turbine control system, next to the generator torque, the controller dynamics also need to be taken into account. This results in a multidisciplinary system as illustrated in Figure 2.2.

The purpose of this section is to give an introduction to the main system dynamic characteristics of FOWTs and available methods for numeric simulations, looking first at the structural dynamics and subsequently at the aerodynamics, hydrodynamics and mooring dynamics. Fig-
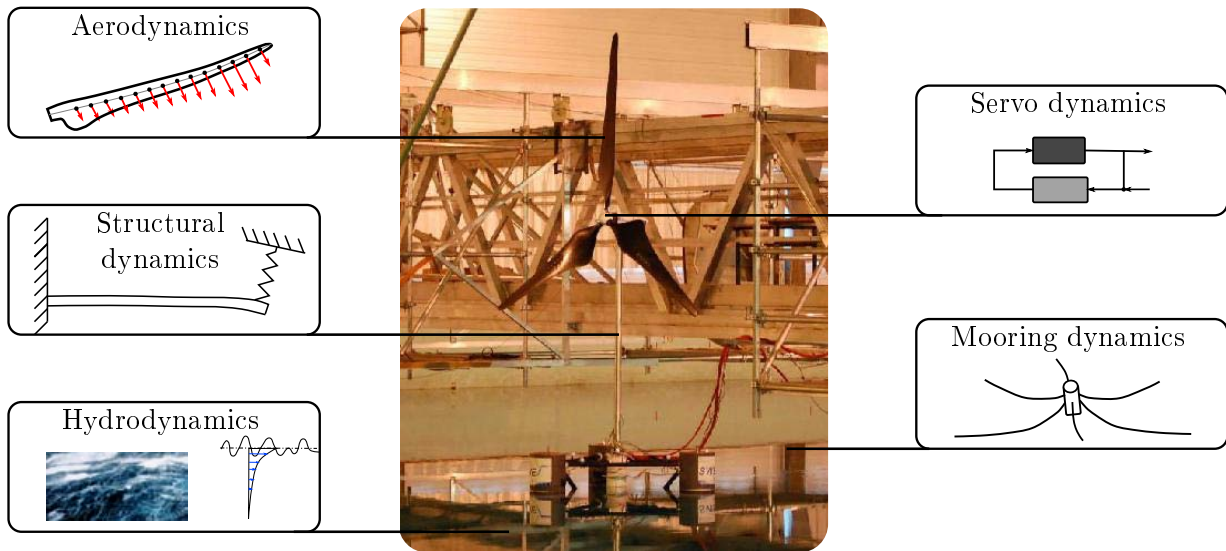
Figure 2.2: Multidisciplinary FOWT system (photograph by Henrik Bredmose, DTU).

ure 2.3 shows a comparison of the most important structural loads in terms of the Power Spectral Density (PSD) from a one-hour simulation. The turbine is the DTU 10 MW Reference Wind Turbine (RWT) on a fixed foundation and on a floating foundation[3] at above-rated wind speeds and a correlated wave environment (see Table 2.1), simulated with the tool FAST [43]. While the maximum energy of the wind spectrum is concentrated at the lower end of the frequency axis, the wave spectrum has a pronounced peak at around 0.1 Hz. Systems with slack mooring lines are usually designed such that the rigid-body modes of the floating substructure are below the wave frequencies. Semi-submersibles and spars usually show a large motion response to low-frequency wind excitation and to second-order wave forces, which will be addressed in Section 2.5.3.

The inertial coordinate system, which is commonly used, is shown with the main Degrees of Freedom (DoF) in Figure 3.1. The rigid-body DoFs of FOWTs are called *surge*, *sway* and *heave* in translational directions and *roll*, *pitch* and *yaw* in rotational directions. Below the first two graphs of Figure 2.3 with the PSD of the wind time series $v_0(t)$, averaged over the rotor-plane and the wave height time series $\zeta_0(t)$ is the PSD of the platform pitch (or nodding) angle β_p and the rotor speed (Ω). The last two are the bending moments M_{yt} in pitching (or nodding) direction at the tower-base and the blade-root bending moment M_{oop}, perpendicular to the rotor plane or Out-of-Plane (OoP). The two signals are selected here because the tower-base is a critical location for the design due to large bending stresses from the overturning moment of the rotor thrust force and the wave forces. The blade-root bending moments determine the structural blade design and pose challenges due to aerodynamic restrictions of the airfoils. The sectional forces at the tower-base and the blade-root are largely proportional to the tower-top displacement and the blade-tip displacement (see Section 3.2.6 for a detailed discussion). In

---

[3]The onshore system is detailed in [42] and the FOWT in Section 2.10.

Figure 2.3, the platform pitch mode at 0.025 Hz is clearly visible in the third plot, and this is reflected in the tower-base loads (fifth plot). Even more significant is the response of the tower-base moment from first-order wave loads at the wave frequency at 0.1 Hz and slightly above. Another distinct difference is the low-frequency response of the rotor speed to wind excitations: The FOWT controller allows larger amplitudes than the onshore turbine. This is due to the fact that the controller gains have to be de-tuned (reduced) for FOWTs to ensure the system's stability if only standard control schemes are applied. Section 2.9 will give an introduction into the controller for FOWTs. The blade moment (lower plot) shows a distinct response at the Once-Per-Revolution (1p) frequency at 0.16 Hz and a response to the turbulent wind field but only a slight excitation from the wave loads. Remarkable is that the 1p-frequency is more dominant for onshore turbines than for the floating counterpart. A possible reason is the shifted modal properties due to the floating substructure.
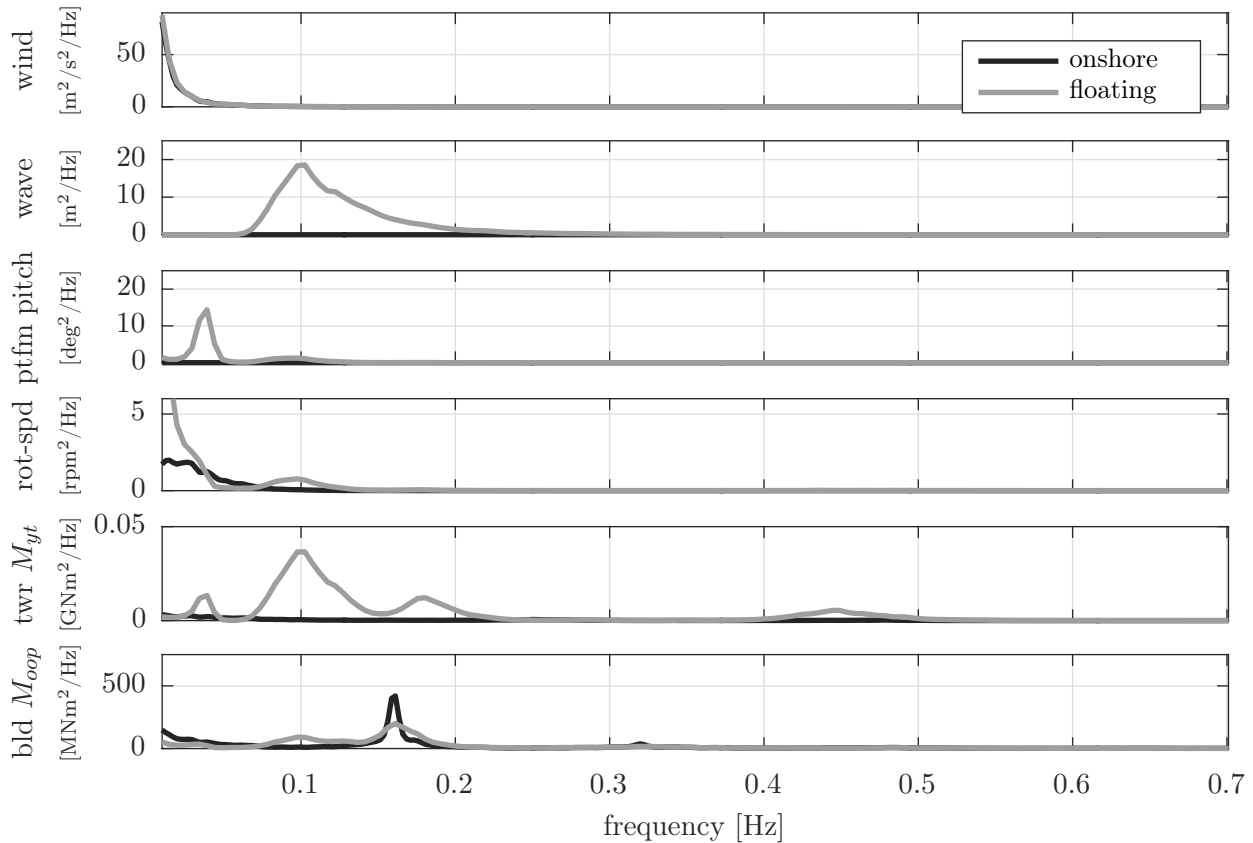
Figure 2.3: Comparison of responses of DTU 10 MW RWT onshore and floating at $\bar{v}_{hub} = 17.9$ m/s.

A distinct feature of FOWT dynamics is the coupling between the platform pitch motion response with the rotor response. This is due to the relative, or apparent, rotor-effective wind speed ("the one that the rotor sees"). A coupling to the controller-induced dynamics appears, since the rotor speed responds to these changes in the relative wind speed and, in turn, the controller reacts to the rotor speed error. The surge-direction is usually not as important

for FOWTs as the pitch mode because it has generally a lower eigenfrequency, which is better damped.

Numerical modeling of FOWTs has large overlaps with the methods of the offshore oil and gas industry, as mentioned above. One major difference is that fatigue analyses are highly important for wind turbines, due to the persistent harmonic excitation [44]. For a structural fatigue assessment, a representative probability distribution of load cycle amplitudes is necessary and this requires extensive numerical simulations. First fatigue calculations were made in the frequency-domain, due to the lower computational effort, see e.g. Dirlik [45]. The calculation of the dynamic wave forcing on vertical piles was presented as early as 1965 by Borgman [46]. Due to the multi-disciplinarity of FOWTs the complexity of numerical models increases significantly and as a consequence, first offshore wind farms were designed using "de-coupled" numerical predictions of the structural stresses. With the increase of computing power, linear frequency-domain analyses for dynamic simulations were slowly replaced by computationally demanding nonlinear time-domain simulations. In offshore wind, so-called multi-physics models are common where different dedicated software tools run simultaneously. Here, the Equations of Motion (EQM) are not set up as a whole but the tools solve their own EQM and exchange states and forces in each timestep. Dedicated wind turbine models, so-called aero-elastic modeling tools, predict the wind turbine loads and dedicated tools for the wave-structure interaction determine the hydrodynamic forcing. Different coupling schemes for FOWTs are described in [26]. A study on the validity of a superposition of the loads at e.g. the tower-base, coming from wind and wave loads can be found in [47] and in a recent study [48]. The first approaches to integrated analyses of (fixed-bottom) offshore wind turbines were made as part of the theses by Kühn [33] and later by van der Tempel [49]. More details on fatigue calculation will be given in Section 2.6 and 2.7.

For FOWTs, the first modeling tools were developed by Henderson [4]. Later, Jonkman [15] provided a detailed description of the theory behind the first and only available open-source FOWT simulation tool FAST [43] by NREL, which is used as a reference in this work. A general overview on FOWT modeling can be found in the recently published book [50]. To date, a variety of mostly commercial simulation tools for FOWTs exist, among others Simpack by Dassault Systèmes, Bladed by Det Norske Veritas - Germanischer Lloyd (DNV-GL), Hawc2 by Technical University of Denmark (DTU) and 3DFloat by Institute for Energy Technology, Norway (IFE). Various other commercial codes exist, in addition to a number of in-house research codes by universities and research organizations. An extensive code comparison project was performed within IEA task 23 and task 30, namely the projects Offshore Code Comparison Collaboration (OC3), Offshore Code Comparison Collaboration, Continued (OC4) and Offshore Code Comparison Continuation, Continued, with Correlation (OC5) where a large number of institutions participated worldwide, running simulations on fixed-bottom and floating wind turbines for various load cases. The results for FOWTs are published in [51, 52, 53, 54]. Other

studies reviewing and comparing the predictions of different simulation approaches can be found in [55, 56, 57] and in the LIFES50+ project report [58].

The next sections will give an overview on the FOWT subsystem dynamics, the structural dynamics, aerodynamics, hydrodynamics and the mooring line dynamics and the respective modeling methods and available simulation tools. Further details are part of the reduced-model derivation in Chapter 3.

2.5.1 Structural dynamics

As shown above, offshore wind turbines show large deflections of the tower and the blades as response to the environmental loads. Therefore a Multibody System (MBS) approach is usually implemented in the structural modeling tools. High-fidelity Finite Element (FE) models can be applied for the flexible components of the wind turbine while the formulation of the MBS accounts for the large reference motion with a correct physical representation of the kinetics of inertial, Coriolis, centrifugal and gyroscopic forces.

In many simulation tools such as FAST, the flexible bodies, mainly the rotor blades and the tower, are simplified through a Model Order Reduction (MOR) and represented in the flexible MBS through a limited number of shape functions following a Ritz approach, see [59]. These shape functions are commonly the mode shapes of the respective bodies, obtained through an eigenanalysis using FE models. Although individual shape functions are defined for each body, they should not be calculated without representing the rest of the coupled system. The Rotor-Nacelle Assembly (RNA) inertial mass, for example, needs to be accounted for when calculating the tower shape functions. The number of necessary mode shapes to be included is usually based on engineering judgment. In state-of-the-art aero-elastic simulation codes, at least the first two modes in fore-aft and side-side direction are used, giving four flexible DoFs of the tower. For the blades made of fiber reinforced epoxy, the mode shapes are more complex: If the blade cross-section is approximately symmetric it can be assumed that the principal axes are aligned with the blade chord, a function of the radius, see [60]. Therefore, the first bending mode shapes are twisted with the blade principal axis in FAST. The most important mode shapes are normally selected as the first two flapwise modes (about the "soft" axis) and the first edge-wise mode (about the "stiff" axis) giving a total of nine DoFs for the rotor. Especially for large blades or for aero-elastic stability analyses, higher modes and at least one torsional mode needs to be included because torsion changes the local angle of attack and consequently the aerodynamic forces and moments, see [61] and recently [62] with a validation of the simulation code FAST with full-scale measurements.

The floating platform is modeled as a rigid body in FAST with six DoFs if all directions are unconstrained. Studies were made recently to include the substructure flexibility in the dynamic system analysis. This has mainly the objective to obtain the structural stresses within

the substructure, which is not possible with state-of-the-art tools. An approach calculating the stresses as a post-processing of the time-domain results of a state-of-the-art model was presented first for Bladed [63] and by NTNU in [64]. In [65] and [66], the flexibility was also considered in the fluid-structure interaction problem.

Additional DoFs of the state-of-the-art FOWT models are the rotor rotation, the drive-train torsion and the blade pitch actuator model DoFs, usually represented by a second-order dynamic system, giving four additional DoFs. While the blade pitch actuator model is not included in FAST and has to be included in a custom Simulink model, the yaw drive actuator is included through a rotational spring-damper element. This yaw drive actuator represents another additional DoF.

All of the mentioned DoFs can be activated in FAST resulting in a total of 25 DoFs. The reduced-order model derived in Chapter 3 considers only a planar platform motion in the vertical 2D plane and neglects the flexibility of the blades in order to focus on the main system dynamics. The structural model, however, is built with the theory of flexible MBS, as described above. The EQM will be derived in Section 3.2.

2.5.2 Aerodynamics

Common state-of-the-art wind turbine simulation codes represent the loading from aerodynamics usually through Blade Element Momentum (BEM) theory. Momentum theory is the part describing the deceleration of the flow across the rotor due to the momentum imposed by the rotor on the steady flow. The other part of BEM theory is the blade element theory, which gives the local forces on each blade section with a discrete width and chord, given an angle of attack and airfoil polar data. This involves an iteration because blade element theory requires the angle of attack, which comes from the momentum theory. The result of this iteration is the induction factor, giving the local velocities in the rotor plane based on the simulation input, the 3D turbulent wind field, see Section 2.7, far upstream and undisturbed by the rotor. Only with the local induction factor, the wind speeds at the rotor plane can be determined and the local forces are calculated using the blade polars. A derivation of the standard BEM-theory can be found in [60].

The basic BEM theory involves many assumptions: First, the rotor is discretized through annuli, each having a constant induction. This means one can imagine the rotor as a disk. The assumption of discrete annuli implies that there is no dependence of the flow in radial direction, which is especially critical for yawed inflow, see [44, Chapter 3]. Another simplification is related to the root and the tip losses, which occur due to shed vortices, which reduce the circulation at these blade sections. The authors of [44] state that this radial dependence of the induction violates the BEM assumptions as it yields a radial exchange of momentum. However, for common operating points, the assumption of radial independence of annular forces is said to

be reasonable. Other assumptions include no special consideration for the situation of heavily loaded rotors under large induction factors, where a recirculation of the flow at the outer radius of the disc occurs, denoted as vortex ring state and, more severe, the turbulent wake state.

Important for control design purposes might be the fact that quasi-steady aerodynamics are assumed, meaning that a stepwise change in the angle of attack yields an instantaneous response of the forces, e.g. [67]. This is not the case for a real rotor as several aerodynamic phenomena yield a dynamic response of the forces. These can be grouped into three categories, see [68] or also [26] and [69]: First, local airfoil dynamic effects, causing a circulation lag, also called Theodorsen Effect – a phenomenon happening in attached flow conditions. Second, for large angles of attack stall occurs reducing the lift and increasing the drag through shed vortices. Considering unsteady changes in the angle of attack the shed vortices, traveling over the blade chord, yield the dynamic stall phenomenon. Apart from these local effects, the third effect is related to the global flow through the rotor disc. It cannot be assumed to behave in a quasi-steady manner, mainly because the flow has to accelerate or decelerate, which cannot happen instantaneously, due to the inertia of the flow. This dynamic inflow or dynamic wake effect causes a delay in the blade forces following a change of, e.g., the blade pitch angle in attached flow conditions.

The computational scheme of BEM theory has proven to be very efficient compared to other methods. Therefore, a variety of correction models has been developed. An important one is, according to [44] and [60], the hub and root loss correction model. This model accounts for the above-mentioned vortices shed at the blade segments at the root and the tip. Correction models to the mentioned dynamic effects of the aerodynamic forces are the dynamic stall and dynamic inflow model. The Glauert correction for large induction factors accounts for the re-circulation effect. The correction of the 2D airfoil data from experiments or potential flow simulations for 3D flow situations is usually done in a pre-processing step. The spreadsheet tool [70] is an example of how to prepare the airfoil data for BEM tools with a 360° range of angles of attack and the correction of effects from a rotating blade, rather than static airfoils. A good review of BEM models including corrections can be found in [71]. A thesis on possible corrections based on experimental analyses can be found in [72].

For FOWTs, especially unsteady aerodynamics can be important in certain flow situations. Although this work focuses on simplified conceptual models, some of these are listed here for a better understanding of the underlying physics of real wind turbine rotors. Recently, a number of studies was made for moving rotors due to the floating foundation. The application of the dynamic inflow correction models for FOWTs is described in [73]. It shows the importance of the time scale of the frequency of the floating platform, compared to the unsteady aerodynamics. It showed that BEM theory-based models are generally valid for FOWT modeling. The importance of the frequency of oscillation of the floating platform has also been investi-

gated by the authors of [74]. Their approaches will be discussed further in the results chapter, Section 6.4.6.

Alternatives to BEM include the second theory implemented in the reference model FAST. Besides BEM-theory it includes the Generalized Dynamic Wake (GDW) model, which is based on the Pitt and Peters dynamic inflow model, see [68], but it includes higher-order terms than the common correction model to BEM theory, see [75]. It is still considered an independent aerodynamic model because, even in steady conditions, the modeling is different than with BEM models: The pressure distribution along the blade is modeled through Legendre functions, which include the above mentioned tip and root losses. One case in Chapter 6 uses this model. A theory guide of the aerodynamic model AeroDyn of FAST can be found in [76].

Higher-fidelity models are potential flow approaches as the Lifting Line and Free-Wake Vortex Method, which models the wake together with the fluid-structure interaction problem. The thesis [77] gives a good description of the method. Its application to FOWTs can be found in [78] and [79]. As in helicopter theory, especially the interaction of the rotor with its wake can be better represented with these models. Even more complex Computational Fluid Dynamics (CFD) models have been applied to FOWTs in [80, 81, 82, 83, 84], showing reasonable results but a challenging implementation and significant computational effort. The project Offwindtech went further, studying the different aerodynamics due to the floating foundation and the consequences of the moving hub condition for blade design with the goal of reducing loads and increasing the power production, see [85]. That work had a comparable objective of the one of this thesis as variations of the design are investigated in order to adapt current concepts better to the floating foundations with the goal of reducing loads and therefore less material usage in the construction.

For this work, simplified, computationally efficient and linearized aerodynamic models are necessary for control design and design optimization. Several approaches exist here, the simplest being the modeling of the entire rotor as a disk with overall aerodynamic coefficients depending on the Tip Speed Ratio (TSR) and the blade pitch angle, which will be described in Section 3.4. Other simplified models avoid the discretization of the blade and the time-consuming iteration to find the induction factor through overall aerodynamic blade coefficients and a representative blade-effective wind speed, but still including a dynamic inflow model, see [69]. According to [86] the above-mentioned vortex methods can also be simplified for control applications. An extensive work on linearized, reduced-order aero-elastic modeling for controller design, was presented in [87]. A simplified dynamic inflow representation is given in [67] with an order reduction of the structural and aerodynamic states (considering dynamic inflow) based on shape functions.

2.5.3 Hydrodynamics

In this section, an introduction will be given to state-of-the-art hydrodynamic FOWT modeling and the methods for hydrostatic and hydrodynamic FOWT design. Besides the available textbooks on offshore hydrodynamics, the book section [88] provides an overview on hydrodynamic modeling of offshore wind turbines, including FOWTs.

Hydrostatics

Archimedes' principle of buoyancy results in static forces on the wetted surface of a FOWT, including position-dependent restoring forces. These restoring forces are important for the static stability of FOWTs and represent a constraint for the dimensioning. Analytical expressions for simple shapes make an approximation of the hydrostatic properties in spreadsheet calculations possible. The hull shape determines important parameters like the submerged volume, the center of buoyancy, which is the center of the submerged volume, and the cross-sectional area of the body at the water surface, the waterplane area A_{wp} [89]. The restoring stiffness in vertical heave direction can be obtained with the water density ρ_w and the gravity constant g as

$$C_{33} = \rho_w g A_{wp}. \tag{2.1}$$

The hydrostatic restoring stiffness C_{55} is responsible for withstanding the aerodynamic thrust force under a limited pitch angle β_p. It depends on the second moment of the waterplane area

$$I_{22,wp} = \iint\limits_{A_{wp}} x^2 \mathrm{d}x \mathrm{d}y. \tag{2.2}$$

With the submerged volume ∇ and the structural mass m, the restoring stiffness in pitch is

$$C_{55} = \rho_w g I_{22,wp} + \rho_w g \nabla z_{cb} - m g z_{cm}. \tag{2.3}$$

Platforms with a small waterplane area usually have a low center of gravity z_{cm}, positive in upward direction. The gravitational forces and the buoyancy forces, acting on the center of buoyancy z_{cb}, result in a restoring moment, contributing to C_{55}. For symmetric bodies $C_{44} = C_{55}$. The linear stiffness matrix $\boldsymbol{C} \in \mathbb{R}^{(6 \times 6)}$ needs to be augmented with restoring forces from the mooring system. For unmoored bodies, all entries but the above-mentioned ones are zero.

Ocean waves

Ocean waves require different levels of complexity of their mathematical description, depending on their nonlinearity. Linear surface waves have a sinusoidal profile, while steeper waves have larger troughs and shorter crests. Different theories exist to model the wave kinematics in time

and space. Usually, potential flow theory is employed with different orders of nonlinearity of the free surface boundary condition, see [89, p. 75] for a visualization of the different regimes. Linear waves can be modeled in a straightforward manner such that the fluid kinematics over depth can be solved for by hand if no obstacles in the domain are considered, see e.g. [90, p. 5-12]. Linear waves travel with the phase speed v_p, a function of the wave frequency. This means that the time series at different locations cannot simply be shifted in time. The dispersion relation represents the link between the time and the spatial dimension of linear waves. It is transcendental but it can be simplified for deep waters with a depth-to-wavelength ratio $h/\lambda > 1/2$ [90, p. 5-2]. The deep water approximation gives the phase speed

$$v_p = \frac{1}{2}\sqrt{\frac{g}{k}} = \frac{1}{2}\sqrt{\frac{g\lambda}{2\pi}}, \tag{2.4}$$

where k denotes the wavenumber, see [91, Chapter 6.2]. With deep water approximation, the wavenumber results from the wave angular frequency ω as $k = \omega^2/g$.

Using linear wave theory, the complex amplitude spectrum of the incident wave elevation $\zeta(\omega)$ at different locations along the wave heading direction x can be obtained through the factor

$$f_x(x,\omega) = \mathrm{e}^{ikx}. \tag{2.5}$$

With this factor, the time series $\zeta_x(t)$ at the new location result from the amplitude spectrum at the original location $\zeta_0(\omega) \equiv \zeta(\omega, x{=}0)$ in a discrete-time notation for a dataset of N elements as

$$\zeta_x(t) = \frac{1}{N}\sum_{\omega_i=0}^{N-1} f_x(x,\omega_i)\zeta_0(\omega_i)\mathrm{e}^{\frac{2\pi\omega_i t}{N}}. \tag{2.6}$$

Numerical toolboxes provide functions for the Inverse Discrete Fourier Transform (IDFT) such that

$$\zeta_x(t) = \frac{1}{N}\mathrm{idft}\left(f_x(x)\zeta_0(\omega)\right). \tag{2.7}$$

The wave kinematics over depth z can now be calculated in the frequency-domain from the amplitude spectrum $\zeta_0(\omega)$. The water particle velocity in horizontal and vertical directions are necessary for the calculation of the wave forces through Morison's equation, Section 2.5.3. Throughout this work, we take advantage of deep water approximation, introduced earlier in this section, and the wave heading direction is always aligned with the global x-coordinate. The horizontal and vertical velocities over depth z result as

$$v_x(\omega,x,z) = \omega\zeta(\omega,x)\mathrm{e}^{kz} \tag{2.8}$$

$$v_z(\omega,x,z) = j\omega\zeta(\omega,x)\mathrm{e}^{kz}. \tag{2.9}$$

Consequently, the horizontal velocity is in phase with the instantaneous free-surface elevation $\zeta(\omega, x) \in \mathbb{C}$, while the vertical velocity is $90\,\text{deg}$ ahead of the free-surface elevation. The water particle acceleration can be written as

$$a_x(\omega, x, z) = j\omega^2 \zeta(\omega, x) \mathrm{e}^{kz} \tag{2.10}$$

$$a_z(\omega, x, z) = -\omega^2 \zeta(\omega, x) \mathrm{e}^{kz}. \tag{2.11}$$

If obstacles are present in the computational domain, e.g. fixed or floating bodies, the dimensions of the body determine the characteristics of the wave-induced forcing. Potential flow panel codes, which include the body in the domain, can model effects from diffraction (of the waves around the floating body) as well as the forces from radiated waves acting back on the body. Viscous loads, on the other side, are entirely neglected by potential flow theory. This is the strength of empirical Morison's equation, addressed later in this section. Morison's equation, however, assumes a transparent body, meaning that the wave field is not affected by the body and diffraction effects are neglected.

Figure 2.4 shows the ocean wave domains as function of the nondimensional characterization of the forcing on a body in waves. The first dimensionless number on the horizontal axis is the diffraction parameter ka, the product of the wavenumber k and the body radius $a = D/2$. It can be alternatively expressed with the wavelength λ as $ka = \pi D/\lambda$. On the vertical axis is the Keulegan-Carpenter number, which is the product of the fluid velocity amplitude $\hat{v}$ and the wave period T, divided by the significant length D [90, p. 12-16]. Alternatively, KC can be obtained from the water particle excursion $\hat{x}$, or, in a simplified manner, from the wave height H as

$$KC = \frac{\hat{v}T}{D} = 2\pi \frac{\hat{x}}{D} \approx \pi \frac{H}{D}. \tag{2.12}$$

The wave breaking limit $H/\lambda = 1/7$, simplified for the case of deep water waves, is shown in Figure 2.4 as function of KC and ka [90, p. 13-4]. It is not dependent on the dimensions of the body. The location of the scaled model parameters and Load Cases (LCs) of Chapter 4 and the LCs used for the parametric design in Chapter 6 are marked in the figure. Acceleration-dependent inertial forces are the dominant ones for small KC. Velocity-dependent drag forces become more important for larger KC. Consequently, a FOWT spar will experience a larger portion of drag forces in a given sea state than a deep water offshore structure of large diameter. The large diameter will also yield a larger diffraction parameter ka and thus more significant wave diffraction. The simulation model should be set up accordingly and consider hydrodynamic coefficients from a panel code or include an additional diffraction correction model, when Morison's equation is used. In general, a limit of $ka = 0.5$ is given in [92, p. 174], above which the diffraction effect is important. Both, potential flow theory, as well as Morison's equation will be introduced for frequency-domain and time-domain computations.
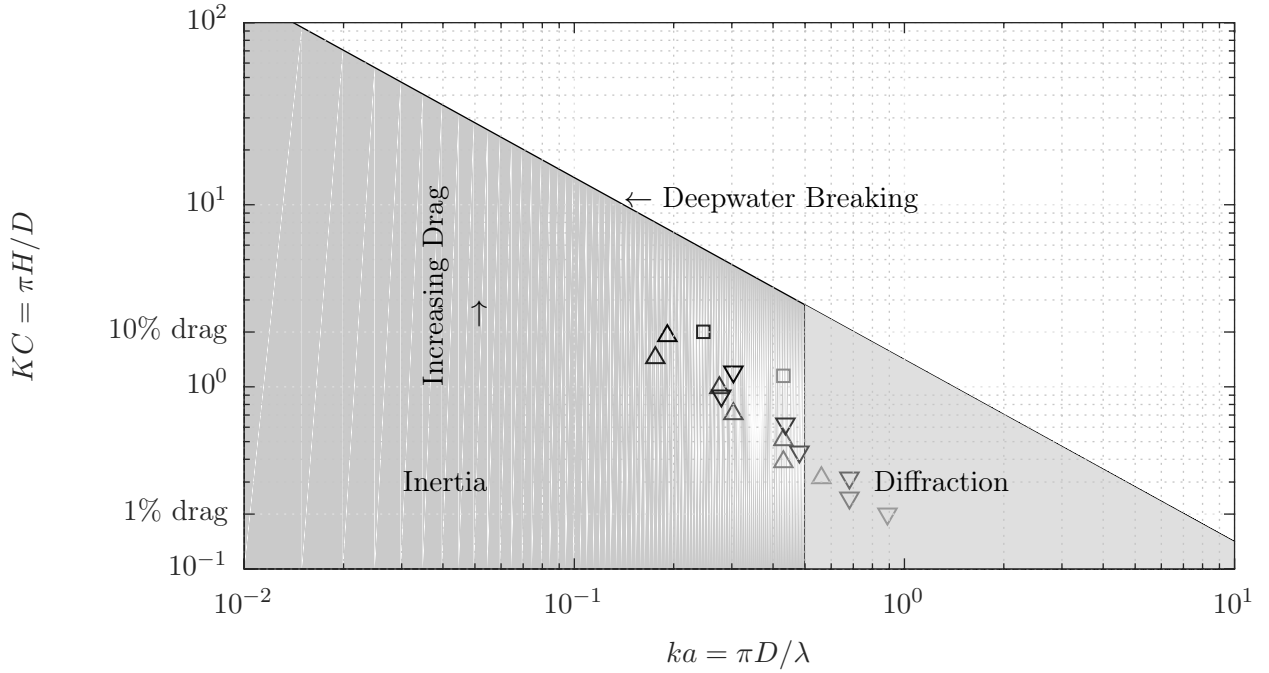
Figure 2.4: Wave-induced force component domains with marks for the geometries and sea-states used in this work. Exprimental sea states of Chapter 4 (□), for LC 7 and LC 9 (darker color for higher sea state) and design space of Chapter 6: Deep-draft design (△) and low-draft design (▽) (darker color for higher sea state). Reproduced for this work from [89, p. 290], originally from S.K. Chakrabarti.

First-order potential flow

Linear potential flow models, called panel codes, solve for the linear first-order coefficients of a body represented by a 3D surface mesh. Assuming linear superposition, two problems can be solved for separately: radiation (or maneuvering) and diffraction (or seakeeping), see [91, Section 6.19]. The radiation problem is represented by a sinusoidally moving body in still water. The integrated surface pressures can be separated for the velocity-dependent radiation damping matrix $\boldsymbol{B}(\omega) \in \mathbb{R}^{(6 \times 6)}$ as function of the frequency and the acceleration-dependent added mass matrix $\boldsymbol{A}(\omega) \in \mathbb{R}^{(6 \times 6)}$. Damping effects are usually not considered in potential flow models, due to d'Alembert's paradox, stating that the wave particle velocity does not yield a force on a floating body. The radiation damping results from the still-water boundary condition far away from the oscillating body. The diffraction problem consists of a fixed floating body with waves of different frequencies (and directions), to obtain the wave pressure on the surface (Froude-Krylov pressure) and the wave pressure from diffraction effects. The integrated pressures give the frequency-dependent wave excitation force coefficient $\boldsymbol{X}(\omega) \in \mathbb{R}^{(6 \times 1)}$. Multiplied with the wave height amplitude spectrum $\zeta_0(\omega)$, it gives the first-order wave force spectrum $\boldsymbol{F}^{(1)}(\omega)$. The force spectrum is given in a generalized form with respect to a selected reference point.

With these linear coefficients, the equation of motion can be set up for a rigid body with the complex vector of linear generalized coordinates in all three directions and orien-

tations $\boldsymbol{\xi} \in \mathbb{R}^{(6 \times 1)}$ as

$$\boldsymbol{\xi} = \left[\begin{array}{cccccc} x_p, & y_p, & z_p, & \alpha_p, & \beta_p, & \gamma_p \end{array} \right]^T, \tag{2.13}$$

see also [91]. For the reduced-order models developed in this work, only the 2D-motion in the xz-plane is considered and $\boldsymbol{\xi}$ reduces to

$$\boldsymbol{\xi} = \left[\begin{array}{ccc} x_p, & z_p, & \beta_p \end{array} \right]^T, \tag{2.14}$$

see also Eq. (3.1), related to the reduced order model derivation. The equation of motion is

$$- \omega^2 \left[\boldsymbol{M} + \boldsymbol{A}(\omega) \right] \boldsymbol{\xi} + j\omega \boldsymbol{B}(\omega)\boldsymbol{\xi} + \boldsymbol{C}\boldsymbol{\xi} = \boldsymbol{X}(\omega)\zeta_0(\omega) = \boldsymbol{F}^{(1)}(\omega), \tag{2.15}$$

with the structural mass matrix $\boldsymbol{M}$. With Eq. (2.15), the Response Amplitude Operator (RAO) $\xi(\omega)/\zeta_0(\omega)$ can be calculated, the transfer function from the wave height ζ_0 to the rigid-body generalized coordinates $\boldsymbol{\xi}$.

The above-mentioned separation of radiation and diffraction is convenient for a linear FOWT description. The matrices $\boldsymbol{A}(\omega)$ and $\boldsymbol{B}(\omega)$ represent the system properties, whereas $\boldsymbol{X}(\omega)$ stands for the external forcing on the right-hand side of the EQM.

Frequency-to-time-domain transformation

FOWTs are usually simulated in time-domain to obtain extreme and fatigue loads while accounting for a transient motion of the floating body. These transients can arise from wind-induced motion, transmitted through nonlinear force models, including the wind turbine controller. Therefore, Eq. (2.15) needs to be transformed into time-domain, which was achieved by Cummins, see [93]. Important is the mathematical description of the forces from radiated waves, resulting from a transient body motion. The dynamics of the bulk of fluid particles surrounding the hull are given in the frequency-domain by

$$\boldsymbol{K}(\omega) = \boldsymbol{B}(\omega) + j\omega \left[\boldsymbol{A}(\omega) - \boldsymbol{A}_\infty \right]. \tag{2.16}$$

The retardation function $\boldsymbol{K}(\omega)$ is the sum of a real part, the damping coefficient, and the imaginary difference of the added mass and its infinite-frequency limit $\boldsymbol{A}_\infty$. The transfer function from a body motion to the resulting forces from radiated waves can be obtained from the fluid impulse response function $\boldsymbol{K}(t)$. Ogilvie [94] realized a time-domain description of Eq. (2.16), by transforming its real part or the imaginary part as

$$\boldsymbol{K}(t) = \frac{2}{\pi} \int_0^\infty \boldsymbol{B}(\omega) \cos(\omega t) d\omega = -\frac{2}{\pi} \int_0^\infty \omega \left[\boldsymbol{A}(\omega) - \boldsymbol{A}_\infty \right] \sin(\omega t) d\omega. \tag{2.17}$$

Consequently, the impulse response function $\boldsymbol{K}(t)$ is available from the first-order panel code coefficients $\boldsymbol{A}(\omega)$ and $\boldsymbol{B}(\omega)$.

With the impulse response function $\boldsymbol{K}(t)$, the generalized radiation forces can be written, according to Cummins, as function of the generalized body acceleration $\ddot{\boldsymbol{\xi}}$ and velocity $\dot{\boldsymbol{\xi}}$ with a convolution integral

$$\boldsymbol{F}_{rad}(t) = -\boldsymbol{A}_\infty \ddot{\boldsymbol{\xi}}(t) - \int_0^t \boldsymbol{K}(t-\tau)\dot{\boldsymbol{\xi}}(\tau)\mathrm{d}\tau. \tag{2.18}$$

Cummins' equation is the complete time-domain EQM, including the radiation forces of Eq. (2.18)

$$(\boldsymbol{M} + \boldsymbol{A}_\infty)\ddot{\boldsymbol{\xi}}(t) + \int_0^t \boldsymbol{K}(t-\tau)\dot{\boldsymbol{\xi}}(\tau)d\tau + \boldsymbol{C}\boldsymbol{\xi}(t) = \boldsymbol{F}^{(1)}(t). \tag{2.19}$$

It is commonly implemented in state-of-the-art floating wind simulation tools like FAST, see [95] and others. The exciting forces $\boldsymbol{F}^{(1)}(t)$ on the right-hand side of Eq. (2.19) are usually obtained through an IDFT of a complex force spectrum $\boldsymbol{F}^{(1)}(\omega)$. Alternatively, a transfer function can be fitted to the dynamics from wave height ζ_0 to the generalized forces $\boldsymbol{F}^{(1)}$. The convolution integral of Eq. (2.19) is numerically demanding because a time history of platform states has to be kept in the memory for the integration over times τ. Also here, a transfer function can be fitted to avoid this problem. These approaches are subject of the next section.

In summary, Eq. (2.19) has several important properties. Firstly, the added mass, or the forces in phase with the body acceleration, depend on the body frequency of oscillation. Thus, the eigenvalue problem needs to be iterated, as discussed in [96]. Secondly, the damping force, due to the dissipated energy with the radiated waves, depends on the frequency of oscillation. For many FOWT types, this linear radiation damping is small compared to the viscous damping through shed vortices. This will be discussed in more detail in the Section 3.5.

Parametric dynamic models

The above EQM in frequency-domain, Eq. (2.15), and in time-domain, Eq. (2.19), are both based on "numerical" transfer functions, due to the hydrodynamic coefficients, $\boldsymbol{A}(\omega)$, $\boldsymbol{B}(\omega)$ and $\boldsymbol{X}(\omega)$ from the panel code, but they are not parametric equations in the Laplace domain. In this section, an alternative is presented, which is especially useful for the controller design of Chapter 5. The term "parametric" means here a Linear Time-Invariant (LTI) model with a nonzero number of states in the case of a state-space model, or poles, in the case of a linear transfer function. The coefficients of these models are parameterized such that the new LTI model represents the best fit to the original model from the panel code through methods of system identification. The advantage of these models is mainly that the complete time-domain

dynamics are described as a "unified", parametric system with a general form

$$\dot{\boldsymbol{x}} = \boldsymbol{A}\boldsymbol{x} + \boldsymbol{B}\boldsymbol{u}$$
$$\boldsymbol{y} = \boldsymbol{C}\boldsymbol{x} + \boldsymbol{D}\boldsymbol{u}.$$

(2.20)

The state vector is denoted by $\boldsymbol{x}$, the input vector by $\boldsymbol{u}$ and the output vector by $\boldsymbol{y}$. Such a model has been applied for control-oriented representations of floating systems, especially in order to avoid the convolution integral of Eq. (2.19). In this case, the fitted dynamic model of Eq. (2.20) represents the dynamics from platform position to the radiation forces on the platform. Such LTI models for the radiation problem were proposed in [97] and [98] for wave energy converters and in [99] and [100] for vessels with the description of the corresponding Matlab toolbox in [101]. The method of a fitted state-space model has been applied to floating wind turbines and incorporated in the FAST model [39], in [102]. It is therefore possible to directly compare the performance of coupled time-domain simulations of floating wind turbines using Cummins' equation with the fitted LTI radiation model.

Also the wave excitation force coefficient $\boldsymbol{X}(\omega)$, part of Eq. (2.19), can be subject to a system identification for an LTI model. As part of the research on this thesis, the theory provided in [97] was applied to two FOWT platforms in [103]. The original model with the heave-DoF, only was extended to the surge and pitch-direction for the non-cylindric shapes of a semi-submersible.

The input to this dynamic wave force model is the incident wave height ζ_0. This is a more intuitive input than the hydrodynamic forces $\boldsymbol{F}^{(1)}$, which are the inputs in other models. The new method is especially advantageous for the set up of parametric transfer functions, either of the plant (from system inputs $\boldsymbol{u}$ to outputs $\boldsymbol{y}$, or system states $\boldsymbol{x}$) or from a disturbance (wave height ζ_0 to outputs or system states). These "disturbance models" are important for the design of controllers like Dynamic Positioning (DP) control [104] for vessel stabilization and disturbance rejection. Here, a slow feedback control attenuates the excitations from second-order drift forces on offshore supply vessels. For the complex dynamics of FOWTs, such disturbance rejection methods are important, see e.g. [105] for structural control using Tuned Mass Dampers (TMDs), [106] and [107] for nonlinear and linear model predictive control and [108] for feedforward control. Feedforward control is seen as a promising application of the wave model of this work since a better system description together with advanced wind and wave sensors can help to reduce fatigue and also extreme loads. The parametric wave excitation model will be included in the reduced-order model development in Chapter 3.

Morison's equation

Morison developed a semi-empirical force model for the wave forces on slender vertical piles [109]. It has been extended for floating bodies and has a number of practical advantages over Cummins' equation. Morison's equation gives the horizontal force $\Delta \boldsymbol{F}$ on a cylindrical sec-

tion or "strip" i in the normal directions k of the body surface with diameter D and length Δl. The force is a function of the undisturbed fluid accelerations a_{ik} and the velocities v_{ik}. The Morison forces in the two horizontal directions in the inertial frame are given by

$$\frac{\Delta F_{ik}}{\Delta l} = k_M a_{ik} + k_D\, v_{ik}|v_{ik}| \tag{2.21}$$

with

$$k_D = \frac{1}{2}\rho_w C_D D \qquad \text{and} \qquad k_M = C_M \rho_w \pi \frac{D^2}{4}. \tag{2.22}$$

Several parallels are present between Cummins' equation (2.19) and Morison's equation (2.21). The inertia coefficient C_M can be obtained from the added mass coefficient C_A as $C_M = 1 + C_A$. In Eq. (2.21), no body motion is yet considered such that the first summand represents the Froude-Krylov wave forces, represented by $\boldsymbol{F}^{(1)}$ in Eq. (2.19). The Froude-Krylov wave forces from Morison's equation are equal to the panel code results for low frequencies, where diffraction is negligible, with $C_A = 1$, see [92]. Both coefficients, for drag C_D, and added mass C_A, need to be obtained from experiments or from the literature, e.g. [110]. For simple shapes, the zero-frequency limit $\boldsymbol{A}_0$ of the added mass coefficient from the panel code can be used as a reference as shown in [111] and [112].

An extension of Morison's equation has been made for moving bodies [113]. Additional to the undisturbed wave kinematics, the floating body velocity $v_{b,ik}$ and their derivatives $\dot{v}_{w,ik}$ and $\dot{v}_{b,ik}$ determine the external Morison force

$$v_{ik} = v_{w,ik} - v_{b,ik} \qquad \text{and} \qquad a_{ik} = \dot{v}_{w,ik} - \dot{v}_{b,ik}. \tag{2.23}$$

Thus, the Froude-Krylov forces and the radiation added mass forces are represented, as in Cummins' equation, Eq. (2.19). The fluid kinematics are usually calculated as explained in Section 2.5.3 assuming "hydrodynamically transparent" structures, neglecting diffraction effects. In Morison's equation, the acceleration-dependent force (first part of Eq. (2.21)) is independent of the frequency. This simplification is valid for slender cylinders, which experience little radiation forces.

The semi-empirical nature of Morison's equation offers several advantages. No pre-computation of the hydrodynamic coefficients $\boldsymbol{A}(\omega)$, $\boldsymbol{B}(\omega)$ and $\boldsymbol{X}(\omega)$ of Eq. (2.19) with a panel code is necessary. As a consequence, the distributed forces over the body axial coordinate can be obtained. This is not generally possible with Cummins' equation, because the panel code pre-processor integrates the pressures over the wetted surface. With the distributed pressures, the deformation and the structural stresses of the floating platform can be calculated. This is only possible through a post-processing with Cummins' equation, as discussed in Section 2.5.1. Additionally, the quadratic drag force is considered in Morison's equation, which is neglected by the panel code.

Many of the widespread FOWT simulation codes combine Cummins' equation with Morison's equation. The advantage of Cummins' equation with the panel code coefficients is that diffraction is generally considered such that no restriction on the body dimensions, like the column diameter-to-wavelength ratio D/λ, is present. This is especially important for the FOWT types barge and semi-submersible. The quadratic viscous drag forces, however, are not part of Cummins' equation. This is the reason why the drag force component of Eq. (2.21) is often added as additional component to Cummins' equation (2.19) as shown in [53]. Morison's equation has also been extended for vertical directions, which is important for semi-submersibles with heave plates. A vertical drag force is here necessary to model, see [112]. The importance of the vertical drag forces of heave plates will be discussed in more detail in Chapter 3 and Chapter 4.

For the present model, a linearization of Morison's equation is necessary for the frequency-domain model. It will be described in Chapter 3 on the simplified simulation model. The nonlinear drift loads at low frequencies will be introduced next.

Second-order slow-drift forces

The discussed wave force transfer function $\boldsymbol{X}(\omega)$ of Eq. (2.15) is a linear description. As will be discussed in Section 2.8, experimental tests have shown that non-negligible wave forces outside the frequencies of the free-surface elevation ζ_0 appear for FOWTs. These forces result mathematically from nonlinear effects, especially from the free-surface boundary condition. With the quadratic boundary condition, regular waves exert a steady mean drift load on a vertical wall in the wave propagation direction, which is not the case if linear potential flow is applied. The theory of mean drift and slow drift forces is well explained in the lecture notes [114]. The same model, solved for a bichromatic wave, includes forces which are out of the range of their own frequency. The forces appear at the sum and the difference of the two wave frequencies. The resulting force transfer function has two frequencies as input and is therefore called a Quadratic Transfer Function (QTF). The low-frequency force (at the difference frequency) may coincide with the system eigenfrequencies and yield large amplitudes of motion of the floating body and large stresses in the mooring system, see [115]. Thus, the drift force has a frequency lower than the two input waves and therefore the force spectrum contains energy where the wave height spectrum does not contain any energy. The same effect is known from acoustics. The so-called "beat pattern" arises from the interference of two waves of close frequencies. These two waves sum up to a resulting wave with an envelope of a low frequency, also called "bounded long waves", see [90].

The physical effects included in second-order potential theory are, as opposed to linear potential flow: (1) the integration of the forces up to the instantaneous waterline and (2) the nonlinear boundary condition at the free surface (Bernoulli equation with quadratic dynamic

pressure, e.g. [89, p. 48]). Two numerical options are available to calculate the second-order potential. The more efficient one is the farfield solution, based on the momentum equation. It gives, however, only translational forces. The other option is a pressure integration over the floating body wetted surface. This option is called the nearfield solution.

In [116] and [117] the phenomenon of second-order potential flow forces coming from sum and difference frequencies on FOWTs were analyzed and compared among different computational codes. They showed that especially the difference frequency component can yield platform resonances. A comparison of slow drift forces with aerodynamic forces for the OC3 spar [111] was made in [118] and it was shown that the energy of the motion response due to slow drift forces is of smaller magnitudes than the aerodynamic force. In [119] the slow drift forces were parametrically calculated for a fixed cylinder with a simplified approach showing that the response magnitude is a function of the platform diameter. Especially for large diameter structures (offshore oil and gas industry), a large response is to be expected for large waves. Analyses for FOWTs on TLPs were presented in [120] and [121] showing that the slow drift is of less importance for FOWTs with taut moorings, although it is noted in [8] that the sum-frequency forces are important for the prediction of vertical motions and tendon tensions. Many of the studies also mention that the effect of aerodynamic damping is of importance when rating the significance of second-order forces and therefore the controller dynamics, idling cases or cases of misaligned waves can be critical. The possibility to include second-order potential flow forces in time-domain FOWT simulations was added to FAST in version 8, see [95].

In this work, Newman's approximation is implemented in the simulation model. It is a simplification in order to avoid the calculation of the full Quadratic Transfer Function (QTF). Especially for the comparisons with the experiments of Chapter 4, these forces are important and will be analyzed in more detail.

2.5.4 Mooring dynamics

As for the previously described submodels of aerodynamics and hydrodynamics, also the mooring lines, responsible for the station-keeping of the FOWTs, can be modeled with different fidelity levels. The major difference among the widespread models is the static or dynamic description: Static mooring line models predict the section force in the line or at the anchor/fairlead as a function of its position only. Dynamic models include also velocity and acceleration-dependent effects such as the mooring line inertial mass, added water mass and damping through vortex shedding.

A detailed analysis comparing static and dynamic models for all three types of FOWTs was carried out in the thesis by Azcona [122]. It could be shown that usually the fatigue loads in the line itself are highly affected by the mooring model type and to a lesser extent the wind turbine and rotor loads. The same author concluded in [123] that the tower-base fatigue loads

are also affected by the mooring model for TLPs and to a lesser extent for semi-submersibles, mostly the portion of the tower-base bending moment in side-side direction. These general findings were confirmed in a comparison of different models with experimental data [124].

Several numerical tools are available for mooring line simulations like the ones integrated into FAST, the quasi-static MAP++ model [125] and the dynamic model MoorDyn [126], which both allow the modeling of multi-segmented lines. Another dynamic mooring line model is the one developed in Simpack, see [26, 127] and Opass, verified through experiments in [128]. A study on different available methods for the derivation of the equations of motion for dynamic models can be found in [129]. Due to the nonlinearity of mooring line forces, higher-fidelity models are necessary for the computation of extreme mooring tensions for FOWTs in storm conditions, where slack line events can happen, yielding large ultimate loads. A study on such load conditions can be found in [130]. For linear frequency-domain analyses, the mooring line properties are usually linearized such that the mooring line restoring forces on the platform are represented by a 6×6 stiffness matrix. For the reduced-order model developed in this work, a quasi-static model is implemented due to its computational efficiency and its suitability for linearization, see Chapter 3.

2.6 Linear Frequency-Domain Modeling

As mentioned at the beginning of Section 2.5, linear frequency-domain methods had been used for offshore oil and gas and wind turbine modeling before computing power increased significantly in the last 15 years and the attention goes more towards nonlinear high-fidelity models. However, for the purpose of this work with large parametric studies and dynamic system analyses, linear frequency-domain modeling is highly advantageous. Even the full load response to a stochastic environmental excitation can be computed efficiently through a multiplication of transfer functions. Especially in ocean engineering such methods are advantageous because the external loads from waves and wind are stochastic in nature. In the frequency-domain, the power spectrum $S_{xx}(\omega)$ can be calculated numerically with a Discrete Fourier Transform (DFT) of the stationary stochastic process $x(t)$. The stationarity means that the expected value $E[x(t)]$ and $E[x(t)x(t+\tau)]$ are both independent of the time t. The complex amplitude spectrum $x(\omega)$ results from the discrete DFT, normalized with the number of elements N of the frequency vector, as

$$x(\omega) = \frac{\mathrm{dft}(x(t))}{N}, \tag{2.24}$$

where N includes also negative frequencies in the Fourier space. Thus, $x(\omega)$ is a two-sided amplitude spectrum, which is consequently half the magnitude of the one-sided amplitude spectrum. In the Laplace domain, no negative frequencies exist but the transient dynamics are covered by the complex Laplace variable s, while the frequency variable in Fourier space is the

real angular frequency ω. With a Single-Input-Single-Output (SISO) state-space model with system matrix $\boldsymbol{A}$, input vector $\boldsymbol{b}$ and output vector $\boldsymbol{c}$, the linear transfer function $G(j\omega)$ in the imaginary Laplace domain can be calculated with the identity matrix $\boldsymbol{E}$

$$G(j\omega) = \boldsymbol{c}^T(j\omega\boldsymbol{E} - \boldsymbol{A})^{-1}\boldsymbol{b}. \qquad (2.25)$$

The PSD, the response auto-spectrum is defined as

$$S_{xx}(\omega) = \frac{dt}{N}\left|\mathrm{dft}(x(t))\right|^2 = dtN\left|x(\omega)\right|^2. \qquad (2.26)$$

In offshore wind turbine analyses, the wind and wave disturbances can be described as spectra of stochastic processes, defined in standards such as [131], which will be detailed in Section 2.7. A good introduction to stochastic processes and spectral methods is given in [46] and the references therein. For a Multi-Input-Multi-Output (MIMO) system $\boldsymbol{G}(\omega)$, the response auto-spectrum $\boldsymbol{S}_{yy}(\omega)$ to the matrix $\boldsymbol{S}_{uu}(\omega)$ of the input spectra is simply given by the multiplication

$$\boldsymbol{S}_{yy}(\omega) = \boldsymbol{G}^{*T}(\omega)\boldsymbol{S}_{uu}\boldsymbol{G}(\omega), \qquad (2.27)$$

where $\boldsymbol{G}^{*T}(\omega)$ denotes the complex conjugate transpose. The argument ω covers positive frequencies $\omega > 0$ and therefore the PSD is single-sided. The imaginary unit of the Laplace-domain frequency axis will be omitted for the calculation of response spectra. From a power spectral density $S_{xx}(\omega)$, the standard deviation σ or Root Mean Square (RMS) can be calculated from the zeroth spectral moment m_0 using Parseval's theorem by numerically integrating over the positive frequencies

$$\sigma = \sqrt{m_0} = \sqrt{\int_0^\infty \left|S_{xx}^{1sdd}(f)\right|\mathrm{d}f}. \qquad (2.28)$$

Therefore, no integration or "time-stepping" as in time-domain methods is necessary for solving the Ordinary Differential Equation (ODE) of the state-space model, which can save orders of magnitude of computational time. The large amount of simulation time necessary for calculating a sufficient number of load cycles of all relevant frequencies for fatigue load estimation makes time-domain simulations challenging, see [132] for a good elaboration of fatigue design methods for wind turbines. This is why these efficient methods reappeared recently in offshore wind simulation studies, see [16, 69, 133, 134]. A selection of published frequency-domain simulation tools for wind turbines includes the tool Turbu by the Energy Research Center of the Netherlands (ECN) described in [135] and Hawc2Stab by DTU, see [136].

For wind turbines, the dependency of the system dynamic properties on the azimuth angle of the rotor presents a challenge for the frequency-domain modeling. This is usually handled through the transformation of the states defined in the rotating frame into the non-rotating

frame. An application of this Coleman transformation can be found in [69]. In the same reference also the challenges arising from nonlinearities of the aerodynamic forces are discussed. One of these cases is when the flow is not anymore attached to the airfoil and stall occurs, see Section 2.5.2. For large rotor blades, also structural nonlinearities play a significant role such that linear beam model might not always be sufficient as was discussed in Section 2.5.1.

For hydrodynamics, nonlinearities occur if steep or braking waves are modeled or when considering the nonlinear potential flow problem (quadratic free-surface boundary condition), see Section 2.5.3. Next to the wave model, the forcing model is also of importance. The linearization of the viscous drag is a challenging task. This is discussed in detail in Chapter 3.

Linear models are only valid to represent nonlinear physics, where a small change of Δx about an operating point x_0 occurs. These nonlinearities have to be considered with respect to the phenomenon being analyzed. In summary, frequency-domain methods are very useful for conceptual design calculations, optimizations and for applying linear control design methods, where an understanding of the overall system properties is important. The linear model used in this work will be derived in Chapter 3.

2.7 Environmental Conditions and Load Calculation

The structural loads are usually the response quantity of interest for limit-state design, where the Ultimate Limit State (ULS) can be a design driver but, especially for wind turbine components, also the Fatigue Limit State (FLS). Additionally, also displacements and accelerations can be a constraint, e.g. the maximum blade tip deflection or the maximum acceleration at the nacelle. This section will introduce the characteristics of wind and waves and their modeling. Eventually, a simplified set of Design Load Cases (DLCs) will be defined and the principles of load calculation and requirements for the design.

2.7.1 Wind

The wind can be modeled either as a deterministic time-dependent function or as a random stochastic process. For stochastic load simulations, the mean wind speed is constant in time periods between $10\,\text{min}$ to $60\,\text{min}$. The fluctuating component is determined by the turbulence spectrum, where the standard deviation σ_x in the longitudinal direction is defined for the Normal Turbulence Model (NTM) by the IEC [131] as

$$\sigma_x = I_{ref} \left(0.75 \bar{v}_{hub} + b \right).$$
(2.29)

The expected value of the turbulence I_{ref} at $15\,\text{m/s}$ depends on the class the turbine is designed for. In this work, the lowest turbulence class (C) is used due to the reduced turbulence at sea.

In [131] factor b is defined as $b =0.56\,\mathrm{m/s}$. With σ_x, the Kaimal spectrum can be defined based on [131, Appendix B.2]. The standard also defines an exponential coherence model for the longitudinal component, with which it is possible to generate 3D turbulent wind fields. The more advanced Mann model, also part of the standard, defines additionally a coherence model for the lateral and vertical wind speed components. For time-domain analyses, the spectra at each grid point over the rotor plane are augmented with a random phase and transformed to the time-domain with an IDFT. A wind profile is a representation of the boundary layer due to surface friction, which depends on the surface roughness. In this work, a logarithmic profile for the longitudinal wind speed $\bar{v}(z)$ is used

$$\bar{v}(z) = \bar{v}_{hub}(\frac{z}{z_{hub}})^{\alpha} \tag{2.30}$$

with a logarithmic exponent $\alpha = 0.14$ following the offshore standard [137].

The basic theory of spectral wind models and time-domain realizations can be found in [138] and in the TurbSim user guide [139]. The tool is used in this work for generating the wind fields.

2.7.2 Waves

Linear wave theory for the calculation of the hydrodynamic forces was already discussed in Section 2.5.3. The definition of the met-ocean conditions determining the properties of the external loading is the subject of this section. For load calculations, deterministic regular waves, or focused waves can be used for an efficient representation of extreme situations. Alternatively, irregular, stochastic waves represent more realistic sea-states. Common parametric wave spectra are the Pierson-Moskowitz spectrum and the Jonswap spectrum, see [89, Chapter 5.8]. They are defined as a function of the peak spectral period T_p and the significant wave height H_s, the mean of the highest third crest heights. The instantaneous free surface elevation $\zeta_0(t)$ is usually the one at the Center of Flotation (CF) at the initial position of the FOWT without wind forces. Figure 2.5 shows the Jonswap wave spectra according to the met-ocean conditions of Table 2.1.

2.7.3 Design loads

With the standards specific to FOWTs by DNV-GL [28] and the International Electrotechnical Commission (IEC) [140] the necessary set of DLCs is defined and the previous standards for bottom-fixed offshore wind turbines, see [137] and [141], are extended. The IEC standard references additionally the standard for onshore wind turbines for all requirements related to the wind models, see [131]. A variety of operational, idling and fault cases are defined under normal and extreme environmental conditions. For a representative selection of met-ocean conditions
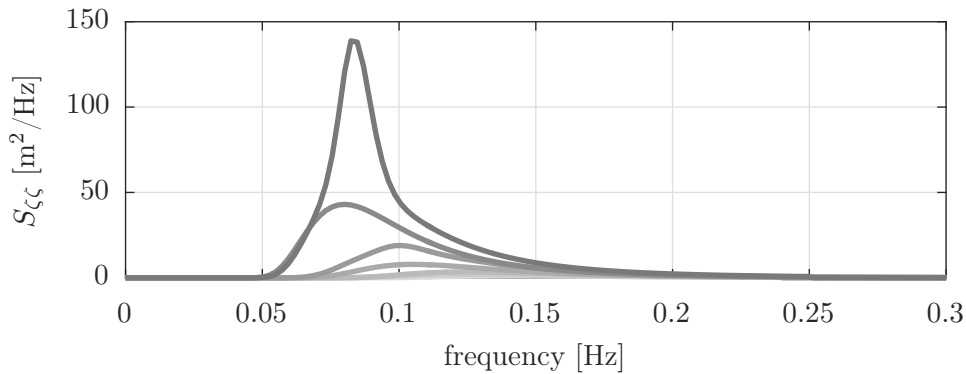
Figure 2.5: Jonswap wave spectra used in this work with parameters of Table 2.1. Darker colors for increasing sea state.

for the design calculations according to the standard, site data is necessary. For ULS conditions it is necessary to perform a reliable extreme value extrapolation, see [131]. For FLS conditions the set of operational plus fault cases has to be selected according to [137], using a binning with respect to short-term mean wind speeds. In each bin, the most likely set of combinations of wind speed, significant wave height and peak spectral period has to be determined. Based on measurements, joint probability functions can be derived, see [142], allowing a selection of the combinations for the power production case (DLC1.2, [137]). A reduced set of these operational conditions from the project LIFES50+ can be found in Table 2.1, taken from [143, Chapter 7]. Figure 2.6 shows the Probability Density Function (PDF) for the wind speed fitted with a Weibull distribution. These environmental conditions will be used in the remainder of this thesis.
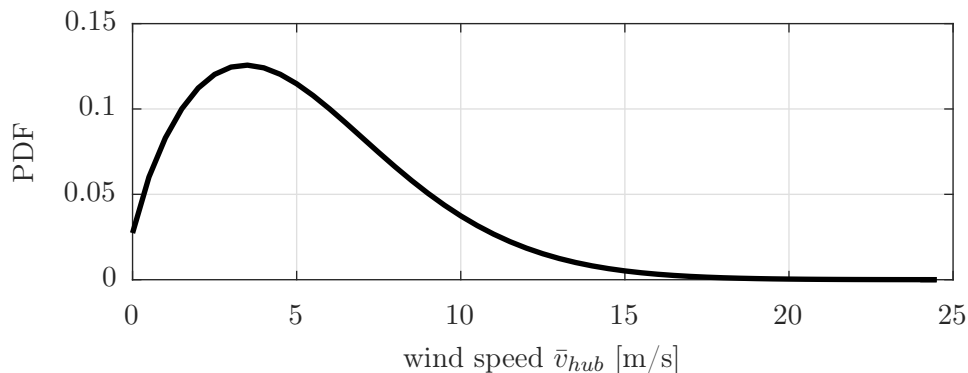
Figure 2.6: Wind speed Weibull PDF for fatigue design.

As mentioned in Section 1.3, the focus of this work are operational load cases, where the wind turbine control is active. Extreme loads are not addressed as extensively as fatigue loads. This is due to the fact that the employed simplified models are valid in a small range about an operating point. Extreme load simulations require models of higher fidelity due to large excursions, deflections where nonlinear effects become important. The main objective of this

Table 2.1: Met-ocean conditions of LIFES50+ fatigue load case (DLC1.2).

Wind speed $\bar{v}_{hub}$ [m/s]	Significant wave height H_s [m]	Peak spectral period T_p [s]
5.0	1.38	7.0
7.1	1.67	8.0
10.3	2.2	8.0
13.9	3.04	9.5
17.9	4.29	10.0
22.1	6.2	12.5
25.0	8.31	12.0

thesis is to provide overall indications of platforms with limited excitations to wind and waves. The fatigue loads can be evaluated using load cycle counting methods. These will be introduced in the following.

Damage-equivalent loads from time series

Whereas many civil engineering structures can be designed using static load calculation, fatigue can be critical for wind turbines depending on the component material. Fatigue damage assessment usually relies on dynamic time-domain simulations. A load cycle counting reveals the damage caused by cyclic stresses in the components. The load calculation procedure for steel structures is detailed in the standards Eurocode [144] or DNV [145], specific to offshore structures. The load cycles from simulations are compared to experiments of a given material and a given configuration, e.g. different geometries and mechanical joints. For these specimen, the failure event is recorded depending on the stress amplitude (S) and the related number of load cycles (N). This results in S-N-curves, usually plotted in a lin-log scale. Typically for steel structures is an S-N curve of a decaying straight line, which flattens for high load cycle numbers and low load ranges, where no fatigue failure occurs (fatigue endurance). The S-N curves from experimental tests, relevant for wind turbine towers, can be found in [144]. For simplified assessments, the S-N relation can be modeled for $N < 10^6 \ldots 10^7$ cycles as

$$N = a_d S^{-m} \tag{2.31}$$

with the slope $-1/m$ of the straight line in a graph with logarithmic x-scale and an intersection of the curve with the y-axis at a_d. Now the total damage caused by a load spectrum of different load amplitudes each with a different number of cycles can be assumed to accumulate linearly, according to the Palmgren-Miner rule. The rainflow counting method is commonly applied to the time series from load measurements or simulations for the cycle counting. The algorithm

used here is the one by Adam Nieslony[4]. The result is a histogram of the number of cycles n_j for a given load range S_j. The total damage D is according to [146, p. 114] the sum of the individual damage of each load range bin with n_j cycles divided by the corresponding cycle number N_j causing failure

$$D = \sum_{j=1}^{k} \frac{n_j}{N_j} = \frac{1}{a_d} \sum_{j=1}^{k} n_j \left(S_j \right)^m \leq \eta. \tag{2.32}$$

Here, the simplified S-N curve model of Eq. (2.31) is used. Failure occurs when D exceeds the usage factor η, depending on the component, see [146]. Fatigue is only assessed qualitatively in this work as structural design calculations are outside the scope of this thesis. Therefore, a reduced parameter representing the fatigue damage from a given load spectrum is used. It is the load amplitude (usually a section force or moment), exerted during a hypothetical number of cycles (here $N_r = 2 \times 10^6$) giving the same D as the full load spectrum. The Damage-Equivalent Load (DEL), represented by ΔS_{eq}, can be calculated as

$$\Delta S_{eq,i} = \sqrt[m]{\frac{1}{N_r} \sum_{j} \Delta S_j^m n_{ij}}. \tag{2.33}$$

A weighting using a distribution function such as the one of Figure 2.6 is possible by multiplying the load range number n_{ij} of the respective load range bin j with the lifetime fraction T_i/T_{life} of wind bin i giving

$$n_{ij} = n_j \frac{T_i}{T_{life}}. \tag{2.34}$$

In this simplified fatigue assessment, the influence of the mean stress and stress amplification factors due to the component geometry are not considered. Stress amplification at notches is neglected and, as a consequence, the uniaxial stress is proportional to the section force, or moment, see Section 3.2 for more details.

Damage-equivalent loads from frequency-domain spectra

The damage estimation from a given load spectrum with Eq. (2.32) requires load time series from measurements or time-domain simulations to get the histogram with the cycle numbers n_j through a rainflow counting algorithm. Various attempts have been made to obtain an estimation of the load histogram from a frequency-spectrum. This has the advantage of a reduced simulation time through frequency-domain methods as introduced in Section 2.6 and was especially necessary for the design of offshore oil and gas structures under stochastic loading before computational power became affordable. A comparison of the different approaches can

---

[4]`http://de.mathworks.com/matlabcentral/fileexchange/3026-rainflow-counting-algorithm`, accessed on January 22, 2018.

be found in [147]. The most accepted method is the one from Dirlik [45]. It approximates the number of cycles N for the different load ranges S. The Dirlik formula is written as

$$n_j = E[P] \, p(S_j) \, T, \tag{2.35}$$

where $E[P]$ is the expected value of the number of peaks, a function of the second and fourth spectral moments. The parameter $p(S)$ is a nonlinear function of the zeroth, first, second and fourth spectral moments, see [147, Eq. 6]. The resulting number of cycles for each stress range bin n_j is given for a time period T. In order to obtain a representative set of cycle numbers for each load range bin, the method of inverse transform sampling can be applied: From the load range histogram n_j a Cumulated Distribution Function (CDF) can be calculated through an integration of the histogram over the bins of the load cycle numbers. The representative set of samples (equal to the result of a rainflow counting) can be obtained by assuming equally distributed cycle counts, which are then mapped through the CDF from the count running sum on the load ranges. The method has been implemented in the linearized model of Chapter 3 and compared to the conventional rainflow counting method, see Section 3.9.

For the assessment of the controller, additional signals are of relevance, apart from the structural loads. These are summarized together with the selected constraints for this work in Table 2.2. The constraints on the left may not be exceeded, whereas the targets, usually the signal Standard Deviation (STD) is sought to be minimized for optimal performance. The indicated overshoots are evaluated in this work for one-hour time series. This is a simplification for a straightforward quantitative design assessment, while for detailed design the probability for a signal to exceed its bounds with respect to its lifetime needs to be calculated. The main loads to be minimized by design and controller optimization are the tower-base loads. These loads are the highest of FOWTs, compared to onshore turbines, see Section 2.5. Furthermore, they represent the response of the tower-top displacement and also of the platform pitch motion. These are important signals when looking at the overall FOWT system dynamics as already discussed in Section 2.5.

Table 2.2: Requirements on controller performance.

Requirement		Target	
Rotor speed overshoot	max. 15 %	STD rotor speed	min.
El. power overshoot	max. 15 %	STD el. power	min.
Generator torque overshoot	max. 15 %	STD generator torque	min.
		STD blade pitch angle	min.

Estimation of short-term extremes from frequency-domain spectra

A means to obtain short-term extreme responses from frequency-domain spectra will be introduced in this section. This is especially useful for controller tuning when it is necessary to get an estimate of the overshoot of the electrical power or the generator torque, the design requirements shown in Table 2.2.

Assuming stationary Gaussian waves and a narrow-banded response signal, the response amplitudes are Rayleigh distributed [90]. The short-term probability density function f_{st} of the amplitudes y is then given by

$$f_{st}(y) = \frac{y}{m_{0y}} \exp\left(-\frac{y^2}{2m_{0y}}\right). \tag{2.36}$$

The zeroth spectral moment m_{0y} of the response is equal to σ_y^2, the squared STD.

The probability of exceedance of the amplitudes y for a given time T can now be estimated with the CDF P_{st} or the integral over the amplitude range of Eq. (2.36) as

$$P_{st}(y > a) = \int_a^\infty \frac{y}{m_{0y}} \exp\left(-\frac{y^2}{2m_{0y}}\right) \mathrm{d}y. \tag{2.37}$$

The total number of occurrences N_T of the values of y exceeding a limit a can be estimated from the average zero-upcrossing period T_{2r}. This follows from the conception that "there is only one peak value between an upcrossing and a subsequent downcrossing of any level a" [148, p. 237]. It results

$$N_T = \frac{T}{T_{2r}} P_{st}(y > a). \tag{2.38}$$

The amplitude which is reached or exceeded N_T times in a given time T can be calculated with Eq. (2.38), solving for the amplitude a. A comparison of this estimation with time-domain data is also shown in Section 3.9, see Figure 3.29.

2.8 Model Tests

Experimental testing has become especially important for FOWTs due to the additional dynamics from the floating substructure, mooring lines and wave forces. Thus, model tests have the objective to validate software tools in general, but as the TRL increases with the first tests in a realistic environment, model tests also helped to reduce the risk associated with the deployment of a prototype.

It is common to the scaled testing of offshore structures to maintain a constant Froude number Fr, see e.g. [91]. The Froude number is written with the characteristic length D, the

velocity v and the gravitational constant g as

$$Fr = \frac{v}{\sqrt{gD}}. \tag{2.39}$$

Consequently, if the length scaling factor is λ (e.g. $\lambda = 1/60$ for the TripleSpar, see Section 4) forces are scaled with λ^3. The scaling factors for masses, forces and frequencies are collected in Table 2.3. Scaling with this method shows that the frequency increases in model scale and the time coordinate decreases, which results in a smaller simulation timestep and a higher sampling rate for sensors, processors, communication interfaces, etc. Froude-scaling has been successfully employed in offshore engineering, see e.g. [90] or [91]. A difficulty arises if the drag becomes important, as it is usually Reynolds-dependent.

The Reynolds number

$$Re = \frac{vD}{\nu}, \tag{2.40}$$

is the ratio of inertia to viscous forces, a function of the kinematic viscosity ν. Since the working fluid of experiments is usually not modified (air or water) the viscosity remains constant and Re cannot be maintained while scaling down the system. Many offshore structures have small viscous forces compared to inertia forces and therefore for FOWTs the problem is more significant for the aerodynamic model of the wind turbine rotor, see [149] for an introduction. A solution has been to re-design the rotor for low Reynolds numbers. The most discussed tests of the FOWT community were the DeepCWind tests, [150] and [151], and the comparison to different simulation methods in the ongoing OC5 project. New methodologies of scaled testing include also Hardware-in-the-Loop (HIL) methods, where either the hydrodynamic or the aerodynamic model is replaced by a force actuator, which is real-time controlled. A simulation model calculates the forces, which are then imposed on the physical model. Such a test with a fan imposing the aerodynamic forces was conducted within INNWIND.EU, see [152]. A comparable approach was made in [153] and [154]. The same methodology but with an actuation of the hydrodynamic forces, instead of a physical wave basin was topic of the study [155] of the project LIFES50+. An overview of reported FOWT model tests with a comparison of the employed methods and outcomes can be found in [156]. The numerical FOWT design process including experimental tests is the focus of [157].

Table 2.3: Froude-scaling.

Parameter	Unit	Scaling factor
Length	L	λ
Mass	M	λ^3
Force	MLT^{-2}	λ^3
Frequency	T^{-1}	$\lambda^{-\frac{1}{2}}$

In the course of this research, two model tests were performed. One at the Research Laboratory in Hydrodynamics, Energetics & Atmospheric Environment, Nantes, France (LHEEA) in 2014 with the DeepCwind semi-submersible as part of the project INNWIND.EU[5], see [158, 159]. The other one focused on active blade pitch control on the TripleSpar semi-submersible concept designed as part of this research and described in Section 2.10 with a scaled 10 MW turbine, see [160]. This test was performed in a joint effort with DTU and National Renewable Energy Centre of Spain (CENER). The experience from both tests was fed back into the development of the reduced-order model of this thesis and a first validation study was done by Wei Yu in her thesis, see [161]. The hydrodynamic drag model of the simplified simulation model of Chapter 3 will be validated through these tests and the drag coefficients of the TripleSpar platform will be identified in Chapter 4.

2.9 Control

This section provides the basics of modern wind turbine control and a review of challenges and state-of-the-art control design methods for FOWTs.

2.9.1 Variable speed blade-pitch-to-feather-controlled turbines

The control system of modern wind turbines includes supervisory control for special events like start-up and shut-down. The safety system regulates emergency shut-down events when failures are detected to prevent damage to the turbine. Feedback control is mainly responsible for capturing the maximum amount of energy from the wind through controlling the rotor speed, depending on the wind conditions. In this work, the focus is on the feedback control of the rotor speed. Feedforward control is beneficial when information of the incoming disturbance is known, such as wind and waves for wind turbines, see [162]. Feedforward control is not considered in the present work.

The feedback control of wind turbines depends on the operating point with three regions and the switchings in between. Region 1 covers wind speeds not relevant for energy production. In region 2, the rotor speed is controlled by actuating the generator torque in a way that the optimal TSR is maintained in order to capture the maximum amount of energy. Region 3 is the above-rated region, where the blade pitch angle is actuated to control the rotor speed at its rated speed and consequently maintaining the rated power. Earlier control methodologies make use of the stall effect to reduce the lift force. This method avoids the blade pitch actuator but is not present anymore in most modern wind turbines. An introduction to wind turbine control can be found in [44] and [163].

---

[5]`http://www.innwind.eu/`, accessed on January 22, 2018.

2.9.2 Floating wind turbines

Whereas below-rated control does usually not imply challenges for the design of FOWT controllers, the coupled dynamics of the floating system pose difficulties together with the blade-pitch controller for above-rated wind speeds. A standard rotor-speed controller for above-rated wind will pitch the blades when the rotor speed exceeds its rated value. In the case of FOWTs, this feedback loop can imply, as a side-effect, that the tower or the platform experiences large excursions. This is due to the aerodynamic properties of the rotor: When the relative wind speed (the one seen by the rotor) increases, the controller will pitch the blades towards feather (increasing blade pitch angle) and thereby reduce the aerodynamic rotor torque. As a consequence, the thrust also decreases. This means, on the other hand, that an oscillation of the platform in pitch (about y, Figure 3.1) will become unstable if the controller reacts sufficiently fast to the sinusoidally oscillating relative wind speed.

The contradicting goals of stabilizing power for above-rated wind speeds and minimizing platform motion are a key challenge for FOWTs and of general importance for the fatigue life, see [164]. A too aggressively tuned blade-pitch controller results in unstable platform behavior. This is due to a Non-Minimum Phase Zero or Right Half-Plane Zero (RHPZ) of floating platforms. This leads to a bandwidth reduction of the blade pitch controller. A good explanation of this "negative damping" problem is given in [165]. A simple pole-placement method to adjust the Proportional-Integral (PI)-controller to mitigate this negative damping problem was proposed by [10]: The de-coupled rotor (including drivetrain) is considered as rigid body in the closed loop (with active blade pitch control). Then the rotor closed-loop eigenfrequency has to be selected lower than the critical support structure eigenfrequency, which is usually the platform pitch frequency. This is roughly aligned with the general control rule of thumb to limit the bandwidth for systems with RHPZs to half the frequency of the RHPZ according to [166, p. 187]. The advantage of this procedure is that no linearized model of the complete FOWT system is necessary but only the isolated rotor model and a quick definition of reasonable control gains for conceptual design is rather straightforward. The disadvantage is that first, the isolated rotor eigenfrequency might deviate from the coupled rotor eigenfrequency and therefore also the desired pole will deviate from the real pole of the coupled system. Second, the overall system stability is not ensured with this method and therefore, instabilities might still exist for certain operating points. The method was applied in [15] and compared with an additional tower-feedback controller in [11] for a barge-type platform. An evaluation of this method, also called "de-tuning of gains" was carried out by [167] and [168]. The comparison in [169] includes also controllers with more than one feedback loop, in order to further improve the control performance.

More advanced strategies are, among others, Multi-Input-Multi-Output (MIMO) controllers: Here, the feedback of additional signals, the addition of more loops to the control architecture,

can help to reduce the coupling effects in the system. The feedback of, e.g. the tower-top acceleration is possible such that the blade pitch angle reacts not only to the rotor-speed deviation but also to the tower-top acceleration. A sequential, "manual" tuning of feedback loops and their respective gains, comparable to decentralized control, has been called "multi-SISO" control, see [3, Appendix]. Real MIMO control looks at the FOWT system as a dynamic system with multiple inputs (actuators like generator torque and blade pitch angle) and outputs (rotor speed, tower-top displacement, etc.). As several standard linear control design methods do not hold anymore for MIMO systems, the design process is more complex, see [170] for a study on onshore turbines. Therefore, the authors of [12] published a "parallel path modification" approach to mitigate the constraints from the RHPZ through the feedback of the tower-top acceleration on the generator torque – an approach published in the early stages of MIMO control research, see [171].

Furthermore, optimal control design approaches have been presented, where optimization algorithms are applied to find the best feedback law, mostly using a linearized system description. Such optimal controllers are a Linear Quadratic Regulator (LQR), as presented in [172], with a state-feedback law. The LQR problem was extended to include nonlinearities of the FOWT system in [173]. The optimal control problem in the frequency-domain can be solved with H_2 or H_∞ controllers, see [166]. Here, a target response (sensitivity function) is defined in the frequency-domain with a given set of available sensors. This has been applied to onshore wind turbines in [174, 175] and to FOWTs in [14] and [176]. Other multivariable controllers were developed by [177], mostly using all or the most relevant system states as controller input. A model development and Linear Model-Predictive Control (MPC) design can be found in [106] and, especially aiming at wave disturbance preview in [178]. A comparison of different approaches for model predictive control for wind turbines can be found in [179]. An advanced controller addressing specifically the purpose of reducing disturbances is Disturbance Accomodating Controller (DAC): A waveform of the disturbance is assumed and augmented to the system as a feedforward term to cancel out the disturbance forcing. This was applied by [180] and [181] to onshore wind turbines and to FOWTs in the thesis [182], among others.

Additional actuators to stabilize the tower were implemented in [105]. As was noted by [183], the standard actuators of a turbine (generator torque and blade pitch angle) might not be strong enough to mitigate first-order wave loads. Here, additional actuators can help to improve the motion response of a FOWT. For onshore turbines, passive systems like TMDs or tuned liquid column dampers have been investigated. Also active systems are possible, see e.g. [105] and the Master's thesis [184]. An additional actuator on the nacelle of a FOWT was proposed by [185], an active vane to damp tower-top vibrations. A semi-active liquid column damper with an optimal control approach was presented in [186]. In the project MARINA-platform, the combination of a FOWT and a wave-energy converter was investigated and the potential to produce energy from the waves. Possible approaches for such multipurpose offshore structures

are compiled in [187]. For fixed-bottom foundations structural damping devices have been analyzed to reduce structural loads for large offshore wind turbines in [188], especially focusing on the adaptation of the control to the actual structural properties. A general report on methods for the mitigation of tower loads can be found in [189]. For offshore wind turbines, various control approaches including tower feedback control were compared and assessed in the thesis by Fischer [190]. Within the project INNWIND.EU different members and cross-braces with specific dynamic properties are placed inside the tower or foundation to optimize the load response – something which is in general also feasible for FOWTs. Especially for damping the blade response and smoothen the electrical power, smart blades, e.g. with flaps, are subject to research, see e.g. [191]. Many of these studies show that additional actuators offer the prospect of damping the structural response with more or less use of actuator power. Some of these systems are already being applied, i.e. TMDs in civil engineering, whereas others, like vanes are still being analyzed in research projects.

With Individual Pitch Control (IPC), the blade pitch angles are not controlled simultaneously, as in the case of Collective Pitch Control (CPC), but individually. Thus, azimuth-dependent forcing is possible, especially for reducing the 1p blade loads and the Three-Times-Per-Revolution (3p) tower loads due to the vertical wind profile, see Section 2.7.1. A basic IPC controller for wind turbines was proposed by Bossanyi in [192]. For FOWTs an extensive study on IPC for FOWTs can be found in the thesis by Namik [182]. A FOWT controller for all operational regions combining the prospects of DAC and Nonlinear Model-Predictive Control (NMPC) with IPC is presented in [193] with a good improvement in terms of load reduction compared to a standard controller but only short description of the modeling assumptions is given.

Special approaches to improve the control performance for FOWTs were presented: In [194] a set point change of the rotor speed as function of the platform pitch velocity was proposed. This might be comparable to feedforward control such that the knowledge of the change in relative wind speed at the rotor is used to determine the feedforward gain. Another proposed approach is to use an estimator in real-time to distinguish the origin of the rotor speed deviation: Whether it results from a forcing of waves on the support structure or from a change in the wind field. With an estimator it is possible to have the controller react primarily on the effects from the wind field fluctuation and not the platform oscillation and thereby overcome the RHPZ limitations. Additional sensors, mainly for disturbance preview for FOWTs, have been studied with promising results: A feedforward controller using wind preview information on a FOWT was shown in [108] and [195]. Light Detection And Ranging (LiDAR) signal data, used for an advanced NMPC is presented in [106] and extended for IPC in [196].

First scaled experimental tests of FOWTs including active control were performed in [197] in order to validate simulation models and assess the robustness of the control. Experimental testing of FOWTs including control will be topic of Chapter 4 of this thesis.

The topic of the necessary model fidelity for the controller design was discussed for onshore turbines in [198] and several aerodynamic models suitable for controller design are presented in [87]. Especially coupling effects are important for FOWTs as resonances might shift or interact with each other. This was shown for the interaction of blades and tower in [199]. The next section on the model development of this research addresses the question of the necessary model fidelity for FOWTs.

In this thesis, especially the problem of MIMO control for FOWTs is addressed, studying the dynamic properties and the coupling effects of the standard actuators blade pitch and generator torque on the different outputs such as rotor speed and tower-top displacement, see Chapter 5. This is done with the goal of understanding the dynamic properties of the wind turbine mounted on a floating foundation, subject to wave loads. Based on these findings, an optimal LQR assuming perfect measurements has been designed and an automated method for designing a state-of-the-art SISO PI-controller. The optimal controller is seen as a benchmark for the upper bound of what is achievable with control to be compared with the baseline controller. Both controllers are parameterized and will be integrated in the optimization study of the platforms, Chapter 6.

2.10 Reference Design

Within the project INNWIND.EU, a platform design competition among the project partners resulted in three different concepts, described in [200]. For the one initially designed at Stuttgart Wind Energy (SWE) within this thesis, a detailed design was done towards the end of the project, see [123]. Figure 2.7 shows a sketch of the concept: It is a deep-drafted semi-submersible with the prospect of combining the advantages of a spar with those of a semi-submersible: Spars usually have lower material costs due to its simple, cylindrical shapes and a restoring, dominated by gravitational forces. Semi-submersibles, on the other side, are more flexible with respect to the site as the draft is smaller. The TripleSpar draft is, with less than $60\,\mathrm{m}$, smaller than the one of typical spar platforms and still, the material cost advantage of spars can be maintained. These simple cylindrical columns can be made of concrete or steel. The columns are only connected through a three-legged steel structure above SWL in order to enable an assembly at site, as for the Hywind Scotland wind farm, see [201]. The use of concrete for the columns was initially investigated in the project Alternative Floating Platform Designs for Offshore Wind Turbines using Low Cost Materials (AFOSP) for a concrete spar, see [202]. Recently, reinforced concrete has been proposed by various platform designers. The properties of the TripleSpar concept are summarized in Table 2.4. The concept is public and the FAST model can be downloaded from [203]. The full set of parameters used in this work is listed in Table A.1.
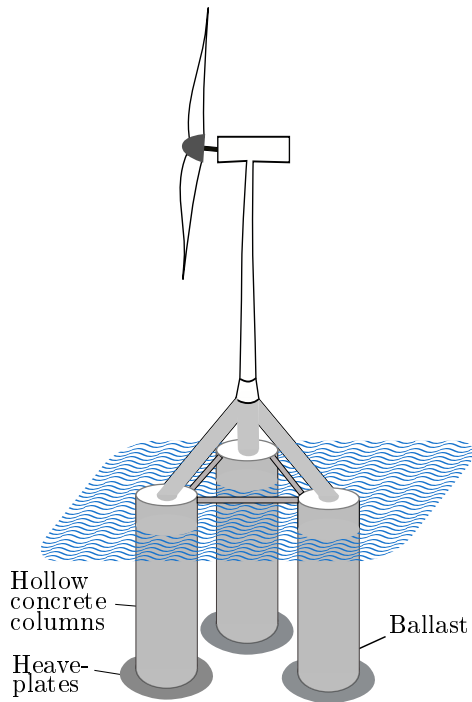
Figure 2.7: INNWIND.EU TripleSpar concept for DTU10 MW wind turbine.

Platform draft [m]	54.5
Platform column diameter [m]	15.0
Platform column spacing (to centerline) [m]	26.0
Platform mass [10^6 kg]	28.3
Number of mooring lines [-]	3
Water depth [m]	180.0
Mooring line length [m]	610.0
Turbine mass [10^6 kg]	1.1
Rated rotor speed [rpm]	9.6
Rated wind speed [m/s]	11.4

Table 2.4: INNWIND.EU TripleSpar platform and DTU10 MW wind turbine main parameters.

3 Development of a Low-Order Simulation Model

A tailored numerical model will be derived in this chapter, first for a linear system analysis and model-based control design and second, for a computationally efficient load calculation and design optimization. A description of the model, together with exemplary results and verification will be published in [204]. After the derivation of the structural model, all submodels related to aerodynamics, hydrodynamics and the mooring lines will be described. The derivation is shown for a nonlinear time-domain formulation with a linearization of each submodel. A verification of the model, called Simplified Low-Order Wind turbine (SLOW) in the remainder, through a comparison with FAST [43] will terminate the chapter. The next section will list the functional requirements of the model with respect to its applications.

3.1 Requirements

State-of-the-art simulation models for FOWTs as introduced in Section 2.5 are engineering models, which can be handled on standard PCs. Nonetheless, the computational efficiency is usually not high enough for large parameter variations in preliminary design stages.

Here, a list of requirements is formulated, for a simulation model enabling the goals specified in Section 1.1. Full system optimizations shall be possible at early design stages with a reduced simulation time to bridge the gap between simple spreadsheet calculations and DLC simulations:

- Fidelity: Representation of overall system dynamics, no resolution of components
- Speed: High computational efficiency
- Functionality:
    - Suitability for model-based controller design and DLC-simulations
    - Nonlinear and linearized equations of motion
    - Only scalar disturbance inputs
- Architecture:
    - Fully parameterized
    - Flexible definition of Multibody System (MBS)
    - Portability among different platforms (symbolic Equation of Motion (EQM))

Based on these requirements, a model will be developed with dynamic equations derived from physics rather than through system identification approaches using a more advanced model. For a reduction of the computational time and code portability, the EQM are set up symbolically. This means that the right-hand side of the ODE is not set up step by step with numeric values but is available in the program code directly in terms of symbolic variables.

3.2 Structural Model

This section introduces MBS theory applied to the FOWT system with the goal of deriving EQM with a reduced number of DoFs – first, for models of rigid bodies, linked by spring-damper elements and then adding the theory of flexible bodies for beam structures. Although the derivation is conducted for a FOWT system, the description and also the code is set up in a way that it is possible to simulate other mechanical systems as well. This differs from many other MBS models in wind energy, which are exclusively set up for modeling HAWTs.
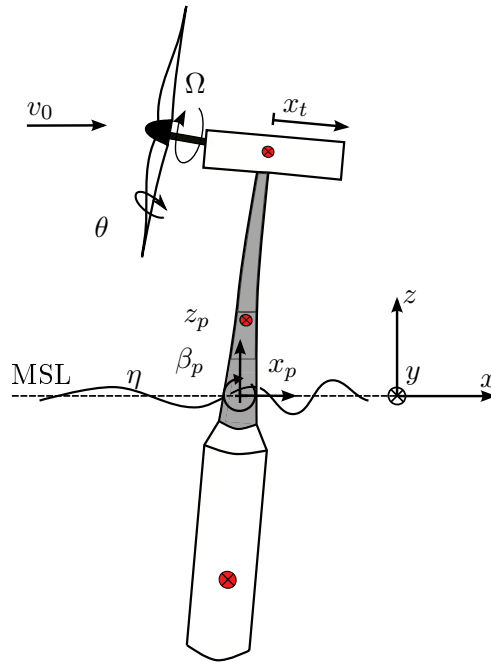
Figure 3.1: Topology of the simplified multibody model (independent of floating platform concept), [205].

A MBS model is based on the assumption of a large rigid-body reference motion together with small elastic deformations. This holds especially for rotating systems, such as any kind of turbines. Wind turbines are especially challenging to model due to the flexible tower and the highly flexible blades of ever increasing size. If no flexible bodies are involved the rigid-body MBS consists of point-mass bodies coupled with spring-damper elements. Newton's second law for

translational motion and Euler's law for rotational motion is set up for each of the different bodies and the momentum equations are set up directly. No conservation of energy is applied as in Lagrange's principle. The Newton-Euler algorithm is documented in [206] and in [207]. It can be used for rigid and flexible MBS. The MBS topology can have an open (tree) structure or a loop structure (imagine a Darrieus rotor of a Vertical-Axis Wind Turbine (VAWT), where the blade is connected at both ends). In the latter case, additional constraint equations are necessary for imposing the joint condition, where the loop connects, resulting in a system of Differential Algebraic Equations (DAEs), see e.g. [207]. For the HAWT on the floating plat-form, only open (tree) structures are necessary. The constraints for describing the system joints can be geometric, meaning only dependent on the position or kinematic, if also the velocity is constrained. The constraints for the systems analyzed here are all purely geometric and time-independent (scleronomic), although time-dependent constraints can generally be implemented, e.g for modeling a deterministic rotor speed or blade pitch angle maneuver as function of time. The derivation of the equation of motion of FAST using Kane's method [208] seems similar to the present one. However, in this work a formalism is used, which aims at a user-defined MBS layout. This is unlike the FAST equations.

3.2.1 Rigid multibody systems

For systems undergoing large excursions with small elastic deformations, a modeling through rigid MBS can be an efficient but accurate approach as the body forces such as centrifugal, Coriolis and gyroscopic forces are accounted for using a limited number of DoFs. The rigid bodies with a lumped mass and lumped mass moments of inertia are connected through spring-damper elements, whose forces are part of the applied forces acting on the bodies. The book by Wörnle [209] gives a general overview on rigid MBS. The notation here follows the one of Eberhard and Schiehlen [206] and Seifried [207]. The EQM for rigid bodies, described in the following, are set up in the inertial reference frame, which is, in case of a FOWT, located at the center of flotation in equilibrium position without external forces, see Figure 3.1.

Kinematics

The EQM require a suitable formulation of the system kinematics, which are a function of the generalized coordinates consisting of the system DoFs, collected in the vector $\boldsymbol{q}$. For the FOWT allowed to move in 2D, the f generalized coordinates $\boldsymbol{q}$ are

$$\boldsymbol{q} = \left[\begin{array}{ccccc} x_p, & z_p, & \beta_p, & \varphi, & x_t \end{array} \right]^T \tag{3.1}$$

with platform surge x_p, platform heave z_p, platform pitch β_p and rotor azimuth φ and the elastic tower fore-aft deformation x_t, see Figure 3.1. For FOWTs the translational displacement

coordinates of the floating platform x_p and y_p are i.e. usually defined at the center of flotation of the platform and not at its Center of Mass (CM) in the same way as the inertial coordinate system as described above.

The kinematic quantities of the translational velocity $\boldsymbol{v}_i$ and the translational acceleration $\boldsymbol{a}_i$ of each body's CM in inertial coordinates can now be calculated from the position vectors $\boldsymbol{r}_i$ to each body's CM. The velocity $\boldsymbol{v}_i$ results from the position vector $\boldsymbol{r}_i$, differentiated with respect to time, as

$$\boldsymbol{v}_i(\boldsymbol{q}, \dot{\boldsymbol{q}}) = \dot{\boldsymbol{r}}_i(\boldsymbol{q}, \dot{\boldsymbol{q}}) = \frac{\partial \boldsymbol{r}_i(\boldsymbol{q}, \dot{\boldsymbol{q}})}{\partial \boldsymbol{q}} \dot{\boldsymbol{q}} = \boldsymbol{J}_{t,i}(\boldsymbol{q}, \dot{\boldsymbol{q}}) \dot{\boldsymbol{q}} \tag{3.2}$$

omitting the partial differentiation with respect to time, since no time-dependent boundary conditions exist (scleronomic system). One can see that the Jacobian matrix $\boldsymbol{J}_{t,i}$ transforms the kinematics, described in the inertial coordinate system, into the space of minimal coordinates, see [206]. The same will be done later with the global Newton-Euler equations. As a result, the EQM are a set of ODEs with one scalar equation per generalized coordinate and constrained directions are not anymore part of the EQM. This has the major advantage that no additional constraint equations are necessary and the EQM are available as ODE instead of a set of Partial Differential Equations (PDEs).

The translational accelerations $\boldsymbol{a}_i$ are

$$\boldsymbol{a}_i = \dot{\boldsymbol{v}}_i(\boldsymbol{q}, \dot{\boldsymbol{q}}) = \frac{\partial \boldsymbol{v}_i(\boldsymbol{q}, \dot{\boldsymbol{q}})}{\partial \dot{\boldsymbol{q}}} \ddot{\boldsymbol{q}} + \frac{\partial \boldsymbol{v}_i(\boldsymbol{q}, \dot{\boldsymbol{q}})}{\partial \boldsymbol{q}} \dot{\boldsymbol{q}} = \boldsymbol{J}_{t,i}(\boldsymbol{q}, \dot{\boldsymbol{q}}) \ddot{\boldsymbol{q}} + \bar{\boldsymbol{v}}_i(\boldsymbol{q}, \dot{\boldsymbol{q}}) \tag{3.3}$$

with the component $\bar{\boldsymbol{v}}_i$, called the local velocity.

The rotational generalized coordinates are also called quasi-coordinates as they cannot be differentiated directly yielding the angular velocity vector $\boldsymbol{\omega}_i$. The vector of rotation angles $\boldsymbol{\alpha}_i$ is connected to the rotation tensor $\boldsymbol{S}(\boldsymbol{q})$ according to the selected description of the rotation. For a rotation in three dimensional space, various descriptions are possible [210]. With Kardan and Euler angles, the rotation matrix describes a successive rotation about the instantaneous axes of the coordinate system. Therefore, it is important to keep in mind that simulation results showing an angle about one axis represent the rotation about a rotated axis, not a fixed one. In this work, Kardan angles are selected with the sequence *XZY*, which is of advantage for the rotation of the floating platform as the largest rotational displacement is usually in pitch-direction (about y) due to wind and wave forcing. Consequently, the Kardan angle β_p is approximately the one about y of the inertial frame I. The rotation tensor can be written as

$$\boldsymbol{S} = \begin{bmatrix} 1 & 0 & 0 \\ 0 & \cos(\alpha) & -\sin(\alpha) \\ 0 & \sin(\alpha) & \cos(\alpha) \end{bmatrix} \begin{bmatrix} \cos(\gamma) & -\sin(\gamma) & 0 \\ \sin(\gamma) & \cos(\gamma) & 0 \\ 0 & 0 & 1 \end{bmatrix} \begin{bmatrix} \cos(\beta) & 0 & \sin(\beta) \\ 0 & 1 & 0 \\ -\sin(\beta) & 0 & \cos(\beta) \end{bmatrix}. \tag{3.4}$$

The angular velocity vector $\boldsymbol{\omega} = [\begin{array}{ccc} \omega_1, & \omega_2, & \omega_3 \end{array}]^T$ results from the rotation matrix according to [206]

$$
\dot{\boldsymbol{S}}\boldsymbol{S}^T = \begin{bmatrix} 0 & -\omega_3 & \omega_2 \\ \omega_3 & 0 & -\omega_1 \\ -\omega_2 & \omega_1 & 0 \end{bmatrix} = \tilde{\boldsymbol{S}}\left(\boldsymbol{\omega}\right), \tag{3.5}
$$

where the cross-product operator $\tilde{\boldsymbol{S}}$ replaces the cross product

$$
\boldsymbol{\lambda} \times \boldsymbol{a} = \tilde{\boldsymbol{S}}\left(\boldsymbol{\lambda}\right)\boldsymbol{a}. \tag{3.6}
$$

Note that a linearization of Eq. (3.4) yields a transformation matrix $\boldsymbol{S}_{lin}$, which does not preserve the vector magnitude as $\mathrm{tr}(\boldsymbol{S}_{lin}) \neq 1$. Corrections are possible, such as the one used in the reference model FAST [15]. No corrections are employed for the linearized model in this work. With the sequence of rotation of Eq. (3.4), the angular velocity vector remains as

$$
\boldsymbol{\omega}_i = \begin{bmatrix} \dot{\alpha} \\ 0 \\ 0 \end{bmatrix} + \begin{bmatrix} 1 & 0 & 0 \\ 0 & \cos(\alpha) & -\sin(\alpha) \\ 0 & \sin(\alpha) & \cos(\alpha) \end{bmatrix} \begin{bmatrix} 0 \\ 0 \\ \dot{\gamma} \end{bmatrix} +
$$
$$
+ \begin{bmatrix} 1 & 0 & 0 \\ 0 & \cos(\alpha) & -\sin(\alpha) \\ 0 & \sin(\alpha) & \cos(\alpha) \end{bmatrix} \begin{bmatrix} \cos(\gamma) & -\sin(\gamma) & 0 \\ \sin(\gamma) & \cos(\gamma) & 0 \\ 0 & 0 & 1 \end{bmatrix} \begin{bmatrix} 0 \\ \dot{\beta} \\ 0 \end{bmatrix}. \tag{3.7}
$$

This angular velocity holds for the body i, rotated by $\boldsymbol{S}_i$ such that its local coordinate system ${}^i\boldsymbol{e}_i = [\begin{array}{ccc} 1 & 1 & 1 \end{array}]^T$ is transformed to its counterpart in the inertial coordinate system ${}^I\boldsymbol{e}_i$ by

$$
{}^I\boldsymbol{e}_i = \boldsymbol{S}_i \, {}^i\boldsymbol{e}_i \tag{3.8}
$$

In this chapter, all quantities are defined in the inertial frame ${}^I\boldsymbol{e}$ and the superscript is omitted for simplicity. This description of the rotation is used for all bodies in the MBS of the FOWT in this work. In rotational directions, the Jacobian matrix $\boldsymbol{J}_{r,i}$ can be calculated from the angular velocity vectors as

$$
\boldsymbol{J}_{r,i} = \frac{\partial \boldsymbol{\omega}_i(\boldsymbol{q}, \dot{\boldsymbol{q}})}{\partial \dot{\boldsymbol{q}}}. \tag{3.9}
$$

The rotational acceleration of body i is then

$$
\boldsymbol{\alpha}_i(\boldsymbol{q}, \dot{\boldsymbol{q}}) = \dot{\boldsymbol{\omega}}_i(\boldsymbol{q}, \dot{\boldsymbol{q}}) = \frac{\partial \boldsymbol{\omega}_i(\boldsymbol{q}, \dot{\boldsymbol{q}})}{\partial \dot{\boldsymbol{q}}}\ddot{\boldsymbol{q}} + \frac{\partial \boldsymbol{\omega}_i(\boldsymbol{q}, \dot{\boldsymbol{q}})}{\partial \boldsymbol{q}}\dot{\boldsymbol{q}} = \boldsymbol{J}_{r,i}(\boldsymbol{q}, \dot{\boldsymbol{q}})\ddot{\boldsymbol{q}} + \bar{\boldsymbol{\alpha}}_i(\boldsymbol{q}, \dot{\boldsymbol{q}}). \tag{3.10}
$$

Again, with the vector of the local angular acceleration $\bar{\boldsymbol{\alpha}}_i(\boldsymbol{q}, \dot{\boldsymbol{q}})$, following the notation of [206].

Kinetics

Applied forces have to be defined for each body in the inertial coordinate system in the same way as the kinematics. Applied translational forces $\boldsymbol{F}_i^a$ and torques $\boldsymbol{L}_i^a$ of rigid MBS are any type of external forces, like aerodynamic or hydrodynamic forces, gravitational forces and forces from the MBS coupling elements, e.g. spring-dampers. These forces are, other than the reaction forces, known a-priori and not only after solving the EQM. They are usually calculated in every timestep by external force models, which will be described in the following sections. The bodies of the FOWT having a significant flexibility or elasticity are the tower and the blades. In this work, a flexible MBS with flexible tower was generally used, except for the scaled experiments of Chapter 4, where a rigid MBS was more suitable. In this case, a translational spring-damper element at the tower-top can be defined. The overall stiffness can be calculated by integrating the sectional stiffnesses assuming a static shape and an approximate modal damping, see [211, p. 375]. With this approach one portion of the tower mass is attributed to the platform and another to the tower-top (RNA). A recommendation given in [163, p. 294] is to attribute 25 % of the tower mass to the tower-top. Note that for the tower elastic restoring stiffness the forces on the nacelle are $\boldsymbol{F}_{nac}^a = \boldsymbol{F}_{nac}^{spring} = -\boldsymbol{F}_{twr}^{spring}$ due to the principle "actio = reactio".

The reaction forces $\boldsymbol{F}_i^r$ and torques $\boldsymbol{L}_i^r$ acting on joints are unknown. For the calculation of the response, they do not have any influence and can be eliminated with the transformation into minimal coordinates as is done in the next section. A discussion on how to calculate these reaction forces and sectional forces of flexible bodies will be made in Section 3.2.6.

Newton-Euler equations

With the described kinematics and kinetics, the equations of motions can be written. For the translational directions, Newton's second law remains for each body i as

$$\boldsymbol{m}_i \boldsymbol{a}_i = \boldsymbol{F}_i^a + \boldsymbol{F}_i^r. \tag{3.11}$$

with the acceleration $\boldsymbol{a}_i$ given by Eq. (3.3). The mass matrices $\boldsymbol{m}_i \in \mathbb{R}^{(3 \times 3)}$ contain the body masses m_i on the diagonal. In the same way as for translational motion, the angular momentum (Euler-) equations are set up. The mass moments of inertia $\boldsymbol{I}_i$ of each body i are needed in the inertial coordinate system. As they are usually known in the body frame, a transformation with the rotation tensor $\boldsymbol{S}_i$ is necessary to obtain $\boldsymbol{I}_i$. The Euler equation becomes with the angular acceleration $\boldsymbol{\alpha}_i$ of Eq. (3.10) following [206]

$$\boldsymbol{I}_i \boldsymbol{\alpha}_i + \tilde{\boldsymbol{S}}\left(\boldsymbol{\omega_i}\right) \boldsymbol{I}_i \boldsymbol{\omega}_i = \boldsymbol{L}_i^a + \boldsymbol{L}_i^r. \tag{3.12}$$

The global Newton-Euler equations for a total of p rigid bodies can now be put together

resulting in a set of $(2 \cdot 3 \cdot p)$ equations as

$$
\begin{bmatrix} \boldsymbol{m}_i \boldsymbol{J}_{t,i} \\ \vdots \\ \boldsymbol{I}_i \boldsymbol{J}_{r,i} \\ \vdots \end{bmatrix} \ddot{\boldsymbol{q}} + \begin{bmatrix} \boldsymbol{m}_i \dot{\boldsymbol{J}}_{t,i} \dot{\boldsymbol{q}} \\ \vdots \\ \boldsymbol{I}_i \dot{\boldsymbol{J}}_{r,i} \dot{\boldsymbol{q}} \ + \ \tilde{\boldsymbol{S}}\left(\boldsymbol{\omega_i}\right) \boldsymbol{I}_i \boldsymbol{\omega}_i \\ \vdots \end{bmatrix} = \begin{bmatrix} \boldsymbol{F}_i^a \\ \vdots \\ \boldsymbol{L}_i^a \\ \vdots \end{bmatrix} + \begin{bmatrix} \boldsymbol{F}_i^r \\ \vdots \\ \boldsymbol{L}_i^r \\ \vdots \end{bmatrix} . \tag{3.13}
$$

Now the reaction forces $\boldsymbol{F}_i^r$ and torques $\boldsymbol{L}_i^r$ can be eliminated according to the principle of d'Alembert by multiplying Eq. (3.13) with the global Jacobian matrix

$$
\boldsymbol{J} = \begin{bmatrix} \boldsymbol{J}_{t,1}, & \dots & \boldsymbol{J}_{t,p}, & \boldsymbol{J}_{r,1}, & \dots & \boldsymbol{J}_{r,p} \end{bmatrix}^T \tag{3.14}
$$

from the left. Since the reaction forces always point into the constrained directions, perpendicular to the generalized coordinates $\boldsymbol{q}$, they are eliminated with this operation. After the transformation Eq. (3.13) takes the form

$$
\boldsymbol{M}(\boldsymbol{q})\ddot{\boldsymbol{q}} + \boldsymbol{k}(\boldsymbol{q}, \dot{\boldsymbol{q}}) = \boldsymbol{p}(\boldsymbol{q}, \dot{\boldsymbol{q}}) \tag{3.15}
$$

with the mass matrix $\boldsymbol{M} \in \mathbb{R}^{(f \times f)}$, the Coriolis, centrifugal and gyroscopic forces $\boldsymbol{k} \in \mathbb{R}^{(f \times 1)}$ and the applied forces $\boldsymbol{p} \in \mathbb{R}^{(f \times 1)}$. For a convenient numerical solution, Eq. (3.15) can be transformed into state space by solving for the second derivative of the generalized coordinates $\ddot{\boldsymbol{q}}$ and defining the state vector $\boldsymbol{x}$ as

$$
\dot{\boldsymbol{x}} = \frac{\mathrm{d}\boldsymbol{x}}{\mathrm{d}t} = \begin{bmatrix} \dot{\boldsymbol{q}} \\ \ddot{\boldsymbol{q}} \end{bmatrix} = \begin{bmatrix} \dot{\boldsymbol{q}} \\ \boldsymbol{M}^{-1}(\boldsymbol{p} - \boldsymbol{k}) \end{bmatrix} . \tag{3.16}
$$

With the state vector of Eq. (3.1), selected for this work, the rotor is considered a rigid disk and the structural model does not contain any dependency on the azimuth angle φ. In this case, the azimuth angle is not a state as it is not necessary for a complete description of the system and can be deleted from $\boldsymbol{x}$. It is noted that the closed-loop system includes φ as state again when introducing an aerodynamic force model, which includes an azimuth-dependency or a rotor speed controller with an integral term.

Added mass forces

For floating bodies, an acceleration-dependent force needs to be added to the inertia-term of Eq. (3.13) in the same way as in the rigid-body EQM, Eq. (2.19). The added fluid mass depends on the hull shape and is usually calculated by potential flow (or panel-) codes. Depending on the reference point and the symmetry, the added mass matrix $\boldsymbol{A}(\omega) \in \mathbb{R}^{(6 \times 6)}$ has coupling elements

between translational and rotational DoFs. These coupling terms need to be respected in Eq. (3.13). In the present model this is solved by writing the structural mass matrices for all bodies i as $\boldsymbol{M}_i \in \mathbb{R}^{(6\times6)}$ including the translational mass matrices and the mass moments of inertia. From these, the left summands of Eq. (3.13) result from

$$\begin{bmatrix} \boldsymbol{m}_i \boldsymbol{J}_{t,i} \\ \boldsymbol{I}_i \boldsymbol{J}_{r,i} \end{bmatrix} = \boldsymbol{M}_i \begin{bmatrix} \boldsymbol{J}_{t,i} \\ \boldsymbol{J}_{r,i} \end{bmatrix} . \tag{3.17}$$

For the planar (2D) EQM, the most important coupling terms are usually the surge-pitch (5,1) and (1,5)-elements. This becomes even more important when the reference point for the added-mass matrix is the CF (at the water surface, as is the usual procedure and also done in this work) because this point is distant from the Center of Buoyancy (CB). The frequency-dependency of $\boldsymbol{A}$ is further discussed in Section 3.5.1.

3.2.2 Flexible multibody systems

In this section, the EQM for rigid MBS will be extended to account also for flexible (elastic) bodies. The flexible MBS approach simplifies the inclusion of all body forces from large displacements of the reference frame. These are difficult to obtain from standard FE approaches, which require the computationally expensive absolute nodal coordinate formulation, see [210] for details, or hybrids like the co-rotational frame formulation implemented in 3DFloat, see [212]. A derivation of a nonlinear FE model for wind turbines can be found in [213] for the tool FAST.

The notation here follows the one from Schwertassek and Wallrapp [59]. The assembly of the equations, equivalent to the ones of rigid systems, Eq. (3.13), follows Seifried [207], because he uses d'Alembert's principle, as opposed to [59], who use Jourdain's principle for the elimination of the reaction forces. The vector of generalized coordinates $\boldsymbol{q}$ will be a combination of rigid and flexible (elastic) DoFs $\boldsymbol{q} = [\boldsymbol{q}_r, \boldsymbol{q}_e]^T$. With a flexible tower, the vector $\boldsymbol{q}$, defined for rigid bodies in Eq. (3.1), is composed of a rigid and a flexible part as

$$\boldsymbol{q}_r = \begin{bmatrix} x_p, & z_p, & \beta_p, & \varphi, & \theta_1 \end{bmatrix}^T \qquad \text{and} \qquad \boldsymbol{q}_e = \begin{bmatrix} x_t \end{bmatrix} . \tag{3.18}$$

In Chapter 5 and 6, the collective blade pitch actuator is included in the flexible MBS with a single DoF θ_1. The next sections describe the derivation of the additional equations to the Newton-Euler equations of Eq. (3.13) to represent flexible bodies. Therefore, the index i refers to a flexible body in this section.

Kinematics

The present derivation follows the "floating frame of reference" method, see [59] and [214]: It is a reference coordinate system for the definition of the flexible body, which is not necessarily its CM but any reference point that is convenient for the description of the elastic properties. This formulation simplifies parts of the equations and is useful for a pre-computation of the elastic properties of the bodies, which is detailed at the end of this section. Eventually, the kinematics of an elastic body i can be described by the reference kinematics with a large nonlinear motion and the small linear motion described by the $f_{e,i}$ generalized elastic coordinates $\boldsymbol{q}_{e,i} \in \mathbb{R}^{(f_{e,i} \times 1)}$ of body i.

The coordinates (in the local body reference frame R) of the nodes k of a flexible body in the reference configuration (undeformed) with respect to the reference system are collected in the vector $\boldsymbol{R} = {}^{R}\boldsymbol{R}$. The deformation field ${}^{R}\boldsymbol{u}_i^k(t)$ of the body is defined in the local frame for each node k relative to the reference coordinates ${}^{R}\boldsymbol{R}$. The position vector $\boldsymbol{\rho}_i^k(t)$ to the flexible nodes k, using the floating frame of reference is in the local reference frame R

$$
{}^{R}\boldsymbol{\rho}_i^k(t) = {}^{R}\boldsymbol{r}_i(t) + {}^{R}\boldsymbol{R}_i^k + {}^{R}\boldsymbol{u}_i^k(t) = \boldsymbol{S}_i^{T\,I}\boldsymbol{\rho}_i^k(t). \tag{3.19}
$$

For the orientation the same description holds: In the same way as $\boldsymbol{R}_i^k$, the tensor $\boldsymbol{\Gamma}_i^k$ represents the orientation of node k of the flexible body i in the reference configuration with respect to the reference frame.

Looking at a straight rotor blade with the z-coordinate of $\boldsymbol{e}_i$ pointing to the blade tip, the beam reference coordinates $\boldsymbol{R}_i$, aligned with the shear axis of the beam, see [60], will have zero x and y-coordinates and the entries in x-direction are the radial position of the blade stations, the same as in FAST [39]. For a pre-bent blade such as those of the DTU 10 MW RWT, this is not the case and also the orientation of $\boldsymbol{\Gamma}_i^k$ is not constant for different k, due to the blade twist and the pre-bending.

A deformed body has the nodal orientation

$$
\boldsymbol{D}_i^k = \boldsymbol{\Theta}_i^k(t)\boldsymbol{\Gamma}_i^k \tag{3.20}
$$

with the additional rotation from the deformation defined by the rotation tensor $\boldsymbol{\Theta}_i^k(t)$. The rotation tensor $\boldsymbol{D}_i^k$ is defined in the same way as $\boldsymbol{S}_i$ according to the convention of Eq. (3.8).

Shape functions As in FE models, shape functions are used to avoid having to solve the PDEs of continuum mechanics. With the Ritz-approach, the time-dependent and space-dependent solution can be separated: Time-independent characteristic shapes are used to approximate the deformation and are integrated to the ODE to solve for a time-dependent response. For MBS, this approach can also be used by approximating the deformation of a flexible body with a

characteristic shape. This is part of MOR techniques, one of which is the Guyan reduction, which uses static modes of the flexible body as shape functions. In the present model, the mode shapes of importance for the system dynamics will be used. For a recent work on MOR methods in structural dynamics see [215] and specifically to wind turbines [216].

The shape function for translation $\mathbf{\Phi}_i^k \in \mathbb{R}^{(3 \times f_{e,i})}$ for each node k has f_e columns, as many as generalized elastic coordinates defined for flexible body i. For the rotation, the shape function is $\mathbf{\Psi}_i^k \in \mathbb{R}^{(3 \times f_{e,i})}$. Note that one shape function represents a translational and at the same time rotational displacement. The nodal rotation tensor $\mathbf{\Theta}_i^k(t)$ can be calculated from the rotation shape function $\boldsymbol{\vartheta}_i^k$ for small displacements with the identity matrix $\boldsymbol{E}$ as

$$\mathbf{\Theta}_i^k(t) = \boldsymbol{E} + \tilde{\boldsymbol{S}}\left(\boldsymbol{\vartheta}_i^k\right). \tag{3.21}$$

The general relative deformation field for translation $\boldsymbol{u}_i^k(t)$ of Eq. (3.19) and for rotation $\boldsymbol{\vartheta}_i^k(t)$ of Eq. (3.20) can now be written as function of the generalized coordinates of the elastic body $\boldsymbol{q}_{e,i}(t)$

$$\boldsymbol{u}_i^k(t) = \mathbf{\Phi}_i^k \boldsymbol{q}_{e,i}(t) \qquad \boldsymbol{\vartheta}_i^k(t) = \mathbf{\Psi}_i^k \boldsymbol{q}_{e,i}(t). \tag{3.22}$$

For beam models, used in this work for the tower, the shape functions are written as function of the beam axis $x \equiv R_1$. Here, one mode shape is used to represent the tower elasticity in fore-aft direction. The shapes for a linear Bernoulli beam with only one DoF for bending take the form[1]

$$\mathbf{\Phi}_i(\boldsymbol{R}) = \begin{bmatrix} W_{i,1}(x) \\ 0 \\ -R_2 W_{i,1}'(x) \end{bmatrix}, \tag{3.23}$$

where $W_{i,1}(x)$ stands for the lateral deflection of the beam axis for the first shape. The shape function for the beam element rotations reads

$$\mathbf{\Psi}_i(\boldsymbol{R}) = \begin{bmatrix} 0 \\ W_{i,1}'(x) \\ 0 \end{bmatrix}. \tag{3.24}$$

Looking at Eq. (3.22), it becomes clear that the shape functions $\mathbf{\Phi}_i(\boldsymbol{R})$ and $\mathbf{\Psi}_i(\boldsymbol{R})$ have more than one column for $\boldsymbol{q}_{e,i}$ containing more than one coordinate.

As a result, the overall orientation ${}^I\boldsymbol{S}_i^k$ with respect to the inertial coordinate system I of

---

[1]Here written as continuous function of $\boldsymbol{R}$ and not for the nodes k as the shape functions are usually approximated by analytic expressions.

node k can be calculated using Eqs. (3.21) and (3.22) as

$$\boldsymbol{S}_i^k = \left(\boldsymbol{E} + \tilde{\boldsymbol{S}} \left(\boldsymbol{\Psi}_i^k \boldsymbol{q}_{e,i}(t) \right) \right) \boldsymbol{\Gamma}_i^k \boldsymbol{S}_i(t), \tag{3.25}$$

where the rotation of the reference system of body i is $\boldsymbol{S}_i^{k=0} = \boldsymbol{S}_i$. Equation (3.25) is of importance for the definition of the orientation of a new body attached to a flexible body, for example the nacelle mounted at the tower-top. In that case, the end node $\hat{k}$ of the tower gives the nacelle orientation $\boldsymbol{S}_{nac} = \boldsymbol{S}_{twr}^{\hat{k}}$. In the same way the angular velocity $\boldsymbol{\omega}_i^k$ can be calculated from the rotation tensor $\boldsymbol{S}_i^k$ using Eq. (3.5) or, as done in this model, from the definition of Kardan angles, Eq. (3.7). The nodal velocities relative to the inertial frame I can be obtained by differentiating Eq. (3.19) with respect to time in either the reference or the inertial frame.

Eventually, the kinematic functions for velocity $\boldsymbol{z}_{II,i}$ and acceleration $\boldsymbol{z}_{III,i}$ can be expressed using minimal coordinates with the Jacobian matrices $\boldsymbol{J}_{t,i}$ and $\boldsymbol{J}_{r,i}$ following [207] as

$$\boldsymbol{z}_{II,i} = \begin{bmatrix} {}^R\boldsymbol{v}_i \\ {}^R\boldsymbol{\omega}_i \\ \dot{\boldsymbol{q}}_{e,i} \end{bmatrix} = \begin{bmatrix} \boldsymbol{J}_{t,i}(\boldsymbol{q}) \\ \boldsymbol{J}_{r,i}(\boldsymbol{q}) \\ \boldsymbol{J}_{e,i} \end{bmatrix} \dot{\boldsymbol{q}} \quad \text{and} \quad \boldsymbol{z}_{III,i} = \begin{bmatrix} {}^R\boldsymbol{a}_i \\ {}^R\boldsymbol{\alpha}_i \\ \ddot{\boldsymbol{q}}_{e,i} \end{bmatrix} = \begin{bmatrix} \boldsymbol{J}_{t,i}(\boldsymbol{q}) \\ \boldsymbol{J}_{r,i}(\boldsymbol{q}) \\ \boldsymbol{J}_{e,i} \end{bmatrix} \ddot{\boldsymbol{q}} + \begin{bmatrix} \dot{\boldsymbol{J}}_{t,i}(\boldsymbol{q},\dot{\boldsymbol{q}}) \\ \dot{\boldsymbol{J}}_{r,i}(\boldsymbol{q},\dot{\boldsymbol{q}}) \\ \boldsymbol{0} \end{bmatrix} \dot{\boldsymbol{q}}. \tag{3.26}$$

Consequently, the kinematics of elastic bodies are described by a reference translational and rotational motion as for rigid bodies, see Eq. (3.2)–(3.7), but additionally by the generalized coordinates of the elastic motion $\boldsymbol{q}_{e,i}$. Thus, there are f_e additional equations in the $(2 \cdot 3)$ Newton-Euler equations (Eq. (3.13)) for each elastic body i. The selection matrix $\boldsymbol{J}_{e,i}$ assigns the elastic coordinates $\boldsymbol{q}_{e,i}$ of $\boldsymbol{q}$ to the corresponding bodies and therefore these elastic equations are unchanged when transforming the system into minimal coordinates. The global Jacobian matrix $\boldsymbol{J}$, defined for rigid bodies in Eq. (3.14), is for flexible bodies

$$\boldsymbol{J} = \begin{bmatrix} \boldsymbol{J}_{t,1}, & \boldsymbol{J}_{r,1}, & \boldsymbol{J}_{e,1}, & \dots & \boldsymbol{J}_{t,p}, & \boldsymbol{J}_{r,p}, & \boldsymbol{J}_{e,p} \end{bmatrix}^T. \tag{3.27}$$

In the case of elastic bodies, the kinematics are written in the reference coordinate system denoted by the superscript R, taking advantage of the floating frame of reference approach as introduced at the beginning of this section. The kinematics of the rigid bodies within the global MBS of rigid and flexible bodies, however, are still written in the inertial coordinate system I as derived in Section 3.2.1.

Selection of the body reference frame The reference frame R for the elastic body does not have to be the body-CM as for rigid bodies of Section 3.2.1. A guidance for the choice of the location of the reference frame is given in [59, p. 257]. For the tower-body, the tower-base is

selected with the z-axis aligned with the beam axis. Thus,

$$\boldsymbol{u}_i^0(t) = \boldsymbol{0} \qquad \text{and} \qquad \boldsymbol{\vartheta}_i^0(t) = \boldsymbol{0}. \tag{3.28}$$

In this case also the shape functions $\boldsymbol{\Phi}_i^k$ and $\boldsymbol{\Psi}_i^k$ need to obey this condition, i.e. for a beam the derivative of the shape functions is with respect to the beam axis $\boldsymbol{W}'(x=0) = \boldsymbol{0}$. For a hinge joint at the reference frame of the flexible body, the reference frame orientation depends on the elastic generalized coordinates, $\boldsymbol{q}_{e,i}$. For a FOWT tower this can be the case due to the floating foundation. It is possible to obtain the tower mode shapes including a flexible foundation with an unreleased version of the tool BModes [217] by NREL. This has not been done in this work for simplicity. With the kinematics the body forces consisting of inertial, gravitational, centrifugal, Coriolis, gyroscopic and elastic forces can be calculated.

Kinetics

The kinetics of elastic bodies differ from those of rigid bodies as the effects of the body deformation have to be included in the calculation of the body forces. The notation is different from the one of rigid bodies, following the reference book for the model setup [59] (in German). In the book by Shabana [214], the same derivation can be found in English, although with a different notation and a description in the inertial frame instead of the body reference frame.

The Newton-Euler equation for an elastic body i includes the mass matrix $\boldsymbol{M}_i$, the quadratic velocity vector $\boldsymbol{h}_{\omega,i}$ with Coriolis, centrifugal and gyroscopic forces, gravitational forces $\boldsymbol{h}_g$, applied discrete forces $\boldsymbol{h}_{d,i}$, inner elastic forces $\boldsymbol{h}_{e,i}$, based on the selected deformation tensor and again, the reaction forces $\boldsymbol{h}_{r,i}$

$$\boldsymbol{M}_i \boldsymbol{z}_{III,i} + \boldsymbol{h}_{\omega,i} = \boldsymbol{h}_{g,i} + \boldsymbol{h}_{d,i} + \boldsymbol{h}_{e,i} + \boldsymbol{h}_{r,i}. \tag{3.29}$$

In the following the components of Eq. (3.29) will be derived. For simplicity, the index for the body i will be omitted as all equations are set up initially for a single body.

Mass matrix   The mass matrix for a flexible body i for the generalized coordinates $\boldsymbol{z}_I$ is according to [59]

$$\boldsymbol{M} = \begin{bmatrix} \boldsymbol{M}_{tt} & & sym. \\ \boldsymbol{M}_{rt} & \boldsymbol{M}_{rr} & \\ \boldsymbol{M}_{et} & \boldsymbol{M}_{er} & \boldsymbol{M}_{ee} \end{bmatrix} = \begin{bmatrix} \boldsymbol{m} & & sym. \\ m\tilde{\boldsymbol{S}}(\boldsymbol{c}) & \boldsymbol{I} & \\ \boldsymbol{C}_t & \boldsymbol{C}_r & \boldsymbol{M}_e \end{bmatrix}. \tag{3.30}$$

One can see that the entries of $\boldsymbol{M}$ related to translations t, rotations r and elastic coordinates e contain coupling elements. This means that inertial forces on the flexible body frame R

result from a generalized acceleration $\ddot{\boldsymbol{q}}_e$ and vice-versa. Couplings between translations and rotations do not appear in the case of rigid bodies, Eq. (3.13), because for rigid bodies the position vectors $\boldsymbol{r}_i$ always point to the respective CM. The same happens when transforming the rigid EQM from one reference point to another (meaning that the Newton's and Euler's law are written with a reference point other than the body-CM) using the system transformation matrix defined in [218, p. 176], see also Section 3.5.3.

The CM $\boldsymbol{c}$ of the flexible body can be obtained for beams with cross-section A, length l and density ρ through an integration along the beam axis x as

$$\boldsymbol{c} = \frac{1}{m_i} \int_0^l \rho A x \mathrm{d}x + \frac{1}{m_i} \boldsymbol{C}_t^T \boldsymbol{q}_e. \tag{3.31}$$

The second summand, $\boldsymbol{C}_t \in \mathbb{R}^{(f_e \times 3)}$, is the influence from the body deformation

$$\boldsymbol{C}_t = \int_0^l \rho A \boldsymbol{\Phi}_i^T(x) \mathrm{d}x. \tag{3.32}$$

The mass moment of inertia $\boldsymbol{I} = \boldsymbol{I}(\boldsymbol{q}_e)$ is the sum of the one of the undeformed body $\boldsymbol{I}_0$ and the contributions from elasticity $\boldsymbol{I}_1(\boldsymbol{q}_e)$ and $\boldsymbol{I}_2(\boldsymbol{q}_e)$

$$\boldsymbol{I}(\boldsymbol{q}_e) = \boldsymbol{I}_0 + \boldsymbol{I}_1(\boldsymbol{q}_e) + \boldsymbol{I}_2(\boldsymbol{q}_e) \qquad \text{with} \tag{3.33}$$

$$\boldsymbol{I}_1 = \int_0^l \left(\tilde{\boldsymbol{S}}\left(\boldsymbol{R}\right) \tilde{\boldsymbol{S}}\left(\boldsymbol{\Phi}\boldsymbol{q}_e\right)^T + \tilde{\boldsymbol{S}}\left(\boldsymbol{\Phi}\boldsymbol{q}_e\right) \tilde{\boldsymbol{S}}\left(\boldsymbol{R}\right)^T \right) \mathrm{d}m \quad \text{and} \quad \boldsymbol{I}_2 = \int_0^l \tilde{\boldsymbol{S}}\left(\boldsymbol{\Phi}\boldsymbol{q}_e\right) \tilde{\boldsymbol{S}}\left(\boldsymbol{\Phi}\boldsymbol{q}_e\right)^T \mathrm{d}m.$$

The coupling between elasticity and rotations $\boldsymbol{C}_r$ is given by

$$\boldsymbol{C}_r = \int_0^l \boldsymbol{\Phi}^T \tilde{\boldsymbol{S}}\left(\boldsymbol{\Phi}\boldsymbol{q}_e\right)^T \mathrm{d}m. \tag{3.34}$$

The mass matrix of the generalized elastic coordinate $\boldsymbol{M}_e$ can be calculated by integrating over the squared shape functions

$$\boldsymbol{M}_e = \int_0^l \boldsymbol{\Phi}\boldsymbol{\Phi}^T \mathrm{d}m. \tag{3.35}$$

Gravitational forces The gravitational body forces $\boldsymbol{h}_g$ also depend on the deformation of the body with the vector of the gravitational acceleration $\boldsymbol{g} = \begin{bmatrix} 0, & 0, & g \end{bmatrix}^T$ as

$$\boldsymbol{h}_g = \begin{bmatrix} \boldsymbol{E} \\ \tilde{\boldsymbol{S}}\left(\boldsymbol{R} + \boldsymbol{\Phi}\boldsymbol{q}_e\right) \\ \boldsymbol{\Phi}^T \end{bmatrix} \mathrm{d}m\, \boldsymbol{g} = \begin{bmatrix} \boldsymbol{m} \\ m\tilde{\boldsymbol{S}}\left(\boldsymbol{c}\right) \\ \boldsymbol{C}_t \end{bmatrix} \boldsymbol{g}. \tag{3.36}$$

Inner elastic forces   The inner elastic forces give, integrated over the volume of the flexible body for each mode shape, the restoring stiffness and structural damping forces on the MBS. Thus, the strain can be calculated with the parameterized shape of deformation of the body. From the strain the stresses can be computed with the material law. A number of transformations is necessary, depending on the coordinates used to parameterize the deformed shape as a space curve. Here, a short overview is given for Bernoulli beams, which are used in this work. The Green-Lagrange strain tensor reads in a linearized formulation for small displacements following [59, p. 79]

$$G_{ij} = \frac{1}{2}\left(\frac{\partial u_i}{\partial R_j} + \frac{\partial u_j}{\partial R_i}\right) \tag{3.37}$$

and gives the strain vector

$$\boldsymbol{\epsilon} = \left[\begin{array}{cccccc} G_{11}, & G_{22}, & G_{33}, & 2G_{12}, & 2G_{23}, & 2G_{31} \end{array}\right]^T. \tag{3.38}$$

With this definition, the strains can be calculated from a given deformation. Often the deformation is written in terms of the beam coordinates

$$\boldsymbol{\nu}(x,t) = \left[\begin{array}{cccc} w_1(x,t), & w_2(x,t), & w_3(x,t), & \vartheta_1(x,t) \end{array}\right]^T, \tag{3.39}$$

where

$$\boldsymbol{w} = \boldsymbol{W}\boldsymbol{q}_e. \tag{3.40}$$

Thus, $\boldsymbol{W} = \boldsymbol{W} \in \mathbb{R}^{(3 \times f_e)}$ has the same dimension as the matrix of shape functions $\boldsymbol{\Phi}$, compare Eq. (3.23). For Bernoulli beams deformed in 3D including torsion about the beam axis ϑ_1, the general displacement field is given by [59, Eq. (4.86)] as

$$\boldsymbol{u} = \left[\begin{array}{lll} w_1 & +R_2\left(-w_2' + w_1'w_2' - \vartheta_1 w_3'\right) & +R_3\left(-w_3' + w_1'w_3' + \vartheta_1 w_2'\right) \\ w_2 & -\frac{1}{2}R_2\left(w_2'^2 + \vartheta_1^2\right) & -R_3\left(\vartheta_1 + w_2'w_3'\right) \\ w_3 & R_2\vartheta_1 & -\frac{1}{2}R_3\left(w_3'^2 + \vartheta_1^2\right) \end{array}\right]. \tag{3.41}$$

Applying now Eq. (3.37) on the displacement field, Eq. (3.41), the strain for Bernoulli beams results as

$$\begin{aligned} G_{11} &= w_1' - R_3 w_3'' - R_2 w_2'', \\ G_{12} &= G_{21} = -\frac{1}{2}R_3\vartheta_1', \qquad G_{13} = G_{31} = \frac{1}{2}R_2\vartheta_1', \\ G_{22} &= G_{33} = G_{32} = G_{23} = 0, \end{aligned} \tag{3.42}$$

see [59, Eq. (6.423)]. For large reference motions, the assumption of small deflections is often not valid anymore. This is for example the case for a rotating blade on a wind turbine rotor, which usually shows increasing blade eigenfrequencies with an increasing rotational speed through centrifugal stiffening. Here, quadratic terms are necessary, which can be included in a linearized fashion in $\boldsymbol{G}$, see [59, Eq. (6.424)].

The remaining part is a transformation of the strain tensor $\boldsymbol{G}$, because the strain is needed as function of the generalized elastic coordinates $\boldsymbol{q}_e$. With this end the matrix $\boldsymbol{B}_L$ is introduced

$$\boldsymbol{\epsilon} = \boldsymbol{B}_L \boldsymbol{q}_e. \tag{3.43}$$

Note that $\boldsymbol{B}_L \in \mathbb{R}^{(6 \times f_e)}$ contains only the linear terms. For the nonlinear terms $\boldsymbol{B}_N$, resulting for example from geometric stiffening (centrifugal stiffening) refer to [59, p. 356]. Comparing now the definition of the strain vector $\boldsymbol{\epsilon}$, using Eqs. (3.38), (3.42) and (3.43), one can derive $\boldsymbol{B}_L$ and consequently the strains $\boldsymbol{\epsilon}$ as function of the generalized elastic coordinates $\boldsymbol{q}_e$. For a linear Bernoulli beam without the DoFs for longitudinal extension and torsion, as implemented in this model, all elements of the Green-Lagrange strain tensor $\boldsymbol{G}$ vanish except for G_{11} and the linear restoring stiffness for mode $k = 1$ can be calculated with the Young's modulus E as

$$\boldsymbol{K}_{eL} = \int_V \boldsymbol{B}_L^T E \boldsymbol{B}_L \mathrm{d}V = \int_{x=0}^l E J_{22} W_1''^2(x) \mathrm{d}x. \tag{3.44}$$

The integration over the cross-section A with the lateral coordinate R_1 yields the second moment of area J_{22} about y. The linear generalized stiffness matrix $\boldsymbol{K}_{eL} \in \mathbb{R}^{(f_e \times f_e)}$ has as many rows and columns as elastic degrees of freedom, defined for the body. Thus, the diagonal entries are the modal stiffnesses, which can be also used as spring stiffness when using the rigid MBS of Eq. (3.13). For the tower, the first mode can be used as dominant mode giving $\boldsymbol{F}_{twr}^a(1) = K_{eL,twr}(1,1)\, x_t$. Looking at Eq. (3.44), it becomes clear that the modal stiffness matrix, which determines the dynamics of the flexible MBS, depends on the material, but clearly on the shape function (with its second derivative W'', squared). Thus, a modified shape, i.e. from defining a different tower-top mass in tools like BModes [217], will change the modal stiffness.

The structural modal damping matrix $\boldsymbol{D}_e \in \mathbb{R}^{(f_e \times f_e)}$ can be calculated from the modal stiffness $\boldsymbol{K}_{eL}$ and the modal mass $\boldsymbol{M}_e$ for mode k assuming a given structural damping ratio ξ_k

$$\boldsymbol{D}_e = \mathrm{diag}(D_{ek}) \qquad \text{with} \qquad D_{ek} = 2\xi_k \sqrt{K_{ek} M_{ek}}. \tag{3.45}$$

Thus, for a constant structural damping ratio different modal damping ratios can be calculated, depending on their corresponding modal stiffness. The modal damping ratios are user-defined inputs in FAST [43].

Finally, the vector of inner elastic forces $\boldsymbol{h}_e$ results as

$$\boldsymbol{h}_e = \begin{bmatrix} \boldsymbol{0} \\ \boldsymbol{0} \\ -\boldsymbol{K}_{eL}\boldsymbol{q}_e - \boldsymbol{D}_e\dot{\boldsymbol{q}}_e \end{bmatrix}. \tag{3.46}$$

External applied forces   External forces in this FOWT model are the ones from aerodynamics and hydrodynamics, subject of the next sections. In order to include them, they need to be transformed into the space of the generalized coordinates representative for the flexible bodies. The discrete applied forces $\boldsymbol{h}_d$ of Eq. (3.29) are again a combination of translational, rotational and elastic forces, aligned with the generalized coordinates $\boldsymbol{z}_{II}$ and $\boldsymbol{z}_{III}$, defined in Eq. (3.26). Based on the nodal forces $\boldsymbol{F}^k$ and torques $\boldsymbol{L}^k$ in the reference frame the generalized forces are

$$\boldsymbol{h}_d = \begin{bmatrix} \boldsymbol{h}_{dt} \\ \boldsymbol{h}_{dr} \\ \boldsymbol{h}_{de} \end{bmatrix} = \sum_k \left(\begin{bmatrix} \boldsymbol{E} \\ \tilde{\boldsymbol{S}}\left(\boldsymbol{R}^k + \boldsymbol{\Phi}^k\boldsymbol{q}_e\right) \\ \boldsymbol{\Phi}^{k^T} \end{bmatrix} \boldsymbol{F}^k + \begin{bmatrix} \boldsymbol{0} \\ \boldsymbol{E} \\ \boldsymbol{\Psi}^{k^T} \end{bmatrix} \boldsymbol{L}^k \right). \tag{3.47}$$

Quadratic velocity vector   The contributions from centrifugal, gyroscopic and Coriolis forces are combined in the quadratic velocity vector $\boldsymbol{h}_\omega$ of Eq. (3.29). As these forces are of minor importance for the FOWT moving in 2D and no bodies are attached to the spinning rotor, the derivation is omitted here and can be looked up in [59, p. 296] (for a reference in English see [207]). Still, the quadratic velocity vector is implemented in the present model.

The global Newton-Euler equations of each, rigid and elastic, body are now complete and can be transformed into minimal coordinates with the assembled global Jacobian matrix $\boldsymbol{J}$ for rigid bodies of Eq. (3.14) and for flexible bodies of Eq. (3.27) such that the nonlinear EQM result in the form of Eq. (3.15).

Standard Input Data   Many kinematics and kinetics functions can be written as function of the generalized elastic coordinates $\boldsymbol{q}_{e,i}$. They can therefore be computed independently of the response of the MBS. This is due to the description of the flexible body in the body reference frame R. A standard format was defined in [219] to provide an interface between FE models calculating the elastic properties in a pre-processing step for the subsequent solution of the MBS model. With this format, flexible bodies can be pre-computed in FE tools and exported to be used in MBS codes. The Standard Input Data (SID) format is object oriented and the arrays are stored depending on the order of $\boldsymbol{q}_e$. Part of the SID are the reference coordinates $\boldsymbol{R}$, the shape functions, $\boldsymbol{\Phi}$ and $\boldsymbol{\Psi}$, the product $m\boldsymbol{c}$, the elements of the mass matrix $\boldsymbol{M}$, Eq. (3.30) and the stiffness and damping matrices $\boldsymbol{K}_e$ and $\boldsymbol{D}_e$, respectively, among others. The SID is calculated in the present model in a dedicated function for beam structures.

3.2.3 Additional dynamic couplings

Next to the MBS equations derived above, the FOWT includes several dynamic couplings, which do not require a mechanical multibody model. The blade pitch actuator, for example, is usually modeled as a time-delay or a second-order dynamic transfer function from the commanded blade pitch angle to the measured blade pitch angle. Another example is the drivetrain flexibility resulting in a dynamic coupling between the aerodynamic torque and the reaction torque between the gearbox housing and nacelle. These dynamics can be written as user-defined dynamics, setting up the right-hand-side of an ODE in the input file to the EQM.

In the present model, the rotor shaft flexibility is neglected. This can be justified with the controller bandwidth. All controllers used have a bandwidth below the tower eigenfrequency. This reduces significantly the external forcing at the torsional shaft eigenfrequency, which is usually above the tower eigenfrequency. The blade pitch actuator is modeled as a second-order transfer function with eigenfrequency and damping ratio given in Appendix A.

3.2.4 Symbolic programming

As main target of the SLOW model a high computational efficiency was highlighted in Section 3.1. In order to meet this goal and to allow for a high independence of the platform and the programming language, the EQM of the structural model are written using symbolic programming. As a result, the EQM are well portable and can be implemented on real-time systems. However, when using symbolic programming, a number of limitations has to be kept in mind: The size of the equations must not exceed a certain limit depending on the compiler and the code optimization routines implemented in it. Especially multiple rotations in the tree structure of the MBS increase the size of the equations and lead to long compilation times. An assessment of the compilation times for symbolic codes can be found in [38]. On the other side, the above derivations, specific to flexible bodies as opposed to rigid bodies, do not directly lead to large equations and do not necessarily increase the computational time. A flow chart with the tool architecture from the derivation of the EQM down to the time-domain and frequency-domain results is shown in Section 3.7.

3.2.5 Linearization

The structural EQM are linearized symbolically by calculating the Jacobians with respect to the states $\boldsymbol{x}$ of all variables of the global nonlinear EQM, Eq. (3.15), of rigid and flexible bodies. With system inputs (control and disturbance inputs) defined in vector $\boldsymbol{u}$ (e.g. rotor-effective wind speed v_0, blade pitch angle θ, etc.), the equations are linearized about the set point of the

states $\boldsymbol{x}_0$ and the setpoint of inputs $\boldsymbol{u}_0$

$$\boldsymbol{x} = \boldsymbol{x}_0 + \Delta\boldsymbol{x} \qquad\qquad \boldsymbol{u} = \boldsymbol{u}_0 + \Delta\boldsymbol{u}, \qquad (3.48)$$

where $\Delta\boldsymbol{x}$ and $\Delta\boldsymbol{u}$ are the new vectors of differential states and inputs, respectively. For all linear descriptions, Δ will be omitted in the following for brevity. The coupled nonlinear equations of motion in state-space description can be separated for position- and velocity-dependent terms. It remains with the input matrix $\boldsymbol{B}$

$$\dot{\boldsymbol{x}} = \underbrace{\begin{bmatrix} \boldsymbol{0} & \boldsymbol{E} \\ -\boldsymbol{M}^{-1}\boldsymbol{Q} & -\boldsymbol{M}^{-1}\boldsymbol{P} \end{bmatrix}}_{\boldsymbol{A}} \boldsymbol{x} + \boldsymbol{B}\boldsymbol{u}. \qquad (3.49)$$

One can identify the position-dependent matrix $\boldsymbol{Q}$ and the velocity-dependent matrix $\boldsymbol{P}$, which both result from the transformation of the vector of Coriolis, centrifugal and gyroscopic forces and the applied forces. The linearization of the force model will be addressed together with the description of the external force submodels in Section 3.3–3.6. The linearization is most critical for the aerodynamic force coefficients due to its highly nonlinear behavior.

3.2.6 Time-domain motion and load response signals

For structural design, especially the stresses inside the components are of interest to assess static or dynamic integrity in ULS or FLS analyses as initially introduced in Section 2.7.3. For controller design, also the position, velocity and acceleration of components are of interest, in order to damp certain responses and make sure design limits are not exceeded. Therefore, coordinate systems or nodes of flexible bodies can be defined at locations other than the ones where the generalized coordinates $\boldsymbol{q}$ are defined, or be expressed in other coordinate systems. Often the absolute tower-top displacement, in inertial coordinates is needed and not the one relative to the tower-base frame as the generalized coordinate x_t.

Section forces or structural stresses can be calculated based on the generalized elastic coordinates of flexible bodies $\boldsymbol{q}_e$, see [59, p. 357]. The therein presented approximation of the section forces is straightforward and can be easily implemented in computational algorithms. It neglects, however the dynamic component, as it depends only on the position of the elastic coordinate: Looking at bending only, as for the inner elastic force calculation in Eq. (3.44), the information on the second derivative of the shape function $W_l''(x)$, related to the considered elastic coordinate l, is necessary. The bending stress σ_b as function of the beam longitudinal coordinate x and the lateral coordinate in the cross-section R_1 is

$$\sigma_b(x, R_1) = -ER_1W_l''(x)q_{e,l}. \qquad (3.50)$$

The approximation remains for the internal bending moment $L_b(x)$

$$L_b(x) = E J_{22} W_l''(x) q_{e,l}. \tag{3.51}$$

For a more exact calculation, considering also velocity-dependent sectional loads (including inner elastic forces due to structural damping), the same approach is used here for rigid and flexible MBS. Assuming a "modal spring-damper element" at any longitudinal location along the beam axis gives the section forces as the forces exerted by this spring-damper element. At the tower-top, the sectional forces $\boldsymbol{F}_{tt}$ are

$$^R\boldsymbol{F}_{tt} = \begin{bmatrix} -k_{twr}x_{twr} - d_{twr}\dot{x}_{twr} \\ 0 \\ 0 \end{bmatrix}, \tag{3.52}$$

with the tower modal stiffness k_{twr} and damping d_{twr}. These constants can be selected to be equal to the dominant modal stiffness and damping coefficients within $\boldsymbol{K}_{eL}$ and $\boldsymbol{D}_e$ of Eq. (3.46). This force produces a sectional moment along the tower axis, which can be used to calculate the stresses with the second moment of area J_{22} using the basic laws of mechanics.

3.2.7 Frequency-domain motion and load response spectra

From the linear state-space description of Eq. (3.49), SISO transfer functions from a specific input to a specific output can be derived using Eq. (2.25). Applying frequency-domain spectral methods the response spectra can be calculated without time integration. The response PSD $\boldsymbol{S}_{yy}(\omega)$ results with the transfer function $\boldsymbol{G}(\omega)$ and its complex conjugate transpose $\boldsymbol{G}(\omega)^{*T}$ and the disturbance spectrum S_{dd} as

$$\boldsymbol{S}_{yy}(\omega) = \boldsymbol{G}(\omega) S_{dd} \boldsymbol{G}(\omega)^{*T}. \tag{3.53}$$

Note that the FOWT plant model $\boldsymbol{G}(\omega)$ includes the structural model and the disturbance models, part of Section 3.3–3.6. In order to simplify the computation, the response spectra from wind and waves ($\boldsymbol{d} = [v_0, \zeta_0]^T$) are calculated by assuming that the cross-spectral density between wind and waves is zero $S_{dd}(1,2) = S_{dd}(2,1) = 0$. It results

$$\boldsymbol{S}_{yy}(\omega) = \boldsymbol{G}_v(\omega) S_{vv} \boldsymbol{G}(\omega)_v^{*T} + \boldsymbol{G}_\zeta(\omega) S_{\zeta\zeta} \boldsymbol{G}(\omega)_\zeta^{*T}. \tag{3.54}$$

Section forces

The section force calculation will be derived here in the frequency-domain with the refined method of Eq. (3.52), including the velocity-dependent forces. The simplified method, neglect-

ing the velocity-dependent forces, does not always yield a good agreement with the reference model FAST. Based on Eq. (3.52), the tower-base bending moment M_{yt} can be calculated. Additionally to the elastic forces, which depend on the tower DoFs, the pitch-DoF-dependent forcing due to gravity needs to be included. The static transfer function

$$
\boldsymbol{H}_{My} = \begin{bmatrix} \boldsymbol{c}_{0,z}^T \\ \boldsymbol{K}_{eL} z_{tt} \\ \boldsymbol{D}_e z_{tt} \end{bmatrix}, \qquad \boldsymbol{H}_{My} \in \mathbb{R}^{(3 \times f_e)} \tag{3.55}
$$

is used to calculate the tower-base bending moment cross-spectral density matrix $\boldsymbol{S}_{MyMy}$. The vector $\boldsymbol{c}_{0,z}^T$ of Eq. (3.36) represents the center of mass of the tower in tower-base coordinates (tower reference frame). As the tower is modeled through a single mode shape, $\boldsymbol{H}_{My}$ is a column vector here. The PSD of the tower-base bending moment results as

$$
\boldsymbol{S}_{MyMy}(\omega) = \boldsymbol{H}_{My}(\omega) \boldsymbol{S}_{yy}(\omega) \boldsymbol{H}_{My}^{*T}(\omega). \tag{3.56}
$$

For the computation, the reduced response spectral density matrix $\boldsymbol{S}_{yy}(\omega)$ is used, which includes a reduced set of system outputs: The pitch (β_p)-DoF and the tower-top states x_t and $\dot{x}_t$.

Electrical power

The calculation of the electrical power P is a quadratic problem, it is the product of the generator speed Ω_g and the generator torque M_g. This is why it is especially addressed here for the frequency-domain model. In the time-domain, the electrical power can be calculated with the static components M_{g0} and Ω_{g0} and the fluctuating components ΔM_g and $\Delta \Omega_g$ with the efficiency of the generator η_{gen} as

$$
P = \eta_{gen} M_g \Omega_g = \eta_{gen} (M_{g0} + \Delta M_g)(\Omega_{g0} + \Delta \Omega_g). \tag{3.57}
$$

Here, the electrical power spectrum $S_{PP}(\omega)$ is calculated from the frequency-domain complex response amplitude spectra $y_i(\omega)$ in order to keep the nonlinearity. These spectra can be obtained using the linear transfer functions $G_{ij}(\omega)$ and the input amplitude spectra $d_j(\omega)$, compare Eq. (2.24), as

$$
y_i(\omega) = G_{ij}(\omega) d_j(\omega). \tag{3.58}
$$

It results for the electrical power spectrum $S_{PP}(\omega)$ with $y_i = \Delta \Omega_g$ and the control input ΔM_g

$$
S_{PP}(\omega) = (M_{g0} + \Delta M_g(\omega))(\Omega_{g0} + \Delta \Omega_g(\omega))(M_{g0} + \Delta M_g(\omega))^*(\Omega_{g0} + \Delta \Omega_g(\omega))^*, \tag{3.59}
$$

where $(\cdot)^*$ denotes the complex conjugate. Expanding the sums and neglecting the static component $M_{g0}\Omega_{g0}$ it remains

$$S_{PP}(\omega) = (M_{g0}\Delta\Omega_g(\omega) + \Omega_{g0}\Delta M_g(\omega) + \Delta\Omega_g(\omega)\Delta M_g(\omega))(M_{g0}\Delta\Omega_g(\omega) +$$
$$\Omega_{g0}\Delta M_g(\omega) + \Delta\Omega_g(\omega)\Delta M_g)^*(\omega). \quad (3.60)$$

The complex response amplitude spectra $y_i^v(\omega)$ to wind excitation $v_0(\omega)$ without a dynamic disturbance model is

$$y_i^v(\omega) = G_{v,i}(\omega)v_0(\omega) \quad (3.61)$$

and to wave excitation $\zeta_0(\omega)$ with the wave-force RAO $\boldsymbol{X}(\omega)$ of Eqs. (2.15) and (3.71)

$$y_i^\zeta(\omega) = \boldsymbol{G}_{F,i}(\omega)\boldsymbol{X}(\omega)\zeta_0(\omega). \quad (3.62)$$

Here, the additional drag-excitation of Morison's equation, see Section 3.5.4 is neglected for simplicity. From the amplitude spectra $y_i(\omega)$, the PSD is calculated using Eq. (2.26). Again, the wind and wave response is added neglecting the cross-correlation such that the total response of P is the sum of the contribution from wind excitation and from wave excitation

$$S_{PP}(\omega) = S_{PP}^v(\omega) + S_{PP}^\zeta(\omega). \quad (3.63)$$

A comparison of this approximate computation against nonlinear time-domain results can be seen in Figures 6.19–6.23. Especially, in the wave frequency range the linear approximation underpredicts the power response. This might be due to the negligence of the cross-correlation between wind and waves.

3.3 Wind Model

The 3D turbulent wind field time series are generated with TurbSim v1.06.00 [139] and subsequently averaged over the rotor plane to obtain the rotor-effective wind speed $v_0(t)$ as input to the model described in the next section. To capture the 3p forcing, a rotational sampling of turbulence as e.g. in [69] is carried out instead of averaging over the entire rotor plane. Here, the blade-effective wind speed, as function of time, is calculated assuming a constant rotor speed at the operating point. The thrust force is calculated according to Eq. (3.65) of the next section, by summing over the three blades. The resulting 3p forcing due to wind shear can be observed in Figures 6.19–6.23.

3.4 Aerodynamic Model

A large variety of aerodynamic models with respect to computational effort and accuracy exists, as described in the introduction, Section 2.5.2. For control design, the approach of modeling the rotor as a rigid disk with a thrust and power coefficient has proven to be a reasonable representation, especially in regard to its simplicity and efficiency. The nonlinear model, described in the following, can be linearized in a straightforward manner as is shown subsequently.

3.4.1 Nonlinear model

The model uses one scalar input signal, the rotor-effective wind speed v_0. It is computed a-priori from the 3D wind field in the time-domain, see Section 2.5.2. If the model is applied as a real-time model for model-predictive control, v_0 can also be calculated from LiDAR measurements. Another input is the velocity component of the hub $\boldsymbol{v}_{hub}$ in global $^I x$-direction to calculate the relative wind speed v_{rel} seen by the rotor

$$v_{rel} = v_0 - {}^I\boldsymbol{e}_{I1} \cdot {}^I\boldsymbol{v}_{hub}, \tag{3.64}$$

where $(\cdot)$ denotes the dot-product. The outputs of the aerodynamic model are the torque about the shaft M_{aero} and the thrust force in shaft-direction F_{aero} as

$$M_{aero} = \frac{1}{2}\rho_a \pi R^2 \frac{c_p(\lambda, \theta_1)}{\Omega} v_0^3 \quad \text{and} \quad F_{aero} = \frac{1}{2}\rho_a \pi R^2 c_t(\lambda, \theta_1) v_0^2. \tag{3.65}$$

The power and thrust coefficient c_p and c_t are calculated as functions of the TSR $\lambda = \Omega R/v$ and the (measured, not the commanded) blade pitch angle θ_1. This is done using FAST [43] with rigid blades, a rotor shaft aligned with the global x-axis at the steady state with a static uniform wind speed and varying rotor speeds Ω for the different TSR λ. The coefficients for the DTU 10 MW RWT can be seen in Figure 3.2. Eventually, the force F_{aero} and the torque M_{aero} are included in the right hand side of equation (3.13), described in Section 3.2.1.

For a better agreement with BEM-models, this simplified model can be augmented with the rotationally sampled turbulence as described in Section 3.3.

The simple rotor-disk model has been extended to include the blade structural elasticity with the flexible MBS described in Section 3.2.2. For the aerodynamic forcing, it was coupled to the code Aerodyn v14 [76]. Results on this model are, however, not included in this thesis. The aim is to include simple engineering models for the unsteady aerodynamic forcing of FOWTs in the future as described in Section 2.5.2.

3.4.2 Linearized model

The aerodynamic torque M_{aero} acting on the rotor about the shaft axis can be written as a Taylor series up to the first order with the partial derivatives with respect to the differential rotor speed $\Delta\Omega$ about the operating point, the differential blade pitch angle $\Delta\theta_1$ and the differential relative wind speed Δv as

$$
\begin{aligned}
M_{aero} = \quad & \underbrace{\frac{\rho_a \pi R^2}{2}}_{k_a} \frac{v^3}{\Omega} c_p(\lambda, \theta) \\
\approx \quad & k_a \left[\frac{v_0^3}{\Omega_0} c_{p,0} \right. \\
+ \quad & \left(-\frac{v_0^3}{\Omega^2} c_{p,0} + \frac{R v_0^2}{\Omega_0} \left. \frac{\partial c_p}{\partial \lambda} \right|_0 \right) \Delta\Omega + \frac{v_0^3}{\Omega_0} \left. \frac{\partial c_p}{\partial \theta} \right|_0 \Delta\theta_1 \\
+ \quad & \left. \left(\frac{3 v_0^2}{\Omega_0} c_{p,0} - R v_0 \left. \frac{\partial c_p}{\partial \lambda} \right|_0 \right) \Delta v \right].
\end{aligned}
\tag{3.66}
$$

The thrust force F_{aero} can be written similarly as

$$
\begin{aligned}
F_{aero} = \quad & k_a v^2 c_t(\lambda, \theta) \\
\approx \quad & k_a \left[v_0^2 c_{t,0} \right. \\
+ \quad & R v_0 \left. \frac{\partial c_t}{\partial \lambda} \right|_0 \Delta\Omega + v_0^2 \left. \frac{\partial c_t}{\partial \theta} \right|_0 \Delta\theta_1 \\
+ \quad & \left. \left(2 c_{T,0} v_0 - R\Omega_0 \left. \frac{\partial c_t}{\partial \lambda} \right|_0 \right) \Delta v \right].
\end{aligned}
\tag{3.67}
$$

As the coefficients are pre-computed as function $c_p = c_p(\lambda, \theta)$, see Figure 3.2, the relations

$$
\frac{\partial c_p}{\partial v} = \frac{\partial c_p}{\partial \lambda} \frac{\partial \lambda}{\partial v} = \frac{R\Omega}{v^2} \frac{\partial c_p}{\partial \lambda}
\tag{3.68}
$$

and

$$
\frac{\partial c_p}{\partial \Omega} = \frac{\partial c_p}{\partial \lambda} \frac{\partial \lambda}{\partial \Omega} = \frac{R}{v} \frac{\partial c_p}{\partial \lambda},
\tag{3.69}
$$

and in the same way for c_t, are used for the derivation of Eqs. (3.66)–(3.67). In the work by [16], different methods for linearizing the aerodynamic force model were implemented and compared, i.e. the tangent and the harmonic linearization. The calculation of the partial derivatives $\frac{\partial c_*}{\partial x}$ was done in the present work by applying a central-difference scheme, interpolating linearly between the data points. For a model verification, a comparison of the rigid-body rotor dynamics was done with a transfer function $G(j\omega)_{v \to \Omega}$ and $G(j\omega)_{v \to F}$ calculated by the tool Simulink. The alternative method, the harmonic linearization would seek an error minimization from the linearization for a given amplitude of oscillation of the aerodynamic model inputs.
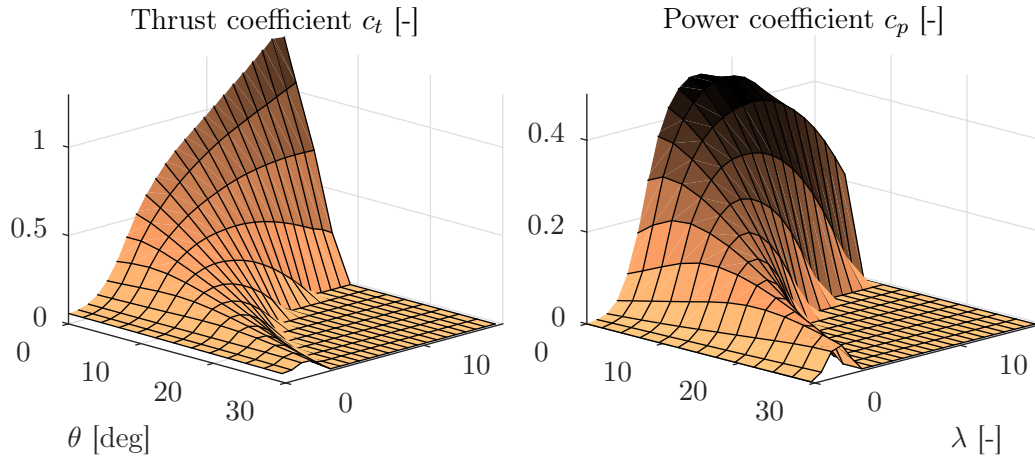
Figure 3.2: Thrust and power coefficients of the DTU 10 MW RWT.

The tangent linearization using a rigid disk for the rotor showed a reasonably good agreement with the reference code FAST, coupled to Aerodyn v14. The fact that such a simple model delivers satisfying results for FOWTs is because it is able to represent the dynamics of the RHPZ through the controller, introduced in Section 2.9, and the low-frequency excitation from the turbulence. These are the dominant aerodynamic effects for FOWTs, whereas the rotor speed harmonics are either more damped than for onshore turbines, Figure 2.3, or merely of a lower order of magnitude than the first-order wind and wave loads. A comparison of the simple model compared to two other aerodynamic models can be found in Section 6.4.6.

3.5 Hydrodynamic Model

The common approach for FOWT modeling is a time-domain representation with Cummins' equation, Eq. (2.19), with additional Morison drag forces to represent the viscous forces neglected by potential flow theory, as introduced in Section 2.5.3.

In order to achieve the goal of computational efficiency, a simplification of the convolution integral of Cummins' equation is necessary, avoiding a time-consuming numerical solution and to obtain an equivalent LTI model. The next sections will introduce the still-water (radiation) problem, a conventional and a parametric first-order wave excitation model, before Morison's equation and the formulation of slowly-varying drift forces is introduced. Special attention is paid to the linearization of the Morison drag in Section 3.5.4 because first, the system damping is important for a robust controller design of Chapter 5 and second, a good drag parameterization is necessary for the parametric design studies of Chapter 6.

3.5.1 Radiation model

A simplification of the radiation problem in numerical representations has been subject to research for many years. One example is the approximation of the radiation force dynamics with a parametric LTI model as described in the introduction, Section 2.5.3. In this case, a dynamic model is fitted to the dynamics from the motion of the floating body to the resulting forces on the body itself. The model has a number of states depending on the quality of the fit in each DoF of the floating body. As a consequence, the radiation force model adds a significant number of states to the FOWT model (usually 3–6 states for each DoF).

A dynamic state-space radiation model was implemented for this model according to [101]. However, for the results shown in this work it was not applied. Instead, the frequency-dependency of the added mass $\boldsymbol{A}(\omega)$ is neglected in the present nonlinear time-domain model and a constant frequency is chosen, at which the added mass matrix is interpolated. This simple and efficient model has shown very promising results, see Section 6.4.6. With this "constant matrix" approach, reported in [220], reasonable frequencies have to be selected for the interpolation to obtain the frequency-independent $\boldsymbol{A}_c \equiv \boldsymbol{A}(\omega_c)$. In this case, the EQM of a rigid body of Eq. (2.15) is transformed to the time-domain as

$$(\boldsymbol{M} + \boldsymbol{A}(\boldsymbol{\omega}_c))\ddot{\boldsymbol{\xi}}(t) + \boldsymbol{B}(\boldsymbol{\omega}_c)\dot{\boldsymbol{\xi}}(t) + \boldsymbol{C}\boldsymbol{\xi}(t) = \boldsymbol{F}^{(1)}(t). \tag{3.70}$$

One approach is to select the constant frequencies of vector $\boldsymbol{\omega}_c$ according to the respective eigenfrequencies of the rigid floating body. This approach has the disadvantage that the solution is in fact only valid for the selected frequency ω_c. Section 6.4.6 will show, however, that the response deviation at other frequencies is limited. In the present implementation, the coupled entries of $\boldsymbol{A}(\omega)$ are interpolated at the eigenfrequency of the motion-DoF (index i) instead of the force-DoF (index j). Figure 3.3 shows the frequency-dependent added mass with the interpolated values.

For the radiation damping matrix $\boldsymbol{B}(\omega)$, an interpolation is not possible due to the strong dependence on the frequency. The nonlinear SLOW model does not include any frequency-dependent parameters and completely neglects radiation damping. The linear frequency-domain SLOW model includes the frequency-dependent radiation damping and the frequency-dependent added mass. The linear state-space description, Eq. (3.49) is solved sequentially for all frequencies. A drawback is here the significant computational effort, due to the inversion of the mass matrix. A comparison of the computational speed for the entire model is shown in Section 3.9.

As discussed in the introduction, the radiation model has two major effects: One is the (frequency-dependent) damping due to the radiated waves and the other is a frequency-dependent added mass. The damping effect is often quite small for FOWTs, compared to
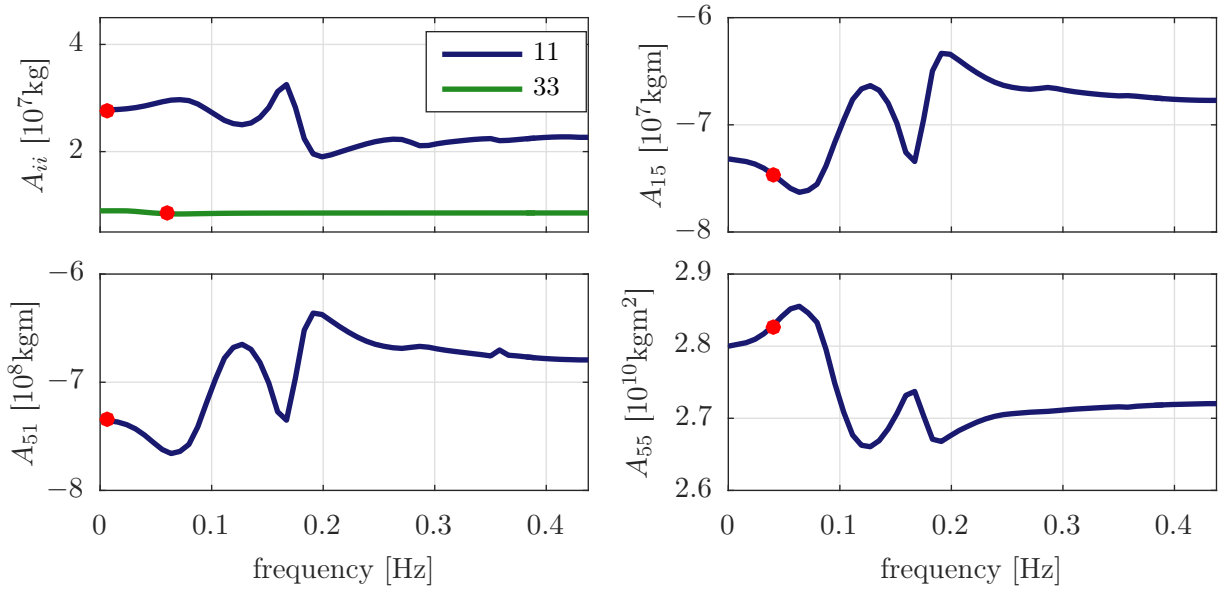
Figure 3.3: Panel code added mass of TripleSpar platform with values interpolated at respective eigenfrequencies.

the viscous damping from flow separation, but the magnitude depends finally on the floater hull shape. The assessment of Section 6.4.6 shows that the radiation damping is small for the shapes used in this work. It is commonly large at frequencies outside the rigid-body natural frequencies. Therefore, radiation damping is neglected for most results of this work.

3.5.2 First-order wave force model

The driving force of the right-hand side of Eq. (2.19) in time-domain, the wave excitation force $\boldsymbol{F}^{(1)}(t)$, is usually obtained through an IDFT of the wave force spectrum. It is, however, also possible to derive a parametric transfer function from the wave height (which can be measured by buoys or radars) to the six forces on a floating body, as introduced in Section 2.5.3. This new approach was investigated as part of this thesis in order to prepare the necessary models for model-predictive control including a preview of the incoming waves. Both methods are presented in the following.

Fourier transform-based model

The six first-order force amplitude spectra $\boldsymbol{F}^{(1)}$ on a floating body for a given sea state can be obtained in the frequency-domain by multiplying the force coefficient $\boldsymbol{X}(\omega)$ with the complex wave amplitude spectrum $\zeta_0(\omega)$

$$\boldsymbol{F}^{(1)}(\omega) = \boldsymbol{X}(\omega)\zeta_0(\omega). \tag{3.71}$$
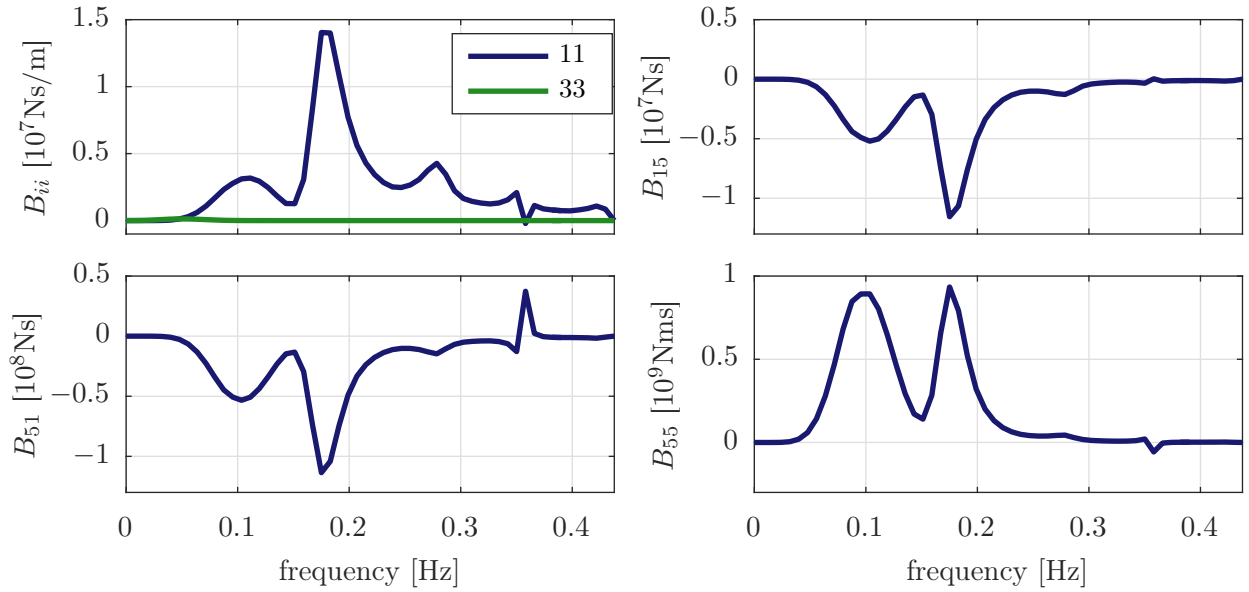
Figure 3.4: Panel code radiation damping of TripleSpar platform.

This is realized numerically in the present model by interpolating the panel code results at the wave spectrum $S_{\zeta\zeta}(\omega)$ frequencies. These depend on the simulation length as $T = N\,dt = N/f_s$. For conventional time-domain simulations of FOWTs, the wave height spectrum magnitude is a model input. Prior to the simulation, the wave force time series $\boldsymbol{F}^{(1)}(t)$ in all six directions are calculated for the entire simulation time through an inverse Fourier transform

$$\boldsymbol{F}^{(1)}(t) = \frac{1}{N}\mathrm{idft}\left(\zeta_0(\omega)\boldsymbol{X}(\omega)\right). \tag{3.72}$$

Note that the wave spectrum $\zeta_0(\omega) \in \mathbb{C}$ in Eq. (3.72) is the complex amplitude spectrum with a random phase, not the power spectrum. This random phase introduces equally random time realizations, see also [15] for a clear derivation. The complex amplitude spectrum $\zeta_0(\omega)$ can be generated through a user-defined spectrum, see Section 2.7.2, or through a DFT of measured time series. This is especially useful for the time-domain comparison with experiments or between models as in Figure 3.26.

The procedure described above employing a DFT is not possible for real-time applications as it requires the knowledge of the complete wave force time series $\boldsymbol{F}^{(1)}(t)$ prior to a time-domain simulation. However, it is possible to apply the same method as for state-space radiation force models to the wave excitation problem. This makes it possible to obtain a unified model of the FOWT with only the rotor-effective wind speed and the current incident wave height as disturbance inputs. The next section will shortly introduce the parametric wave excitation model for FOWTs.

Parametric model

This section deals with the system identification of the frequency-dependent wave excitation force coefficient $\boldsymbol{X}(\omega)$ as presented in [103]. It is originally calculated by 2D strip-theory or 3D panel codes employing linear potential flow theory. The force vector $\boldsymbol{X}(\omega)$ contains two components: The Froude-Krylov force due to the incident wave pressure on the hull and the force due to diffraction of the wave field. The difficulty of fitting the wave excitation force to an LTI model is the fact that the wave height ζ_0, used as reference in the panel code for the calculation of $\boldsymbol{X}(\omega)$, is the wave height at the longitudinal position of the FOWT CF. This results in a "non-causal" transfer function, which means that the forces might arrive at the floating body prior to the wave elevation. In this case the disturbance model input ζ_0 would no longer be the cause for the output, the wave excitation force. Potential flow theory shows that ocean waves are dispersive, i.e. they travel at different phase velocities v_p depending on the wavenumber k, see Section 2.5.3. When selecting a wave height sensor position at some distance from the body against the wave heading direction, the wave excitation force model can be made causal. Falnes has elaborated this problem comprehensively in [221].

A system identification approach will be followed with an impulse response being subject to the fit of a parametric model. see [222]. The next sections will address the causalization of the wave excitation force and the model fit.

Causalization   The wave excitation problem, or the wave excitation transfer function will now be modified to obtain a causal relationship between the wave height ζ_0 and the six forces on the platform $\boldsymbol{F}^{(1)}$. Figure 3.5 shows the response of the wave excitation force coefficient $\boldsymbol{X}(\omega)$ to a wave height impulse at $t = 0\,\mathrm{s}$ in red. The response has been calculated through an IDFT of the wave excitation force coefficient $\boldsymbol{X}(\omega)$. It can be seen that there is a response at negative times, showing the non-causality as described above. A model fit of a non-causal transfer function is not possible and therefore, as discussed above and in [221], a time delay τ_c will be introduced in order to make sure that the transfer function $G_{F,i} \equiv G_{\zeta \to F_i}$ is causal for all directions i.

The time delay τ_c is the time by which the causalized impulse response is lagged compared to the original one. This means that the response time of the causalized system is $t_c = t - \tau_c$. Thus, a wave height time series at the position of the platform at time t yields its physically corresponding wave force response at the time t_c. In frequency-domain, the time delay τ_c is converted to a frequency-dependent phase lag $\varphi_c(\omega)$ as

$$\varphi_c(\omega) = \omega\,\tau_c. \tag{3.73}$$

The time delay τ_c, selected for the OC3-Hywind spar in Figure 3.5 is $\tau_c = 6\,\mathrm{s}$.
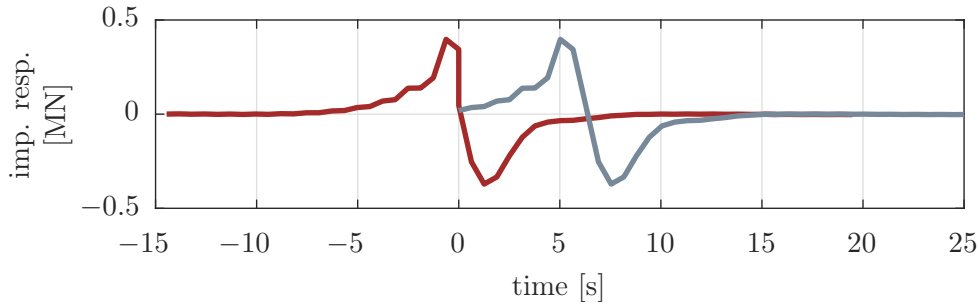
Figure 3.5: Non-causal (red) and causalized (gray) wave excitation impulse response of the OC3-spar [111] in surge [103].

Impulse response fit   The causalized impulse response is now subject to the system identification. For an identification in the time-domain, the error of the original impulse response $\hat{y}_i(t)$, compared to the simulated response $y_i(t)$ is minimized through an optimization of the model parameters and the initial conditions $x_{0,i}$. The model parameters are the parameters of a state-space system with m states, which has therefore m free parameters in canonical form. Further details on the model fit can be found in [103].

In this work, the model structure is selected such that the infinite frequency limit of the identified transfer function $G_{F,i}(j\omega)$ is zero, $\lim_{\omega \to \infty} G_{F,i}(j\omega) = 0$. Therefore, the relative degree is $r \geq 1$ and the transfer function $G_{F,i}(j\omega)$ is strictly proper. A nonzero steady state amplification is not a problem in the case of the wave excitation problem because the wave height $\zeta_0(t)$ has a zero mean. A relatively small number of states (or poles) around $m = 6$ has given reasonable results for the floater geometries studied here.

The fitting procedure has been applied to a three-column semi-submersible shape (OC4, [112]) with the impulse response function shifted in time by a delay of $\tau_c = 7.5$ s. The quality of the model fit is assessed in Figure 3.6 for models with $m = [4, 6, 8]$ states (depicted by increasing darkness). For this rather complex hull, compared to a single-cylinder spar shape, $m = 4$ states do not give a satisfying agreement. But the models with five and six states show a good agreement in both, the frequency and time response. Figure 3.7 shows the response of the fitted model to irregular waves with a comparison to the inverse Fourier transform approach. Especially for the high-frequency waves on top of Figure 3.7, the identified model does not capture all characteristics. For the longer waves of $T_p = [10, 15]$ s, the surge and pitch responses show a better agreement than the heave response. This might be due to the shape of the phase response of the causalized model, which is not captured for all frequencies $f > 0.1$ Hz, see Figure 3.6 (center).

A more detailed evaluation of the identified wave force model can be found in [103] together with results of the wave force model coupled to the structural FOWT model. The parametric model of this section will be used to obtain the transfer functions in Section 5.1. The presented methodology has been incorporated in OpenFAST [223], the successor of FAST v8 [224].
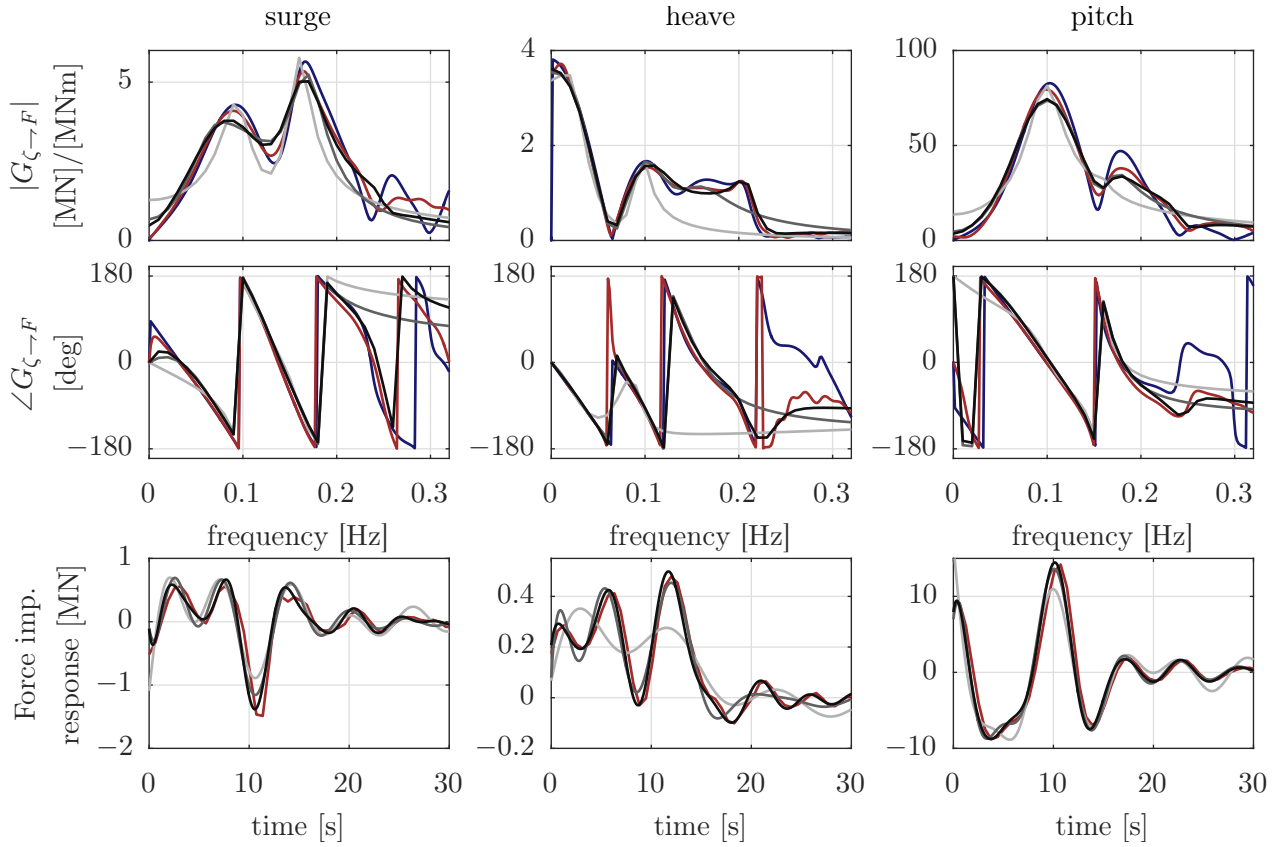
Figure 3.6: Panel code (blue), causalized (red), model fit with $m = [4, 6, 8]$ states (gray, increasing darkness), OC4 semi-submersible [103].

3.5.3 Transformation of hydrodynamic coefficients

The panel code calculations are usually done with respect to the floater CF as discussed in Section 3.2.1 on the formulation of the MBS mass matrices. The convention for the rigid bodies of the MBS, however, is to define all properties with respect to their CM. Therefore, the hydrodynamic coefficients $\boldsymbol{A}(\omega)$, $\boldsymbol{B}(\omega)$ and $\boldsymbol{X}(\omega)$ need to be transformed from the CF to the platform CM. This can be done with the system transformation matrix $\boldsymbol{H}(\boldsymbol{r}_p)$ with $\boldsymbol{r}_p = [0, 0, -z_{cm}]^T$, see [225, p. 176]. The matrix reads

$$\boldsymbol{H}(\boldsymbol{r}_p) = \begin{bmatrix} \boldsymbol{E}^{3\times3} & \tilde{\boldsymbol{S}}\left(\boldsymbol{r}_p\right)^T \\ \boldsymbol{0}^{3\times3} & \boldsymbol{E}^{3\times3} \end{bmatrix}. \tag{3.74}$$

The transformation of the added mass matrix follows (for all frequencies) as

$$\boldsymbol{A}_{cm} = \boldsymbol{H}^{-T}(\boldsymbol{r}_p)\boldsymbol{A}_{cf}\boldsymbol{H}^{-1}(\boldsymbol{r}_p) \tag{3.75}$$

and the transformations of $\boldsymbol{B}(\omega)$ and $\boldsymbol{X}(\omega)$ work equally through a linear transformation.
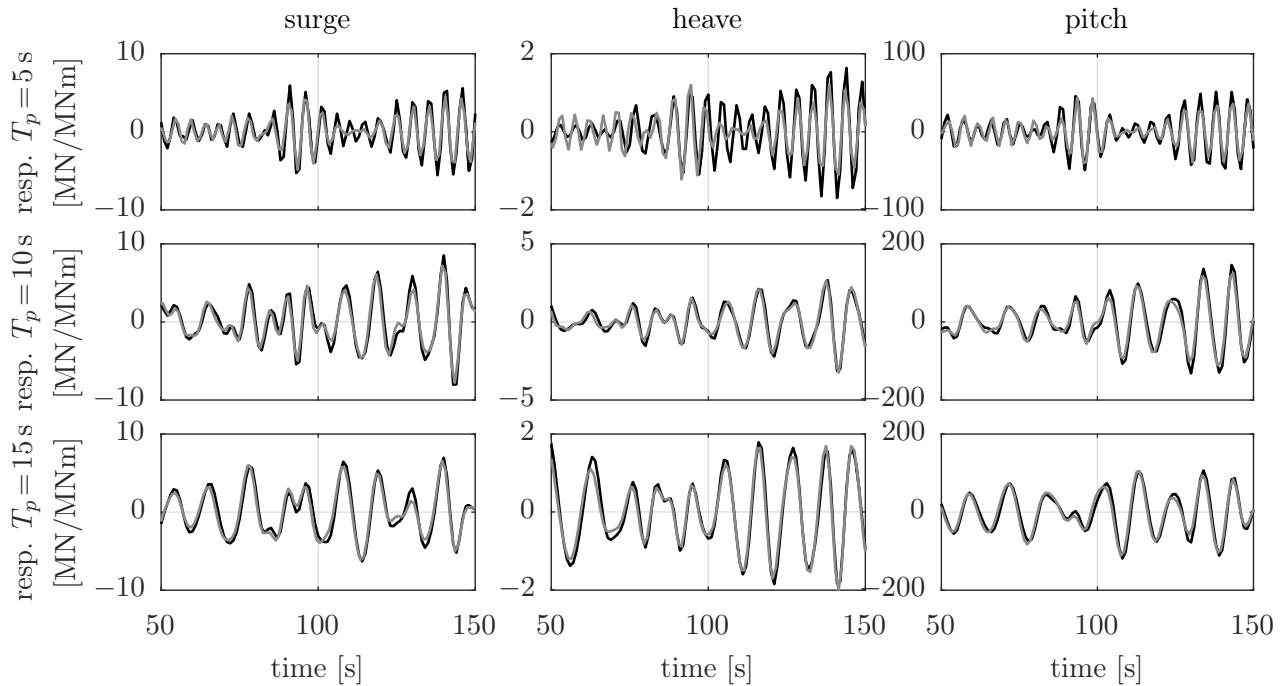
Figure 3.7: Wave force response by inverse Fourier transform (black) and 6-state fitted model (gray) for $T_p = [5, 10, 15]$ s, OC4 semi-submersible, [103].

3.5.4 Morison's equation

For the modeling of viscous drag forces, Cummins' equation with the linear panel code coefficients needs to be augmented with Morison's quadratic drag term. This is the main objective of this section, although Morison's full equation has been implemented in the model. The implementation accounts for viscous damping as well as drag-induced excitation forces. A publication, dedicated to the application of Morison's equation with the linearized SLOW-model of this work can be found in [226].

The drag coefficients C_D for cylindrical structures in horizontal cross-flow can be found in the literature, e.g [227]. They depend usually on the Keulegan-Carpenter KC and the Reynolds number Re, see Eqs. (2.12) and (2.40) in the introduction. Although Morison's equation (2.21) provides only horizontal forces, a quadratic drag term can be applied to heave plates in vertical direction. Chapter 4 on the experiments will deal more in detail with the identification of the drag coefficients of the different members of the floater. Exemplary results are shown in this section for the scaled TripleSpar model of Chapter 4 and the full-scale TripleSpar, introduced in Section 2.10 and subject of Chapter 6.

The next sections will first address the nonlinear implementation of Morison's equation and subsequently the linearization procedure.

Morison's equation nonlinear

For the present model, the submerged part of the floating platform is discretized through nodes, as shown in Figure 3.8. Thus, Morison's equation for a cylinder, Eq. (2.21), is extended to account for the relative fluid velocities. The necessary wave kinematics for solving Morison's equation to obtain the excitation forces were introduced in the frequency-domain in Section 2.5.3. For the time-domain, an inverse Fourier transform according to Eq. (2.6) gives the time-dependent velocities $\boldsymbol{v}(t, z)$ and accelerations $\boldsymbol{a}(t, z)$. Morison's equation is in this work based on nodes k, each having associated modified Morison drag $C_{D,ik}^*$ and added mass coefficients $C_{A,ik}^*$ for all three directions i, which include the respective hull surface area A_{ik}, projected on direction i in the body-fixed coordinate system or the volume ∇_k in case of the added mass coefficients. Reformulated Morison's equation reads

$$F_{mor,ik} = C_{M,ik}^* \, a_{w,i} - C_{A,ik}^* \, a_{b,i} + C_{D,ik}^* \left(v_{w,ik} - v_{b,ik} \right) \left| v_{w,ik} - v_{b,ik} \right| \tag{3.76}$$

with the modified drag coefficients

$$C_{D,ik}^* = \frac{1}{2} \rho_w A_{ik} C_{D,ik}. \tag{3.77}$$

This quadratic drag term yields third-order excitations of the system due to the relative velocity magnitude. For the semi-submersibles analyzed in this work, the horizontal and vertical drag coefficients are set according to Figure 3.8: The vertical heave plate drag force is applied to the keel nodes with $C_{D,hp} = C_{D,zk}$ and calculated with the cross-sectional area associated with the same node. No transverse drag forces in horizontal direction are calculated for the heave plates, only for the slender columns. For large heave plates, it might be necessary to calculate the heave plate kinematics at more than one node due to the nonlinearity of the drag forces. The same restriction holds for the reference model FAST, which calculates the heave plate velocity $v_{b,zk}$ at the center node and uses the value for the entire heave plate.

horizontal drag: $C_D > 0$

vertical drag: $C_{D,hp} > 0$

black/green: $C_D = 0$
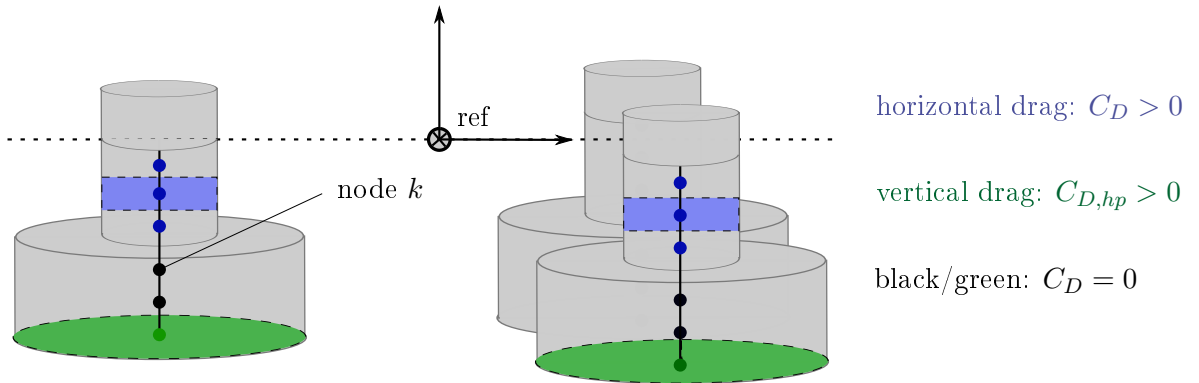
Figure 3.8: Integration of horizontal and vertical node-based Morison drag coefficients [226].

The modified inertia coefficients are defined as

$$C_{M,ik}^* = \rho_w \nabla_k (1 + C_{A,ik}) = C_{A,ik}^* + \rho_w \nabla_k. \qquad (3.78)$$

The modified added mass coefficient $C_{A,ik}^*$, related to the body acceleration, is in the reduced-order model already included in the structural mass matrix in order to avoid forces dependent on the generalized accelerations (which are on the left-hand side of the EQM, Eq. (3.16) and therefore only known for the previous integration step). For heave plates, the modified added mass coefficient is usually referenced with the volume of a half sphere as

$$C_{A,zk}^* = \frac{2}{3}\pi r_i^3 \rho_w C_{A,zk}. \qquad (3.79)$$

Although the vertical Froude-Krylov forces are not part of Morison's equation, they are also calculated based on the nodes in Figure 3.8: For every submerged surface having a projected horizontal component A_{zk}, a node k is defined giving the force $F_{fk,zk}$. The dynamic Froude-Krylov pressure is calculated based on linear wave theory using deep water approximation as

$$F_{fk,zk}(\omega) = A_{zk}\zeta_0(\omega)\mathrm{e}^{-k(\omega)z_k}. \qquad (3.80)$$

The drag-excitation part poses a challenge for the time-domain model in satisfying the initial goal of Section 3.1 because no measurable, scalar, time-dependent disturbance can be fed to the force model of Morison's equation. Instead, an IDFT is necessary, based on a wave height spectrum. Within this work, simplifications have been tested, i.e. assuming the wave height is a narrow-banded stochastic process such that Eqs. (2.8)–(2.10) can be solved for a constant frequency and a constant wavenumber $k = k_p = (2\pi/T_p)^2/g$, calculated at the peak spectral period T_p. With this simplification it is possible to calculate the wave kinematics in vertical and horizontal direction as a function of the incident wave height $\zeta_x(t)$ and its derivative $\dot{\zeta}_x(t) = \mathrm{d}\zeta_x/\mathrm{d}t$ at the longitudinal location x (assuming the wave heading direction is x). In spite of these advantages, the nonlinear dispersion relationship of Eq. (2.4) produces a quadratic dependency between the wavenumber k and the wave angular frequency ω, yielding large errors for frequencies outside the selected narrow band of frequencies. Especially in heave-direction, the Froude-Krylov force transfer function decays quickly with increasing frequencies such that the simplification yields large errors in the low-frequency regime. As a consequence, the simplification is not employed in the present study but the wave kinematics are calculated a-priori from an IDFT. The implementation of the Morison model for Linear Model-Predictive Control (MPC) with a disturbance measurement input for the waves needs further investigation.

For the linearized frequency-domain FOWT model, a linear transfer function will be derived in the following with a linearizaton of the quadratic Morison drag term.

Morison's equation linearized

Morison's equation contains external excitation forces (all summands of Eq. (3.76) which are a function of the wave kinematics, subscript w) and damping forces (all summands of Eq. (3.76), which are a function of the body velocity, subscript b). This nonlinear drag term is a challenge for the linearization. A recent publication by Pegalajar-Jurado [96] presents a method, simplifying the quadratic problem of relative velocities. Although the linearization method selected in this work is different, it also separates the external forcing and the damping terms.

All external forcing terms of Morison's equation (velocity and acceleration-dependent) can be written as a transfer function within the linearized model. With the water velocity $\boldsymbol{v}_w(\omega, x, z)$ and the water acceleration $\boldsymbol{a}_w(\omega, x, z)$ from Eqs. (2.8)–(2.10), the transfer functions from wave height ζ_0 at the initial position to the three translational (superscript t) forces on the CF are

$$\boldsymbol{G}_{Fmor}^t(\omega) = \sum_{k=1} \left(\bar{C}_{D,ik}^{w*} v_{w,ik} + C_{M,ik}^* a_{w,ik} \right) \frac{1}{\zeta_0(\omega)}. \tag{3.81}$$

The overline denotes the linearized drag coefficients to be identified. For the transfer function in rotational direction (superscript r) from ζ_0 to the three moments on the platform about the CF remains

$$\boldsymbol{G}_{Fmor}^r(\omega) = \sum_{k=1} \boldsymbol{r}_{ik} \times \boldsymbol{G}_{Fmor}^t(\omega), \tag{3.82}$$

the cross product with the position vector $\boldsymbol{r}_{ik}$ to each node k. Note that it has shown to be important to calculate the wave kinematics at the longitudinal positions of the respective member of node k, see Eq. (2.5). A comparison of the acceleration-dependent parts (Froude-Krylov forces, last two summands of Eq. (3.81)) using Morison's approach with the potential flow approach is shown next, before the linearization to obtain the equivalent coefficients $\bar{C}_{D,ik}^{w*}$ is addressed.

Froude-Krylov excitation The transfer functions for the Froude-Krylov (acceleration-dependent) part are shown in Figure 3.9, without the velocity-dependent part, in order to compare to the panel code results. Here, the added mass coefficients $C_{A,ik}^*$ are chosen such that the integral added mass from the panel code results equals the added mass from Morison's equation. It can be seen that there is a fairly good agreement for low frequencies. In the introduction, a limit of $ka = 0.5$ was given, above which diffraction becomes important, see Figure 2.4. The diffraction limit is here $0.997\,\text{Hz}$ for $ka = 0.5$. Beyond this frequency the agreement is poor, especially in surge-direction. The wiggles result from the dependence of the kinematics on the longitudinal position and represent the interference of the wave length with the floater members, Eq. (2.5). The linearization of the (velocity-dependent) drag coefficients for the excitation part is subject of the next section, followed by the drag-induced damping.
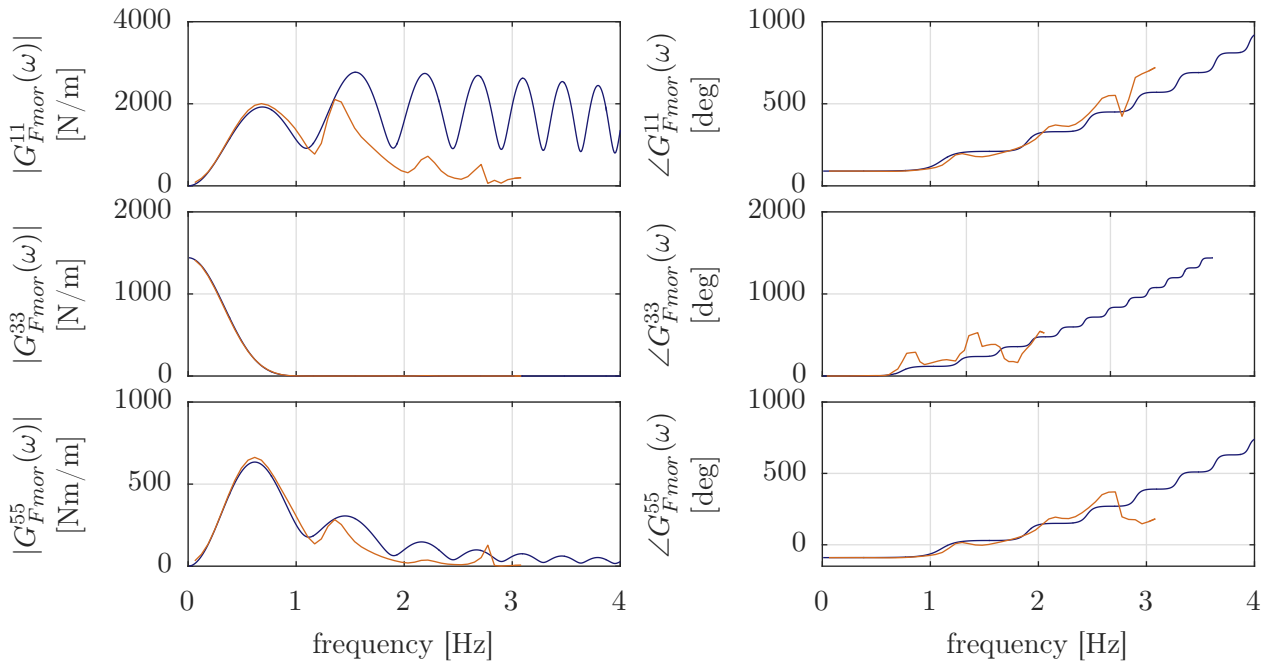
Figure 3.9: Morison excitation transfer functions $\boldsymbol{G}_{Fmor}(\omega)$ for Froude-Krylov component only (blue) compared to panel code transfer functions $\boldsymbol{X}(\omega)$ (orange), scaled TripleSpar of Chapter 4.

Drag linearization   Various procedures for the linearization of the drag term of Eq. (3.76) have been proposed, mainly for stationary vertical cylinders. The general challenge of a correct modeling of the drag forces is the dependence of the quadratic coefficients C_D on the relative flow around the body, usually quantified through Re and KC, see Section 2.5.3. The flow situation, on the other hand, depends on the sea state, the member shape and its motion response. So does the relative velocity about which the quadratic drag C_D is linearized depend on these parameters. Chapter 4 on the experimental tests will deal more in detail with the determination of the Morison drag coefficients.

For the linearization itself, the method most commonly used in literature, following Borgman [46], is based on the standard deviation of the relative fluid velocity. A discussion on the method with a comparison to alternatives can be found in [228]. The authors conclude that Borgman's method underestimates the Morison force for flows around cylindrical structures, dominated not by inertia but by drag forces. A different method, minimizing the residual between the linear and nonlinear response, was presented by [229] and applied to FOWTs in [16]. In this work, a procedure was developed for the damping part as well as the drag excitation part of Morison's equation employing Borgman's formula.

The velocity-dependent term of Morison's equation (3.76) includes one part contributing to the external fluid velocity-induced or viscous drag-induced excitation and one part related to the damping. An efficient method for the linearization of the velocity-dependent part of Eq. (3.76) is selected: The nonlinear drag coefficient $C_{D,ik}$ is split into a wave-velocity and

a body-velocity dependent part. The velocity-dependent linearized nodal Morison force $\bar{F}_{D,ik}$ results with the approximation as

$$\bar{F}_{D,ik} = \bar{C}_{D,ik}^{w*} v_{w,ik} - \bar{C}_{D,ik}^{b*} v_{b,ik} \tag{3.83}$$

in direction i. The part related to the external drag-excitation is $(\bar{C}_{D,ik}^{w*} v_{w,i})$, and the damping part is $(-\bar{C}_{D,ik}^{b*} v_{b,i})$. While the cross-correlation between fluid and body velocity is neglected in Eq. (3.83), it is respected for the identification of the linearized coefficients $\bar{C}_{D,ik}^{w*}$ and $\bar{C}_{D,ik}^{b*}$.

Following [46], the linearized drag coefficients $\bar{C}_{D,ik}$ for wave and body velocities are based on the STD $\sigma(v_{ik})$ of the scalar velocity in direction i of a node k with characteristic cross-sectional area A_{ik}, normal to direction i, as

$$\bar{C}_{D,ik}^{*} = \sqrt{\frac{8}{\pi}} \sigma(v_{w,ik} - v_{b,ik}) \frac{1}{2} \rho_w A_{i,k} C_{D,ik}. \tag{3.84}$$

In the following both, the part representing an external forcing and subsequently the damping part of Eq. (3.83) will be addressed. Additionally, a parameterized formulation of the quadratic drag coefficient C_D for heave plates is implemented, as a function of the KC-number. This is possible because the drag forces from flow around the edges is usually not Re-dependent.

Drag excitation For the linearization according to Eq. (3.84), the actual relative fluid velocity STD is necessary. However, this is difficult as the body response is not yet known. In order to avoid an iterative procedure, a first approach is to consider a stationary body for the identification of the excitation problem. The drag force transfer function $\boldsymbol{G}_{Fmor}(\omega)$ for the velocity-dependent components is shown in Figure 3.10 for surge, heave and pitch. Looking at the magnitudes it can be seen that for the TripleSpar, the velocity-induced excitation is very small, approximately 20 times smaller than the Froude-Krylov forcing of Figure 3.9.

Next to the above approach, an improved alternative method for obtaining the relative fluid velocities in Eq. (3.84) was implemented: Here, the cross-spectral density matrix of the generalized velocities $\boldsymbol{S}_{\dot{\xi}}(\omega)$ in the 2D xz-plane with the reference point SWL is used, see Eq. (2.14). To obtain these, the generalized body velocity response spectrum is calculated with the panel code RAO. Equation (2.15) is differentiated to obtain the generalized velocity transfer function

$$\boldsymbol{G}_{\zeta \to \xi}(\omega) = j\omega \frac{\xi(\omega)}{\zeta_0(\omega)} \tag{3.85}$$

and the cross-spectral density matrix for the generalized platform velocities becomes

$$\boldsymbol{S}_{\dot{\xi}\dot{\xi}}(\omega) = \boldsymbol{G}_{\zeta \to \xi}(\omega) \, S_{\zeta\zeta} \, \boldsymbol{G}_{\zeta \to \xi}^{*T}(\omega). \tag{3.86}$$
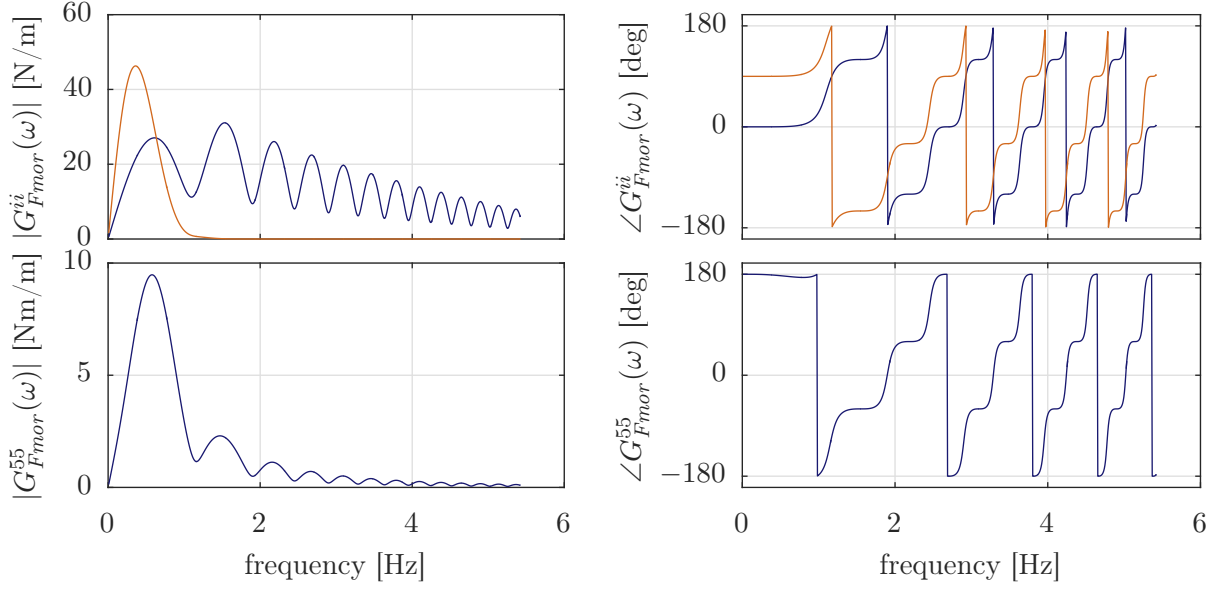
Figure 3.10: Morison excitation transfer functions $\boldsymbol{G}_{Fmor}$ for drag-induced component only with $C_D = 0.6$ and $C_{D,hp} = 20$. Top: Surge (blue) and heave (orange), bottom: pitch, scaled TripleSpar of Chapter 4.

The velocity spectrum $\boldsymbol{S}_{v_k v_k}(\omega)$ at each of the nodes k of Figure 3.8 can be calculated using the cross-spectral density matrix $\boldsymbol{S}_{\dot{\xi}\dot{\xi}}(\omega)$ of the reference point with the transformation matrix for the nodes, here assuming a rigid platform

$$\boldsymbol{H}_k = \boldsymbol{H}(\boldsymbol{r}_k) = \left[\begin{array}{cc} \boldsymbol{E}^{3\times3} & \tilde{\boldsymbol{S}}\left(\boldsymbol{r}_k\right)^T \end{array} \right]. \tag{3.87}$$

The nodal velocity cross-spectral density matrices $\boldsymbol{S}_{v_k v_k}(\omega) \in \mathbb{R}^{(3\times3)}$ with the three translational velocity components result as

$$\boldsymbol{S}_{v_k v_k}(\omega) = \boldsymbol{H}_k \boldsymbol{S}_{\dot{\xi}\dot{\xi}}(\omega) \boldsymbol{H}_k^T. \tag{3.88}$$

Thus, the body nodal velocity STD $\sigma(v_{b,ik})$ is available together with those of the water velocities $\sigma(v_{w,ik})$ using Eq. (2.28). Consequently, Borgman's formula, Eq. (3.84), can be solved using the relative velocities. This approach using the RAO implies, however, that the body response is calculated with the panel code only, neglecting the hydrodynamic viscous drag, the wind forcing and the structural flexibilities. In the results section, Chapter 6, it will be shown that the response to first-order waves does not depend on the system's damping, which encourages the use of the RAO for the drag excitation identification.

Drag damping Now, the drag coefficients related to the damping of the FOWT, $\bar{C}_{D,ik}^{b*}$ are identified. Generally, the same procedure is applied as in the previous paragraph. However, now the full system response is used to obtain the body nodal velocities $v_{b,ik}$. This is due to the fact that there is an important interaction of the hydrodynamic damping properties of the FOWT
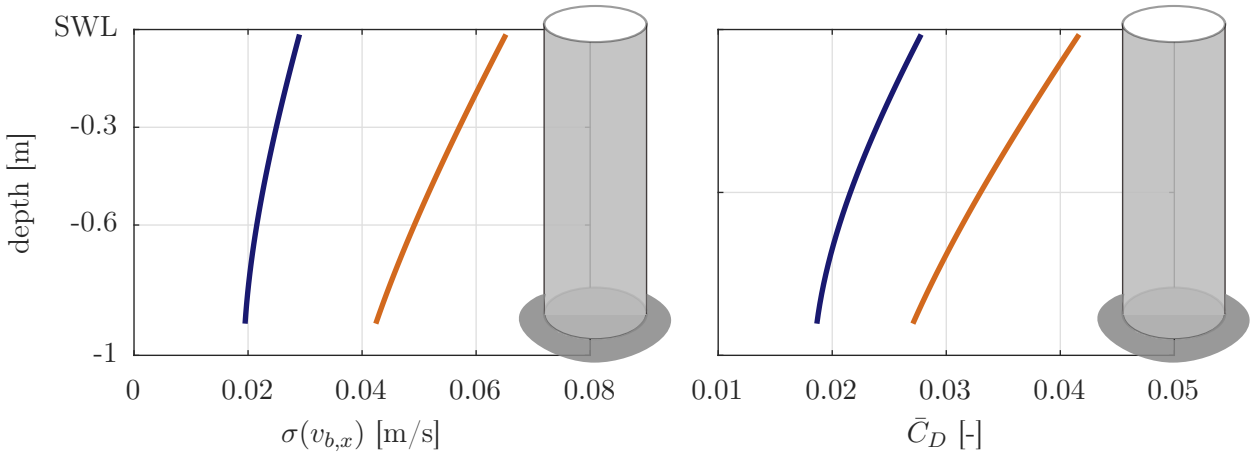
Figure 3.11: Nodal transversal body velocity STD over column length (left) and obtained linearized drag coefficients $\bar{C}_D$ (right) for two sea states, LCs 7 (blue) and LC 9 (orange) of Chapter 4, [226].

and the rotor dynamics and thus, a coupling with the wind turbine controller. The proposed procedure uses the previously calculated wave force spectra but now an iteration is necessary: The hydrodynamic damping is updated as a function of the response, until it converges.

For the identification of the system damping from Morison's equation, only the body velocities are considered and the fluid velocity through the wave kinematics theory, Eqn. (2.8)–(2.10), is set to zero. This simplification allows to separate the above excitation force problem from the present damping problem (which is important for separating the external force calculation (pre-processing) from the calculation of the system response). The relative nodal velocity $(v_{w,ik} - v_{b,ik})$ is usually dominated by the body velocity at the low-frequency eigenmodes and by the water velocity at the first-order wave frequencies. Thus, for the identification of the damping component (important for the low-frequency resonances, see Chapter 4) the negligence of the wave kinematics can be considered reasonable.
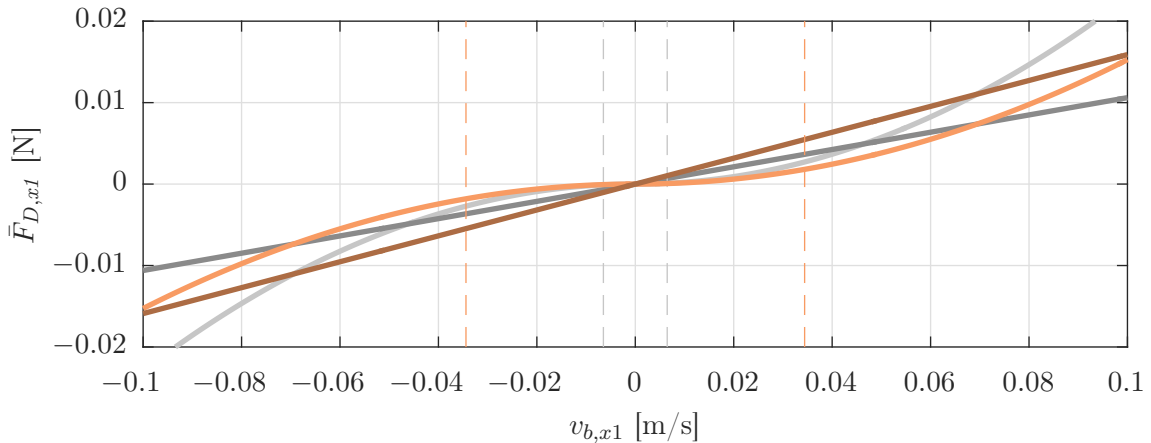
Figure 3.12: Nonlinear (light) and linearized (dark) Morison drag force $\bar{F}_{D,x1}$ for two sea states, LCs 7 (gray) and LC 9 (orange) of Chapter 4 with indication of velocity STD, [226].

Figure 3.11 (left) shows the velocity standard deviation over the length of the scaled Triple-Spar used in Chapter 4 for two sea states. It can be seen how the body velocity depends on the depth. Equally does the drag coefficient, Figure 3.11 (right), depend on the body velocity as given by Eq. (3.84). The linearized nodal drag force $\bar{F}_{D,x1}$ for node 1 at SWL is shown in Figure 3.12 together with the nonlinear drag force as function of the nodal velocity $v_{b,x1}$. The figure shows $\bar{F}_{D,x1}$ for the same two sea states as Figure 3.11, LCs 7 and LC 9 of Chapter 4. Clearly, the linearization depends on the response magnitude (STD marked by dashed lines).

The obtained linear nodal drag coefficients $\bar{C}_{D,ik}^{b*}$ can be integrated resulting in the generalized coefficient matrix $\boldsymbol{D} \in \mathbb{R}^{(6\times6)}$ such that the generalized linearized Morison drag force $\bar{\boldsymbol{F}}_D^b$ results as

$$\bar{\boldsymbol{F}}_D^b = \boldsymbol{D}\dot{\boldsymbol{\xi}}. \tag{3.89}$$

This is convenient as only a single damping matrix for the entire platform results, equal to the hydrostatic stiffness matrix $\boldsymbol{C}$. It can be used, for example, to update the RAO, Eq. (2.15), with the viscous drag forces. The integration to obtain the coefficient matrix $\boldsymbol{D}$ is written again using the transformation tensor $\boldsymbol{H}(\boldsymbol{r}_k)$ of Eq. (3.87) as

$$\boldsymbol{D} = \sum_{k=1} \boldsymbol{H}^T(\boldsymbol{r}_k)\boldsymbol{D}_k^b\boldsymbol{H}(\boldsymbol{r}_k) \tag{3.90}$$

with the nodal drag matrix

$$\boldsymbol{D}_k^b = \mathrm{diag}\left(\left[\bar{C}_{D,xk}^b, \ \bar{C}_{D,yk}^b, \ \bar{C}_{D,zk}^b\right]\right). \tag{3.91}$$

The procedure can be seen as a transformation of the nodal drag coefficients into the generalized coordinates, which are defined at the reference point. The iteration and the final damping matrix $\boldsymbol{D}$ is shown in Figure 3.13 for the scaled model of Chapter 4. It can be seen that the solution converges already with about 4 iterations. The implemented algorithm checks for convergence with an exit criterion of 5%. For the same model, time series of the overall Morison drag forces $\boldsymbol{F}_D^b(t)$ were calculated for the (severest) LC 9 in Figure 3.14: Once with the linearized drag force and once with the quadratic drag force. The drag excitation of Morison's equation is set to zero in this case, so that the only velocity-dependent force is the drag force. The forces on the right are the integrated generalized forces in the respective directions. It can be seen that the linearized drag follows well the nonlinear one, except for the largest velocity peaks, where the nonlinear model reaches higher values. The generalized damping matrix $\boldsymbol{D}$ over the bins of Table 2.1 is shown for the full-scale TripleSpar concept in Figure 3.15. It can be seen that the linearized damping coefficients increase in magnitude for higher wind speeds (correlated with higher sea-states according to Table 2.1). This is due to the increased response amplitude at these more severe conditions. However, Figure 3.15 also includes a

$$\boldsymbol{D} = \begin{bmatrix} 7.7 & 0 & 0 & 0 & -3.3 & 0 \\ 0 & 0 & 0 & 0 & 0 & 0 \\ 0 & 0 & 40.2 & 0 & 2.6 & 0 \\ 0 & 0 & 0 & 3.2 & 0 & 0 \\ -3.3 & 0 & 2.6 & 0 & 6.3 & 0 \\ 0 & 0 & 0 & 0 & 0 & 0.7 \end{bmatrix}$$
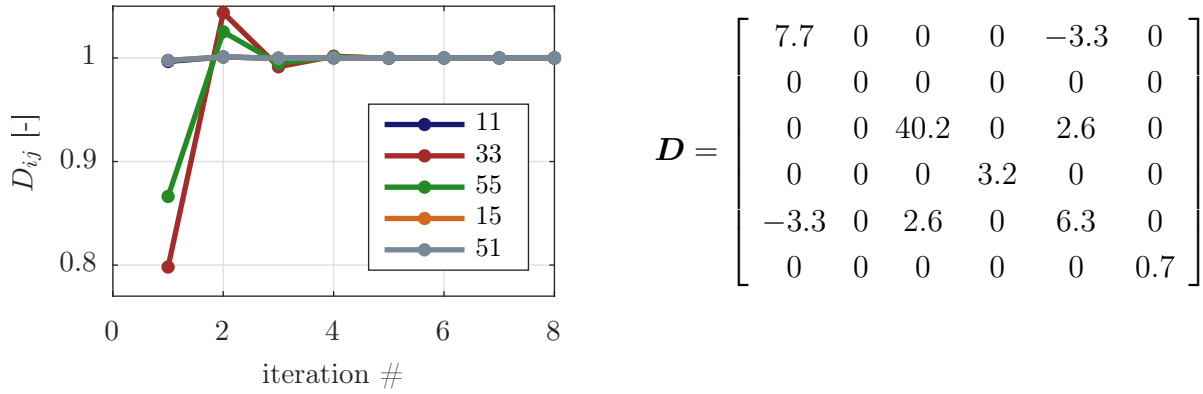
Figure 3.13: Iterative solution of Morison drag coefficient matrix $\boldsymbol{D}$ for aligned wind and waves (scaled model of Chap 4, LC 7), [226].
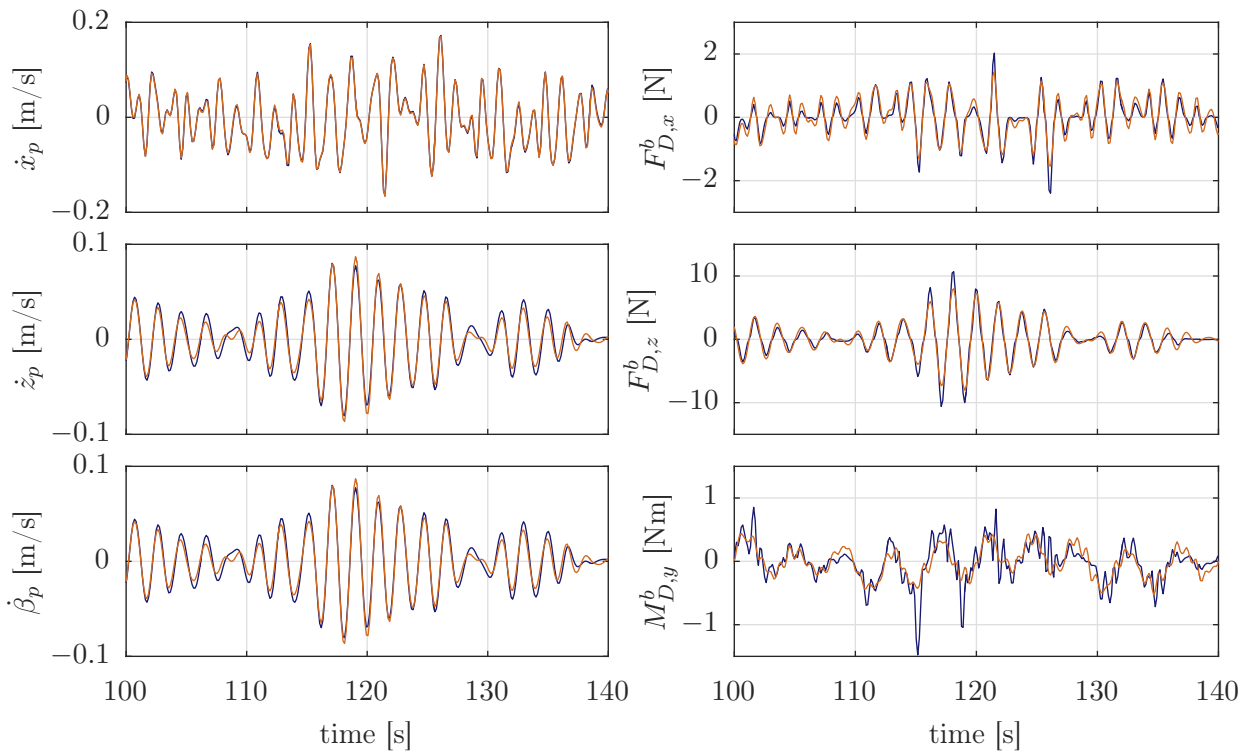
Figure 3.14: Overall Morison drag force time series $\boldsymbol{F}_D^b(t)$, nonlinear (blue) and linearized (orange) for scaled TripleSpar in LC 9 of Chapter 4, [226].

parameterized nonlinear heave plate drag coefficient $C_{D,hp}$, which decreases for larger response amplitudes. This is the subject of the next paragraph.

Keulegan-Carpenter-dependent drag coefficients   After the model validation with the experiments, subject of Chapter 4, showed a good agreement with the heave plate drag coefficients from dedicated experiments published in [230], the quadratic drag coefficients $C_{D,hp}$ were parameterized as a function of KC. The drag coefficient magnitude as function of KC from literature data can be seen in Figure 4.12. For heave plates with sharp edges and detached flow, there is no dependency on Re and the parameterization is more straightforward than for cylindrical structures with various vortex shedding regimes. The general convergence behavior shown in Figure 3.13 does not change with the inclusion of the parametric quadratic drag in the iteration. The resulting heave plate drag coefficient can then be used in the same way for the nonlinear time-domain simulations with the simplified nonlinear model and with FAST. The iterative frequency-domain solution with KC-dependent heave plate drag is the topic of the paper [226].   Figure 3.16 shows the KC-dependent resulting quadratic heave plate drag
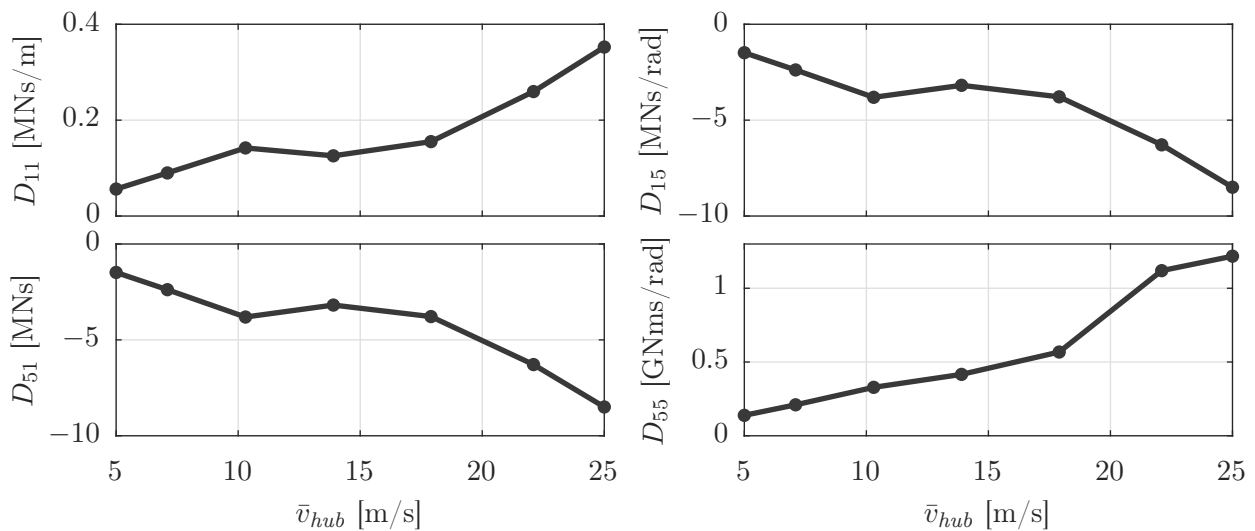
Figure 3.15: Global linearized Morison drag matrix elements for TripleSpar over environmental conditions of Table 2.1, [226].

coefficients over the operating wind speeds for the full-scale TripleSpar concept. It can be seen that KC increases for higher wind speeds, which is due to the increasing response amplitude. As a result, the nonlinear heave plate drag coefficient $C_{D,hp}$ decreases for both, the excitation and the damping problem. The use of a response magnitude-dependent drag coefficient is not common so far but the strong dependency on the LC of Figures 3.15 and 3.16 suggests that this might be necessary. A summary of the hydrodynamic forcing calculation can be found in Figure 3.18, including the iterative linearization of the viscous drag forces.
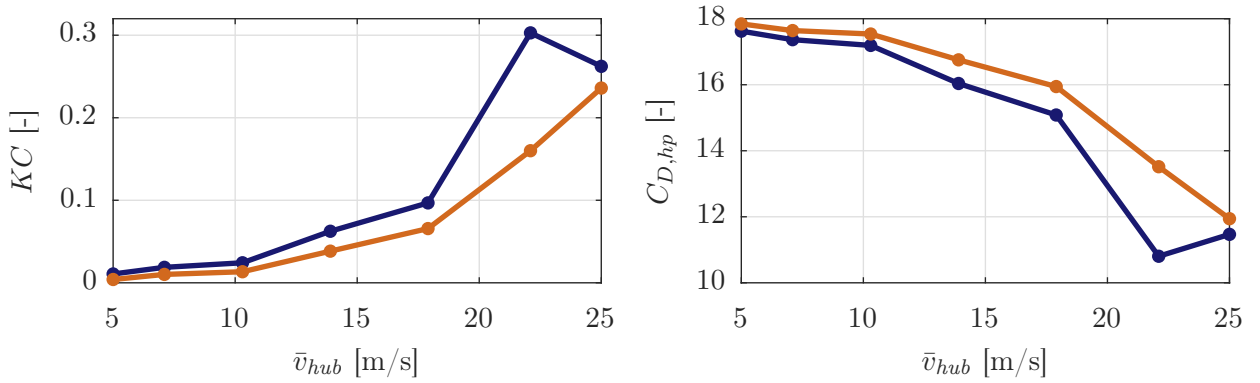
Figure 3.16: Heave plate *KC*-number and resulting quadratic drag coefficient $C_{D,hp}$ from data of Figure 4.12 for environmental conditions of Table 2.1. Case (1): Damping (blue) with Closed Loop (CL) system model iterated until convergence. Case (2): Excitation (orange) with body velocity calculated based on panel code RAO and wave kinematics with linear wave theory, [226].

3.5.5 Second-order slow-drift model

For bichromatic waves, external forces on a floating body appear at the sum and difference of the two wave frequencies, as introduced in Section 2.5.3. A nonlinear force model, representing this effect, was included in the present work because of clear resonances, visible in the model tests of Chapter 4. Pinkster derived the second-order slowly-varying drift force spectrum using the QTF, denoted by $\boldsymbol{T}(\omega, \omega)$, which can be obtained from nonlinear panel codes. The formulation from [229] reads

$$\boldsymbol{S}_{FF}^{(2)}(\mu) = 8 \int_0^\infty \boldsymbol{T}(\omega, \omega + \mu) S_{\zeta\zeta}(\omega) S_{\zeta\zeta}(\omega + \mu) \boldsymbol{T}(\omega, \omega + \mu)^{*T} \mathrm{d}\omega, \qquad (3.92)$$

where $\mu = \omega_i - \omega_j$ is the difference-frequency of the bichromatic wave. Newman proposed in [231] a simplification of Eq. (3.92), calculating the force spectrum $\boldsymbol{S}_{FF}^{(2)}$ with the diagonal $\boldsymbol{T}(\omega_i, \omega_i)$ only, instead of the full QTF. This can be justified by the fact that the QTF does usually not show large variations with the difference-frequency, see [115, p. 157]. A computational advantage of this simplification is that the diagonal of the QTF results from a first-order panel code calculation, already. The force spectrum with Newman's approximation is then

$$\boldsymbol{S}_{FF}^{(2)}(\mu) = 8 \int_0^\infty \boldsymbol{T}(\delta, \delta) S_{\zeta\zeta}(\omega) S_{\zeta\zeta}(\omega + \mu) \boldsymbol{T}(\delta, \delta)^* \mathrm{d}\omega \qquad (3.93)$$

with $\delta = \omega + \mu/2$. In the time-domain, Newman's simplification becomes more important. The force time series result according to [231] from a double IDFT

$$\boldsymbol{F}^{(2)}(t) = \sum_i \sum_j \zeta(\omega_i) \zeta(\omega_j)^* \boldsymbol{T}(\omega_i, \omega_i) \cos\left[(\omega_i - \omega_j)t + \varphi_{\zeta,i} - \varphi_{\zeta,j}\right]. \qquad (3.94)$$

The numerically expensive double summation over ω_i and ω_j of Eq. (3.94) can be written, as proposed in [231], as the square of a single sum over suitable frequency ranges. In this case, the time series result in the formulation of [117] as

$$\boldsymbol{F}^{(2)}(t) = \boldsymbol{\theta}^2\big|_{T(\omega_i, \omega_i) > 0} - \boldsymbol{\theta}^2\big|_{T(\omega_i, \omega_i) < 0} \qquad \text{with}$$

$$\boldsymbol{\theta} = \sum_i |\zeta(\omega_i)| \sqrt{2|\boldsymbol{T}(\omega_i, \omega_i)|} \cos(\omega_i t + \varphi_{\zeta,i}),$$

(3.95)

where $|\zeta(\omega_i)|$ is the wave amplitude magnitude at ω_i, i.e. from Eq. (2.26), and $\varphi_{\zeta,i}$ is the phase angle corresponding to the same frequency. In this work, the phase convention is such that $\varphi=0$ on the positive real axis. The single sum accelerates significantly the numerical solution. However, this acceleration comes at the cost of oscillations at high frequencies, appearing in the force time series. These are not physical and need to be filtered. A further development of Newman's approximation was proposed by Standing [232] with the product of two sums as

$$\boldsymbol{F}^{(2)}(t) = \mathrm{Re}\left(\left[\sum_i |\zeta(\omega_i)| \, \mathrm{sgn}(\boldsymbol{T}(\omega_i, \omega_i)) \sqrt{\boldsymbol{T}(\omega_i, \omega_i)} \exp(\omega_i t + \varphi_{\zeta,i}) \right] \cdot \right.$$

$$\left. \left[\sum_j |\zeta(\omega_j)| \sqrt{\boldsymbol{T}(\omega_j, \omega_j)} \exp(-\omega_j t + \varphi_{\zeta,i}) \right] \right).$$

(3.96)

In Figure 3.17, the previously mentioned formulations for the slowly varying drift force of Eqs. (3.93)–(3.96) are compared for a LC of the experiments of Chapter 4 with the 1/60-scaled TripleSpar of Figure 2.7. The mean drift coefficients for the model, calculated with the nearfield solution, are shown in surge-direction in the second plot. The two lower graphs of Figure 3.17 show the force spectra and the corresponding time series. As expected, the drift force spectra $S_{FF,11}^{(2)}(\omega)$ in surge contain energy outside the frequencies of the wave spectrum $S_{\zeta\zeta}(\omega)$ (on top). The direct frequency-domain calculation, Eq. (3.93), predicts the largest response magnitude, especially at low frequencies. The double sum approach of Eq. (3.94) gives slightly smaller force amplitudes. The above-mentioned unphysical force oscillations can be observed for Newman's original formulation, Eq. (3.95). They are not present in the improved formulation by Standing, Eq. (3.96). The response magnitude at low frequencies, however, is the same. The formulation, which is implemented in the model, is the one according to Standing et al., Eq. (3.96), the same which is implemented in HydroDyn, see [95] and [117]. For the linearized frequency-domain model, the spectral densities $\boldsymbol{S}_{FF}^{(2)}(\omega)$ are computed through a DFT of the force time series of Eq. (3.96) in order to ensure equal difference-frequency excitation for both models. In conclusion, it is noted that differences between the various implementations for a simplified representation of the slowly-varying drift forces exist. A response difference in the order of magnitude of Figure 3.17 is also reported in [232, Figure 8]. On the other hand, the dif-
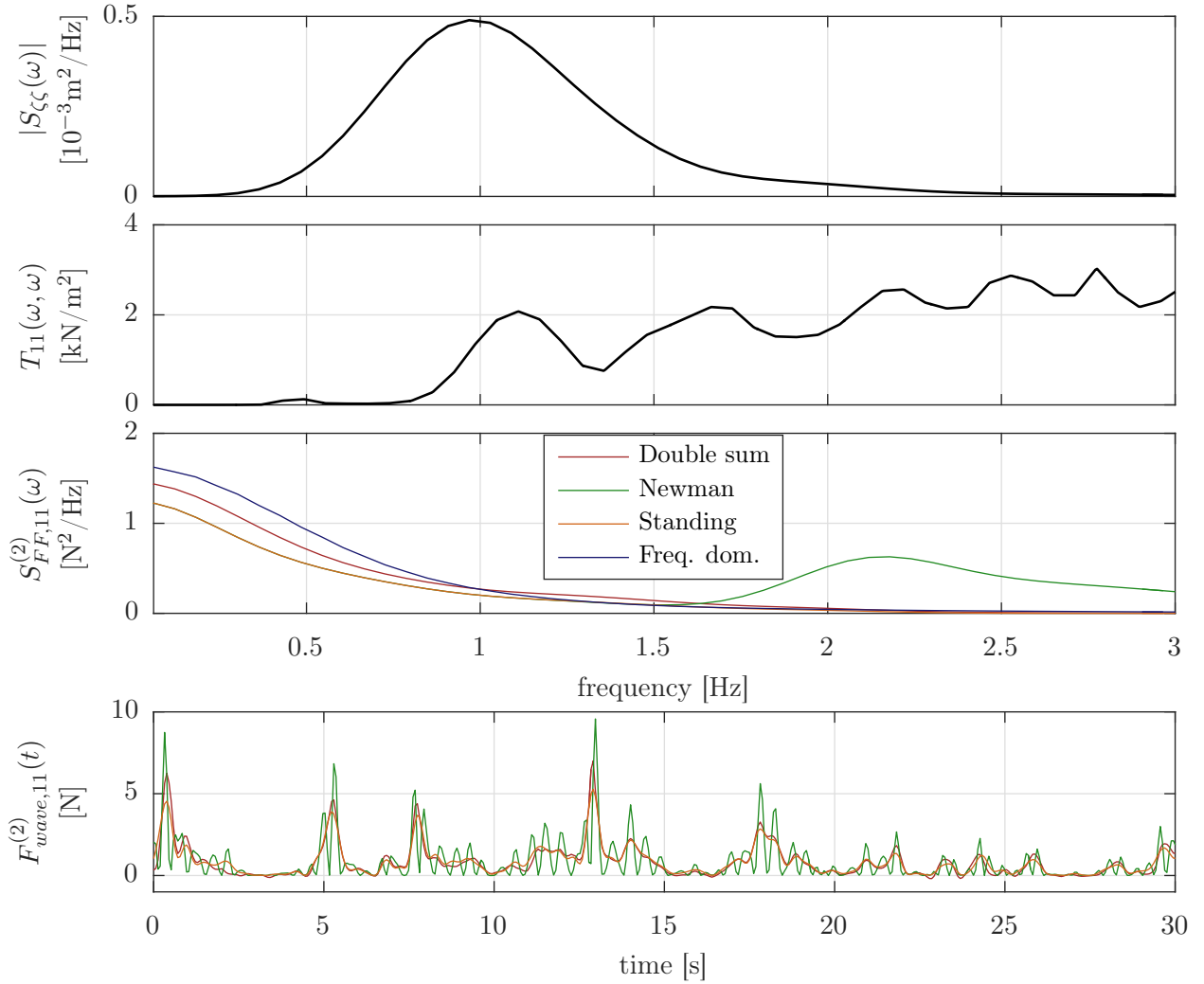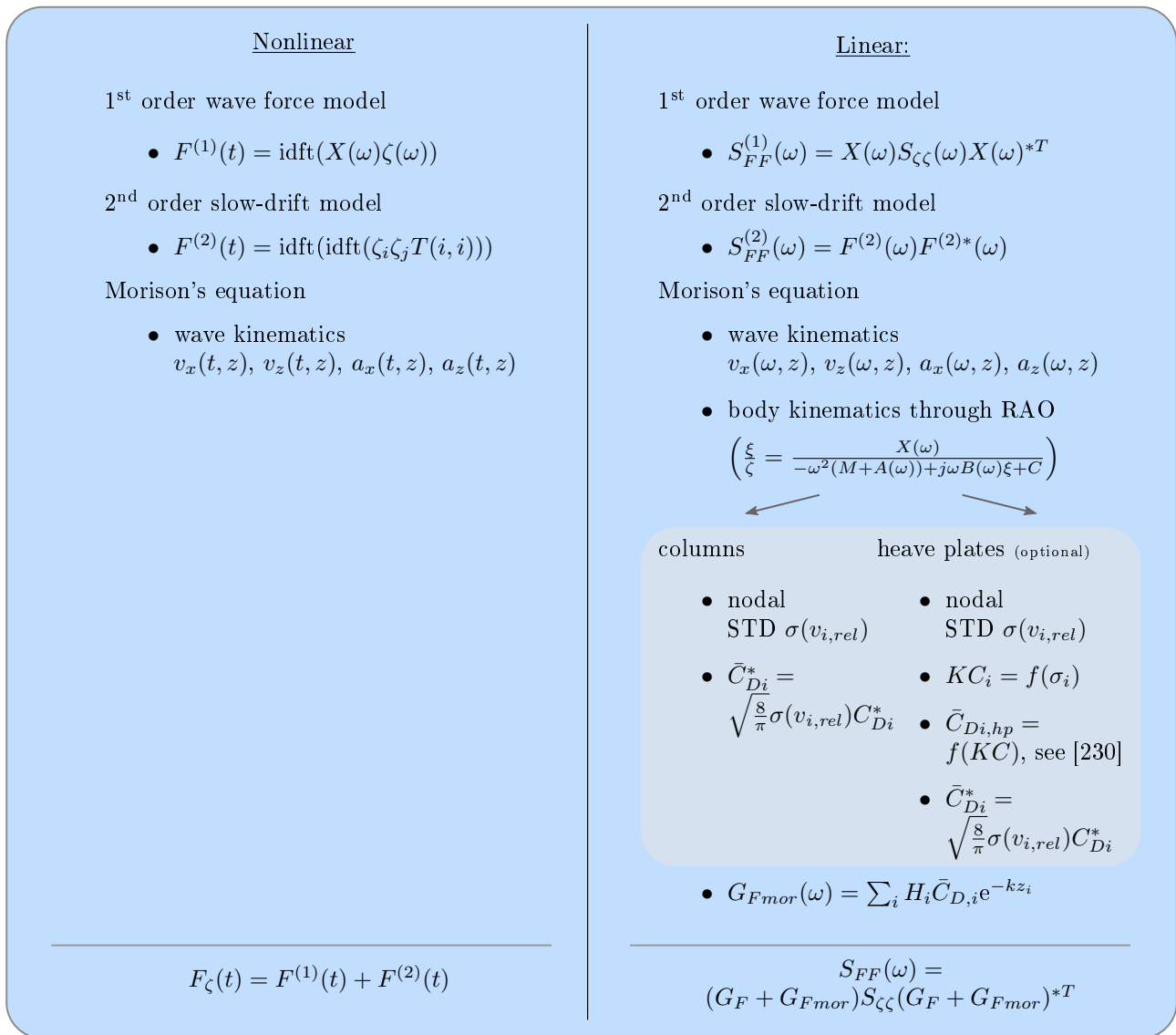
Figure 3.17: Wave spectrum (top), mean drift coefficients $T_{11}(\omega,\omega)$, surge slow-drift force spectrum $S_{FF,11}^{(2)}(\omega)$ and time series $F_{11}^{(2)}(t)$ with frequency-domain calculation (Eq. (3.93)), double IDFT (Eq. (3.94)), original Newman approximation (Eq. (3.95)) and Standing et al.'s formulation (Eq. (3.96)) for scaled TripleSpar of Chapter 4, LC 7.

ference in the computational resources is also significant as the number of function evaluations is N^2 for the double IDFT, compared to $2N$ for Standing et al.'s formulation and the accuracy can be considered sufficient for a conceptual phase design calculation. In this work, Newman's approximation is used for the identification of the viscous drag in irregular wave conditions of the experimental tests of Chapter 4.

3.5.6 Summary

The computational procedure for calculating the wave excitation forces, for both, the nonlinear time-domain model and the frequency-domain model is illustrated in Figure 3.18. This calculation takes place offline, meaning as a pre-processing to the calculation of the FOWT

response. The forces consist of the first-order wave force $\boldsymbol{F}^{(1)}$, the slow-drift forces $\boldsymbol{F}^{(2)}$ and the drag excitation component of Morison's equation $\boldsymbol{F}_{mor}$. The nonlinear time-domain model does not require an offline calculation of the drag excitation from Morison's equation because it is calculated in each timestep, based on the wave kinematics. In the frequency-domain model, the Morison excitation forces are included in the pre-processing through the linearized transfer functions. The linearization is different for columns and heave plates because of the optional KC-dependent drag parameterization for the heave plates. The resulting cross-spectral density matrix of the hydrodynamic excitation forces $\boldsymbol{S}_{FF}(\omega)$ can then be used directly to calculate the response spectra $\boldsymbol{S}_{yy}(\omega)$ according to Eq. (2.27). Chapter 4 will deal with the experimental determination of the Morison drag coefficients.

<div style="border:1px solid #000; padding:10px;">

<u>Nonlinear</u>　　　　　　　　　　　　　　　　<u>Linear:</u>

1st order wave force model　　　　　　　**1st order wave force model**

- $F^{(1)}(t) = \mathrm{idft}(X(\omega)\zeta(\omega))$　　　　- $S_{FF}^{(1)}(\omega) = X(\omega)S_{\zeta\zeta}(\omega)X(\omega)^{*T}$

2nd order slow-drift model　　　　　　　**2nd order slow-drift model**

- $F^{(2)}(t) = \mathrm{idft}(\mathrm{idft}(\zeta_i\zeta_j T(i,i)))$　- $S_{FF}^{(2)}(\omega) = F^{(2)}(\omega)F^{(2)*}(\omega)$

Morison's equation　　　　　　　　　　**Morison's equation**

- wave kinematics
  $v_x(t,z), v_z(t,z), a_x(t,z), a_z(t,z)$

- wave kinematics
  $v_x(\omega,z), v_z(\omega,z), a_x(\omega,z), a_z(\omega,z)$

- body kinematics through RAO
  $\left(\dfrac{\xi}{\zeta} = \dfrac{X(\omega)}{-\omega^2(M+A(\omega))+j\omega B(\omega)\xi+C}\right)$

columns　　　　　　　　　heave plates (optional)

- nodal
  STD $\sigma(v_{i,rel})$

- nodal
  STD $\sigma(v_{i,rel})$

- $\bar{C}_{Di}^{*} = \sqrt{\frac{8}{\pi}}\sigma(v_{i,rel})C_{Di}^{*}$

- $KC_i = f(\sigma_i)$

- $\bar{C}_{Di,hp} = f(KC)$, see [230]

- $\bar{C}_{Di}^{*} = \sqrt{\frac{8}{\pi}}\sigma(v_{i,rel})C_{Di}^{*}$

- $G_{Fmor}(\omega) = \sum_i H_i \bar{C}_{D,i} \mathrm{e}^{-kz_i}$

$F_\zeta(t) = F^{(1)}(t) + F^{(2)}(t)$　　　$S_{FF}(\omega) = (G_F + G_{Fmor})S_{\zeta\zeta}(G_F + G_{Fmor})^{*T}$

</div>

Figure 3.18: Overview on calculation scheme for 1st order, 2nd order and Morison (drag component only) wave excitation forces as input to nonlinear time-domain model and linear frequency-domain model. Some formulations are shortened in this overview.

3.6 Mooring Line Model

The mooring model is a quasi-static nonlinear model according to the nonlinear system of equations given in [125]. The equations are solved numerically using Matlab's root finding algorithm. In order to save simulation time, the force-displacement relationship for a range of vertical and horizontal positions of the fairlead in coordinates of the anchor is stored in a look-up table a-priori. The kinematics of the fairleads in anchor coordinates $\boldsymbol{r}_{anch-frld}$ are computed in the nonlinear code and in the linearized equations through symbolic expressions. For the linearized version, a stiffness matrix $\boldsymbol{C}_{moor} \in \mathbb{R}^{(6\times6)}$ about a body-fixed reference point results from the nonlinear equations through a perturbation analysis, see Figure 3.19.
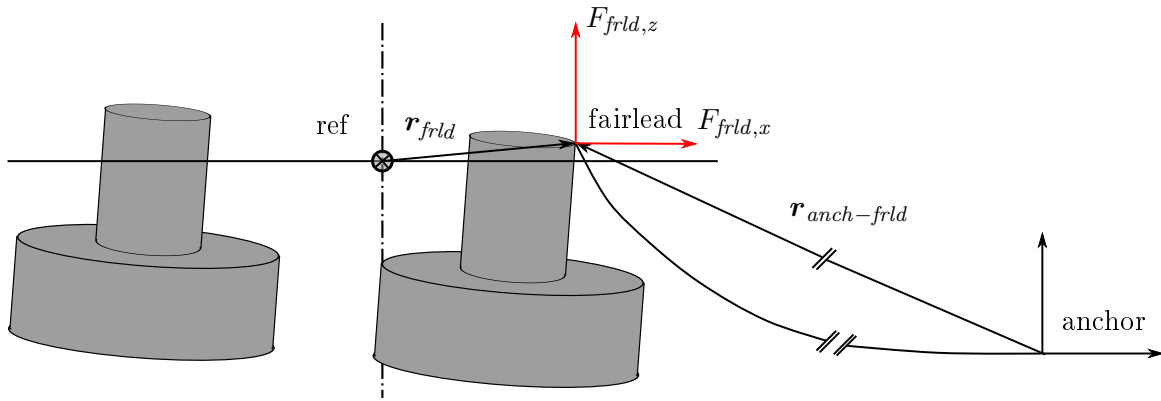
Figure 3.19: Mooring module kinematics.

The standalone kinematics function returns the resulting forces and moments $\boldsymbol{F}_{moor}$ and $\boldsymbol{M}_{moor}$ in inertial coordinates about the selected platform reference point, usually the platform CM. The n single vertical and horizontal force pairs of each line k have to be transformed from the fairleads coordinate system (x pointing towards the anchor) to the inertial coordinate system and be summed as

$$\boldsymbol{F}_{moor} = \sum_{k}^{n} {}^{I}\boldsymbol{F}_{frld,k}, \qquad \boldsymbol{M}_{moor} = \sum_{k}^{n} {}^{I}\boldsymbol{r}_{frld,k} \times {}^{I}\boldsymbol{F}_{frld,k} \qquad (3.97)$$

in order to be included in the Newton-Euler equations, Eq. (3.13). For the generation of the look-up table, the overall forces $\boldsymbol{F}_{moor}$, $\boldsymbol{M}_{moor}$ are computed for various platform positions and rotations. The linearized stiffness matrix $\boldsymbol{C}_{moor} = \boldsymbol{C}_{moor}|_0$ is computed about an operating point $\boldsymbol{r}_{ref}$. Figure 3.20 and 3.21 show the overall forces $\boldsymbol{F}_{moor}$ and moments $\boldsymbol{M}_{moor}$ for a successive displacement in the six directions (see each of the six plots) for the TripleSpar design, introduced in Section 2.10. It can be seen that the forces and moments behave linearly around the equilibrium position but more and more nonlinearly for larger excursions. For the maximum thrust at rated conditions, the translational displacement (x) is about 18 m. The dynamic cable is neglected in FAST and the developed simplified model.
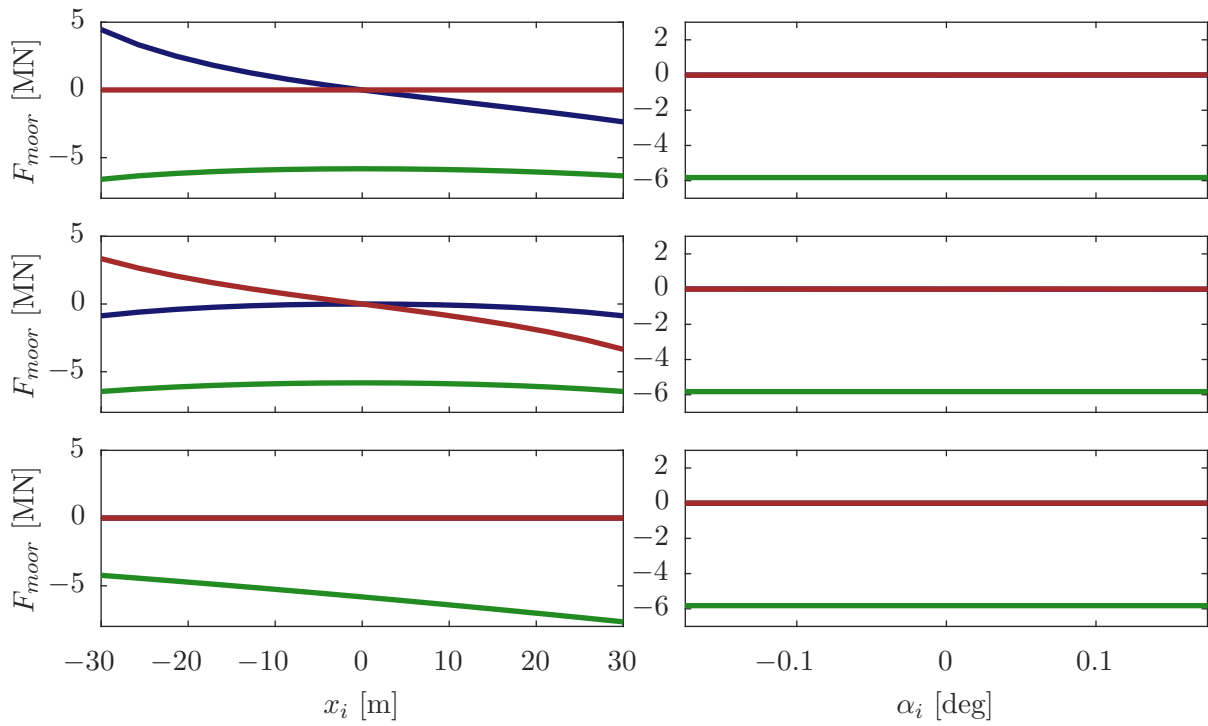
Figure 3.20: Overall mooring forces from all three lines on platform for three independent translations (left) and rotations (right), $F_{moor,x}$ (blue), $F_{moor,y}$ (red), $F_{moor,z}$ (green), TripleSpar.
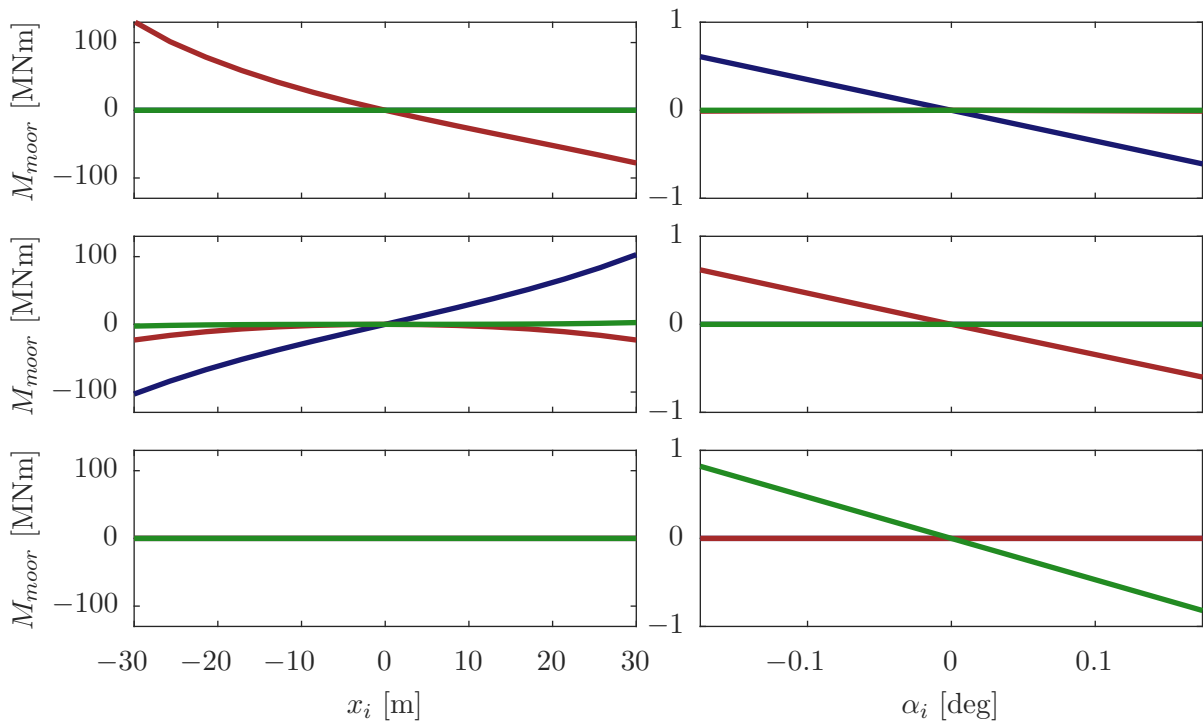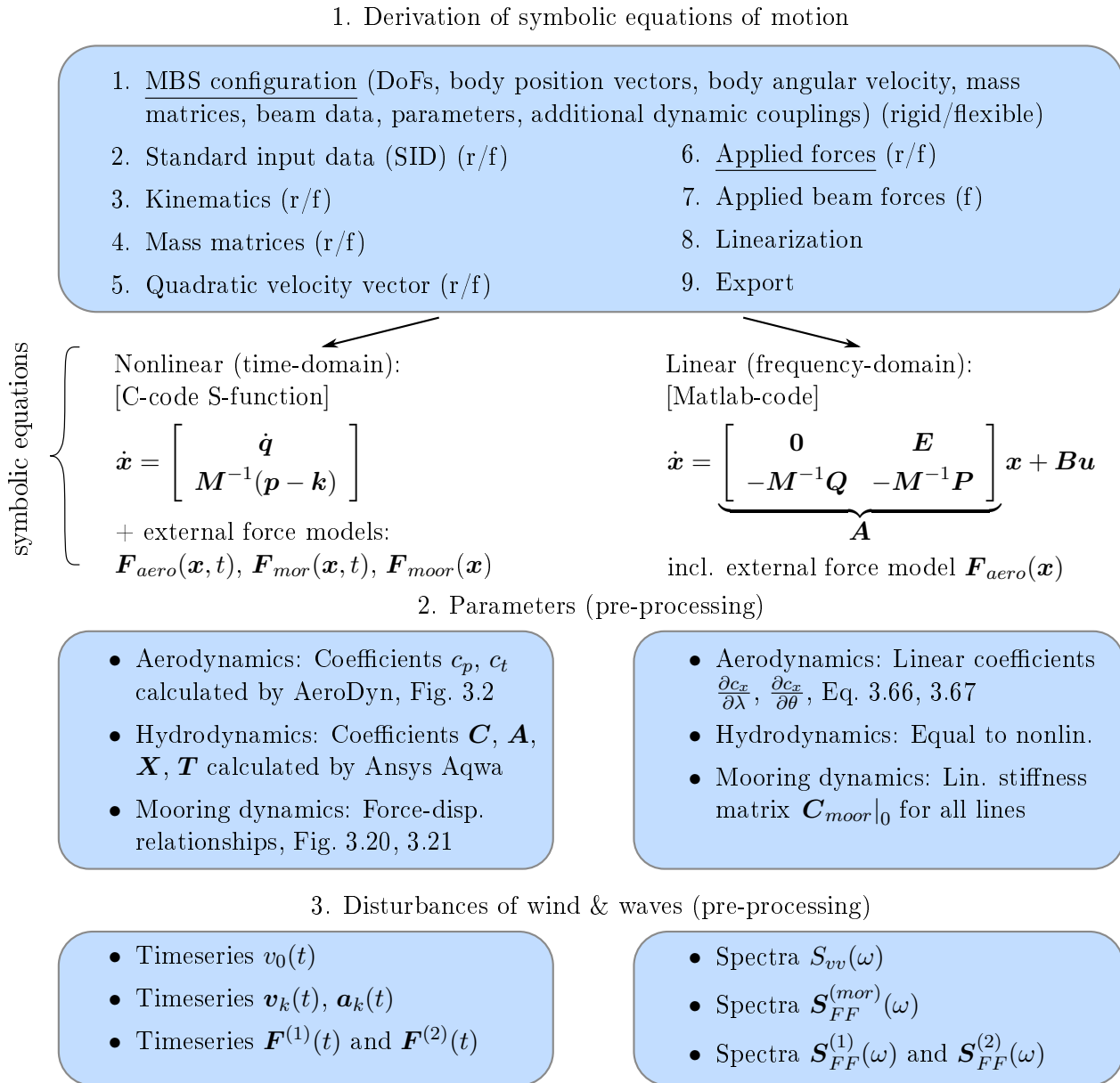

Figure 3.21: Overall mooring moments from all three lines on platform for three independent translations (left) and rotations (right), $M_{moor,x}$ (blue), $M_{moor,y}$ (red), $M_{moor,z}$ (green), TripleSpar.

3.7 Code Architecture

An overview of the implementation of the reduced-order model is shown in Figure 3.22. A peculiarity of symbolic equations is that a symbolic preprocessor is necessary to build the EQM. These EQM are then incorporated into the simulation tool (which is not shown in Figure 3.22). The first block (1.) contains the symbolic preprocessor with the structural EQM, introduced in Section 3.2. The preprocessor is structured with functions applied to each body of the MBS divided into rigid (r) and flexible (f) bodies. This part requires two user-defined input files, one for the MBS configuration and one for the applied forces (see underlines). As a result of the derivation of the EQM, two files are written with the symbolic equations, the nonlinear version in C-code and the linearized version in Matlab-code. The external force models are either included in the C-code S-function and called in every timestep (nonlinear model) or contained in the input matrix of the linear model, Eq. (3.49).

Additionally, the model parameters,(item (2.) in Figure 3.22) need to be defined in an input file. This files is read by the linear and nonlinear simulation tool. A template input file is being written while deriving the EQM. These parameters require pre-processing steps using other tools like a panel code for the hydrodynamic coefficients (Section 3.5) and a BEM model for the aerodynamic rotor coefficients (Section 3.4). The iteration of the linearized hydrodynamic viscous drag coefficients is here omitted and the coefficients are assumed to be known. The mooring line nonlinear and linear restoring properties are calculated by an own mooring model as introduced in Section 3.6.

The lower part (3.) of Figure 3.22 refers to the pre-processing of external disturbances. The time or frequency-dependent disturbances are usually stochastic in nature (although deterministic inputs are also possible). For the time-domain model, as well as for the frequency-domain model, the rotor-effective wind speed is the external disturbance. It can be augmented with rotationally sampled turbulence at the rotor frequency as introduced in Section 3.3.

The hydrodynamic forces from the panel code are again equal for time-domain and frequency-domain. However, the external Morison forces are calculated online (in each time-step) of the nonlinear model, based on the wave kinematics $\boldsymbol{v}_k$ and $\boldsymbol{a}_k$, while these forces are calculated through the transfer functions derived in Section 3.5.4 for the frequency-domain model as part of the pre-processing. Figure 3.22 does not include the parametric wave force model of Section 3.5.2. If it is used, the input in (3.) is the wave height $\zeta_0(t)$ instead of the forces $\boldsymbol{F}^{(1)}(t)$. The frequency-domain model has the option of solving the EQM for all frequencies with $\boldsymbol{A}(\omega)$ and $\boldsymbol{B}(\omega)$, as opposed to the constant matrix approach of the nonlinear model. A 4th order Runge-Kutta solver with fixed timestep integrates the nonlinear model for the time-domain response, whereas the response spectra of the frequency-domain model result from Eq. (3.53).

1. Derivation of symbolic equations of motion

1. <u>MBS configuration</u> (DoFs, body position vectors, body angular velocity, mass matrices, beam data, parameters, additional dynamic couplings) (rigid/flexible)

2. Standard input data (SID) (r/f)   6. <u>Applied forces</u> (r/f)

3. Kinematics (r/f)   7. Applied beam forces (f)

4. Mass matrices (r/f)   8. Linearization

5. Quadratic velocity vector (r/f)   9. Export

symbolic equations

Nonlinear (time-domain):
[C-code S-function]

$$\dot{\boldsymbol{x}} = \begin{bmatrix} \dot{\boldsymbol{q}} \\ \boldsymbol{M}^{-1}(\boldsymbol{p} - \boldsymbol{k}) \end{bmatrix}$$

+ external force models:
$\boldsymbol{F}_{aero}(\boldsymbol{x}, t)$, $\boldsymbol{F}_{mor}(\boldsymbol{x}, t)$, $\boldsymbol{F}_{moor}(\boldsymbol{x})$

Linear (frequency-domain):
[Matlab-code]

$$\dot{\boldsymbol{x}} = \underbrace{\begin{bmatrix} \boldsymbol{0} & \boldsymbol{E} \\ -\boldsymbol{M}^{-1}\boldsymbol{Q} & -\boldsymbol{M}^{-1}\boldsymbol{P} \end{bmatrix}}_{\boldsymbol{A}} \boldsymbol{x} + \boldsymbol{B}\boldsymbol{u}$$

incl. external force model $\boldsymbol{F}_{aero}(\boldsymbol{x})$

2. Parameters (pre-processing)

- Aerodynamics: Coefficients c_p, c_t calculated by AeroDyn, Fig. 3.2

- Hydrodynamics: Coefficients $\boldsymbol{C}$, $\boldsymbol{A}$, $\boldsymbol{X}$, $\boldsymbol{T}$ calculated by Ansys Aqwa

- Mooring dynamics: Force-disp. relationships, Fig. 3.20, 3.21

- Aerodynamics: Linear coefficients $\frac{\partial c_x}{\partial \lambda}$, $\frac{\partial c_x}{\partial \theta}$, Eq. 3.66, 3.67

- Hydrodynamics: Equal to nonlin.

- Mooring dynamics: Lin. stiffness matrix $\boldsymbol{C}_{moor}|_0$ for all lines

3. Disturbances of wind & waves (pre-processing)

- Timeseries $v_0(t)$

- Timeseries $\boldsymbol{v}_k(t)$, $\boldsymbol{a}_k(t)$

- Timeseries $\boldsymbol{F}^{(1)}(t)$ and $\boldsymbol{F}^{(2)}(t)$

- Spectra $S_{vv}(\omega)$

- Spectra $\boldsymbol{S}_{FF}^{(mor)}(\omega)$

- Spectra $\boldsymbol{S}_{FF}^{(1)}(\omega)$ and $\boldsymbol{S}_{FF}^{(2)}(\omega)$

Figure 3.22: Workflow of writing reduced-order model equations of motion and preparing simulation.

3.8 Linear Analysis

In this section, the linearized model is applied to obtain the Open Loop (OL) eigenvalues and eigenvectors (without feedback control). Again, the reference FOWT model defined in Section 2.10 is used. For the mechanical state-space formulation, Eq. (3.49), a quadratic eigenvalue problem can be solved

$$\left(\boldsymbol{M}\lambda^2 + \boldsymbol{Q}\lambda + \boldsymbol{P}\right)\boldsymbol{v} = \boldsymbol{0}, \tag{3.98}$$

giving solutions for the eigenvalues λ and the corresponding eigenvectors $\boldsymbol{v}$. Figure 3.23 shows the eigenfrequencies for the system DoFs surge, heave, pitch and tower-top displacement. For visualization, the eigenvectors have been scaled and the rotor rotation mode was omitted. For FOWTs with slack catenary mooring lines, the platform eigenfrequencies are usually below the peak wave frequency. The peak wave period is mostly in the range $T_p = 5\ldots15\,\mathrm{s}$. The tower system mode is critical for large rotors as these have a smaller rated rotational speed due to the limitation of the maximum tip speed. Hence, the tower mode can interact with the 3p frequency and lead to a resonance. For the TripleSpar design the tower eigenfrequency is in the 3p range, which is for the DTU 10 MW RWT $f_{3p} = 0.3\ldots0.48\,\mathrm{Hz}$. Solutions to this problem were studied in INNWIND.EU, see Deliverable 4.37 [233]. Simulations by the different project partners have shown that the resonance magnitude is limited, compared to the excitations from first-order waves. The problem was also subject in LIFES50+ and the option of designing a stiffer tower to shift its eigenfrequency above the 3p range was discussed. However, this implies a high tower mass and associated costs.
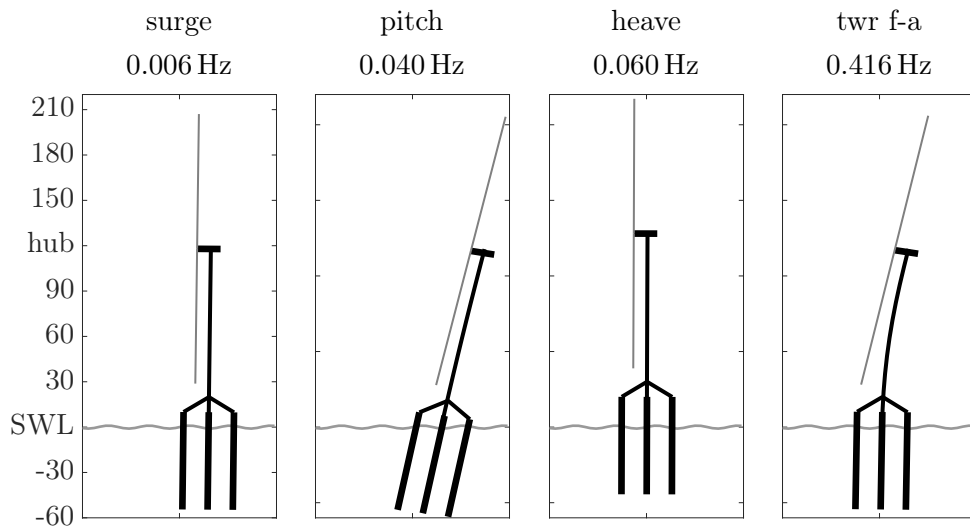
Figure 3.23: Mode shapes calculated by the reduced-order simulation model for TripleSpar concept, Section 2.10, [205].

Figure 3.24a shows the poles (or eigenvalues) in the complex plane and the zeros for a SISO system from the commanded blade pitch angle θ to the rotor speed Ω. It can be seen that
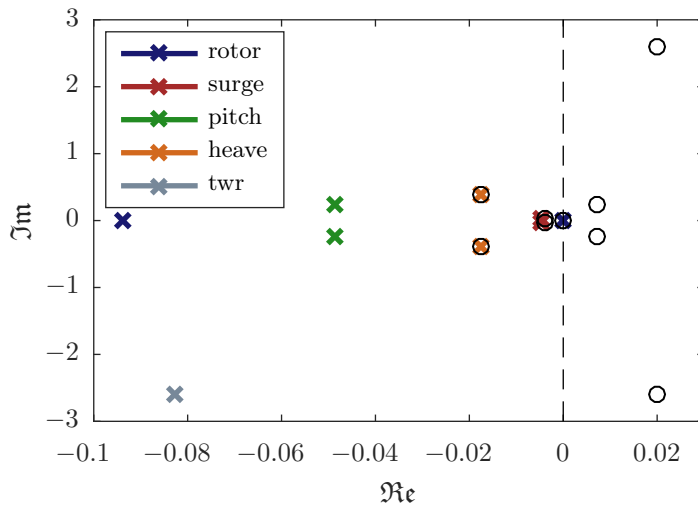
(a) TripleSpar OL with poles (×) @13.9 m/s and zeros (◦) from blade pitch θ to rotor speed Ω.
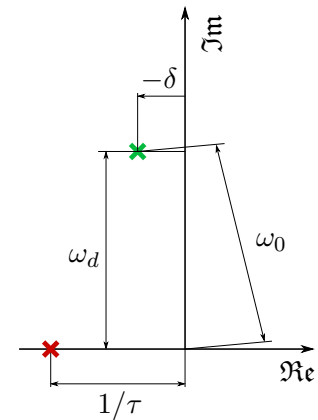
(b) Example undercritically damped pole (green) and overcritically damped pole (red).

Figure 3.24: Pole-zero map.

the surge, pitch, heave and tower modes are undercritically damped with each having complex conjugate poles. In this case, the damped eigenfrequency ω_d (Figure 3.24b) is equal to the imaginary part of the pole λ and the undamped eigenfrequency ω_0 is equal to the magnitude of λ. The damping ratio results as a fraction of the real part δ and the undamped eigenfrequency as $\xi = \delta/\omega_0$. The rotor mode is overcritically damped in this OL configuration and has two poles on the real axis. For poles on the real axis no oscillation is possible as the mode is overdamped. Then, the magnitude of λ is equal to its real part giving the time constant $\tau = 1/\Re(\lambda)$. The pole with the smaller magnitude is then the one dominating the dynamic behavior of the corresponding mode shape $\boldsymbol{v}$.

The RHPZ discussed in Section 2.9 can be seen in Figure 3.24: The imaginary part of the complex conjugate zeros represents the frequency of the zero. For the zeros with smaller frequency, it can be seen that they are very close to the platform pitch eigenfrequency. The zeros with the higher frequency (right-hand side of Figure 3.24a) have approximately the frequency of the damped tower mode. The zeros will be important for control, as the blade pitch signal is not amplified but attenuated at the frequencies of the zeros, see Chapter 5. The results of the eigenanalysis agree well with the time-domain analyses with the nonlinear model.

3.9 Model Verification

For a code-to-code comparison, the tool FAST [43] was used as introduced in Section 2.5.1. The presented simulations are made with FAST v8.16.00a-bjj with the submodules Elasto-Dyn v1.04.00a-bjj, AeroDyn v14.05.01a-bjj, InflowWind v3.03.00, ServoDyn v1.06.00a-bjj, Hy-

droDyn v2.05.01 and MAP++ v1.20.10. The enabled features, compared to the nonlinear and the linearized SLOW model are summarized in Table 3.1.

Table 3.1: Comparison of modeling approaches between FAST, SLOW nonlinear and SLOW linear.

	FAST	SLOW (nonlinear)	SLOW (linear)
Structural dynamics	nonlin. flex. MBS	nonlin. flex. MBS	linearized flex. MBS
	6 platform DoFs	surge, heave, pitch-DoFs	surge, heave, pitch-DoFs
	4 tower DoFs	1 fore-aft DoF	1 fore-aft DoF
	$3 \cdot 3$ blade DoFs	rigid	rigid
	drivetrain torsional DoF	rigid shaft	rigid shaft
	2nd order blade pitch actuator		
Aero-dynamics	BEM with corrections	c_p, c_t-model (nonlin.)	c_p, c_t-model (lin.)
	distrib. forces along blade	lumped rotor forces	lumped rotor forces
	full 3D turb. wind field	blade-averaged wind field with	
		rotationally sampled turbulence	
	quasi-static, no dynamic inflow		
	no tower shadow		
Hydro-dynamics	convolution integral	"constant matrix"	frequency-domain
	radiation damping	–	radiation damping
	relative form of Morison's equation		cross-corr. approximated
	quadr. Morison drag	quadr. Morison drag	linearized Morison drag
	2nd order slow-drift with Newman's approximation		
	no wave stretching		
Mooring-dynamics	quasi-static model	quasi-static model	quasi-static model
	nonlin. force-disp.	nonlin. force-disp.	linearized stiffness
	eq. solved online	eq. solved a-priori	eq. solved a-priori

The most significant difference between the tools is the aerodynamic model and the reduced number of structural DoFs (2D motion, only). For an improved computational efficiency, most of the results in this work of the linearized model are made without the frequency-dependent hydrodynamic coefficients but with a constant added mass and neglecting the radiation damping, see Section 3.5.1.

3.9.1 Stochastic operational condition

Figure 3.25 shows the PSD to stochastic wind and wave loads for a load case with $\bar{v}_{hub} = 17.9\,\text{m/s}$ as described in Section 2.7.3 for the linearized model, the nonlinear model

and FAST. The model includes a SISO PI-controller as described in Chapter 5. All model parameters can be found in Table A.1. It can be seen that the frequencies of the platform resonances in surge x_p, heave z_p and pitch β_p are well captured in frequency and magnitude. The response to the wave loads at $f_{wave} = 0.1\,\text{Hz}$ can be clearly seen in the x_p and x_t signals. The tower-top displacement x_t also shows a second peak above the wave frequency, below its coupled eigenfrequency of $0.42\,\text{Hz}$ at about $0.18\,\text{Hz}$. This is due to the wave force transfer function $\boldsymbol{X}(\omega)$, which shows two peaks, divided by an attenuation range, see "wave cancellation effect" for semi-submersibles. This can be also seen in Figure 3.6 and is a topic of Chapter 6. The slow drift force model of Section 2.5.3 results in large amplitudes at the resonance frequencies of surge x_p and pitch β_p, also reflected in the tower bending x_t. Without this difference-frequency excitation, the response to the turbulence would be visibly smaller. The Morison drag coefficient for the heave plates $C_{D,hp}$ is obtained according to Section 3.5, Figure 3.16 with the linear model and its value is used for both nonlinear models.

The rotor speed Ω responds to the β_p-motion, which is related to the discussed RHPZ, Section 2.5. It will be a further topic in the remainder of this work. Since the torque is constant above rated ($v_{rated} = 11.4\,\text{m/s}$), the rotor speed Ω is proportional to the electrical power P. The tower eigenfrequency is mainly excited by the 3p excitations on the rotor from the vertical wind shear. It is well captured by the reduced-order model with the rotational sampling method of Section 3.3. The tower-base bending moment M_{yt} follows generally the tower-top displacement x_t, except for the structural damping force, as discussed in Section 3.2.6.

For a time-domain comparison of the same load case as Figure 3.25, the same turbulent wind field was input to SLOW and FAST and the wave height time series ζ_0 of FAST were input to SLOW using Section 3.5.2. The results of Figure 3.26 show in this time-domain comparison that also the transients and steady states (means) compare well between SLOW and FAST. The wind speed signal on top shows more high-frequency oscillations for SLOW because of the rotational sampling, as opposed to the rotor-effective wind speed, shown for FAST. The steady state deviation of surge (x_p) and the blade pitch angle θ is due to the tilted rotor: It has a nonzero angle about y, through the shaft tilt of $5\,\text{deg}$ and through the platform pitching β_p. This misalignment results in nonzero force and moment-components in the directions perpendicular to the shaft, see Glauert's yaw model in [44, Chapter 3].

3.9.2 Deterministic operational condition

The response of the nonlinear SLOW model and the FAST model to an Extreme Operating Gust (EOG) at still water can be seen in Figure 3.27. This load case results in large transient rotor loads and an impulse response-like behavior (the duration of the gust is rather short in the time-scales of the FOWT). Nonetheless, the nonlinear SLOW model reproduces well the FAST results. The only visible difference is the steady state in surge (x_p). This is, again, due to the
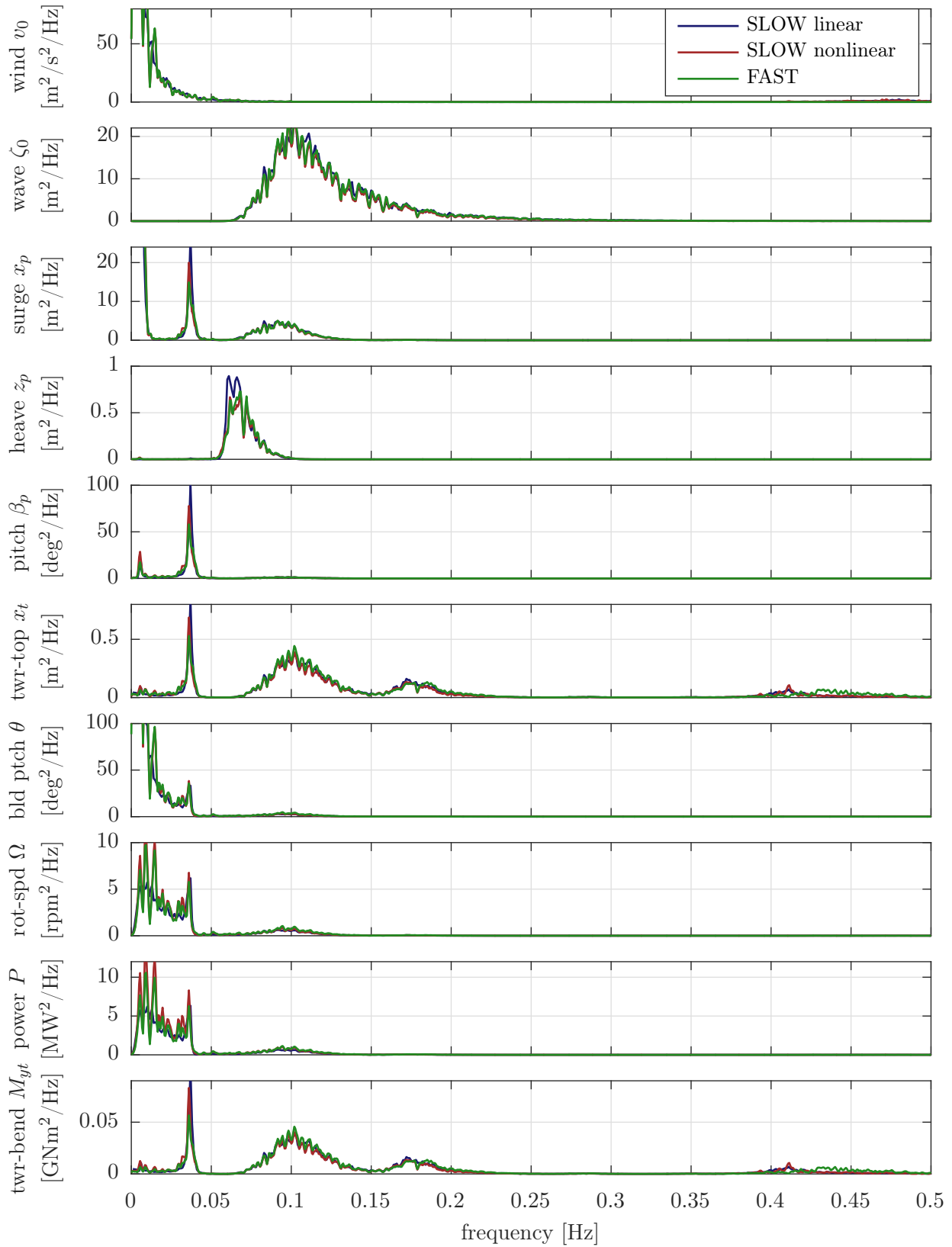
Figure 3.25: Model verification PSD $\bar{v}_{hub} = 17.9\,\text{m/s}$, $H_s = 4.3\,\text{m}$, $T_p = 10.0\,\text{s}$. Linearized model (blue), nonlinear model (red), FAST (green).
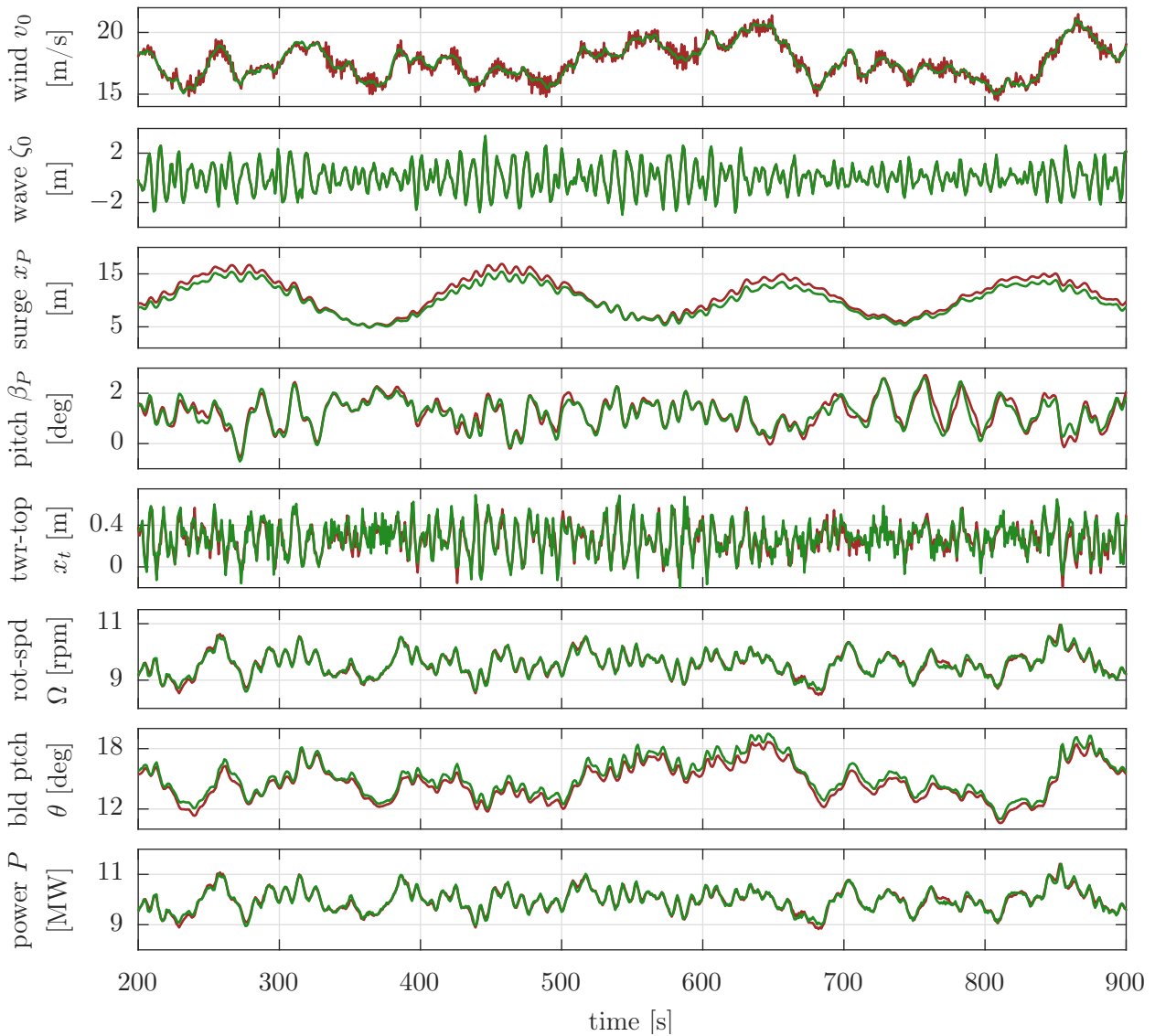
Figure 3.26: Model verification time series $\bar{v}_{hub} = 17.9\,\mathrm{m/s}$, $H_s = 4.3\,\mathrm{m}$, $T_p = 10.0\,\mathrm{s}$. Nonlinear model (red), FAST (green).

different aerodynamic modeling. The linear model was used in this case for a comparison in the time-domain. Even though the state excursions are large, the linear model follows well the transients of the nonlinear models. A notable difference is the damping in surge-direction. The reason for this is that the linearized platform damping was determined for the response STD of the respective stochastic load case of Table 2.1, as introduced in Section 3.5.4.

More references for the verification of SLOW can be found in the paper [234], which addresses its use for the determination of critical DLCs in the conceptual design phase. It shows benchmark comparisons with FAST for the OC3-Hywind spar for a preliminary system analysis with standard DLCs.
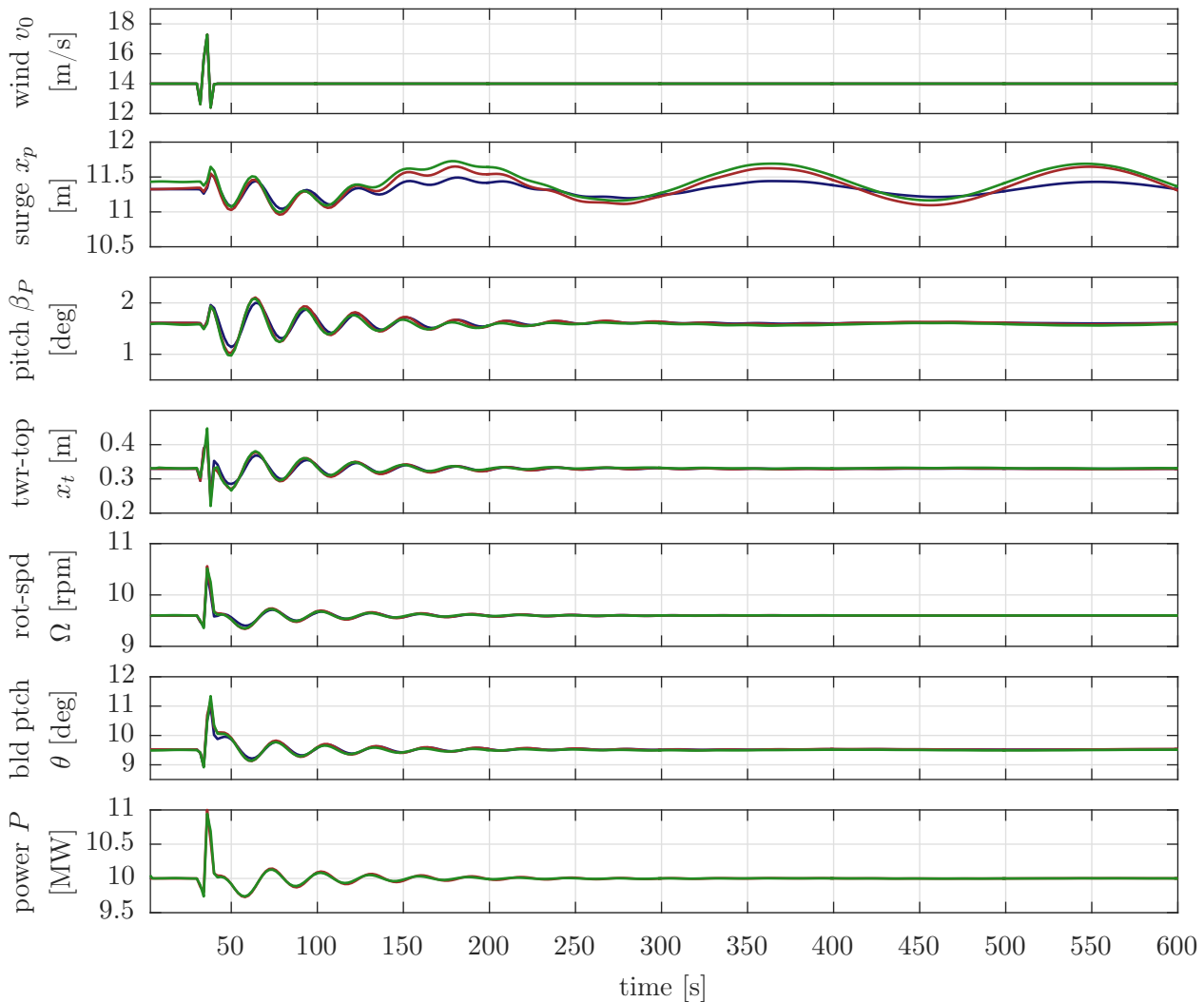
Figure 3.27: Model verification EOG time series $\bar{v}_{hub} = 14.0\,\mathrm{m/s}$ with linear model (blue), nonlinear model (red) and FAST (green).

3.9.3 Fatigue from frequency-domain model

For the DEL estimation introduced in Section 2.7.3, the rainflow counting method, based on time series data, is compared to Dirlik's method, based on PSDs of the respective time signal. The method is especially useful because fatigue loads can be estimated from the linear frequency-domain power spectra. Figure 3.28 shows the DEL for each of the bins of DLC 1.2 of Table 2.1, calculated with the rainflow method of the tower-top displacement signal of the nonlinear model, compared against Dirlik's method, Eq. (2.35).

Dirlik's method was applied twice: Once to the PSD obtained from the time series through Welch's method[2] and once to the spectra obtained from the linear frequency-domain model directly, compare red and blue curve in Figure 3.25. The time series PSD was computed with an $n/4$-point hamming window. However, no impact on the results is expected from the

---

[2]http://mathworks.com/help/signal/ref/pwelch.html, accessed on January 22, 2018.

windowing due to the large amount of hamming points. The DEL values are calculated for each bin independently and not weighted but extrapolated for a lifetime of 20 years.

It can be seen that the match is very good with a maximum deviation of only 0.4 % for the time series data. This confirms Dirlik's method for the nature of the tower-top signal in the given load conditions. As for the linearization methodology, it does not imply larger discrepancies than Dirlik's method itself.
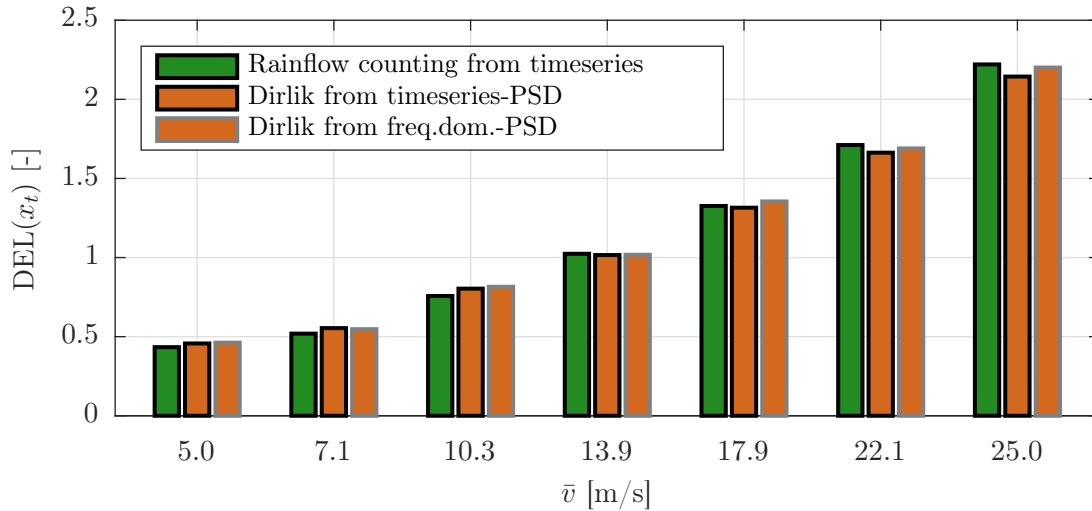
Figure 3.28: DEL for tower-top displacement x_t for operational DLCs of Table 2.1. Calculated with (1) rainflow counting, (2) Dirlik's method with spectra obtained from time series data of (1) and (3) Dirlik's method with spectra obtained from linearized frequency-domain model.

3.9.4 Short-term extremes from frequency-domain model

It is especially important for controller design to obtain the maximum amplitudes of certain signals from a 10 min or a 60 min-responses as a performance indicator. In order to be able to extract these short-term extremes from the linear frequency-domain model, a Rayleigh distribution of the peaks is assumed in order to obtain the expected maximum amplitudes for a given duration, as introduced in Section 2.7.3. Figure 3.29 shows a comparison, as in Figure 3.28, of the maximum amplitude (mean of maxima of three 20 min-segments) of the tower-top displacement x_t from a time-domain simulation, through the Rayleigh distribution using the PSD of the time series and through the linear frequency-domain model. It can be seen that the estimation from the spectrum underestimates the maximum around rated winds, which is likely because in these cases the signal is not normally distributed. In the other cases the method seems to give plausible results for the tower bending.
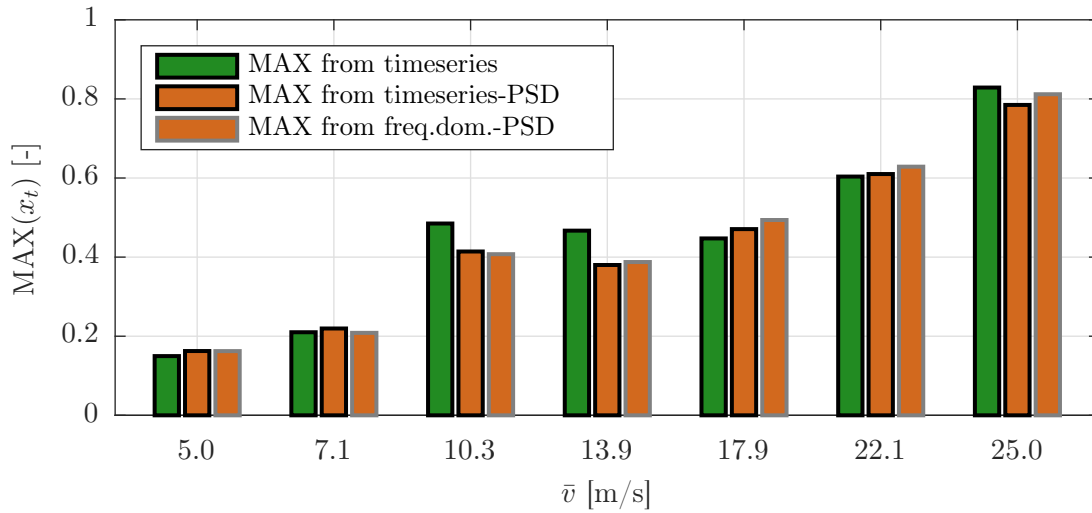
Figure 3.29: Short-term extremes for tower-top displacement x_t for operational DLCs of Table 2.1. Calculated from (1) time series directly, (2) from PSD of time series and (3) from linear frequency-domain model response spectrum using Eq. (2.36).

3.10 Computational Efficiency

A computational speed assessment is shown in Table 3.2. The simulation times are given for a standard PC with a 2.5 GHz processor for one hour simulations and $n = 500$ frequencies for the linear frequency-domain computations. The pre-processing of wind and waves is necessary for each load case due to the environmental conditions, cf. Table 2.1. For the SLOW model, the wave-preprocessing includes the first-order wave force time series and spectra, the Morison external drag force spectra and the difference-frequency spectra and time series using Newman's approximation, see Section 3.5. The pre-processing of the aerodynamics relates to the BEM-calculations to determine the look-up tables for c_p and c_t, Section 3.4. This is only required once for every new wind turbine rotor. The same holds for the mooring dynamics: The force-displacement relationships have to be re-calculated only if a new mooring system is employed.

Table 3.2: Comparison of computational speed between SLOW and FAST. Linear SLOW model calculates response in frequency-domain. Pre-processing of mooring lines and aerodynamics (coefficients c_p and c_t, Eq. (3.65)) only design-dependent, not load case-dependent.

		Pre-processing		Simulation	
	Wind:	75 s	nonlinear		30 s
SLOW	Waves:	30 s	linear		1 s
	Aerodynamics:	7200 s			
	Mooring dynamics:	30 s	linear (incl. radiation)		15 s
FAST	Wind:	560 s			950 s

3.11 Summary

In this chapter, the reduced-order simulation model was derived. The goals, described in Section 3.1, were mainly the high computational efficiency with a correct representation of the main system dynamics in a nonlinear and linearized description. The code developed avoids wherever possible computationally expensive recursions and iterations like the convolution integral for the radiation model or the BEM model for the rotor aerodynamics. It consists mainly of symbolic equations of motion for the structural model and additional external force models. It could be shown through a comparison against FAST in Section 3.9 that the main resonances and the excitations to first-order and second-order slow-drift wave forces are well captured compared to FAST. In spite of the simplifications of the aerodynamic model and the radiation model, the nonlinear model as well as the linearized model can represent the motion and load response of the rotor, the tower and the floating platform satisfactorily. Although simple operational load cases are studied without yawed inflow, misaligned waves, etc., the set goals of a reliable representation of the system dynamics at a significant speed improvement are successfully met. This is true for the nonlinear model, but also for the linearized model in rather severe operational environmental conditions.

Earlier versions of the model were presented in [235] and [205] with a verification across different load cases in [234]. Control-oriented applications were tested in [236] and in the European projects INNWIND.EU [40], LIFES50+ [237] and TELWIND [238]. A comparison of the model against scaled experiments was made in [160, 161]. In [239], SLOW was used to investigate the stability of a 2-bladed onshore wind turbine. The model will be used in the next chapter to identify the hydrodynamic drag coefficients and to validate the results through experimental data.

4 Experiments

Two test campaigns were performed in the course of this thesis project. One in France in 2014 and one in Denmark in 2016. This chapter describes the latter, performed at the Danish Hydraulic Institute (DHI) within a joint project by SWE, DTU and CENER in 2016. The TripleSpar concept introduced in Section 2.10 was built at SWE in a scale of 1/60 and assembled with a turbine model of the DTU 10 MW RWT, built at DTU, see Figure 4.1. The scaling laws applied follow Froude-scaling as introduced in Section 2.8. The test campaign had the primary goal of testing active blade pitch control in a model test and the results were published in [160], [161] and [240]. Additionally, three thesis projects were conducted on the tests. The one at SWE by Wei Yu [241] deals with the simulation model setup, the parameter identification, controller development and implementation. Another one conducted at DTU focused on the wind generator and the rotor design, see [242] and a Bachelor thesis on the electromechanical hardware is not published. Prior to this test, most experimental tests of FOWTs did not include a blade pitch controller. This means that the rotor speed was maintained by a servo motor, which actuates the torque. However, the gains of this servo controller were usually not tuned to match the full-scale controller as implemented on standard wind turbines and the blade-pitch controller was not represented in the tests. As the aerodynamic scaling is challenging, due to the Reynolds number mismatch the rotor was redesigned for low Re-numbers by DTU in order to match mainly the Froude-scaled thrust and rotor speed. Recently, a number of researchers has taken the step to include the control system in scaled model tests after a first attempt had been made for the Hywind concept, see [197]. The negative damping problem was studied in [243]. Later, tests at Marine Research Institute Netherlands (MARIN) with different PI-controllers were presented in [244], assessing the controller influence on the response. Another test in the same basin was presented in [245]. At Osaka Prefecture University, Japan, an H_∞ controller was experimentally studied, see [246].

The objective of this chapter is to validate the previously described hydrodynamic model and to calibrate the Morison drag coefficients. At the same time, comparisons between the simulation model of Chapter 3 and experimental data with active blade pitch controller will be shown to validate the full FOWT model. The findings of this chapter will be used in the parametric design studies of Chapter 6.
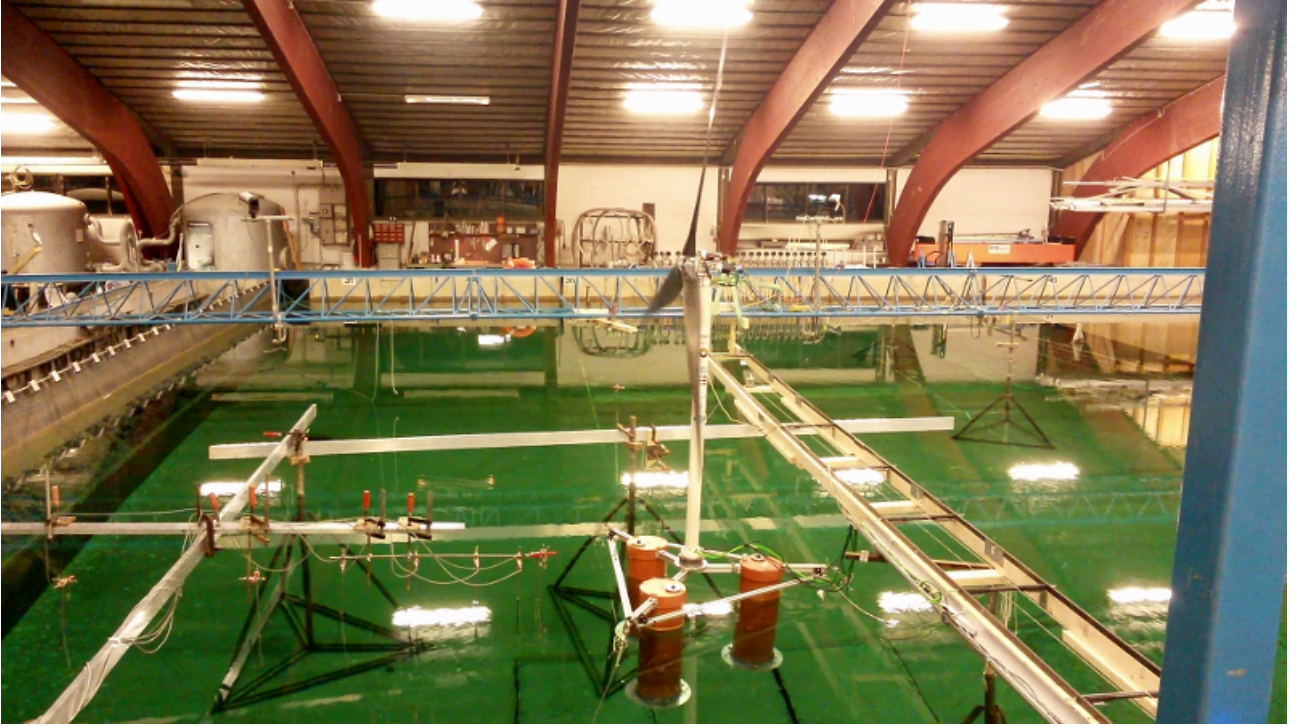
Figure 4.1: TripleSpar test campaign at DHI 2016: Joint project by SWE, DTU and CENER, photograph by Henrik Bredmose, DTU, [240].

Table 4.1: LCs defined for irregular wave tests [160].

	Model scale			Prototype scale		
LC	H_s [m]	T_p [s]	$\bar{v}_{hub}$ [m/s]	H_s [m]	T_p [s]	$\bar{v}_{hub}$ [m/s]
1…6, 8, 10			not used, see [241]			
7	0.091	1.08	1.89	5.46	8.37	14.64
9	0.159	1.43	1.89	9.54	11.1	14.64

4.1 Model Parameters and Load Cases

The simulation model used for the following analyses is the one described in Chapter 3 with the 5 DoFs platform surge x_p, platform heave z_p, platform pitch β_p, tower fore-aft displacement x_t and rotor speed Ω. The tower is modeled through a linear spring through the rigid MBS approach of Section 3.2.1. The model parameters used in [161] were not changed, except that the added mass was calculated with Ansys Aqwa and used in the simulations without further tuning. An additional linear stiffness in x-direction of $8\,\text{N/m}$ was introduced to represent the power and signal cables of the servo motor and blade pitch actuators, which can be seen in Figure 4.1. This is about one third of the horizontal restoring stiffness of the mooring lines in the initial position. In pitch-direction an additional stiffness of $-25\,\text{Nm/rad}$ was necessary to match the natural period from the measurements, equal to about $5\,\%$ of the hydrostatic restoring in pitch.
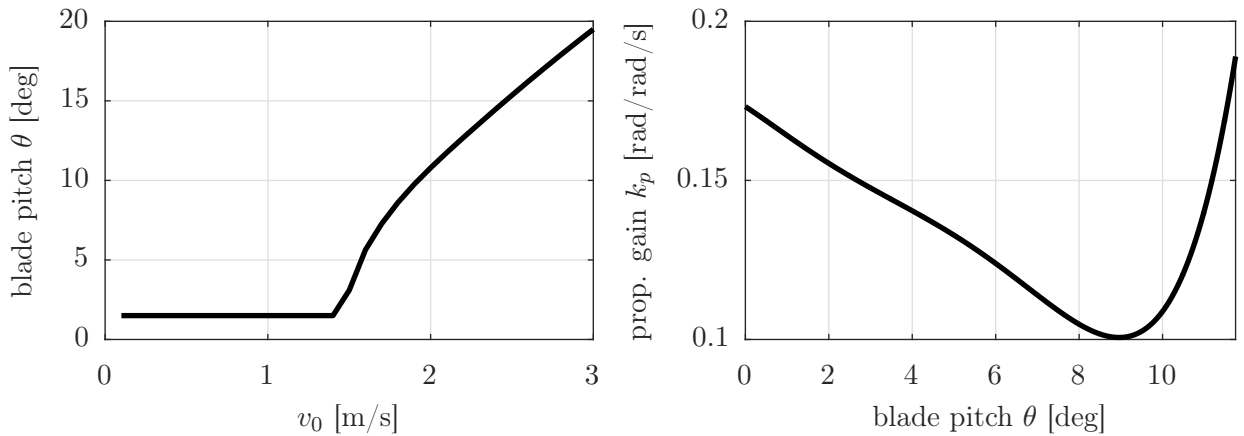
Figure 4.2: Steady state blade pitch angles θ over wind speeds v_0 (left) and proportional gains k_p over steady state blade pitch angles (right) associated with time constant $T_i = 2.9\,\text{s}$ for the 1/60 TripleSpar, [240].

The static vertical force and the vertical stiffness of the power cables on the system is neglected. The model parameters can be found in the Appendix A.2.

The properties of the different components of the FOWT system were verified and identified with different methods: For the rotor, a BEM model was set up in the Master thesis [241] with the polars calculated by DTU and the torque and thrust for different TSR were compared to the measurements as shown in [161]. The tower structural properties were determined for a fixed configuration used in a previous test by DTU, see [247]. For the present work, an impulse response of the tower-top with the tower mounted on the floating platform was measured. It resulted in a slightly higher stiffness than the one assumed in [161]. The mass properties of the platform were calculated in detail by Florian Amann via a parametric Computer-Aided Design (CAD) model with the exact final ballast configuration.

A measurement of the wind field was made without the turbine with a hot wire on a pulley system, see [160]. Due to a misplaced fan on the top of the wind generator array, a higher wind speed could be measured at lower levels, creating a shear. This might have an effect on the presented results later in this chapter. The turbulence intensity was not changed and a constant, uniform wind speed was used for the simulations. The optical motion tracking system was configured to update the reference position every day to the actual position of the CF (as reported in other tests, the steady state of the platform changes due to the static friction between the mooring lines and the seabed). The presented results show the displacements with respect to the global coordinate system, by re-introducing the offset to the signals.

The wave generator was calibrated with numerous wave gauges, see [242]. The highest uncertainty in the model parameters is likely the anchor position, also due to the high sensitivity of the mooring forces with respect to the position of the anchor. As in many other tests, the wind field and blockage effects could not be entirely measured. An assessment of the blockage

effect of the first experiment in Nantes, 2014, using CFD was presented in [159]. The hardware of the feedback controller including encoder and actuator were thoroughly tested, however, the time lags or additional dynamics associated to the control system are not represented in the simulation model.

The rotor speed controller used in the following tests was designed in [241] following a method proposed by myself in [40]. The robust procedure described in Chapter 5 is an extension to it. The gain scheduling of the proportional gain k_p, shown in Figure 4.2 together with the steady state blade pitch angles, ensures a stable system for all operating points with a fixed time constant $T_i = 2.9\,\mathrm{s}$ for all wind speeds (the gain scheduling function was limited to $1.5\,\mathrm{deg} \leq \theta < 11\,\mathrm{deg}$, keeping the last value for $\theta > 11\,\mathrm{deg}$). The shape resembles the one of the full-scale controller of Figure 5.9 with decreasing values for wind speeds above rated and increasing values for higher wind speeds, close to the cut-out wind speed.

The environmental conditions for the test are shown in Table 4.1. Although a large range of sea states (and corresponding LCs) was defined, only the higher-wave conditions are used in the following because of a limited response of the system to small waves. Due to splash water, the motion tracking system did not work satisfactorily in all cases for LC 9. A large number of tests was performed also for regular waves, focused waves and misaligned waves. Therefore, in some cases the number of repetitions had to be limited.

Table 4.2: Coupled system eigenfrequencies.

DoF	Surge	Heave	Pitch	Tower
Eigenfrequency [Hz]	0.05	0.469	0.275	3.23

4.2 Drag Identification

In this section, experimental data with wind and control is compared to the simulation model in order to identify the (horizontal) Morison drag coefficients C_D for the columns and the (vertical) $C_{D,hp}$ for the heave plates, as described in Section 3.5. Several methods to identify the Morison coefficients C_D and C_A are proposed in [90, p. 12-9] (here we focus on C_D and rely on the added mass computed by the panel code). However, these methods are particularly adapted to the times of little computational resources when full simulations of the experiments where not yet possible. In a first step we will analyze free decay tests in surge x_p and pitch β_p by comparing measurements against numerical responses with different drag coefficients.

(a) Surge: Morison
drag $C_D = [0.5, 1.0, 1.5, 2.0]$ (increasing darkness),
$C_{D,hp} = 25$.

(b) Pitch: Morison drag $C_D = [2.0]$,
$C_{D,hp} = [10, 15, 20, 25]$
(increasing darkness).
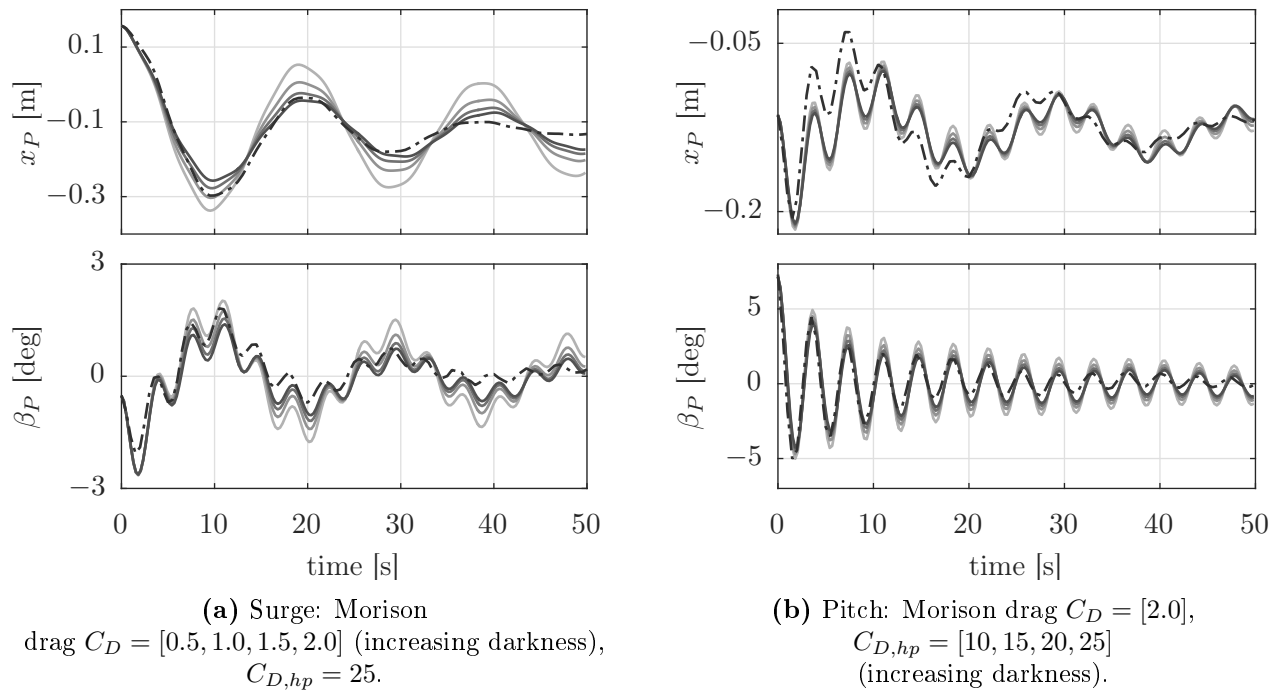
Figure 4.3: Free decay in surge and pitch-directions and experiment (dashed line), [240].

4.2.1 Free-decay

The Morison coefficient C_D influences most the surge response while the heave plate drag $C_{D,hp}$ influences more the heave and pitch response. Figure 4.3 shows simulations of various C_D for the surge-decay on the left and of various $C_{D,hp}$ for the pitch-decay on the right. The best agreement for both cases is with $C_D = 2.0$ and $C_{D,hp} = 25.0$.

4.2.2 Stochastic wind and waves

In a next step, the drag is identified in irregular wave tests: Figure 4.4 shows the PSD of the measured and simulated response for different combinations of the Morison drag coefficient C_D of the TripleSpar columns and the heave plate drag $C_{D,hp}$ for LC 9. The shown sensors are the wave height ζ_0, the platform heave z_p, surge x_p and pitch β_p and the upwind mooring line force F_{line1} (to the right looking upwind, at $60\,\mathrm{deg}$) and the tower-top acceleration $\ddot{x}_{tt}$. Note that $\ddot{x}_{tt}$ is the acceleration measured by the accelerometer and thus in the inertial frame, not relative to the tower-base frame as x_t of Eq. (3.1). Therefore, $\ddot{x}_{tt}$ is obtained from the simulation model through a transformation of the derivative of the state vector $\dot{\boldsymbol{x}}$.

The response to the wave height ζ_0 at around $0.8\,\mathrm{Hz}$ is clearly visible in Figure 4.4. In this range, the damping is of no effect as the waves yield a forced response at frequencies distant from the system eigenfrequencies. The velocity-dependent Morison excitation force term, however, can be of importance for platforms with larger KC numbers (e.g. smaller diameters). This
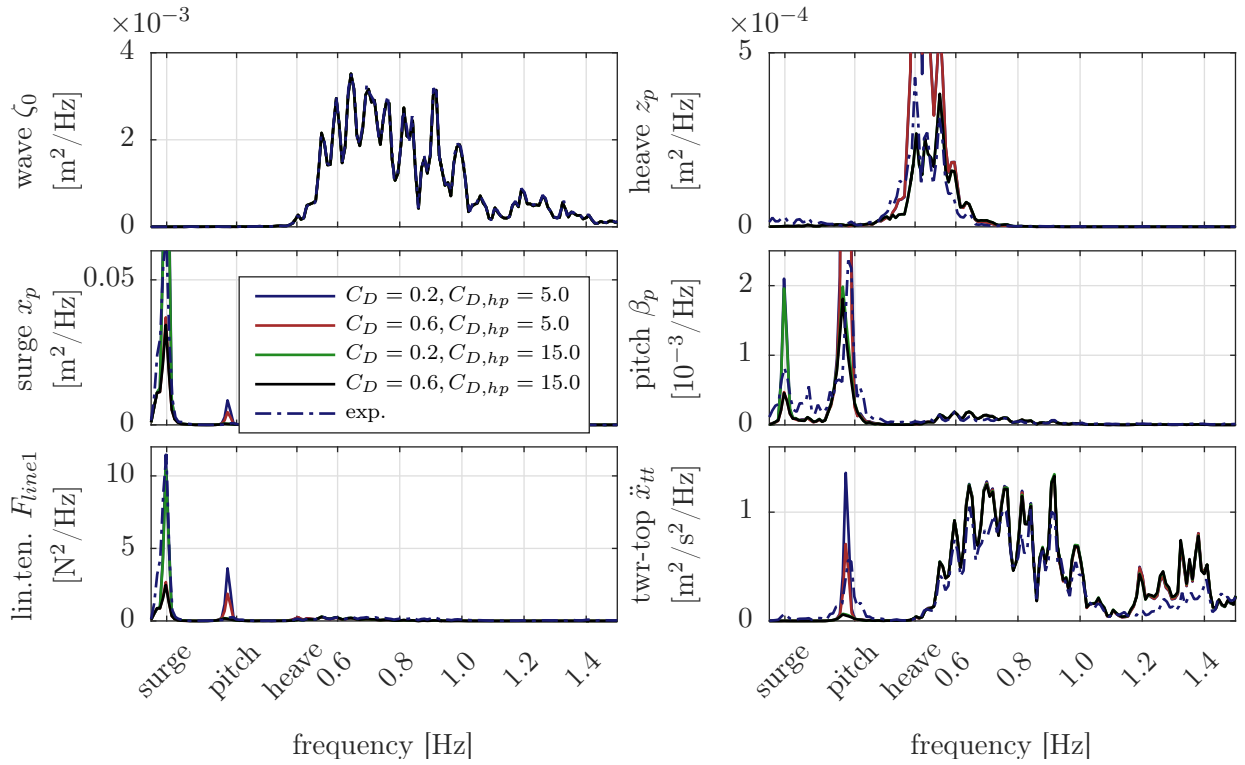
Figure 4.4: Response to wind and waves, LC 9 (Table 4.1) with simulations of various combinations of C_D and $C_{D,hp}$ and experiment (see following graphs for detailed views), [240].

was shown for example for the drag tuning in [248]. In the present work, the inertia forces of Morison's equation are dominant with little velocity-dependent excitation as discussed in Section 2.5.3. A visualization of the regimes of dominant wave forcing terms is shown with an indication of the experimental LCs in Figure 2.4. Figure 4.4 shows that the responses of the different DoFs match well at the wave frequencies. Larger than the first-order wave response is the one below the wave frequencies, at the platform surge, heave and pitch eigenfrequencies, listed in Table 4.2. At these frequencies the wave height spectrum $\zeta_0(\omega)$ is nearly zero, so the excitation results from second-order slow drift loads as introduced in Section 3.5.

The response magnitudes at the platform eigenfrequencies are highly dependent on the Morison drag coefficients: Figure 4.4 shows a large variation of the simulated response magnitudes at the surge and pitch-eigenfrequencies. Therefore, the focus will be on the frequency range below the waves for the identification of the Morison drag coefficients. In the following, the irregular wave response of two LCs will be shown, LC 7 and LC 9. For LC 7, Figure 4.5 shows a variation of C_D with constant $C_{D,hp}$ while Figure 4.6 shows the corresponding variation of $C_{D,hp}$ with constant C_D. From Figure 4.5 it can be seen that the best match of x_p with the measurement results is for $C_D = 0.6$. For the identification of $C_{D,hp}$ (vertical), the focus is put on the pitch-direction because for FOWTs, the heave response is generally not as important as the pitch response. Figure 4.6 shows that with $C_{D,hp} = 20$, reasonable results for pitch and heave
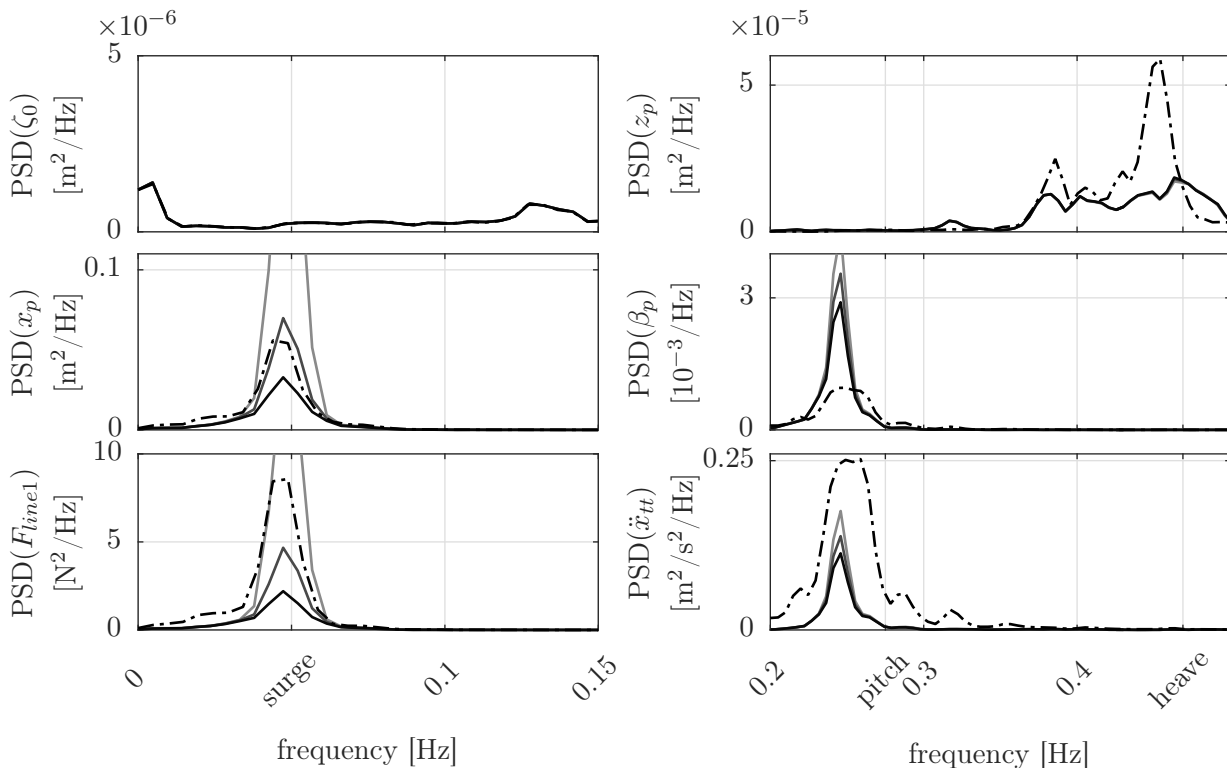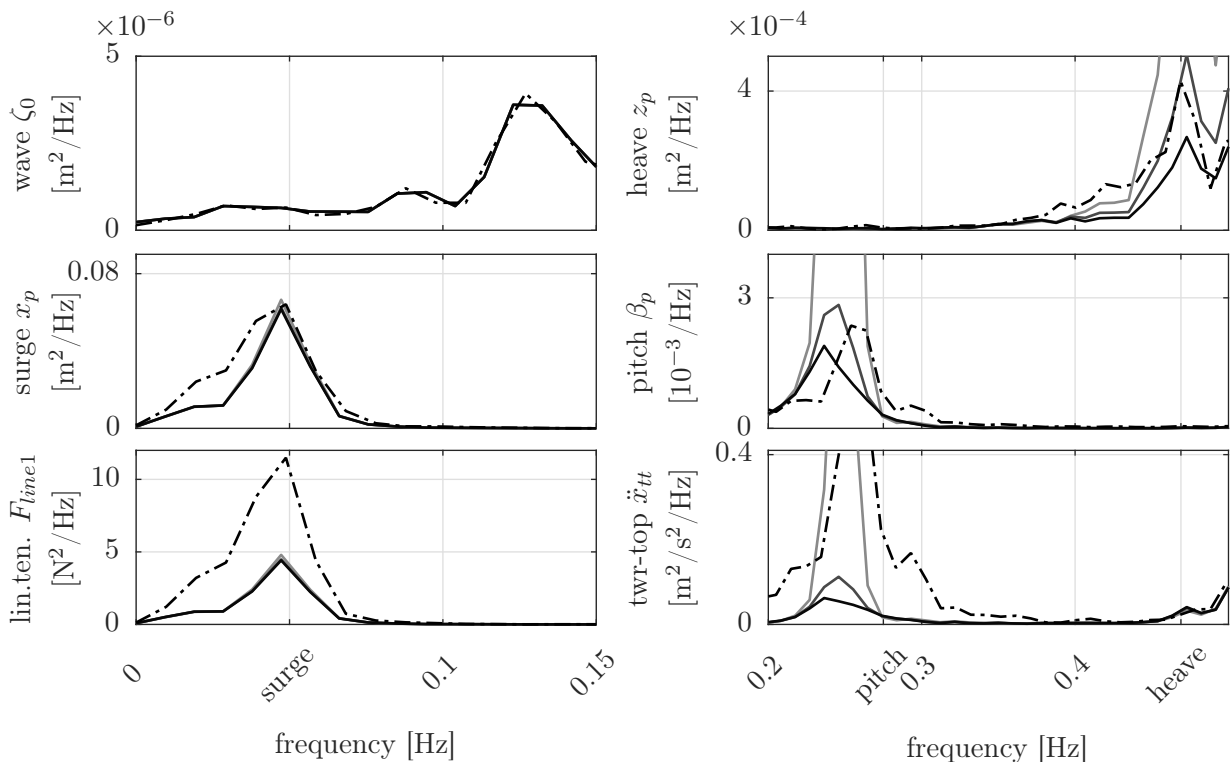
Figure 4.5: Response to wind and waves, LC 7 (Table 4.1) with simulations of Morison drag $C_D = [0.3, 0.6, 0.9]$ (increasing darkness), $C_{D,hp} = 20$ and experiment (dashed line).

can be obtained but the measured pitch response is still smaller. A possible explanation for the smaller measured response magnitude is a conceivable platform pitch velocity-dependent restoring torque on the hub from the vertical wind shear as mentioned before.

The simulated response of the tower $\ddot{x}_{tt}$ at the pitch eigenfrequency (Figure 4.6) does not match as well as those for the wave response. As mentioned above, a main difference between the two response peaks is that for the surge and pitch resonances damping is important, while it is not for the wave response. Consequently, a difference in the aerodynamic damping or the tower structural damping could lead to the underpredicted surge and pitch resonance of $\ddot{x}_{tt}$. It is noted that, although the eigenmode is labeled "pitch", this mode does also include a response of the tower-DoF, which can be seen in the modal analysis, Figure 3.23.

The mooring line force is always underpredicted by the model, in the resonance frequencies (surge and pitch) but also in the wave frequency range. The reason for this is possibly the quasi-static modeling approach as described in Section 3.6. If a mooring line mode lies close to the platform resonances the quasi-static forces can be significantly higher, see also Section 2.5.4. However, Vittori [152] showed for the test in Nantes 2014, that a dynamic mooring model, on the other hand, usually overpredicts the mooring tension compared to experiments. This is significant for the calculation of the mooring section loads but does usually not impact the other FOWT DoFs.
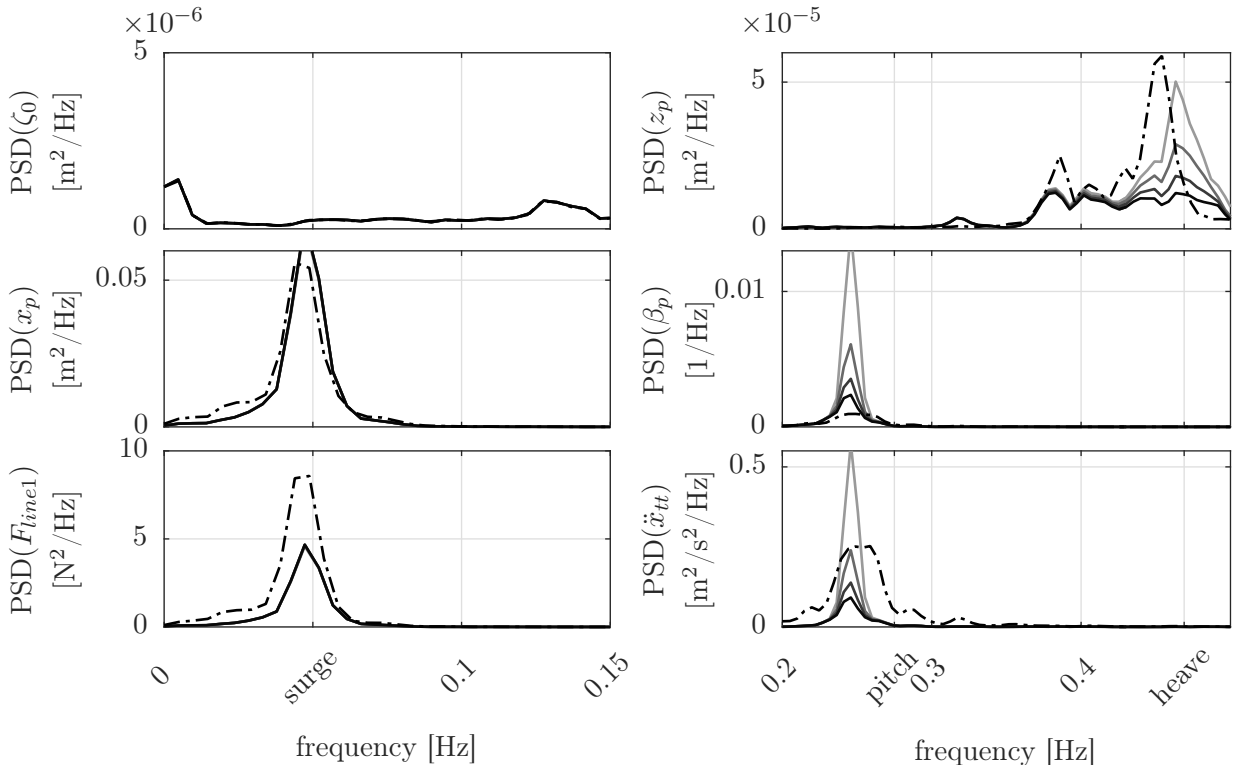
Figure 4.6: Response to wind and waves, LC 7 (Table 4.1) with simulations of Morison drag $C_D = 0.6$, $C_{D,hp} = [10, 15, 20, 25]$ (increasing darkness) and experiment (dashed line).

Looking at the more severe LC 9, Figure 4.7 shows the variation of C_D and Figure 4.8 shows the corresponding variation of $C_{D,hp}$. The surge response x_p for $C_D = 0.4$ gives here the best agreement with the measurements. And a heave plate drag of $C_{D,hp} = 10$ gives the best agreement with the pitch-direction β_p.

A remarkable effect is that the pitch eigenfrequency changes compared to the free-decay test. The labels for the eigenfrequencies in Figure 4.5–4.8 correspond to the ones of the decay test in Figure 4.3. Both, the simulated and measured response in LC 7 and LC 9 have a lower pitch resonance frequency than the one of the free-decay tests. However, the simulated one is slightly smaller than the measured one. This is in line with the results of Chapter 5, which revealed that the platform pitch mode is critical to the blade pitch controller and its damping and frequency can be altered by the control gains, possibly even making the system unstable. An excessively aggressive controller was also tested and presented in [160].
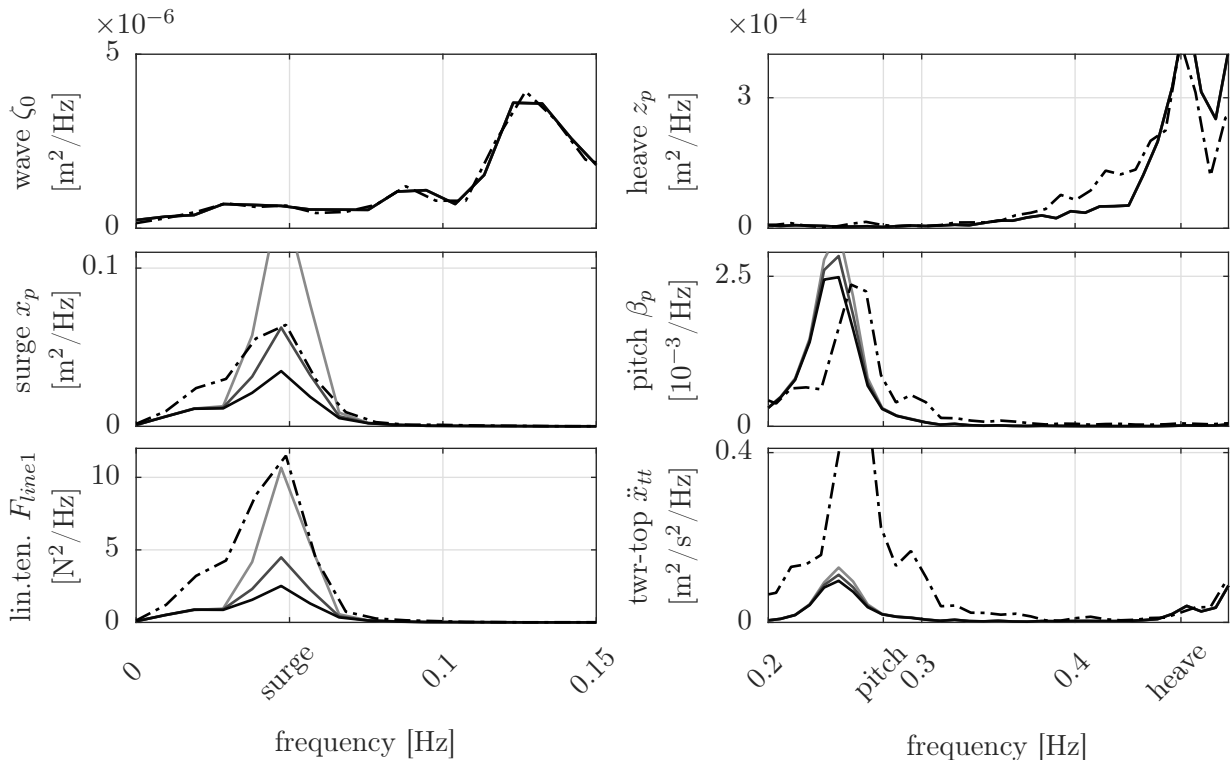
Figure 4.7: Response to wind and waves, LC 9 (Table 4.1) with simulations of Morison drag $C_D = [0.2, 0.4, 0.6]$ (increasing darkness), $C_{D,hp} = 10$ and experiment (dashed line), [240].

Figure 4.8: Response to wind and waves, LC 9 (Table 4.1) with simulations of Morison drag $C_D = 0.4$, $C_{D,hp} = [5, 10, 15]$ (increasing darkness) and experiment (dashed line), [240].

4.3 Full System Response

Figure 4.9 shows again the results of LC 7 but now with the rotor speed signal Ω and the blade pitch θ together with the results of the nonlinear model (as Figure 4.5–4.8) and the linear frequency-domain model. For the previously analyzed signals surge, heave and pitch, the agreement is good, also at the smaller magnitudes visible in the logarithmic y-scale. The frequency-domain model agrees very well with the nonlinear model showing that the response is mostly in the linear range.

The rotor speed and blade pitch signal is underpredicted at the wave frequencies ($f_{wave} \approx 0.8\,\text{Hz}$) by the simulation models. The reason for this is not known exactly. Due to the offset over a large range of frequencies, an incorrect drivetrain model seems one plausible explanation: Especially the numerical damping and friction model is rather simple with a static friction, independent of the rotor speed. Another possible reason is the neglected fluctuation of the wind speed by the simulation model (a constant wind is assumed). The turbulence of the wind generator was not identified in sufficient detail. As will be shown in Section 6.4.6, there is a strong coupling between the rotor speed mode and the platform pitch mode, which is influenced also by the wake dynamics. Research on unsteady aerodynamics for FOWTs was recently presented in [74], confirming the importance of unsteady aerodynamic models for the moving hub of a FOWT. The misplaced wind generator discussed in the introduction might be another effect possibly causing the observed difference on the rotor response.

The different drag values C_D and $C_{D,hp}$, identified for the decay tests, LC 7 and LC 9, are collected in Table 4.3. It can be seen that the drag is highest for the decay tests and decreases with the severity of the sea state or the magnitude of the response with the highest identified drag for the decay tests. It suggests that it is difficult to identify drag coefficients in general. As the drag depends strongly on the state of the flow surrounding the members (KC number) a LC-dependent drag is necessary. This is in line with the findings of [248], who could well identify the drag for irregular sea states but found a mismatch of the simulation results tuned to these cases with the wind-only conditions. After collecting these drag coefficients, it is important to keep in mind that the main excitation of the low-frequency modes is the slow-drift force, which is approximated with Newman's approximation, Section 3.5.5. For this reason, the obtained results will be compared to literature values in the next section.

Table 4.3: Identified Morison drag coefficients, [240].

Load case	Morison drag C_D	Heave plate drag $C_{D,hp}$
Free decay	2.0	25.0
LC 7	0.6	20.0
LC 9	0.4	10.0
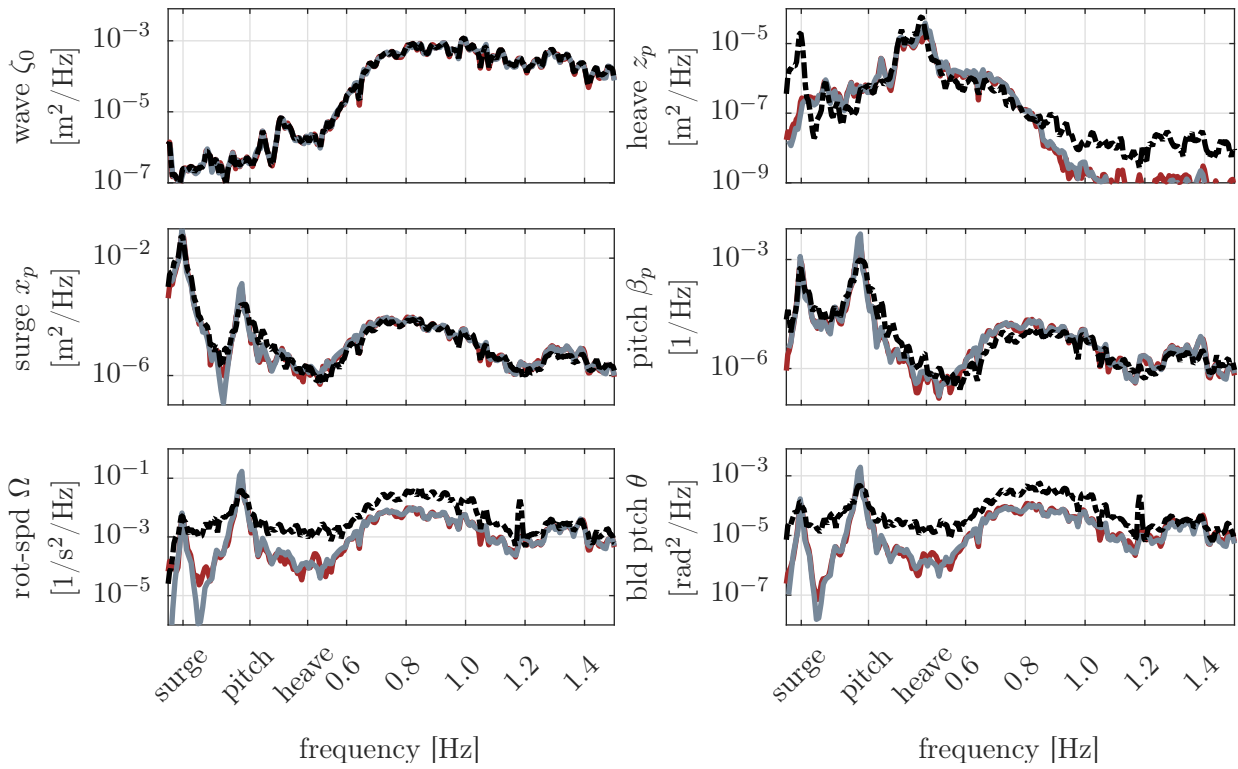
Figure 4.9: Response to wind and waves, LC 7 (Table 4.1) with nonlinear model (red), linear frequency-domain model (gray) and experiments (black, dashed); note logarithmic scale on y-axis, [240].

4.4 Comparison to Drag Coefficients from Literature

The dimensionless numbers Re and KC will be calculated from different LCs for the columns and the heave plates. The experimentally obtained values of the coefficients C_D and $C_{D,hp}$ are compared against literature values for the dimensionless numbers.

4.4.1 Columns

Morison drag is usually a function of the Keulegan-Carpenter number KC, Eq. (2.12), and the Reynolds number Re, Eq. (2.40). Different experimental results for smooth cylinders have been collected by Sumer and Fredsøe [227, p. 144], see Figure 4.11. It can be observed that the drag generally decreases for increasing Re, while larger KC yield a larger drag. In order to judge the identified coefficients of Table 4.3, the dimensionless KC and Re-numbers are calculated for LC 7 and LC 9 over the column length. This is done using the linear frequency-domain model: The velocity amplitude $\hat{v}$ for the calculation of the dimensionless numbers was based on the STD. Assuming a Rayleigh distribution of the maximum and minimum amplitudes of the velocity response over the columns, it is possible to approximate a representative velocity amplitude $\hat{v}$ necessary for the calculation of Re and KC. Here, the mean of the third highest response amplitudes is taken as a reference, the same as for the calculation of the significant

wave height H_s. The velocity $\hat{v}$ is calculated as

$$\hat{v} \approx k_{peak}\sigma(v), \qquad \text{with} \qquad k_{peak} = 2.0. \tag{4.1}$$

Using the linear SLOW model, KC and Re are calculated once for the fluid particle motion, only and once for the body motion, only. The body motion is the one which influences the system damping, which in turn shows the largest sensitivity on the response-STD as shown in the previous section. This is a major difference to the validation of [248] because in that work the Morison drag excitation forces (as opposed to damping forces) are of major importance.
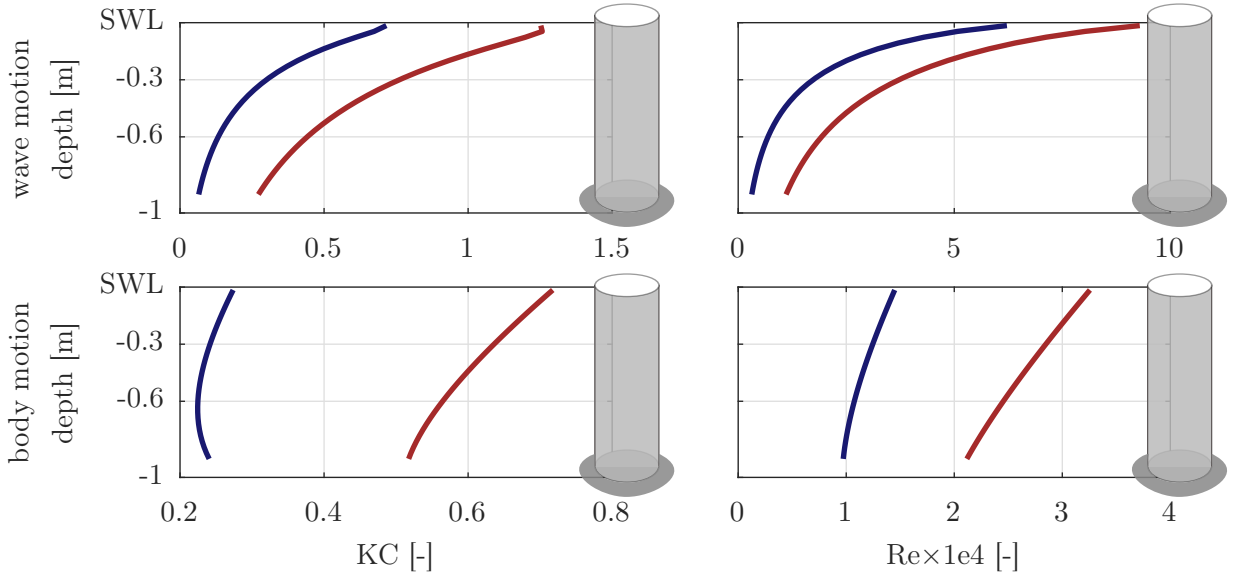
Figure 4.10: Keulegan-Carpenter number and Reynolds number over depth from LC 7 (blue) and LC 9 (red) from linearized model.

The zero-upcrossing period T_2 using the zeroth moment m_0 (Eq.(2.28)) and the first moment m_1 of the respective spectrum (either from body motion or wave motion), is used for the calculation of KC (Eq. (2.12)), see also [90, p. 5-42]

$$T_2 = 2\pi\sqrt{\frac{m_0}{m_1}}. \tag{4.2}$$

Figure 4.10 shows the Reynolds number and Keulegan-Carpenter number over the length of a vertical column for both, LC 7 and LC 9 for the body motion and wave motion. It can be seen that both, Re and KC increase with the sea state. Comparing the values to Figure 4.11, it can be seen that the Keulegan-Carpenter number is $KC < 1$ and therefore out of the range of Figure 4.11, while the Reynolds number $Re \approx 1 \times 10^4$ is at the lower end of the data. Such low KC numbers suggest that the flow is even unseparated, see [115, p. 228]. Looking at the
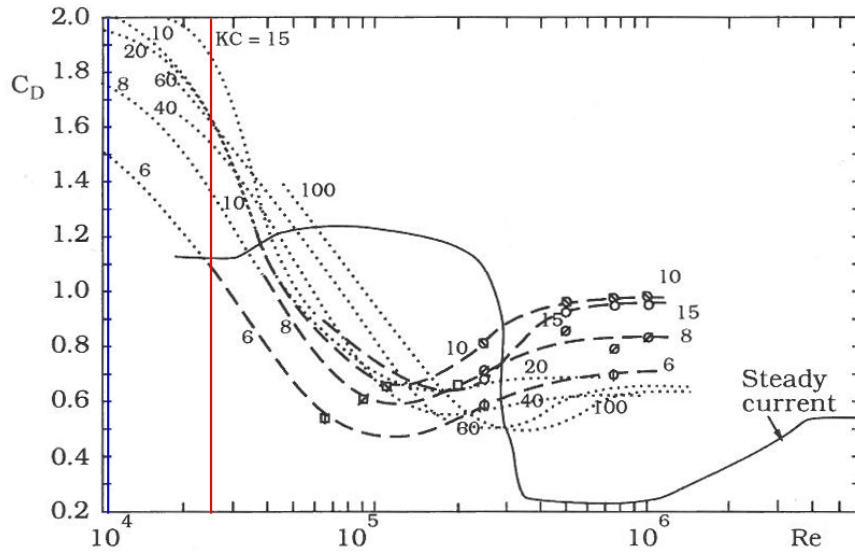
Figure 4.11: In-line force coefficients for a free, smooth cylinder as function of the *Re*-number for various *KC* with vertical lines for *Re*-values corresponding to LC 7 (blue) and LC 9 (red). Adapted from [227, p.144], reprinted with permission from author, 2018.

vertical axis of Fig 4.11 at $Re = 1 \times 10^4$, the C_D values decrease for decreasing KC and the obtained values of Table 4.3 with $C_D = 0.4$ (LC 9 and $C_D = 0.6$ (LC 7) seem in a plausible range.

Another, analytic equation for C_D for circular cylinders of low KC is given by Wang in [115, Eq. (7.21)]. It returns values of $C_D = 0.47$ for LC 7 and $C_D = 0.2$ for LC 9. The values are a bit lower than the identified ones but the trend is the same and confirms the plausibility of the experiments.

4.4.2 Heave plates

The same comparison can be made for the heave plates in vertical direction. Table 4.4 shows the Reynolds number and Keulegan-Carpenter number for both LCs. Due to the low response in heave-direction, the values are even smaller than for the columns. However, now the values are within the range of the literature values taken from [230] and reprinted in Figure 4.12. The data is compared in the publications for heave plates of different porosity, while here only the black diamonds of zero porosity are of interest. For the body motion of the more severe LC 9, we get $KC = 0.35$. Reading the corresponding $C_{D,hp}$ off Figure 4.12 results in $C_{D,hp} \approx 10$. This is equal to the identified value for LC 9 of Table 4.3. For the mild sea state (LC 7), one obtains $KC = 0.054$ with an identified $C_{D,hp} = 20$. This value seems also plausible when extrapolating the present data of Figure 4.12 to the left. The heave plate drag is independent of the Reynolds number due to the sharp corners and small thickness of 3 mm.
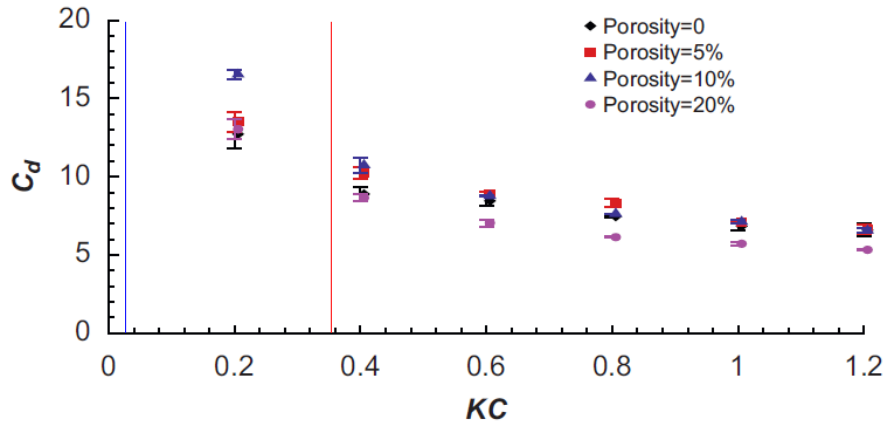
Figure 4.12: Vertical drag coefficient $C_{D,hp}$ for heave plates of different porosities (only 0-porosity relevant) with vertical lines for KC-values corresponding to LC 7 (blue) and LC 9 (red). Adapted from [230, p.1012], reprinted with permission from Elsevier, 2018.

Table 4.4: Keulegan-Carpenter number and Reynolds number for heave plates (vertical direction) from linearized model.

	LC 7		LC 9	
	KC [-]	Re [-]	KC [-]	Re [-]
body motion	0.054	4.9×10^3	0.35	2.6×10^4
wave motion	0.043	4.7×10^3	0.18	1.7×10^4

4.5 Summary

It could be shown in this chapter that the simulation model of Chapter 3 is able to reproduce the platform eigenfrequencies, as well as the response magnitudes. The hydrodynamic model including the first-order panel code coefficients and the second-order slow-drift model show to be correctly implemented as both, the low-frequency and the wave frequency response compare well to the experiments. The Morison model with horizontal and vertical members is well suited to model the experimental tests. Differences exist for the controller-related DoFs, the rotor speed and the blade-pitch angle. This suggests that a drivetrain model with a more detailed identification of the bearing friction might be necessary. Further research should also address the aerodynamic force model, which includes the wake dynamics. The uncertainty of the FOWT model properties, the wind and wave generators and the sensors has not been quantified in this study. Eventually the research shows the importance of a correct modeling of the hydrodynamic drag, depending on the load case. Due to the strong coupling of the platform pitch and the rotor mode, this hydrodynamic damping is important for a robust tuning of the wind turbine controller. The identified drag values seem reasonable after the comparison to literature data. The values given in [230] will be parameterized for the optimization of Chapter 6.

5 Controller Design

This chapter starts with a linear system analysis with the previously developed model to get an understanding of the coupled properties of the dynamic FOWT system, relevant for controller design. After the standard below-rated controller is introduced, a new scheme for a robust PI-controller for above-rated conditions will be developed. It uses only the rotor speed error as input and actuates the blade pitch angle (SISO) and relies therefore on a standard control architecture. However, the gain scheduling is designed such that the system robustness is ensured at all operating points. This criterion is the basis for a new, automated, model-based design algorithm, in order to be used for the integrated optimization of Chapter 6. This gain scheduling controller is subject of the paper [249].

Next to this SISO controller, an optimal MIMO controller will be designed for above-rated conditions. It has the objective of showing the principally possible upper bound of the controller performance, to be compared to the standard SISO controller. Thus, it is another reference for the integrated optimization. The design is here done for the TripleSpar of Section 2.10 but the validity of the controllers is ensured for the entire design space of platforms of Chapter 6. This MIMO-controller and a linear system analysis as in the next section is subject of the paper [205].

5.1 Linear System Analysis

In this section, an input-output scaling will be applied to the transfer function from disturbance inputs $\boldsymbol{d} = [v_0, \zeta_0]^T$ (wind speed and wave height) and control inputs $\boldsymbol{u} = [M_g, \theta]^T$ (generator torque and blade pitch angle) to the outputs $\boldsymbol{y} = [\Omega, x_t]^T$ (rotor speed and tower-top displacement from bending). This allows for a quantization and comparison of the effects of the different system inputs. Next, the coupling of the system from the control inputs and disturbance inputs to the outputs will be examined in a MIMO system analysis. The analyses are made with a focus on the difficulties arising from the RHPZ due to the floating platform, which is especially critical slightly above rated. This is why the operating point is selected as $v_0 = 13\,\mathrm{m/s}$.

5.1.1 Scaling

The scaling law to obtain the dimensionless system transfer function $\hat{\boldsymbol{G}}$ from the dimensional one $\boldsymbol{G}$ following [166] reads

$$\hat{\boldsymbol{G}} = \boldsymbol{D}_y^{-1} \boldsymbol{G} \boldsymbol{D}_{u^*}. \tag{5.1}$$

The scaling matrix for inputs $\boldsymbol{D}_{u^*}$ includes control and disturbance inputs $\boldsymbol{u}^* = [\boldsymbol{u}, \boldsymbol{d}]^T$. For the chosen input and output signals it results

$$\boldsymbol{D}_{u^*} = \text{diag}([\ \hat{M}_g, \ \ \hat{\theta}, \ \ \hat{v}_0, \ \ \hat{\zeta}_0\ ]) \qquad \text{and} \qquad \boldsymbol{D}_y = \text{diag}([\ \hat{\Omega}, \ \ \hat{x}_t\ ]). \tag{5.2}$$

The scaling factors are usually defined based on actuator constraints or maximum allowable excursions, respectively, see [166]. Here, the specified requirements for the controller performance of Table 2.2 were used for the rotor speed Ω and the generator torque M_g. For all others, simulation results of the DTU 10 MW RWT on the TripleSpar at $\bar{v}_{hub} = 13\,\text{m/s}$ in closed-loop were used with the sea states of Table 2.1. The scaling factors are based on the STD σ of the respective signals. The 2σ values are used as in Section 4.4, which is the mean of the third largest amplitudes for a narrow-banded process, see Section 2.7.3. All scaling factors are collected in Table 5.1.

Table 5.1: Scaling factors.

$\boldsymbol{u}$		$\boldsymbol{d}$		$\boldsymbol{y}$	
$\hat{M}_g$	$= 0.15 M_{g,rated} = 31.1\,\text{kNm}$	$\hat{v}_0$	$= 2\sigma = 2.4\,\text{m/s}$	$\hat{\Omega}$	$= 0.15\,\Omega_{rated} = 1.44\,\text{rpm}$
$\hat{\theta}$	$= 2\sigma = 6.0\,\text{deg}$	$\hat{\zeta}_0$	$= 2\sigma = \frac{1}{4} H_s = 1.4\,\text{m}$	$\hat{x}_t$	$= 2\sigma = 0.28\,\text{m}$

5.1.2 Input-output analysis

As discussed in Section 2.9, the biggest challenge for FOWT control is maintaining the rotor speed while at the same time damping the platform motion. With the two standard actuators of blade pitch θ and generator torque M_g, generally two control inputs are available and it is also possible to feed back more signals than the rotor speed Ω. This encourages MIMO controllers, which have the potential of mitigating the RHPZ [166]. In this section, the scaled transfer dynamics from the control inputs $\boldsymbol{u}$ to the outputs $\boldsymbol{y}$ at a wind speed of $v_0 = 13\,\text{m/s}$ is analyzed. Figure 5.1 shows the 2×2 transfer function as Bode plots: At each frequency, a sinusoidal input signal is amplified by the factor of the upper Bode plot. Additionally, the amplified output is shifted by the phase angle of the lower Bode plot. Consequently, Figure 5.1 shows two properties: The transfer functions, including the poles and zeros, causing changes in the phase, depending on their location in the complex plane (Figure 3.24) and additionally, the

authority of both actuators on the outputs. If the amplification of one actuator on the outputs is $|\hat{G}_{u \to y}(j\omega)| \ll 1$ this means that this actuator is likely not to yield a good trajectory tracking and disturbance rejection. This is why the amplification of the disturbance inputs $\boldsymbol{d}$ is shown in Figure 5.1 with gray lines for comparison with the control inputs (it is only shown for $u_2 = \theta$ because the amplification of $u_1 = M_g$ is an order of magnitude smaller, as will be discussed later). The control inputs should always have more authority than the disturbances to be able to reject them successfully. The disturbance transfer function from the wave height to the wave forces on the platform $\boldsymbol{G}_{\zeta \to F}$, which is necessary to calculate the disturbance transfer functions of Figure 5.1, was calculated with the parametric approach of Section 3.5.2.
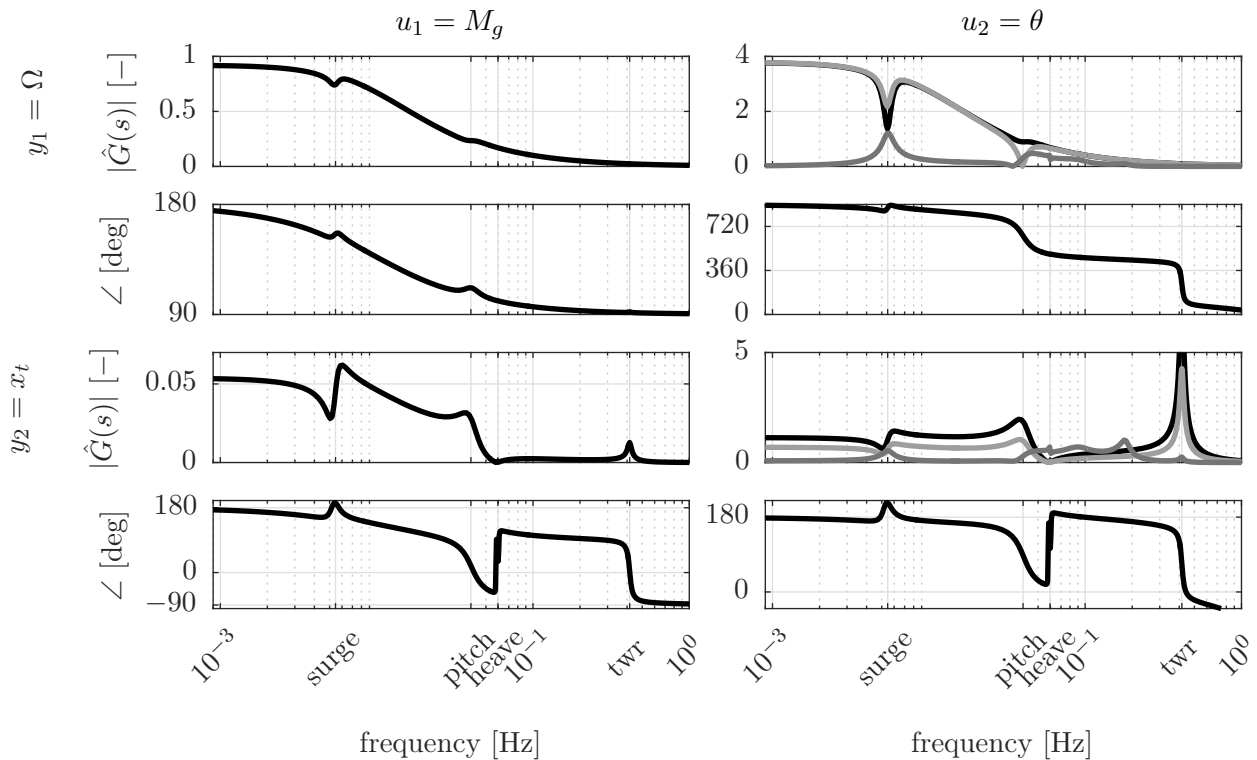
Figure 5.1: I/O transfer function Bode diagram with inputs $\boldsymbol{u} = [M_g, \theta]^T$ and outputs $\boldsymbol{y} = [\Omega, x_t]^T$ (black). For comparison, including magnitude of disturbance transfer functions from wind v_0 (light gray) and wave height ζ_0 (dark gray), @$v_0 = 13\,\text{m/s}$, scaled, [205].

The comparison of the amplification of control inputs as opposed to disturbances in Figure 5.1 shows that the wind speed v_0 has a comparable effect on the rotor speed Ω as the blade pitch θ with a rather low influence from the waves ζ_0. The tower-top displacement x_t, however, sees disturbances from the wind at lower frequencies and from waves at frequencies $f > f_{eig,\beta_p}$, which are in the range of the authority of the blade pitch angle, or even above. This analysis reveals that it is challenging to attenuate the wave disturbance on a FOWT using the standard actuators of the rotor, especially in the wave frequency range, above the pitch frequency.

The 2×2 transfer dynamics of Figure 5.1, on the other side, show the significant phase loss in the dynamics from blade pitch to rotor speed, because of the two RHPZ discussed in

Section 2.9 (the positive phase of $180 \deg$ at $\omega \to 0$ is due to the negative amplification of both control inputs). The generator torque shows about four times less amplification on the rotor speed than the blade pitch angle and even more, about twenty times less amplification on the tower-top displacement. This is generally advantageous as one could decouple the system and control the rotor speed with the generator torque and the tower-top displacement with the blade pitch angle. The same can be found analyzing the Relative Gain Array (RGA), see [166]. Unfortunately, the actuator constraints prohibit such a realization, since the generator is usually not designed with an excessive safety factor on the electrical current and therefore only small fluctuations of the torque at rated wind speed are allowed. A comparison of the magnitudes from blade pitch to the outputs (Figure 5.1, right column) shows that changing the blade pitch angle does not only result in a change of the rotor speed with $|\hat{G}_{\theta \to \Omega}(j\omega)| > 1$ but also of the tower-top displacement x_t with $|\hat{G}_{\theta \to x_t}(j\omega)| > 1$. Thus, the blade pitch yields a "parasitic" disturbance as a side effect, especially in the frequency range of the common bandwidth for SISO controllers at $f > f_{eig,\beta_p}$, which is the reason why a decoupling, diagonal controller is hardly feasible for wind turbines.

5.1.3 Multi-input-multi-output analysis

The previous open loop analysis can also be done systematically through a Singular Value Decomposition (SVD), see [166], transforming the transfer function matrix $\boldsymbol{G}$ into a diagonal matrix of two singular values representing the maximum and minimum gain $\overline{\sigma}$ and $\underline{\sigma}$, respectively in the correlated direction of the outputs $\boldsymbol{U}$ and inputs $\boldsymbol{V}$

$$\begin{bmatrix} G_{11} & G_{12} \\ G_{21} & G_{22} \end{bmatrix} = \begin{bmatrix} \overline{\boldsymbol{U}} & \underline{\boldsymbol{U}} \end{bmatrix} \begin{bmatrix} \overline{\sigma} & 0 \\ 0 & \underline{\sigma} \end{bmatrix} \begin{bmatrix} \overline{\boldsymbol{V}} & \underline{\boldsymbol{V}} \end{bmatrix}^T . \tag{5.3}$$
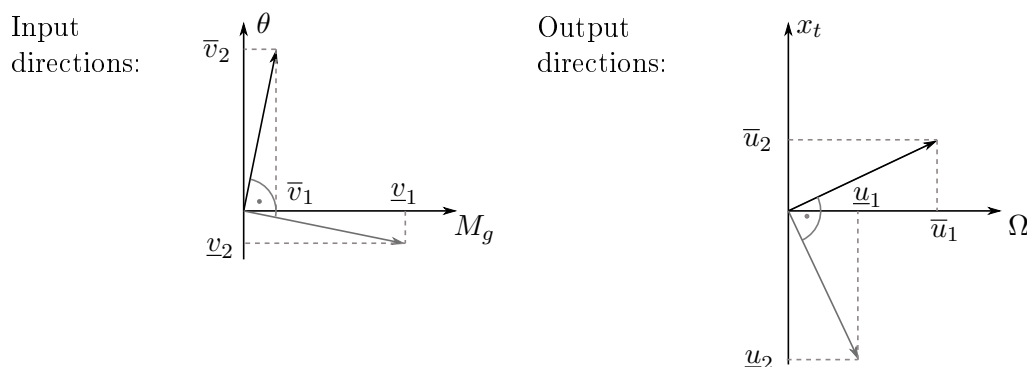
Figure 5.2: Input and output directions for $\omega = 0$. Output amplification is not shown, each output direction will be amplified by $\overline{\sigma}$ and $\underline{\sigma}$, respectively.

Figure 5.2 is a visualization of both directions, applied to the input and output signal of the present system $\boldsymbol{G}$. The strongest and weakest one are always orthogonal and both are
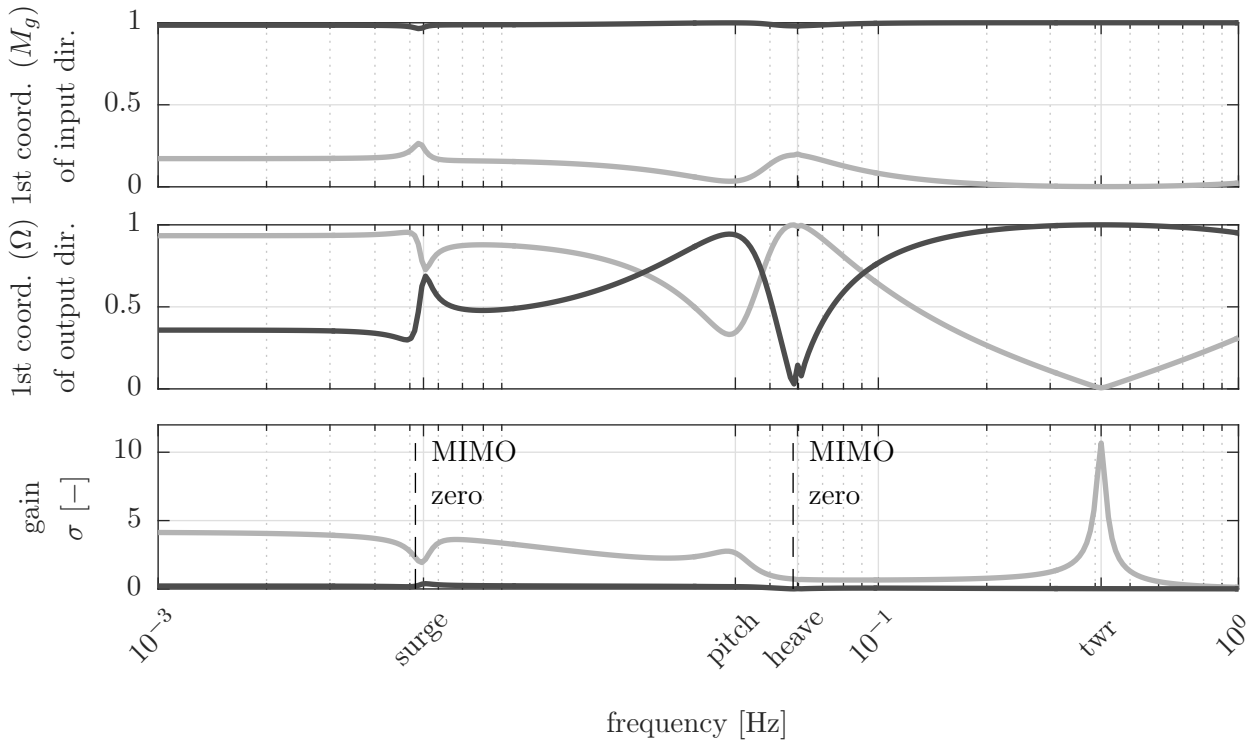
Figure 5.3: Singular-value decomposition of I/O transfer function: Strongest (dark) and weakest (light) input and output directions with associated gains: The first plot shows the first coordinate of the input coordinates $\boldsymbol{u} = [M_g, \theta]^T$ and the second plot the first coordinate of the output coordinates $\boldsymbol{y} = [\Omega, x_t]^T$, the third plot shows the gain associated with the strongest and weakest direction and the MIMO zeros of $\boldsymbol{G}$, @$v_0 = 13\,\mathrm{m/s}$, [205].

amplified individually by $\overline{\sigma}$ and $\underline{\sigma}$, respectively. Figure 5.2 visualizes the zero-frequency limit of the frequency-dependent SVD of Figure 5.3. We can now investigate the combination of the inputs that yield the highest gain on the outputs. This strongest gain $\overline{\sigma}$ is associated with the strongest output direction. Thus, this analysis addresses the true MIMO system with combinations of the inputs and their effect on the outputs, as opposed to Figure 5.1, which shows the independent transfer dynamics.

Figure 5.3 shows in the upper two graphs the first coordinate of the input and output directions (abscissa of Figure 5.2). It can be seen that the strongest singular value in dark color contains only little contribution of the generator torque M_g but a high portion of the blade pitch angle θ, which confirms the findings from the I/O transfer function matrix of Figure 5.1. Looking at frequencies up to the platform pitch eigenfrequency this combination of inputs (or "direction") is well suited to control the rotor speed Ω (second plot, dark color). At the platform pitch eigenfrequency, the strongest gain $\overline{\sigma}$ decreases, showing that the control of both, the rotor speed and the tower becomes rather difficult.

One can assess the effect of using the two control inputs (M_g, θ) as compared to the blade pitch angle, only: The strongest singular value yields slightly higher gains (Figure 5.3, bottom)
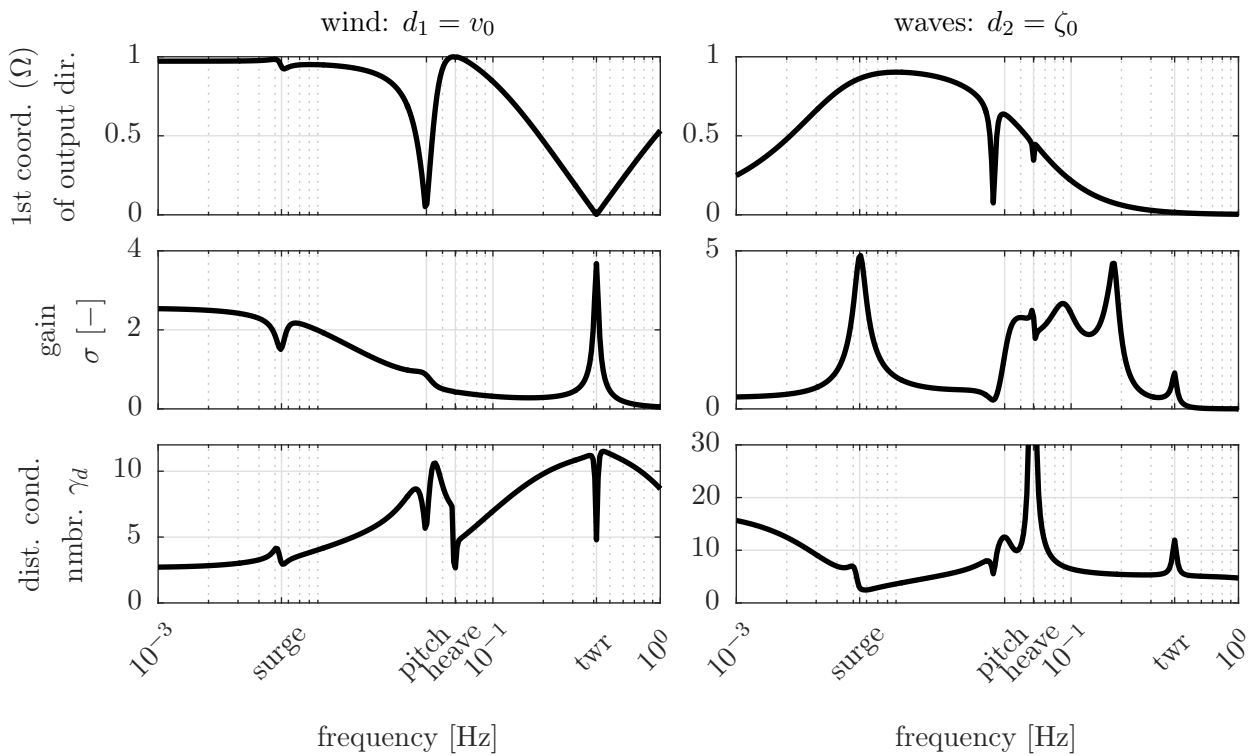
Figure 5.4: Singular-value decomposition of open loop disturbance transfer function for wind (left) and waves (right): The first row shows the first coordinate of the output coordinates $\boldsymbol{y} = [\Omega, x_t]^T$, the second row shows the associated gain and the third plot shows the disturbance condition number γ_d, @$v_0 = 13\,\mathrm{m/s}$, [205].

than the blade pitch angle only (Figure 5.1, upper right) for $f < f_{eig,\beta_p}$. Consequently, the generator torque is a useful actuator, although Figure 5.1 (upper left) shows very small gains associated with it.

The strongest (control) output direction (Figure 5.3, second plot) can now be compared to the output disturbance directions from wind and waves. These are shown in Figure 5.4. For low frequencies, wind and waves affect more the rotor speed than the tower-top displacement (Figure 5.4, top). Interesting are here the gains of the strongest disturbance output directions, compared to the strongest control output directions: The gain of the strongest control input (Figure 5.3, bottom) is of about twice the magnitude of the gain from wind on the outputs (Figure 5.4, middle left). For the waves it is different: The amplifications of the waves on the outputs is of comparable magnitude as of the control inputs. This is confirmed by the disturbance condition number γ, which takes high values if the disturbance direction is aligned with the weakest control output direction. This means that it is high if the disturbance affects directions which are hard to control, see [166]. Here, this is the case for wind excitations of high frequencies and for waves, around the MIMO zero at $0.05\,\mathrm{Hz}$, see Figure 5.4, bottom row.

5.1.4 Summary

The main findings of the OL analysis are first, the different impact of the two actuators blade pitch and generator torque on the rotor speed. The amplification of the blade pitch signal on the rotor speed proves its better suitability for control, compared to the generator torque. However, blade pitch has, as opposed to the generator torque, the negative side effect that it influences more the tower-top fore-aft forcing than does the generator torque. This finding influences the selection of a MIMO control layout: While it would be desirable to have two control inputs with two different controlled variables with no interaction of one loop on the other, this seems not possible due to the generator torque constraints. Second, it was shown that supporting rotor-speed control with a slight portion of generator torque actuation can improve the control performance while exciting less the tower-top motion. However, the control against the wave forcing is found to be challenging, especially at the frequencies of common wave spectra.

5.2 Below-Rated Controller

For wind speeds between cut-in ($4\,\text{m/s}$) and rated wind ($11.4\,\text{m/s}$), a standard $K\Omega^2$-controller is used for both of the above-rated controllers to be designed in the next sections. The below-rated controller will not be adjusted to the different platform designs in this work because it does not influence the system stability as the above-rated controller. The goal is to control the rotor speed for optimal power production at TSR $\lambda = \Omega R/v_0 = \lambda_{opt}$, see Section 2.9. Therefore, the generator torque M_g is a nonlinear state feedback of the rotor speed Ω following [44] as

$$M_g = k_\Omega \Omega_g^2 \qquad \text{with} \qquad k_\Omega = \frac{1}{2}\rho_a \pi R^3 \frac{c_{p,max}}{\lambda_{opt}}. \qquad (5.4)$$

For the DTU 10 MW RWT, the rated generator torque is rather low compared to the rotor properties. Therefore, there is no increase of generator torque necessary in the transition from the optimal-TSR region and the above-rated region. Often, the switching methodology to the above-rated control region substantially influences the overall fatigue loads of the rotor and the tower. In this work, this switching is not a focus but rather the design of the above-rated controller. The tested wind speeds of Chapter 6 yield only few switching events.

5.3 Robust Proportional-Integral Controller

As described in Section 2.9, a common way of designing SISO controllers for FOWTs is to "de-tune" the gains, making the controller less aggressive to avoid instability due to the RHPZ. A common method, described in [10] and [15], and repeatedly used for the generic FOWT concepts OC3 and OC4, see [111, 112], is to model the de-coupled (rigid) rotor including
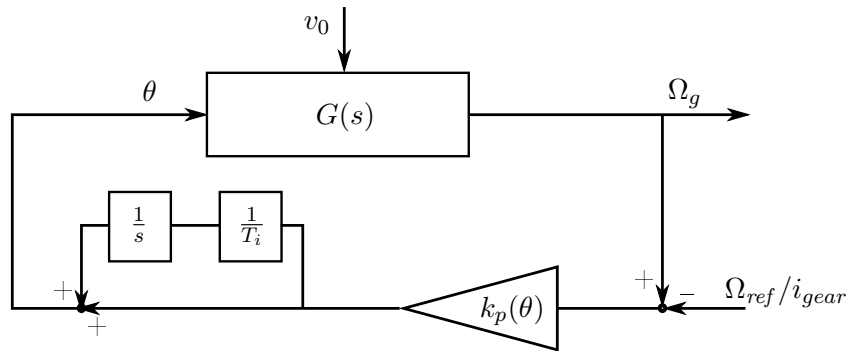
Figure 5.5: PI-controller for above-rated wind speeds.

aerodynamics and design the controller such that the closed-loop-eigenfrequency of the rotor lies below the fundamental platform eigenfrequency (usually platform pitch, see Section 2.5). As discussed already in Section 2.9, this method gives good first guesses for reasonable control gains without large modeling efforts (the floater and tower dynamics do not have to be represented). However, mainly the gain scheduling law does not always yield reasonable results. It suggests constant dynamics over the entire operating range, which is the intention of gain scheduling. But this is not always true because of the neglected fore-aft dynamics in the model. With a more refined simulation model, the rotor dynamics in closed-loop will alter significantly over the operating range, contradicting the design conditions.

Here, a method is proposed based on the linearized model of Chapter 3, which includes the floater dynamics, especially the platform pitch mode. For a robust PI-controller, stability is the first criterion and the rotor eigendynamics (as in the above "de-tuning" method) is a secondary criterion. Thus, the controller ensures a certain robustness over the operating range, which is important considering the RHPZ and also the uncertainty related to the system damping, see Chapter 4.

Figure 5.5 shows the block diagram of the controller. There is no explicit gain scheduling factor included. Instead, the proportional gain is written as a function of the blade pitch angle $k_p = k_p(\theta)$. The controller maintains a constant generator torque M_g in the above-rated wind speed region. The feedback control law reads with the azimuth angle $\varphi = \int \Omega \, dt$, equal to the integral of the rotor speed Ω, the PI time constant T_i and the gear ratio i_{gear}

$$\Delta\theta = \frac{k_p(\theta)}{i_{gear}} \, \Delta\Omega + \frac{k_p(\theta)}{i_{gear} T_i} \, \Delta\varphi. \tag{5.5}$$

Using the Nyquist criterion, see [166], a Gain Margin (GM) and a Phase Margin (PM) can be defined as a design criterion. Here, a different method is chosen, involving only a single criterion, in order to simplify the automation intended for this controller. The single criterion is
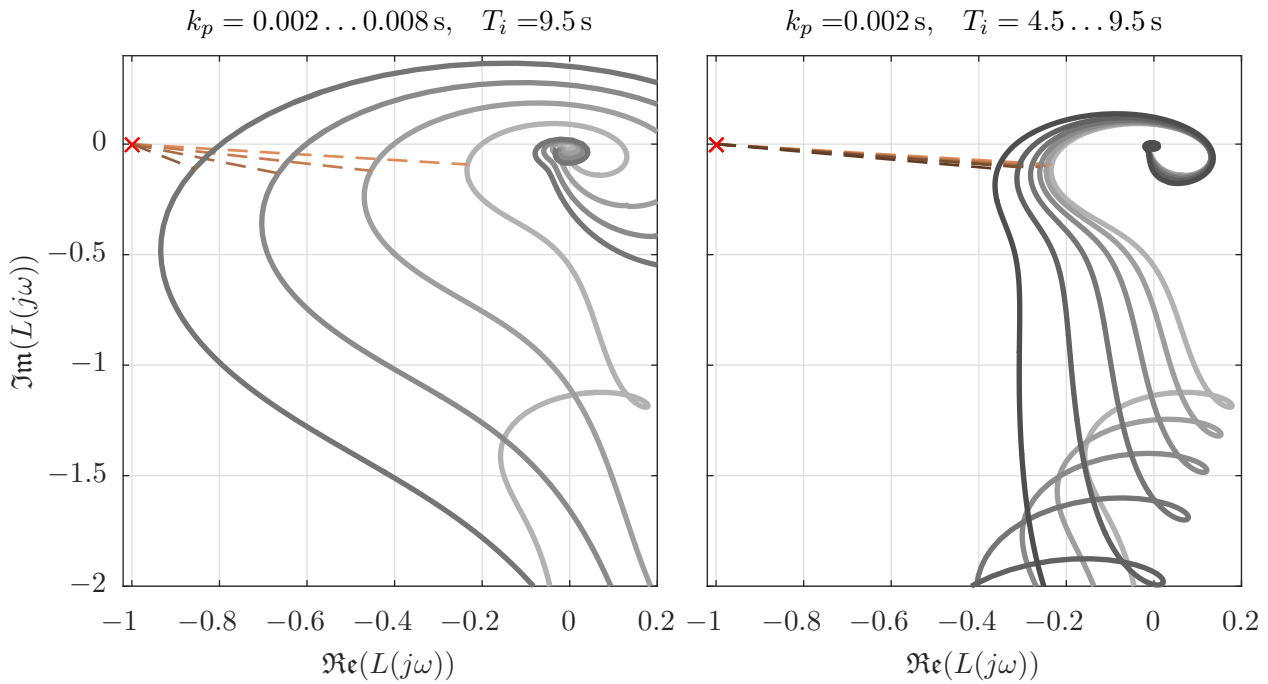
Figure 5.6: Nyquist plot of loop-transfer function $L(j\omega)$ for varying k_p (left, darker colors for increasing k_p) and varying T_i (right, darker colors for decreasing T_i), @16 m/s, with indication of the stability measure $1/M_s$.

the inverse of the maximum sensitivity M_s, as proposed in [250]. Figure 5.6 shows the Nyquist diagram, the loop transfer function $L(j\omega)$ in the complex plane, for different proportional gains $k_p = 0.002\ldots0.008\,\text{s}$ on the left and with varying time constants $T_i = 4.5\ldots9.5\,\text{s}$ on the right. The margin to the stability limit at $[-1, 0]$ is indicated. This distance to this point is exactly $1/M_s$, see [250, p. 13-6]. One can see that the margin is reduced for increasing k_p and decreasing T_i.

Not only the stability is a criterion but especially the rejection of the disturbances is a control goal for FOWTs, as discussed in Section 2.7.3. Therefore, the response in the closed-loop with relevant design loads was calculated for different combinations of k_p and T_i. Figure 5.7 shows the variation of the PSD of the blade pitch angle θ and the rotor speed Ω for the TripleSpar platform of Section 2.10. The other design indicator of Table 2.2, the tower-top displacement x_t, does not visibly depend on the control gains because the wave loads dominate its response. For θ and Ω, on the other side, the significance of the controller settings is observable. Clearly, a more aggressive control (larger k_p and smaller T_i) reduces the rotor speed tracking error at the cost of an increased blade pitch activity. It seems like a more aggressive controller is always better for rotor speed tracking. This is not the case, however, because the stability decreases, yielding a large fore-aft response. Consequently, the lowest possible stability margin can be seen as the best compromise between the two control objectives. A larger hydrodynamic damping can thus help to improve rotor speed tracking through a possible increase of the controller gains.
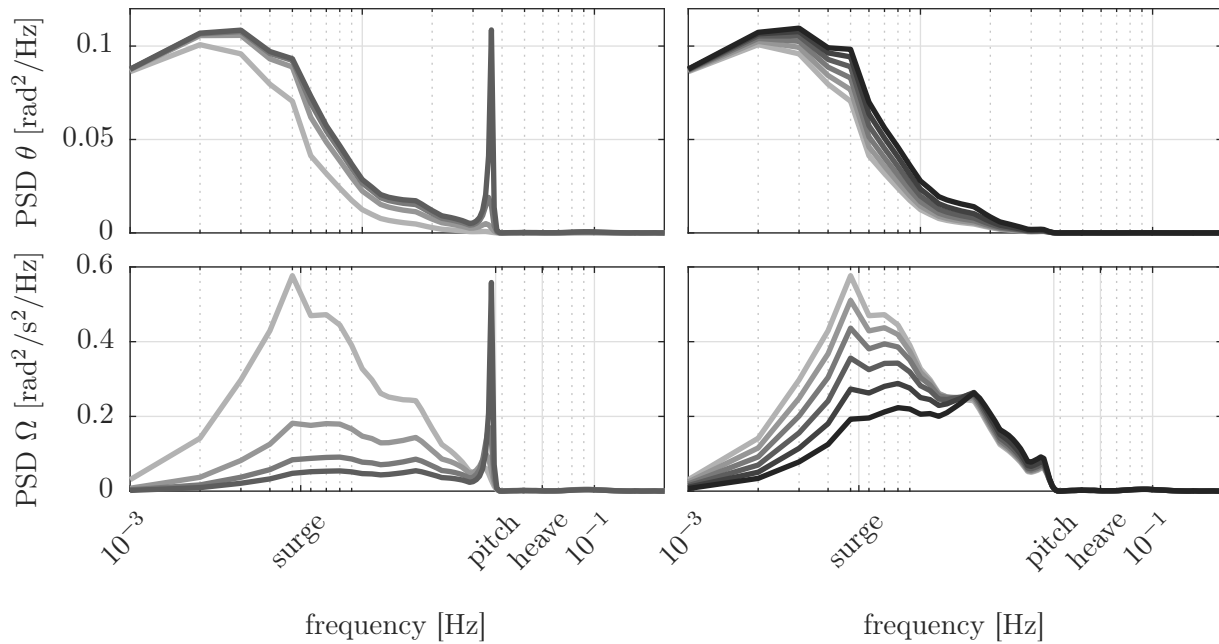
Figure 5.7: PSDs of rotor speed Ω and blade pitch angle θ for $k_p = 0.002\ldots0.008\,\mathrm{s}$ with $T_i = 9.5\,\mathrm{s}$ (left) and $T_i = 4.5\ldots9.5\,\mathrm{s}$ with $k_p = 0.002$ (right), darker colors for more aggressive gains (larger k_p, smaller T_i) @16 m/s.

In a next step, the criteria for setting up a gain scheduling law over wind speeds are set up. The first design criterion is the stability margin of $1/M_s = 0.4$. The corresponding gains k_p can be interpolated after calculating the margins $1/M_s$ for a grid of wind speeds v_0, gains k_p and time constants T_i. Figure 5.8 shows different quantities, all interpolated at the stability limit of $1/M_s = 0.4$ for different T_i. The first is the proportional gain k_p, which decreases initially before it raises again at higher wind speeds. On the right-hand side of Figure 5.8, the STD of the rotor speed Ω, the blade pitch angle θ and the tower-top displacement x_t can be seen. For all signals the largest T_i yield the smallest fluctuations. This might be connected with the observation that larger T_i yield a higher damping of the rotor-speed mode (see pole-zero map, Figure 3.24). The properties of the rotor mode can be seen in the two plots on the lower left of Figure 5.8. The pole magnitude λ_{rot} is equal to the undamped eigenfrequency for undercritically damped poles with $\xi_{rot} < 1$. For overcritically damped poles, only the magnitude of the dominant, smaller pole is shown, which is equal to the inverse of the time constant τ_{rot}, see Figure 3.24b. With higher wind speeds and increasing T_i, the rotor dynamics become faster and the damping ratio increases up to the overcritical range.

Following the observations of Figure 5.8, the time constant was fixed to $T_i = 9.5\,\mathrm{s}$, a value up to which the performance increases slowly with no improvements beyond. For higher wind speeds, stability is not an issue because for $v_0 > 20\,\mathrm{m/s}$, the limit of $1/M_s = 0.4$ cannot be reached anymore for the investigated range of gains k_p, see Figure 5.8. Therefore, the
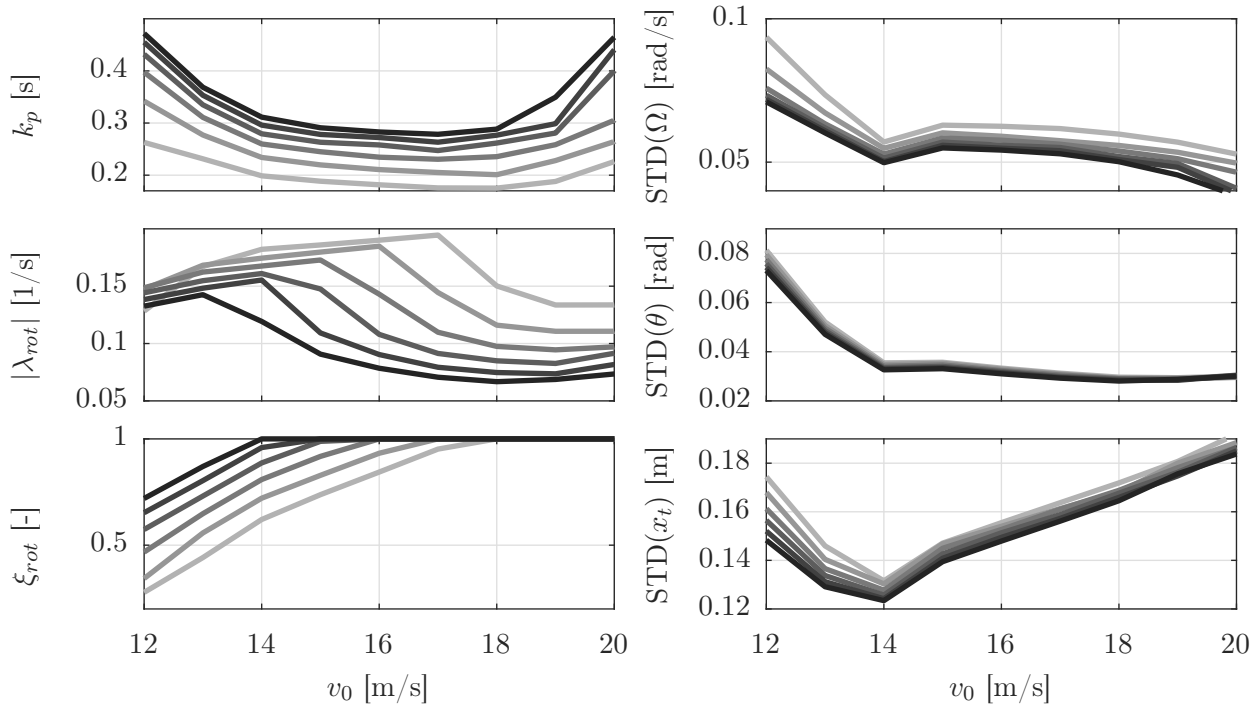
Figure 5.8: Interpolated CL properties at the stability limit $(1/M_s = 0.4)$ over wind speeds v_0 for $T_i = 4.5 \ldots 9.5\,\mathrm{s}$ (increasing darkness).

time constant of the (overdamped) rotor mode is fixed, as a secondary design criterion for the gain scheduling. This is in line with the procedure of [10] but here it is calculated for the coupled model instead of the rotor-only model. An algorithm identifying the eigenvectors and assigning them to the states has been implemented for the automated design algorithm. With this it is possible to interpolate the gains k_p (with a constant T_i again) at the desired eigenfrequency $\omega_{0,rot}$, or the desired time constant τ_{rot} for an overdamped mode.

Figure 5.9 shows the resulting gain scheduling $k_p = k_p(v_0)$ at the desired stability $1/M_s = 0.4$ or the desired rotor closed-loop time constant τ_{rot}, respectively. It can be seen that the stability requirement results in decreasing k_p for wind speeds above rated. Towards the cut-out wind speed of $v_0 = 25\,\mathrm{m/s}$ the stability criterion is not relevant anymore and the gain scheduling takes the values which yield a constant τ_{rot}. At rated wind, the stability is most critical and therefore the proposed criteria yield small k_p. The design of the PI-controller needs to be aligned with the switching procedure to below-rated winds.

The gain margins and phase margins for the gains at $1/M_s = 0.4$ of Figure 5.9 are shown in Figure 5.10. Recommended margins from control engineering textbooks are in the range of $GM \approx 6\,\mathrm{dB}$ and $PM = 40 \ldots 60\,\mathrm{deg}$. The resulting margins of the designed controller are roughly in this range and slightly below for the gain margin at low wind speeds and the phase margin at high wind speeds. This confirms that the chosen value of $1/M_s = 0.4$ is reasonable.
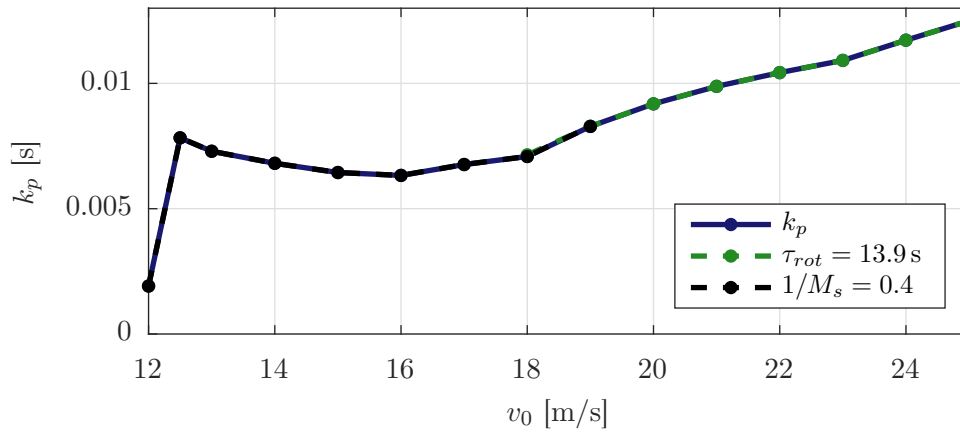
Figure 5.9: Gain scheduling of k_p for $T_i = 9.5\,\mathrm{s}$ obeying the stability limit of $1/M_s = 0.4$ and targeting a CL rotor time constant of $\tau_{rot} = 13.3\,\mathrm{s}$. Gain on high-speed shaft angular velocity is shown.
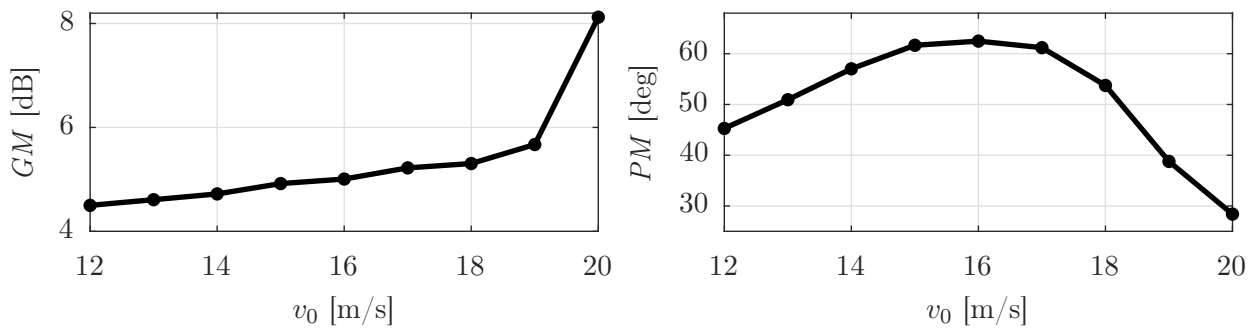
Figure 5.10: Gain margin and phase margin at $1/M_s = 0.4$ over wind speeds.
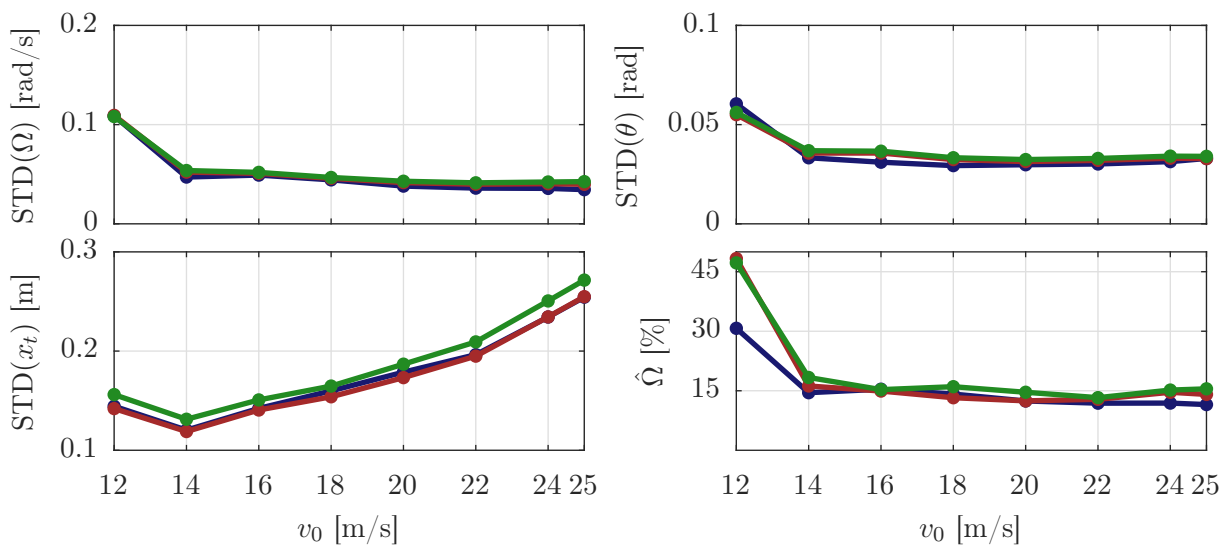
Figure 5.11: Simulation results for PI-controller with linearized model (blue), nonlinear model (red) and FAST (green) for load case of Table 2.1.

A final evaluation of the controller in the load case of Table 2.1 with the nonlinear and linear SLOW models and the FAST model is shown in Figure 5.11 with the STDs of the control inputs and outputs as well as overshoot of the rotor speed $\hat{\Omega}$ over the rated value. It can be seen that the values agree very well among the models. The STD of the rotor speed Ω is roughly constant for wind speeds $\bar{v}_{hub} > 20\,\text{m/s}$, due to the design criterion of the fixed time constant of the rotor τ_{rot}, see Figure 5.9. The linearized model deviates from the nonlinear only slightly for certain wind speeds. The blade pitch angle θ, predicted by FAST, shows larger STDs, which can be due to the blade elasticity. The rotor speed overshoot $\hat{\Omega}$ is above the 15 % design limit of Table 2.2 for the wind speeds around rated. This is likely due to the switching scheme to below rated conditions. Here, additional measures are necessary to improve the performance of this SISO baseline controller. A comparison between the models is further topic of Section 6.4.5.
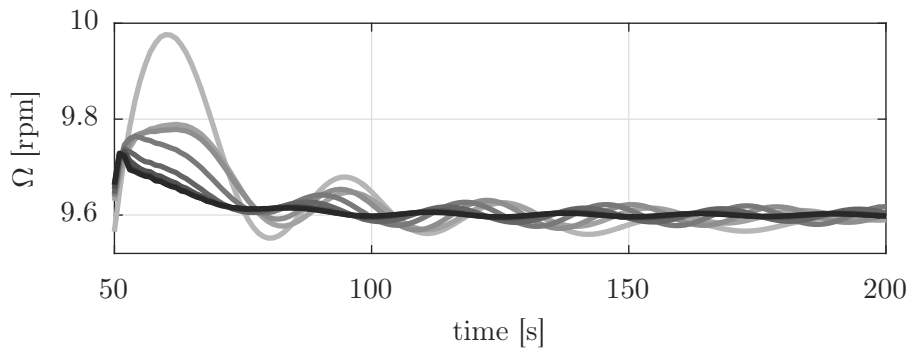
Figure 5.12: Step responses of rotor speed Ω with PI-controller at $v_0 = [12, 14, 16, 18, 20, 22, 24, 25]\,\text{m/s}$ (increasing darkness).

Figure 5.12 shows the step responses of Ω of the nonlinear model at different wind speeds above rated. It can be seen that the dynamics are close to constant for the wind speeds above $20\,\text{m/s}$ at which the controller was designed for a constant rotor time constant τ_{rot}.

5.4 Linear Quadratic Regulator

As a benchmark of a MIMO controller, an LQR is designed using the blade pitch angle and the generator torque as control inputs. Such optimal controllers have already been applied to wind turbines in [175], to FOWTs in [172] and, as part of this research, in [107]. The focus is here put on the definition of the MIMO controller, valid for all platforms analyzed in Chapter 6. Thus, this section gives a short introduction with the definition of the LQR weights but does not describe a new controller design methodology, as previously for the PI-controller. The LQR minimizes a quadratic cost function J of a linear model with weights on the squared control inputs $\boldsymbol{u}$ and states $\boldsymbol{x}$ and their product $\boldsymbol{ux}$, see [166], as

$$J = \lim_{T \to \infty} \frac{1}{T} \int_0^T \left[\boldsymbol{x}^T \boldsymbol{Q} \boldsymbol{x} + \boldsymbol{u}^T \boldsymbol{R} \boldsymbol{u} + 2\boldsymbol{x}^T \boldsymbol{N} \boldsymbol{u} \right] \mathrm{d}t. \tag{5.6}$$

The weights $\boldsymbol{R}$ on the inputs $\boldsymbol{u}$ take the form

$$\boldsymbol{R} = \operatorname{diag}\left(\begin{bmatrix} r_{M_g}, & r_\theta \end{bmatrix}\right) \tag{5.7}$$

and for the weights on the states $\boldsymbol{x}$ only four nonzero weights are chosen as

$$\boldsymbol{Q} = \operatorname{diag}\left(\begin{bmatrix} 0, & 0, & 0, & q_\varphi, & 0, & 0, & 0, & 0, & q_{\beta_p}, & q_\Omega, & 0, & q_{x_t} \end{bmatrix}\right). \tag{5.8}$$

The order of the states follows Eq. (3.18) with the flexible tower-DoF last. The weight on the product of states and outputs is selected as

$$N(10, 1) = n_{\Omega, M_g}, \qquad \boldsymbol{N} \in \mathbb{R}^{(2f \times n_u)}. \tag{5.9}$$

It has the purpose of reducing the power fluctuation, which is the product of the tenth state Ω and the first control input M_g. The weighting factors inside $\boldsymbol{R}$, $\boldsymbol{Q}$, and $\boldsymbol{N}$ are shown in Table 5.2. They are mostly normalized with the square of the scaling values of Table 5.1.

Although Table 5.1 is given for only one wind speed ($v_0 = 13\,\text{m/s}$), the response of most states and inputs is highest around rated and therefore these weights are taken as a representative reference for the entire operating range. In order to calculate amplitudes of the derivatives and integrals of the scaling values of Table 5.1, a reference frequency of $\bar{\omega} = 0.63\,\text{rad/s}\,(= 0.1\,\text{Hz})$ was chosen, the frequency of common wave spectra. The 2σ-value of the platform pitch angle β_p, not included in Table 5.1, is $\hat{\beta}_p = 2.2\,\text{deg}$.

Table 5.2: LQR weights.

$\boldsymbol{R}$		$\boldsymbol{Q}$		$\boldsymbol{N}$	
r_{M_g}	$= \frac{0.01}{\hat{M}_g^2}$	q_φ	$= \frac{5.7 \times 10^{-4}}{(\hat{\Omega}/\bar{\omega})^2}$	n_{Ω, M_g}	$= \frac{31.6}{(\hat{\Omega}\hat{M}_g)^2}$
r_θ	$= \frac{1.4 \times 10^{-3}}{\hat{\theta}^2}$	q_Ω	$= \frac{0.027}{\hat{\Omega}^2}$		
		$q_{\hat{\beta}_p}$	$= \frac{0.038}{(\hat{\beta}_p\bar{\omega})^2}$		
		$q_{\hat{x}_t}$	$= \frac{9.8 \times 10^{-6}}{(\hat{x}_t\bar{\omega})^2}$		

The solution of the Riccati equation [166] results in the state feedback matrix $\boldsymbol{K}_{lqr}$ and the feedback law of the LQR reads

$$\boldsymbol{u}(t) = -\boldsymbol{K}_{lqr}\boldsymbol{x}(t). \tag{5.10}$$

An equivalent integral action for the rotor speed signal is included because the rotor azimuth $\varphi = \boldsymbol{x}(4)$ is part of the state vector $\boldsymbol{x}$. Usually, the state signals, as inputs to the LQR, need to be calculated by an observer. In this work, however, the states are assumed to be perfectly measurable in order obtain a benchmark of an optimal control performance.

The LQR results, per definition, in a stable closed-loop system. However, robustness is not guaranteed. This means also that it might de-stabilize a system, which includes higher-order dynamics than the linear model used for its design. Especially the fact that the coupled tower eigenfrequency lies within the 3p range of the DTU 10 MW RWT yields a coupling between the blade structural dynamics and the tower. As this effect is not covered in the simplified model, the LQR cannot be used with the FAST model.

The LQR can nonetheless be taken as a meaningful benchmark, for the simplified model to compare the performance with a theoretically optimal controller against the simple PI-controller. This will be done in Chapter 6.

5.5 Bandwidth Comparison

The reduced control bandwidth of SISO-FOWT-controllers due to the RHPZ has been discussed in Section 2.9. Figure 5.13 shows the complementary sensitivity $T(j\omega)$, or the transfer function from the reference rotor speed Ω_{ref} to the measured rotor speed Ω. The bandwidth is the frequency at which $|T(j\omega)|$ crosses $1/\sqrt{2}$ from above for the first time. Additionally to the SISO controller and the LQR, a PI onshore-controller is included as a reference. Its design follows the pole-placement method (i.e. [15]) with a rigid-body model of the rotor only (no tower fore-aft motion) and a closed-loop eigenfrequency of $\omega_{rot,CL} = 0.3\,\text{rad/s}$ and a damping ratio of $\xi_{rot,CL} = 0.7$.
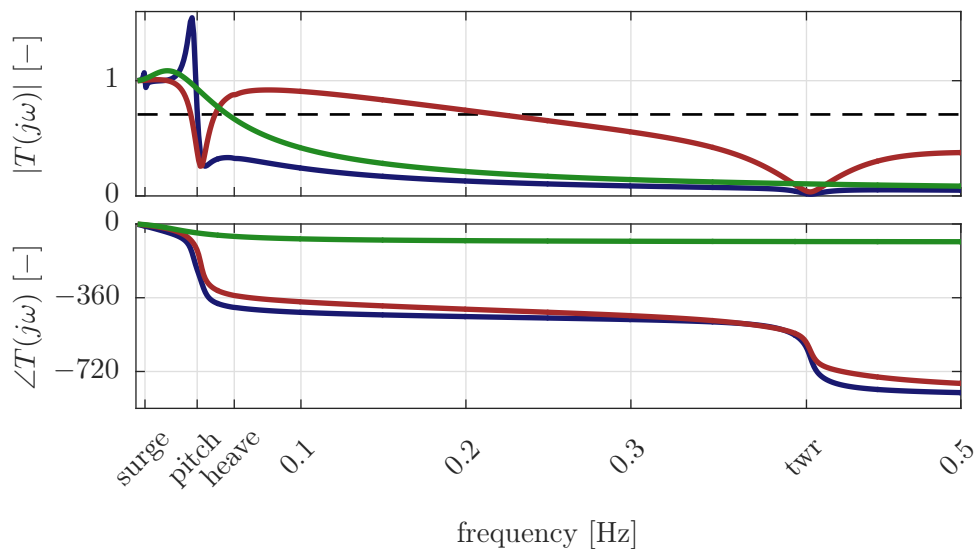
Figure 5.13: Complementary sensitivity functions $T(j\omega)$ (transfer function from Ω_{ref} to Ω) for PI- (blue), LQR (red) and equivalent onshore PI-controller (green) at $v_0 = 13.9\,\text{m/s}$.

For the two FOWT systems, the zero at the platform pitch eigenfrequency is well visible. It is usually this mode which limits the bandwidth for semi-submersibles. The surge-mode (lower frequency than pitch) has a higher damping and the other fore-aft mode, the tower, is of a higher frequency. The onshore system, which does not have the soft fore-aft dynamics, has an about $50\,\%$ larger bandwidth. Even though the LQR is a MIMO controller, feeding back all states, the platform pitch mode is, also here, a limiter of the bandwidth. However, it can be shown that a higher fore-aft damping or a shift of the RHPZ to the left-half plane through more generator torque actuation can increase the bandwidth of the LQR. Such a case was presented in [205], giving a bandwidth comparable to the onshore system through a smaller weight on the generator torque M_g. This would, however, exceed the limits of Table 2.2. The benefits of the LQR are in this work still clearly visible in the results of Chapter 6, especially in Figure 6.12, with an improved attenuation of the resonances and the low-frequency excitations from wind and slow-drift forces.

6 Integrated Optimization

The numerical model of Chapter 3 and the parametric controllers of Chapter 5 will be used in this chapter for an integrated design study. The parametric simulation model, including the pre-processing for the hydrodynamics, allows for a calculation of the response of the coupled system over a design space of floating platform geometries with an individually designed controller. This is seen as a first step towards Systems Engineering of FOWTs, as discussed in Section 2.4. The inherent dynamic properties and the transmission of environmental loads on the structure will be analyzed for the entire design space. The advantages of certain designs over others and the underlying physics causing these differences will be assessed in detail.

The structure of the chapter is such that the optimization methodology, the design space and the parametric design approaches are introduced before various simulation results are shown: Linear system analyses and operational fatigue loads and eventually design indicators for a "cascading" of the obtained knowledge on optimal designs into feasible design criteria. The chapter terminates with a verification of the results obtained from the reduced-order model with the reference model FAST and further studies on the necessary model fidelity.

6.1 Methodology

The integrated optimization of this chapter has the objective of a sensitivity study, or "brute-force optimization" rather than a closed-loop optimization. This has the reason that the focus is not on a distinct optimization algorithm but on the understanding of the FOWT dynamics. The parametric studies allow a clear visualization of the results such as structural loads, but also system properties such as eigenfrequencies, damping ratios and transfer functions. A closed-loop optimization was also done in the course of this thesis for the project LIFES50+, see Deliverable 4.3 [251] and the associated conference paper [237]. The present approach is subject of the publication [252].

Of major importance to the analysis is a reasonable definition of the design space and a clear description of the problem to be answered: As was shown in Chapter 5, the first-order wave loads are of significant magnitude and hardly controllable with the wind turbine actuators. It was also shown that the platform pitch-direction has significant effects on the wind turbine operation as the platform pitch mode is a limiter to the controller bandwidth. Consequently,

the controller is a good means for further tuning of the system response but in the first place the reduction of first-order wave loads, mainly in pitch-direction, is a clear-cut goal of the hull shape optimization. This reduction of the wave loads is known especially for semi-submersibles and is called "wave cancellation", see i.e. [253]. It results from an integration of the pressures of a given wave period over the hull surface. Depending on the wave frequencies, these forces can cancel themselves partially.

The methodology is shown in Figure 6.1. The free variables determine initially the hull shape, which determines further design parameters in the subsequent design steps. The design space is defined for a three-column semi-submersible with heave plates and only two free variables. This allows for a clear visualization of the results and a "full factorial" simulation – an evaluation of all possible parameter combinations. The designs range from a deep-drafted semi-submersible of three slender columns to a design of large breadth, large column radius and shallow draft.

The geometric constraints ensure that the aspect ratio of heave plate radius r_{hp} and column radius r are reasonable regarding the structural design and manufacturing constraints, see Figure 6.2. A simplified structural design methdology is followed for a three-legged steel tripod connecting the concrete columns with the transition piece at the tower-base. With the mass distribution, the hydrostatic calculations can be made, keeping a pre-determined hydrostatic restoring in pitch-direction. This condition is fulfilled by adjusting the draft t, which is the variable that completes the definition of the hull shape. The panel code calculates the hydrodynamic coefficients, the first-order wave force-RAO as well as the mean drift coefficients. The force spectra include also Morison drag excitation forces and slowly-varying drift forces using Newman's approximation, as introduced in Section 3.5. For a realistic representation of the viscous drag at the heave plates, the heave plate drag is parameterized as function of KC using the values confirmed by the experiments of Chapter 4. The linear response spectra are calculated for an initial estimation of KC, and then iterated until convergence, as described in Section 3.5.4. This iteration includes the controller, as shown in the lower part of Figure 6.1: It is re-designed for each updated hydrodynamic damping.

Thus, the two controllers of Chapter 5 are parameterized and automatically adjusted for every new platform design with its load case-dependent hydrodynamic drag. This is straightforward using the optimal LQR, which determines the state-feedback matrix based on a linearized model at the operating point. The simpler PI-controller, however, is usually designed using pole-placement or loop-shaping techniques. This is an iterative procedure and is normally not automated. The stability-based criterion, defined in Section 5.3, however, is the basis for a robust, automated controller design algorithm. The objective of including a simple SISO controller, next to the optimal MIMO controller, is to ensure that the controller design procedure is "fair" for all designs, without biasing the results towards certain types.
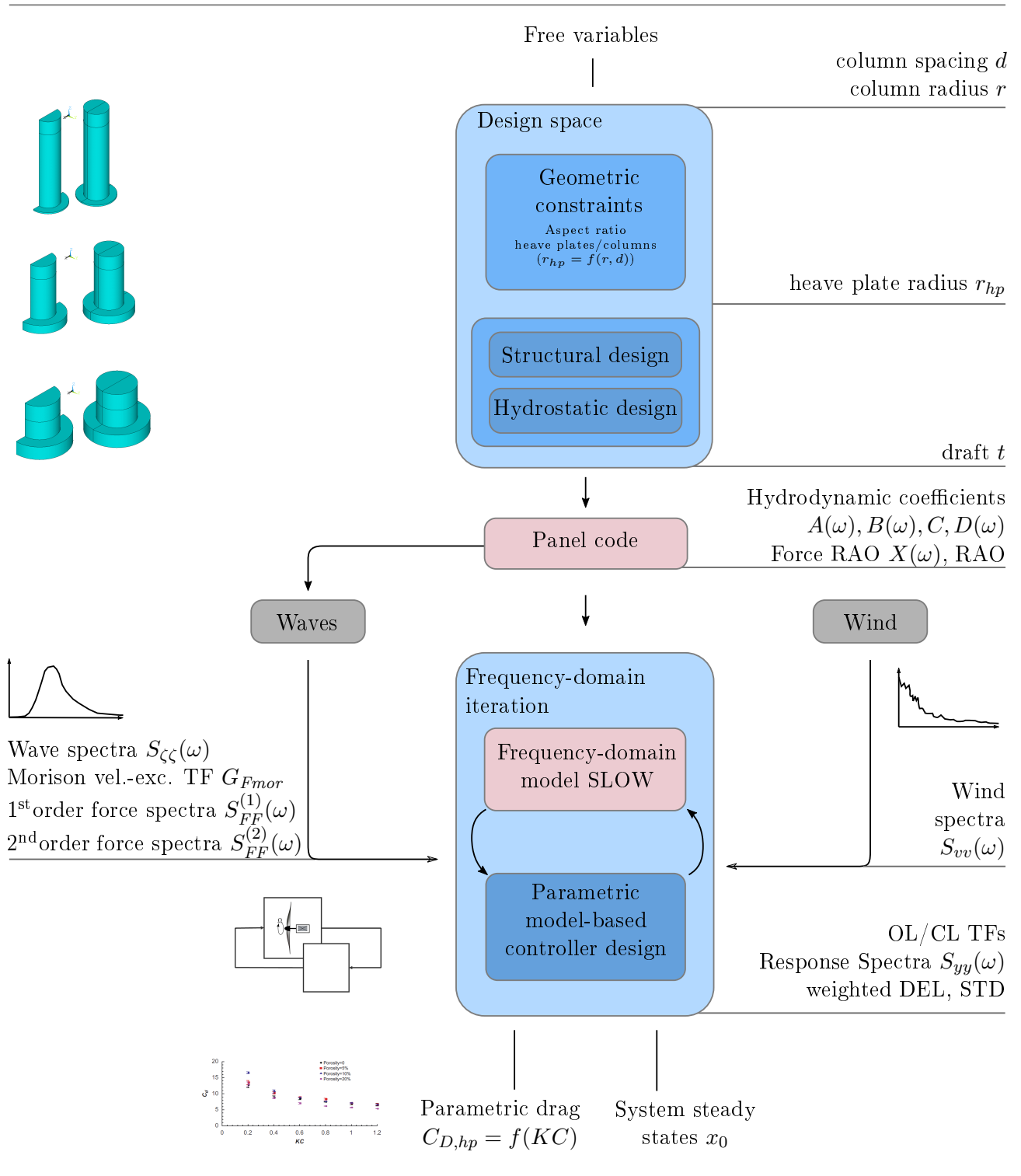
Figure 6.1: Parametric FOWT system design and brute-force optimization scheme.

6.2 Design Space

The selected hull shape parameters include the column spacing from the platform centerline d, the column radius r, the heave plate height h_{hp}, the ratio of heave plate radius to column radius $\hat{r}_{hp} = r_{hp}/r$ and the draft t, as shown in Figure 6.2.

As mentioned, it is a target to have a narrow and reasonable design space with little dimensions in order to produce realistic results, which can be well interpreted. If a large range is used, linear or nonlinear constraint functions are necessary in order to discard unfeasible designs in terms of manufacturing and installation. Also, the distribution of the major system eigenfrequencies has to be verified in order to avoid a resonance due to excitation from the rotor or the waves. Such constraints are thus not known at the beginning of an optimization loop but only at its end.

For this work, it was decided to define upper and lower bounds for each of the free variables such that the design space is Cartesian, meaning that the range of every variable does not depend on the values of the others. This can be easily understood by looking at the range of heave plate radii r_{hp}. For small column spacings d and large column radii r, a design with the largest heave plate radius ratio might not be feasible.
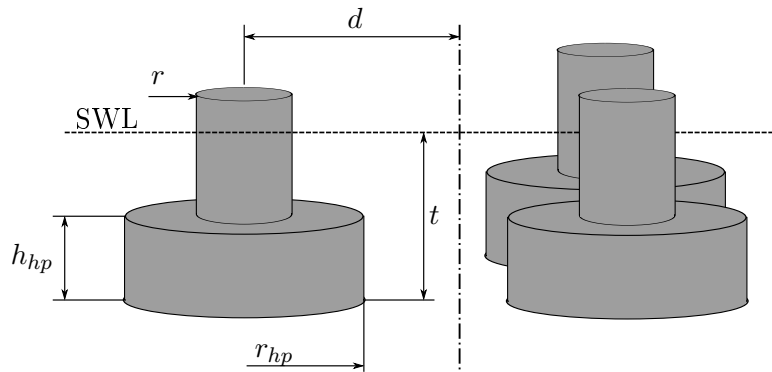
Figure 6.2: Free variables for parametric hull shape design.

The column radius r is defined dependent on the maximum possible column radius r_{max} and is therefore a function of the column spacing d

$$r(d) = 0.52\, r_{max}(d) = 0.52\, d\, \sin(60°) = 0.52\, d\frac{\sqrt{3}}{2}. \tag{6.1}$$

Table 6.1 lists the free variables and the dependent variables. The only free variables are the column spacing d and the heave plate height h_{hp}. The ratio of the heave plate-to-column radius $\hat{r}_{hp}$ is kept constant with $\hat{r}_{hp} = 1.3$. This ensures that the aspect ratio is reasonable and feasible from a manufacturing standpoint. The draft t, which is a result of the hydrostatic constraints as mentioned above, is not an actual constraint of the design space but an upper limit of 80 m was considered in the a-priori definition of the bounds of the free variables.

Table 6.1: FOWT hull shape design parameters.

Free variables	Dependent variables
• Column spacing d	• Column radius r
• Heave plate height h_{hp}	• Heave plate radius r_{hp}
	• Draft t
	• Steel tripod strut width & sheet thickness
	• Ballast mass
	• Platform mass distribution
	• Mooring line fairleads position
	• Wind turbine controller

The overall dimensions of the 2D design space are shown in Figure 6.3 with a column spacing range $d = 15.0(1.0)24.0$ m and a heave plate height range $h_{hp} = 1.0(3.5)8.0$ m. Thus, the designs range from slender deep-drafted platforms to large-breadth shallow-drafted ones. Larger column spacings than the ones considered are expected to result in excessive bending stresses in the tripod structure.

The variable heave plate height adds another degree of freedom of altering the vertical Froude-Krylov forcing on the columns and consequently facilitate the wave cancellation effect. The icons on top of Figure 6.3 show that the column radius is largest for the lowest draft. The cost increases generally for increasing column radii r but decreases again for the ones of shallow draft with a large contribution of buoyancy to the hydrostatic restoring. The assumptions for the material cost estimation will be given in Section 6.3, it is roughly proportional to the submerged volume.

The three designs shown in Figure 6.3 will be selected in a number of the upcoming analyses and indicated by "deep draft", "medium draft", and "low draft", see Table 6.2. The detailed set of parameters of these three platforms, necessary to build a FAST model, can be be found in Table A.3.

Table 6.2: Three selected example designs for detailed analyses.

Parameter	Column spacing d [m]	Column radius r [m]	Heave plate radius r_{hp} [m]	Heave plate height h_{hp} [m]	Draft t [m]
Deep draft	15.0	6.76	10.9	4.5	78.48
Medium draft	19.0	8.56	13.8	4.5	49.95
Low draft	24.0	10.81	17.4	4.5	21.94
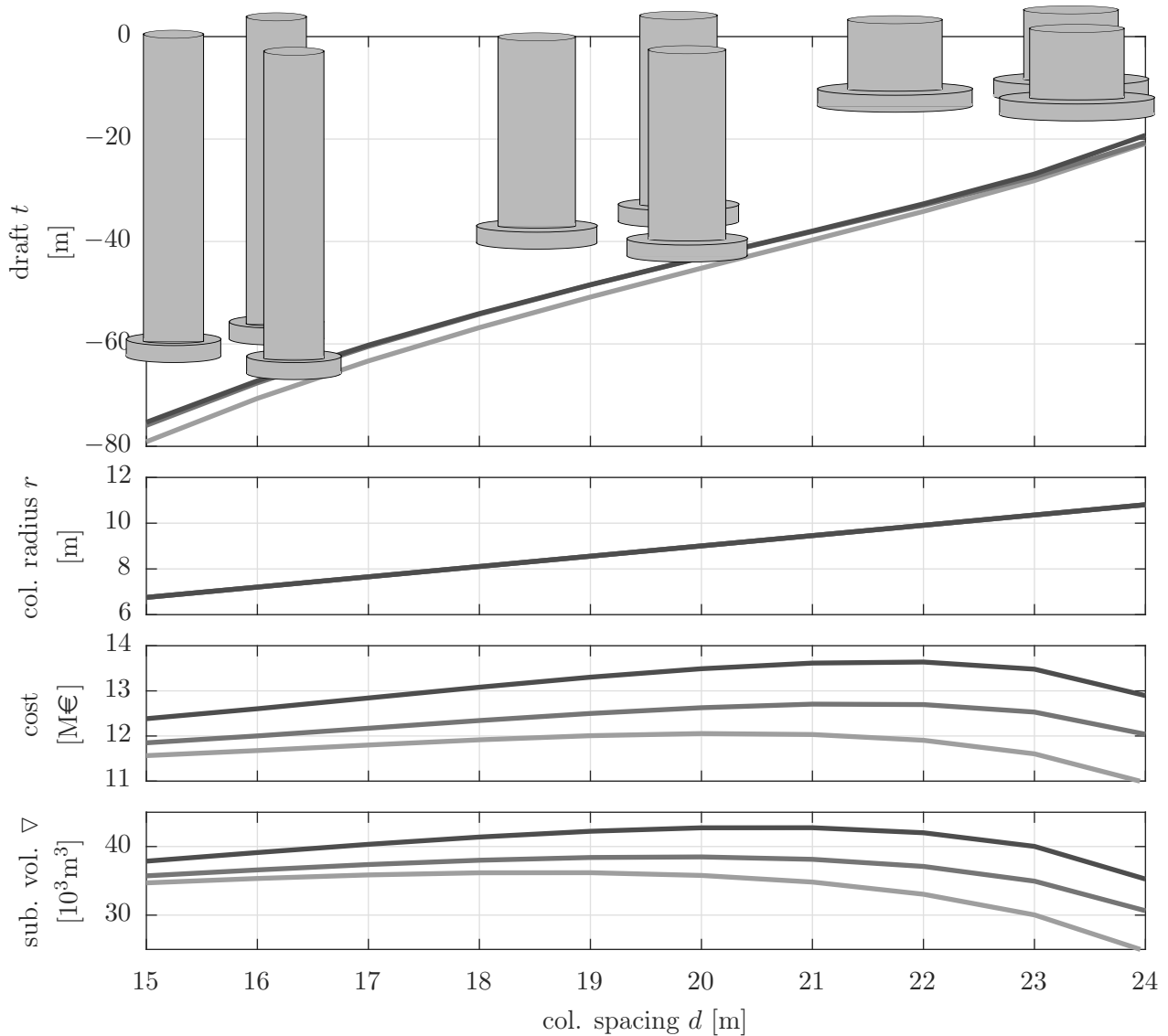
Figure 6.3: Design space with two dimensions: column spacing from centerline and heave plate height. Heave plate height $h_{hp} = [1.0, 4.5, 8.0]\,\mathrm{m}$ (increasing darkness).

6.3 Parametric Design

The dimensioning of the platform is the subject of this section: Various parameterized routines, highlighted as blue boxes in Figure 6.1, determine the component parameters, listed also as dependent parameters in Table 6.1. The first part addresses the structural design assumptions for the concrete platform and the steel tripod interfacing the columns with the tower-base. It follows the hydrostatic calculation yielding the platform draft, based on the small-angle stability requirements. The procedure to obtain the panel code coefficients together with the Morison drag coefficients and the parametric controller properties is introduced thereafter. The section ends with a verification of the assumptions through a comparison of various public designs.

6.3.1 Structural design

Approximate but realistic assumptions for the structural design make it possible to obtain the mass distribution for the overall system simulations. The entire floater is assumed to be rigid but the dimensions are selected reasonably to ensure structural integrity. Further design steps are expected to detail the structural design without substantially changing the values obtained from the presented approximations. The material properties for the following calculations are listed in Table 6.3.

Table 6.3: Structural design assumptions.

Parameter	Unit	Value
Concrete column wall thickness	[m]	0.6
Heave plate upper and lower lid thickness	[m]	0.4
Reinforced concrete average density	[kg/m^3]	2750.0
Steel density	[kg/m^3]	7750.0
Ballast density	[kg/m^3]	2500.0
Processed steel cost	[€/t]	4500
Processed concrete cost	[€/t]	399

Steel tripod
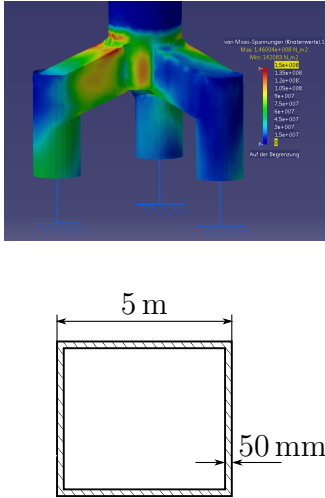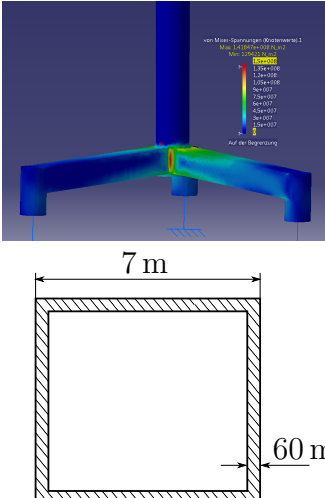
The steel tripod design is based on an approximation from public data of the Bard Tripile, supporting a 5 MW wind turbine. For a parameterization of the dimensions of the steel legs (shell thickness, width, height), FE analyses were performed covering the design space of the distance between the columns. The calculations include a static thrust load at the tower-top of 4.605 kN, as given in [42, p. 61].

The critical failure mode is assumed to be the notch stress at the interface between the tower and the legs. The dimensions of the legs (struts) are selected such that the maximum notch stress at the interface of the legs with the tower is of comparable magnitude as the one resulting from the same calculation with the Bard tripile. The dimensions of the tripod for the minimum and the maximum column spacing are shown in Table 6.4. The Bard tripile data is no longer available online but the details on the upscaling can be found in [233]. The structural design of the TripleSpar concept, which started in 2015, was continued in the project INNWIND.EU with the detailed design calculations of the substructure presented in [233] and [254].

Concrete columns and heave plates

The concrete columns are assumed to be built with pre-stressed concrete following the example of the KIC-AFOSP spar design [202]. The wall thickness is constant for all of the hull shape

Table 6.4: Parametric design of the TripleSpar steel tripod (FE calculations by Florian Amann).

	Minimum column spacing	Maximum column spacing
	5 m, 50 mm	7 m, 60 mm
Column spacing (distance to centerline)	10.0 m	35.0 m
Strut width & height	5.0 m	7.0 m
Steel wall thickness	50 mm	60 mm
Maximum stress	146.0 N/mm²	142.0 N/mm²
Tripod mass	447 t	1716 t

variations, see Table 6.3. The heave plates are also made out of reinforced concrete with the same material properties as the columns. The columns reach down to the keel with heave plates consisting of concrete rings attached to the columns at their lower end. This assumption is rather conservative and accounts for further compartmentation and reinforcements of the detailed design phase. The design of the baseline TripleSpar concept of Section 2.10 has heave plates out of sheet metal and is therefore not directly comparable. The column wall thickness of the TripleSpar is 0.4 m.

Mooring lines

The mooring line characteristics can be found in [58]. They were designed by myself together with Michael Borg of DTU with two upwind lines and one downwind line with fairleads above SWL, at $z_{frlds} = 8.7$ m and a distance from the tower centerline of $d_{frlds} = 26$ m. The same mooring system was used for the scaled experiments of Chapter 4. The parameters of the mooring lines can be found in Appendix A.

Tower

The tower design is not varied in the optimization study but the parameters of the reference TripleSpar are used, see Table A.1. Regarding the placement of resonances with respect to the rotational frequencies, the present method assumes a rather small design space, which is defined based on experience and preceding spreadsheet calculations. Therefore, the scatter of platform eigenfrequencies is limited and consequently no adaptation of the tower stiffness to the substructure stiffness is necessary. As mentioned in Section 3.8, the tower design can generally be a bottleneck for wind turbines as large as 10 MW, due to tower excitation from the 3p-frequency. The shown results for the present designs in Figures 6.19–6.23 indicate that the response of the tower at the eigenfrequency of $f_{d,twr} = 0.416$ Hz is at the analyzed wind speeds, below and above rated, rather small compared to the response to waves. Therefore, the tower design is expected not to alter the findings of the present platform optimization study.

Cost estimation

In different research projects cost models for FOWTs were presented with a good overview and summary in [255]. In the present work, a lumped cost for the processed material, meaning the sum of the material, manufacturing and assembly costs, is assumed. The values are according to LIFES50+ Deliverable 4.3 [251] and can be found in Table 6.3. It needs to be mentioned that these values are rough indications, which can vary due to concrete shrinkage (concrete prices are, as opposed to steel, usually not given per mass but per volume) and also due to price variations over time.

6.3.2 Hydrostatic design

The hydrostatic properties determine mainly the FOWT stability and the system eigenfrequencies together with the mass distribution, see also Section 2.5.3. If no active ballast system is included, the hydrostatic restoring in pitch-direction determines, together with the vertical distance between the fairleads and the hub, the inclination of the rotor to the vertical plane and therefore the power losses, which deteriorate the efficiency by $\eta_{cos} \propto \cos^3(\beta_{rotor})$. The nonlinear intact stability criteria are relevant for certification and might challenge designs with a soft pitch stiffness C_{55}. Another constraint for the maximum (dynamic) pitch angle is the wind turbine gearbox and other components requiring an upright operational position.

For the present study, a hydrostatic restoring in pitch of $C_{55} = 2.255 \times 10^9$ Nm/rad, resulting in a steady state platform pitch angle at rated wind speed (disregarding again the mooring line restoring) of $\beta_{p,rated} = 5.0$ deg, is set as constraint for all geometries of the design space. Depending on the free variables column spacing d and heave plate height h_{hp}, the draft is determined such that this constraint is met. This is realized through a root-finding algorithm

including the structural design and the hydrostatic functions. The steady state pitch angle reduces to about $\beta_{p,rated} \approx 3.0\,\text{deg}$ with the mooring lines.

6.3.3 Hydrodynamic coefficients

The parametric calculation of the hydrodynamic coefficients is performed with Ansys Aqwa with a generation of the parameterized hull geometries by Ansys APDL. The added mass is then interpolated at the respective eigenfrequencies and transformed to the platform CM, according to Section 3.5.3. The radiation damping $\boldsymbol{B}(\omega)$ is neglected in the analysis of this chapter based on the discussion of Section 3.5.1 and the findings of the sensitivity study of Section 6.4.6. The mean drift force coefficient $\boldsymbol{D}(\omega)$ is calculated for all designs and used for Newman's approximation on the difference-frequency excitation, see Figure 6.1.

The column drag coefficient is kept constant for all designs and sea-states. It has been selected as $C_D = 0.4$ because this value was also identified in the scaled experiments of Chapter 4. The selected value is rather conservative, as guidelines suggest minimum values of $C_D = 0.65$, see [256, p. 117]. For the heave plates, the drag coefficient is iterated based on the drag coefficients given in [230], which were parameterized as a function of KC, see Section 4.4. In order to reduce the problem complexity, the vertical drag force is applied only at the lower surface of the heave plates and the same cross-sectional area is used for the calculation of the drag force. The procedure was introduced in Section 3.5, see Figure 3.18.

With the increase of the heave plate radius r, the characteristics of the hydrodynamic forces change. The wave regime graph, Figure 2.4, shows the values of the Keulegan-Carpenter number KC and the diffraction parameter ka for the deep-draft (slender columns) and the low-draft (big columns) design. It can be seen that diffraction becomes more important for smaller sea-states and the drag component of the forcing increases with decreasing column diameters. The vertical drag due to heave plates, on the other side, is not covered by Figure 2.4. This vertical drag becomes more important for increasing heave plate diameters, see Section 3.5. This is a nonlinear effect (quadratic drag), which yields simulation errors when the linearized model is used, see Section 6.4.5.

6.3.4 Controller design

For each of the concepts of the design space (Figure 6.3), a SISO PI-controller and a MIMO LQ-controller is designed. The controllers have the architecture of the ones described in Chapter 5. The advantage of the MIMO controller is that it feeds back more signals and uses the generator torque as additional actuator to the blade pitch angle. It has therefore a higher potential to improve rotor speed tracking and disturbance rejection. As all states of the simulation model are fed back, disregarding the question of how to measure or observe them in reality,

this controller is seen as a means to obtain an upper bound of the possible performance of an optimal controller. The straightforward model-based design makes this controller perfectly suited for this integrated design study.

However, it was found that the advantages of specific gains on e.g. platform pitch β_p depend significantly on the platform shape. Therefore, the comparison of the simple SISO controller offers a means to evaluate the "fairness" of the LQR towards different platform shapes. The SISO controller ensures the same stability for all shapes and does not feed back any states other than the two rotor rotation states. A special challenge with the LQR design is the fact that damping the wave response by feeding back system states is not possible and might even increase the response, see [183] and discussions in Chapter 5. This can result in a reasonable response to wave for one design but in a amplification for another design. The main reason for this is that the system response depends significantly on the characteristics of the force-RAO $\boldsymbol{X}(\omega)$, which is not part of the system matrix $\boldsymbol{A}$ but the input matrix $\boldsymbol{B}$ and therefore not taken into account by the LQR design routine. For this reason, the determination of the matrices $\boldsymbol{Q}$, $\boldsymbol{R}$ and $\boldsymbol{N}$ was made considering all platforms of the design space resulting in the values of Table 5.2.

The new parameterization of the SISO PI-controller was introduced in Section 5.3. The criterion of the maximum sensitivity $1/M_s$ and the rotor time constant τ_{rot}, introduced in Chapter 5, allow for an automation. As opposed to the MIMO controller, the PI-controllers are designed based on the models, linearized at all operational wind speeds above rated. This yields the gain scheduling function of Figure 6.4, including the switching criterion between the stability objective for wind speeds above rated and the one of a constant τ_{rot}, see Section 5.3. The LQR can be designed for each operating point independently and makes the iterative determination of the viscous drag, introduced in Section 3.5.4, easier.

Figure 6.4 shows the feedback gains for the three example designs of the design space for the LQR and PI-controllers over above-rated wind speeds. Generally, the gains of the deep-drafted platform differ from the medium- and low-draft platform. A reason might be the different platform pitch-mode frequency and damping as will be shown in Figure 6.7. The two upper rows show the feedback gains of the generator speed, not as state feedback gains of φ and Ω but as proportional gain k_p and integrator time constant T_i of an equivalent PI-controller, see Figure 5.5. It can be seen that the proportional gains k_p of the LQR are significantly larger than those of the PI-controller. This means that the additional damping of the platform and tower, through the tower and platform velocity feedback, allows for a more aggressively tuned rotor speed control loop. The same approach was selected by [183], who maintained the onshore gains for the FOWT and added additional feedback loops for platform stabilization. The question of stability, however, is then not resolved, as is also the case for the LQR, which might have limited stability margins. The integrator time constant T_i does not change over the wind speeds for the PI-controller, see Section 5, but decreases for the LQR.
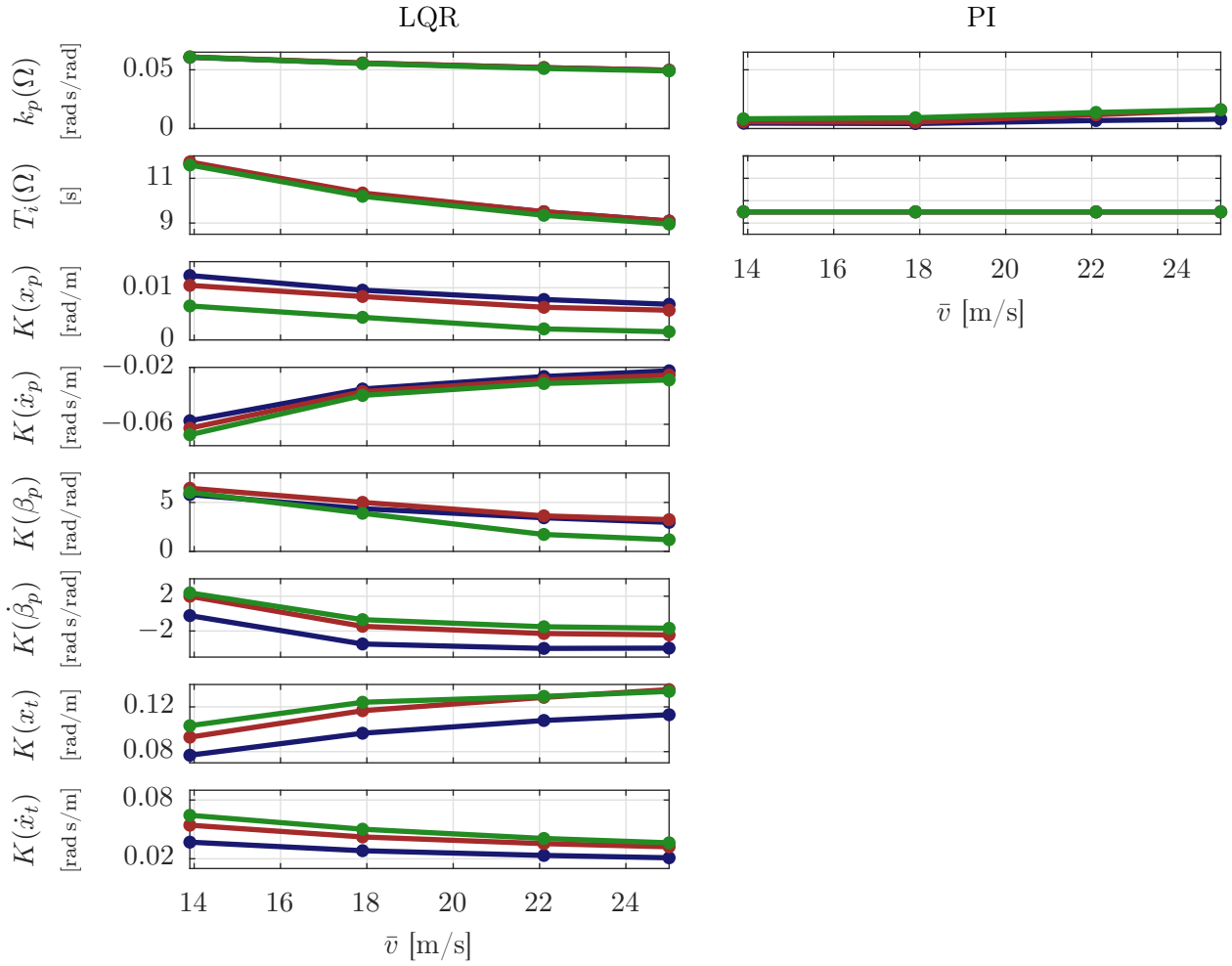
Figure 6.4: Parametric controllers (LQR and PI) for different feedback loops over above-rated wind speed bins. Deep draft (blue), medium draft (red) and low draft (green). First two rows concern rotor speed control: Here, not the state feedback gains are shown but the proportional gain k_p on high-speed shaft speed and the integrator time constant T_i (Eq. (5.5)). For clarity calculated for model without blade pitch actuator, giving 10 states instead of 12 in Eq. (3.18), z_p-loop not shown.

Remarkable is that the surge velocity ($\dot{x}_p$) and pitch velocity ($\dot{\beta}_p$)-feedback is negative. As the system eigenfrequencies do not vary much with the wind speed the changing LQR gains are an adaptation to different system damping ratios due to the aerodynamic operating points, see Section 3.4. The bandwidth for the low-draft and deep-draft platform with the two controllers is shown in Figure 6.5, as in Figure 5.13 for the TripleSpar. The complementary sensitivity function $T(j\omega)$ is shown for above-rated wind speeds. It can be seen that the PI bandwidth is also for these platforms limited by the platform pitch eigenfrequency at $f_{d,\beta_p} \approx 0.03\,\mathrm{Hz}$. Although $|T(j\omega)|$ increases again for $f > f_{d,\beta_p}$, the phase loss and the magnitude drop indicate that the RHPZ is not fully mitigated through the LQR. However, the low-draft platform seems to be better damped than the deep-draft design such that the LQR yields here, for higher wind speeds, an increased bandwidth, comparable to the onshore controller of Figure 5.13.
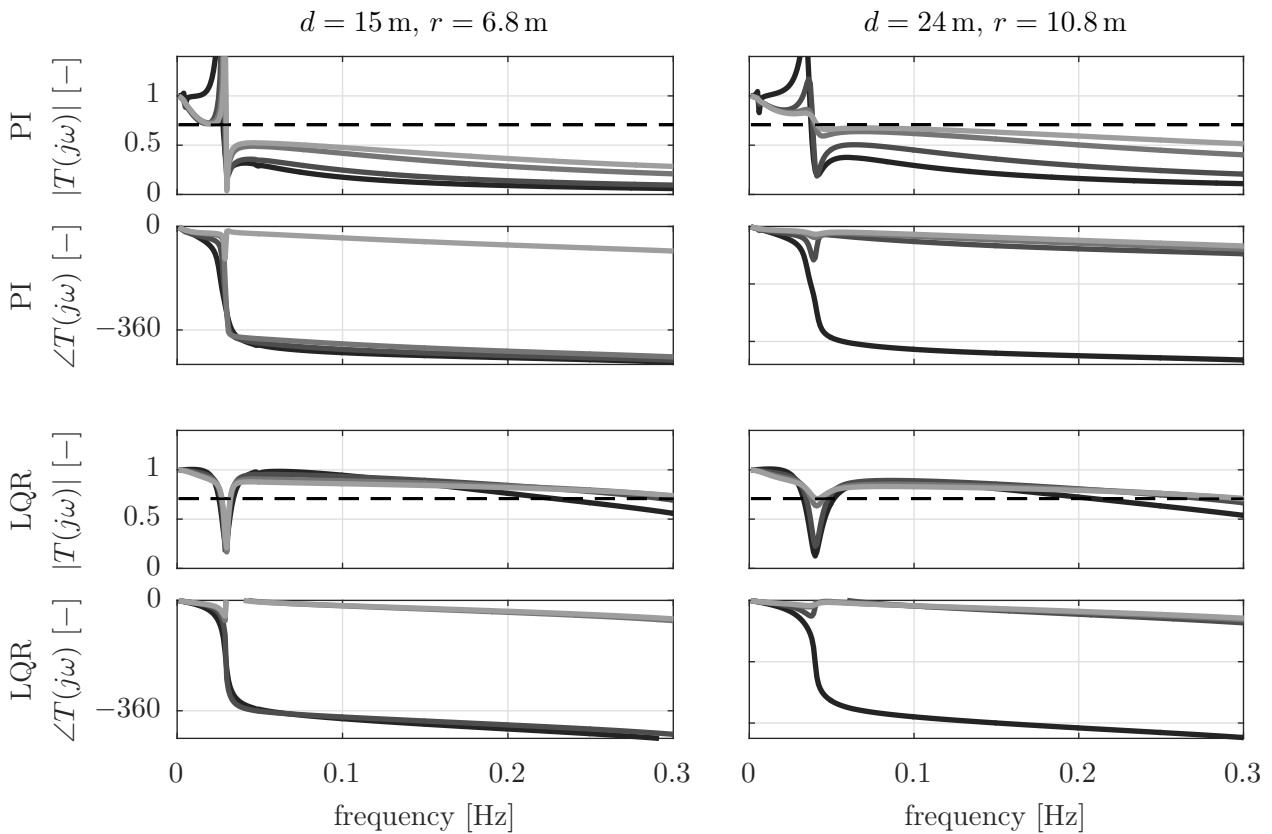
Figure 6.5: Complementary sensitivity $T(j\omega)$ magnitude and phase for PI-controller (top) and LQR (bottom) for deep draft (left) and low draft (right) designs over above-rated wind speeds. Lighter line color for higher wind speeds $v_0 = [13.9, 17.9, 22.1, 25]$ m/s. First intersection of $T(j\omega)$ with dashed line indicates bandwidth.

6.3.5 Design verification

Especially for the concrete columns and heave plates, no structural design calculations have been performed but the numbers are based on the project KIC-AFOSP on which I worked in the course of this thesis. Therefore, the structural design assumptions are verified through a comparison with other public FOWT designs. The platform mass distribution is taken as indicator, represented by the platform center of mass $z_{cm,ptfm}$ and the overall FOWT center of mass $z_{cm,fowt}$, including the wind turbine (without mooring lines).

For semi-submersibles and spars, an effective design has a mass concentration at the lowest possible point, close to the keel, in order to maximize the restoring moment from the gravitational forces. Then the center-of-mass-ratio z_{cm}/t approaches a value of 1. Such high values of z_{cm}/t are not possible in reality, due to the plating, stiffeners and girders, compartmentation and secondary steel, the elements resulting from the detailed structural design, which is not included in the present dimensioning. These elements sum up to a significant amount of mass at higher levels, elevating the center of mass and decreasing the hydrostatic stability.

It is therefore more conservative for the present study to take structural design assumptions yielding smaller ratios of z_{cm}/t instead of assuming a design with unrealistically thin walls and therefore high values of z_{cm}/t.

Figure 6.6 shows the ratios z_{cm}/t over the design space of Figure 6.3. For comparison, the public concepts of the OC3-Hywind steel spar [111], the OC4-DeepCwind steel semi-submersible [112], the OlavOlsen OO-Star concrete semi-submersible [257, 258] and the SWE-TripleSpar concrete semi-submersible design of Section 2.10 are listed in Table 6.5. Comparing the OC3-spar with the OlavOlsen semi-submersible, it can be seen that the spar has larger ratios z_{cm}/t than the semi-submersible. This is because a spar is purely ballast-stabilized, whereas the OlavOlsen concept has a very shallow draft, with a significant restoring from waterplane area. For such concepts, a low center of mass is not as much a design-driver as for spars. The ratios over the design space of the present study, shown in Figure 6.6, are mostly in a range $z_{cm,ptfm}/t = 0.5 \ldots 0.7$ and $z_{cm,fowt}/t = 0.3 \ldots 0.6$, which is comparable with the semi-submersibles of Table 6.5. Therefore the structural design assumptions seem to be reasonably conservative.

The last column of Table 6.5 shows the theoretic platform pitch angle $\beta_{p,rated}$ for the respective rated thrust force of the different wind turbines at hub height ($F_{aero} = 1.65 \, \text{MN}$ for DTU 10 MW RWT and $F_{aero} = 0.738 \, \text{MN}$ for NREL5 MW RWT), disregarding the restoring effect of the mooring lines (applying a pure torque ($F_{aero} \cdot h_{hub}$) to the center of flotation). It can be seen that rather low equilibrium pitch angles are common, due to the beforementioned power losses from the static inclination. Thus, the selected steady pitch angle of $\beta_{p,rated} = 5.0 \, \text{deg}$ seems reasonable.

Table 6.5: Selected design properties of different FOWT concepts.

Concept	Rating [MW]	Draft t [m]	$z_{cm,ptfm}/t$ [−]	$z_{cm,fowt}/t$ [−]	Equiv. pitch $\beta_{p,rated}$ [deg]
OC3-Hywind spar	5.0	120.0	0.75	0.65	3.25
OC4-DeepCwind semi	5.0	20.0	0.67	0.49	3.9
OlavOlsen OO-Star semi	10.0	22.0	0.69	0.36	7.9
SWE-TripleSpar semi	10.0	54.5	0.66	0.57	4.1
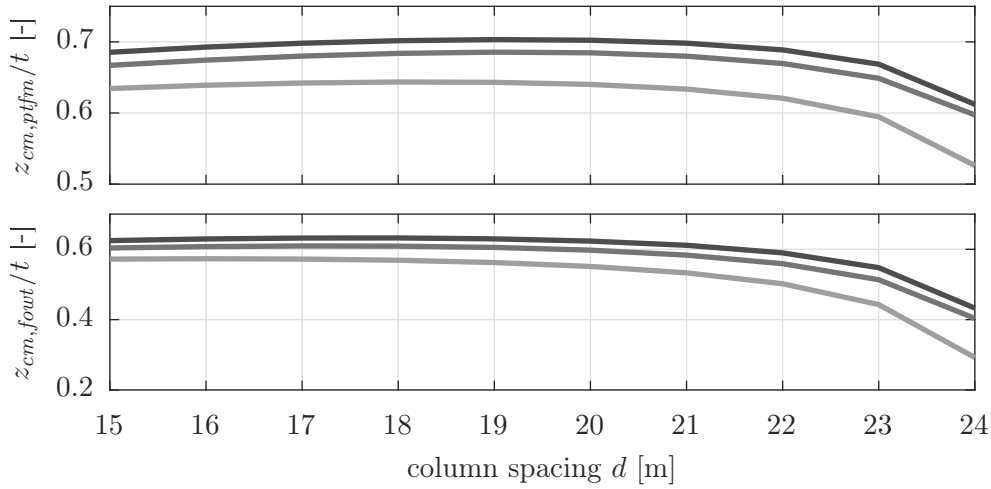
Figure 6.6: Ratio of platform center of mass-to-draft and ratio of overall FOWT center of mass-to-draft over design space. Heave plate height $h_{hp} = [1.0, 4.5, 8.0]\,\mathrm{m}$ (increasing darkness).

6.4 Results

In this section, the results of full operational DLCs over the design space are shown together with linear system analyses revealing the physical reasons for advantages or disadvantages of different platform geometries reflected in the DLC results. Subsequently, the entire design space is simulated with the simplified models (linear and nonlinear) and the full FAST model and different modeling options for comparisons and an assessment of the model fidelity over the design space.

6.4.1 Linear system analysis of open loop system

Figure 6.7 shows the results of the eigenanalysis over the design space using the simplified linearized model in the open loop configuration. Compared to a simpler eigenanalysis with a panel code (assuming a single rigid body, linearized mooring stiffnesses and 1$^{\text{st}}$-order hydrodynamics), the following features are included in SLOW:

- linearized aerodynamics of entire rotor, rotor-DoF
- flexible tower (1$^{\text{st}}$ mode)
- mooring stiffness linearized about operating point
- linearized Morison drag

Therefore, the eigenmodes of the platform can be expected to be more accurate than the ones predicted by the panel code, especially due to the inclusion of the hydrodynamic viscous drag, the tower and aerodynamics. The controller dynamics are not included here but they are subject of the next section. The two columns of Figure 6.7 contain the minimum and maximum heave plate thickness $h_{hp} = [1.0, 8.0]\,\mathrm{m}$ while the column spacing d is on the x-axis of each graph. The two top rows show the surge and pitch eigenfrequencies and the lower rows
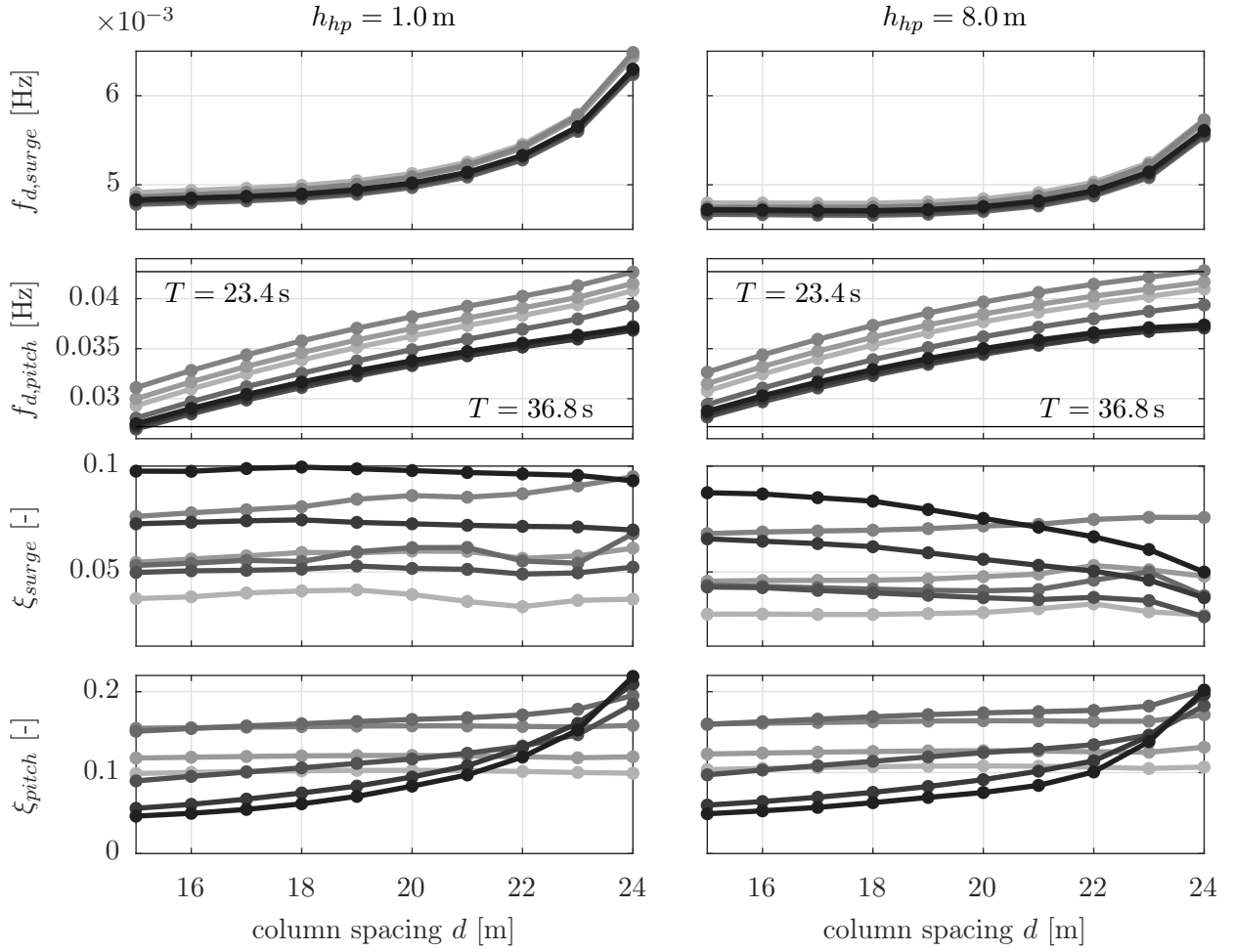
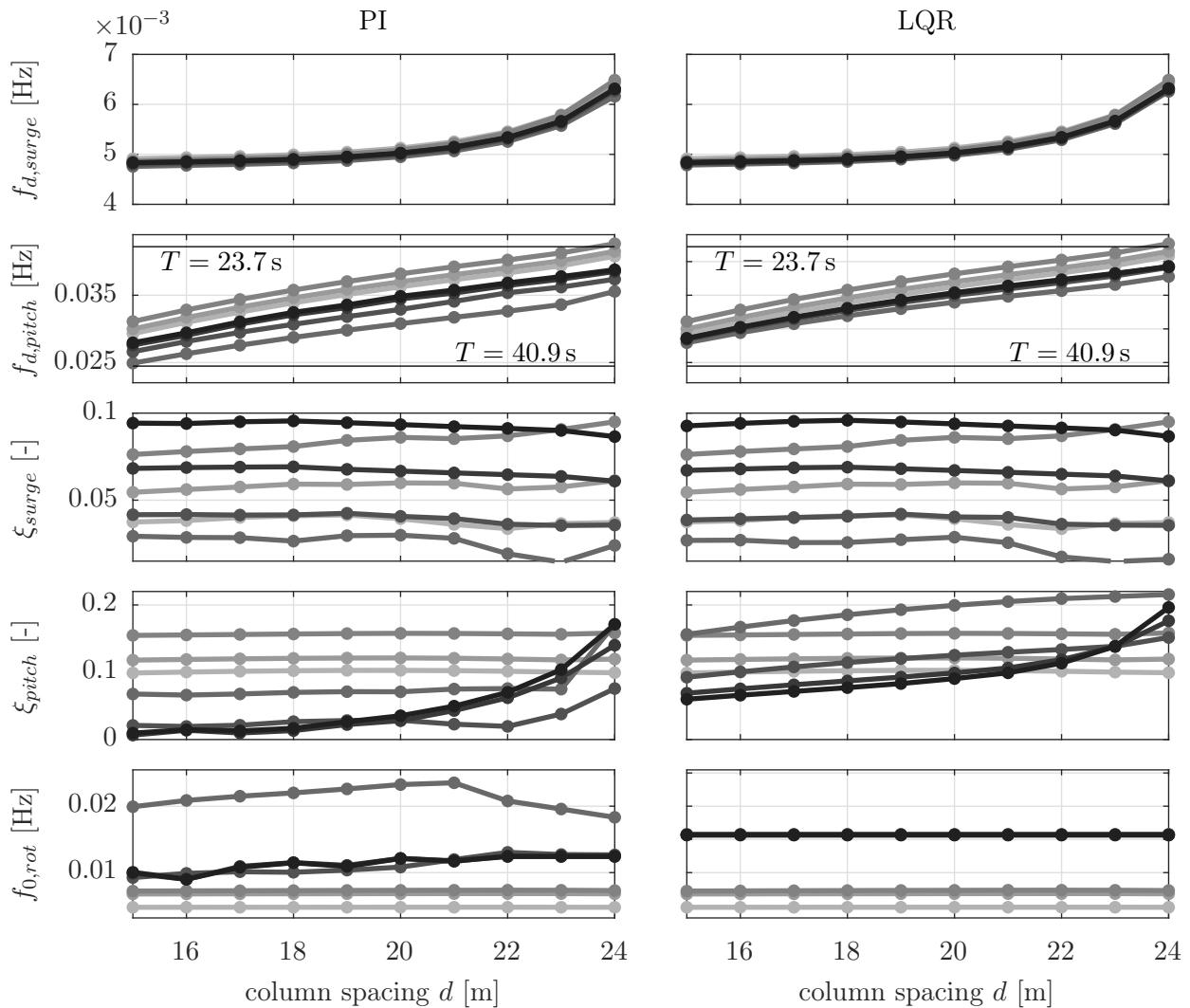**Figure 6.7:** Eigenfrequency for OL with iterated hydrodynamic and aerodynamic damping. $h_{hp} = 1.0\,\mathrm{m}$ (left) and $h_{hp} = 8.0\,\mathrm{m}$ (right) (darker colors for higher wind speeds $v_0 = [5, 7.1, 10.3, 13.9, 17.9, 22.1, 25]\,\mathrm{m/s}$).

show the global modal damping ratios for the surge and pitch mode. It can be seen that the damped eigenfrequencies f_d in surge and pitch increase for increasing column spacings (which corresponds to decreasing drafts, see Figure 6.3). As the hydrostatic stiffness C_{55} is constant for all platforms, the increase results mainly from the different added mass and structural mass/inertia, which is mainly due to the varying draft.

The damping ratio ξ_{surge} increases approximately with the severity of the environmental conditions (see Table 2.1). However, also the aerodynamics seem to have an influence as the damping ratio has a minimum at $\bar{v}_{hub} = 17.9\,\mathrm{m/s}$ above rated. The damping ratios ξ_{pitch}, on the other hand, tend to decrease for higher sea states. This effect can be attributed to the KC-dependent description of the heave plate drag coefficient, see Section 6.3.3. As KC is proportional to the velocity and the heave plate drag decreases for increasing KC (see [230]), the resulting overall damping ratio decreases. Additionally, the increasing heave plate diameter for larger column spacings d yields a disproportionately large damping for the low-draft shapes.

6.4.2 Linear system analysis of closed loop system

The eigenanalysis in the closed-loop for the two controllers of Chapter 5 is shown in Figure 6.8. Comparing the values to the open loop case of Figure 6.7, it can be seen that the damped surge eigenfrequencies are comparable but tend to higher frequencies due to the introduced controller dynamics.

Figure 6.8: Eigenfrequency for CL with iterated hydrodynamic and aerodynamic damping. PI-controller (left) and LQR-controller (right) (darker colors for higher wind speeds $v_0 = [5, 7.1, 10.3, 13.9, 17.9, 22.1, 25]$ m/s).

In pitch-direction, it can be observed that the platform eigenfrequency increases for above-rated wind speeds $\bar{v}_{hub} = [13.9, 17.9, 22.1, 25]$ m/s. The same effect was visible for the experiments, Chapter 4, and can be seen even more clearly in Figure 6.13. The damping ratio ξ also changes with closing the control loop: While in surge-direction the controller affects most the below-rated damping ratios, there is a clear change of damping in pitch-direction for the above-rated wind speeds (darker colors). There is less damping in pitch for the PI-controller,

which is due to the negative damping problem, discussed in Section 2.9. The LQR, on the other hand, re-introduces damping with the state-feedback loop for $\bar{v}_{hub} > v_{rated}$. With this controller-induced additional system damping, it is possible to increase the magnitude of the state feedback gains of the rotor (i.e. making it more "aggressive"), see Section 5.4.

In Figure 6.8, also the undamped closed-loop rotor eigenfrequency is shown. It was discussed in Chapter 5 that the rotor eigenfrequency is usually overdamped for FOWTs above rated. Therefore, the undamped eigenfrequency f_0 is equal to $1/\tau$, where τ is the time constant. The time constant τ_{rot} is kept constant for the PI-controller at wind speeds where stability is not the driving design criterion, see Section 5.3. It can be seen that the weights $\boldsymbol{Q}$, $\boldsymbol{R}$ and $\boldsymbol{N}$, defined independently of the wind speed, result in a constant rotor eigenfrequency for all platforms. With the PI-controller developed here, τ_{rot} is only constant for the higher wind speeds, as opposed to the "de-tuning" procedure discussed in Section 2.9, which designs for a constant τ_{rot} over all wind speeds.

6.4.3 Operational design load cases

In this section, the response to the operational IEC DLC 1.2 for all operational wind speeds with a normal wind speed and normal sea state model as given in Table 2.1 is presented. These are the main results of the optimization study, which will be analyzed, interpreted and explained in the following sections. The statistics for DLC 1.2, weighted over the turbine lifetime, are shown in Figure 6.9. The results are weighted with the Weibull PDF of Figure 2.6. The values for the DEL[1] and the STD are normalized with the corresponding values for the onshore DTU 10 MW RWT with the same wind fields. For onshore turbines, the significant loading from waves is not present and especially the harmonic loads of the 1p and 3p-frequencies are fatigue drivers next to the low-frequency turbulence. It can be seen that the weighted DEL of the tower-base bending moment M_{yt} has a minimum at the low-draft shape. The same holds for the weighted STD of the platform pitch angle β_p and the rotor speed Ω. The blade pitch activity (θ) shows little variation over the design space. These results are quite significant as the tower-base bending damage can be reduced by more than 30 % with a favorable design. The resulting tower-base bending moment fatigue is then not significantly larger than for the equivalent onshore turbine. Although the low-draft platform has a large column spacing of $d = 24$ m and a column radius of $r = 10.8$ m with heave plates of $r_{hp} = 17.4$ m (Table 6.2), the estimated material cost is comparable to the one of the deep-draft shape, see Figure 6.3.

The comparison between the controllers shows that the LQR is able to improve the response in terms of tower-base loads but also in terms of rotor speed variation. However, this advanced controller gives qualitatively the same optimum as the PI-controller.

---

[1] The tower-base bending moment equivalent DEL(M_{yt}) is calculated for a lifetime of 20 years with a Wöhler exponent of $m = 4$, Eq. (2.31).
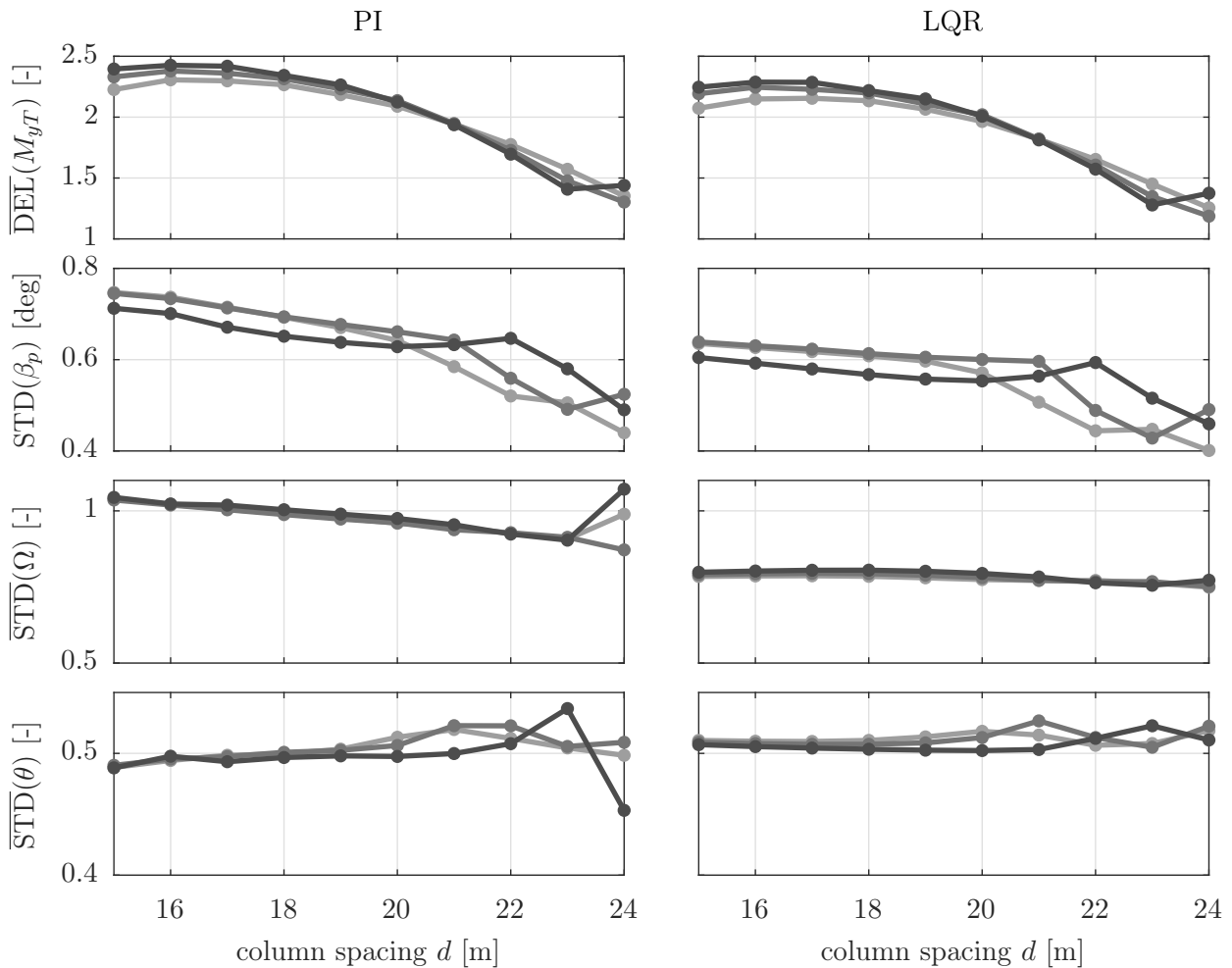
Figure 6.9: Response statistics of operational DLC1.2, Tab 2.1, weighted for all wind speeds with distribution of Figure 2.6. $\overline{\text{DEL}}/\overline{\text{STD}}$ are normalized results with corresponding SLOW onshore simulations of DTU 10 MW RWT with the same wind fields. Left PI-controller, right LQR-controller. Heave plate height $h_{hp} = [1.0, 4.5, 8.0]$ m (increasing darkness).

One finding from this is that the low-frequency platform pitch response to wind and difference-frequency excitations is likely not the reason for the improved performance of the low-draft shape as these resonances are damped by the LQR.

A comparison of the response spectra among the deep draft and the low draft platforms with the PI-controller is shown in Figure 6.10. Since the magnitudes are significantly different, a logarithmic y-axis is selected. It can be seen that the low-draft shape gives a larger difference-frequency and wind-induced response in surge. Other than this, the low-draft platform has clearly smaller responses at the pitch eigenfrequency of $f_{d,pitch} \approx 0.04$ Hz but, more importantly, at the wave frequencies of 0.1 Hz ($\bar{v}_{hub} = 17.9$ m/s, left) and 0.08 Hz ($\bar{v}_{hub} = 25$ m/s, right). This is visible for the platform motion response β_p but even more for the tower bending (x_t, M_{yt}), the rotor speed Ω and the electrical power P.
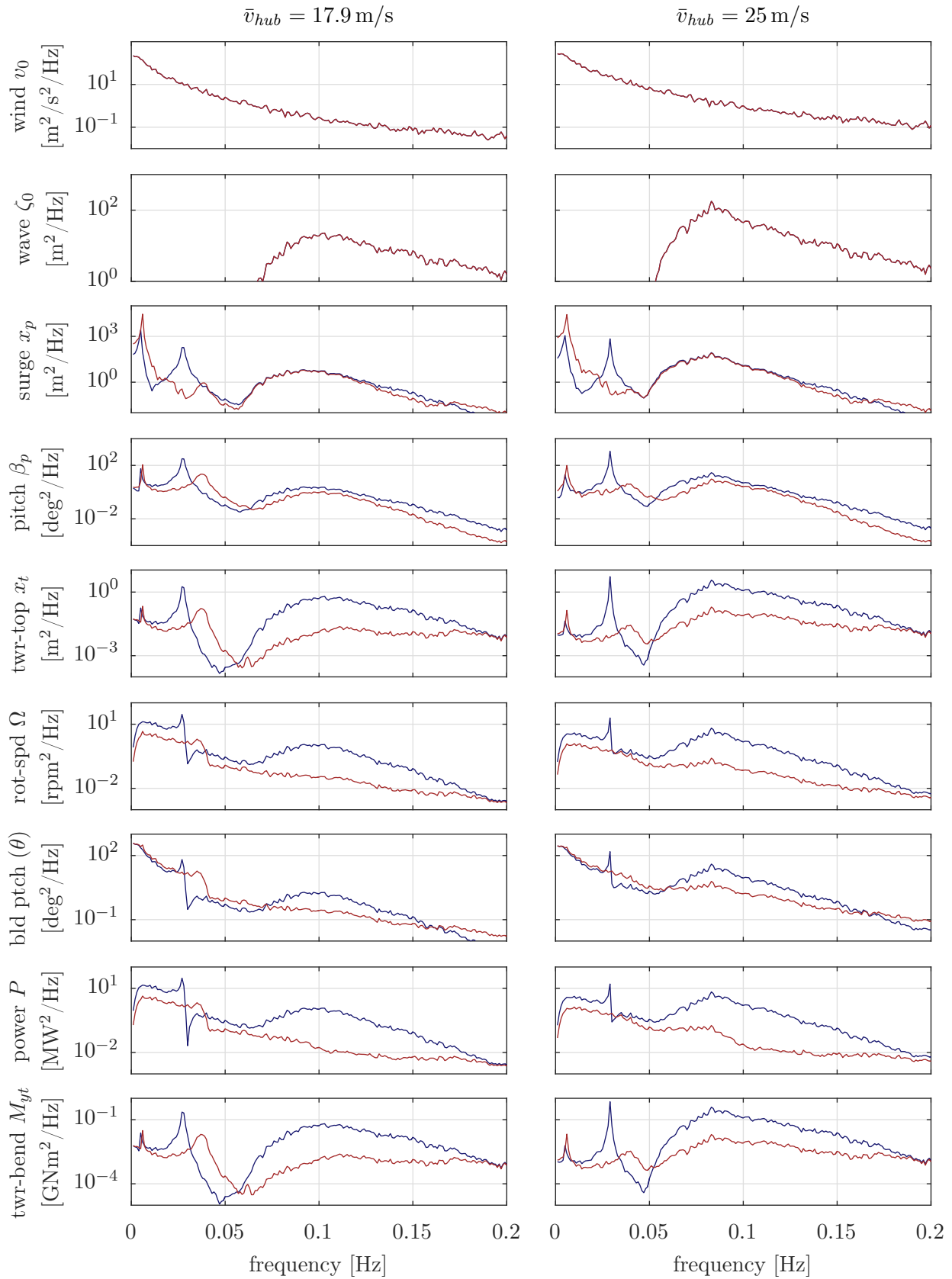
Figure 6.10: Comparison of deep-draft (spacing $d = 15\,\text{m}$, blue) and low-draft (spacing $d = 24\,\text{m}$, red) platforms for $\bar{v}_{hub} = 17.9\,\text{m/s}$ (left) and $\bar{v}_{hub} = 25.0\,\text{m/s}$ (right) with PI-controller.

The validity of the controllers is shown in Figure 6.11 in terms of the criteria defined in Table 2.2. The maximum amplitude is here estimated from the frequency-domain response spectra for a time of $T = 3600\,\mathrm{s}$ with the Rayleigh distribution for the response amplitudes as described in Section 2.7.3. It can be seen that keeping the limits for a FOWT is challenging. This is mainly due to the reduced bandwidth of the controller. The overshoot of the rotor speed can be significantly reduced by feeding back additional signals and by using the generator torque as an actuator above rated. Then, however, it is important to design the controller such that the torque limits are not exceeded. Here, the LQR exceeds the rated torque up to $17\,\%$ for short time periods. The power overshoot can be reduced by the LQR such that the limit of $15\,\%$ is exceeded only for the highest waves.
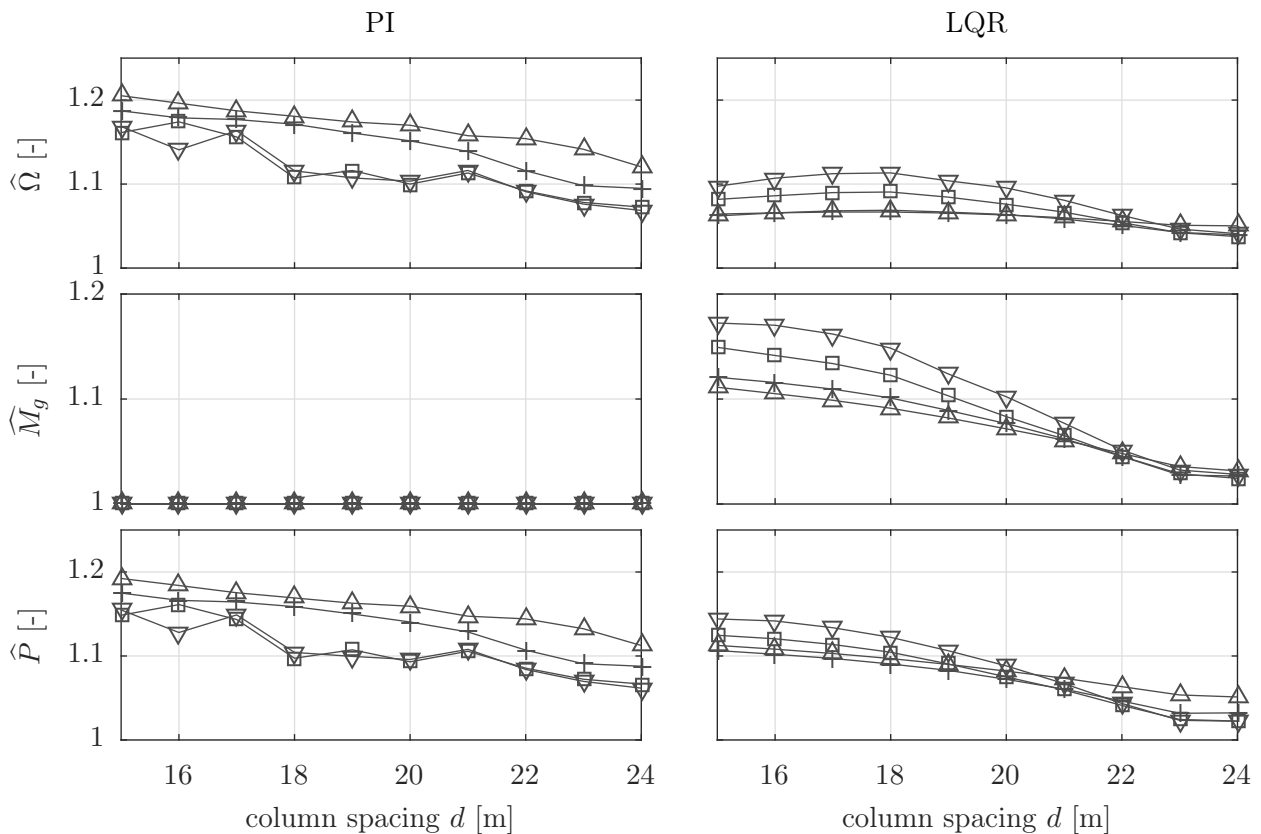
Figure 6.11: Rotor signals percentage of maximum over rated values (overshoot) for operational DLC1.2, Tab 2.1 for above rated wind speeds $v = [13.9\,(\triangle),\ 17.9\,(+),\ 22.1\,(\square),\ 25.0\,(\triangledown)]\,\mathrm{m/s}$ for different column spacings d, $h_{hp} = 4.5\,\mathrm{m}$. Left PI-controller, right LQR.

Comparing the PI-controller and the LQR, it can be seen that the largest amplitudes result from wind speeds around rated, while it is the case for the cut-out wind speed for the LQR. This is because the instability issue of FOWTs is critical at rated wind speeds as discussed in Section 5.3, while the instability is mitigated through the LQR such that the high sea-states drive the response amplitudes.

A direct comparison between the PI-controller and the LQR can be seen in Figures 6.12 and B.1 for the deep-draft and low-draft platforms. For both platforms, the LQR does not damp the low-frequency surge response. It does, however, damp the pitch response to wind and difference-frequency forces. The rotor speed response to the wind is significantly reduced by the LQR and a small reduction of the wave response is visible. This can be attributed to the aid of the generator torque actuation, which is not present for the PI-controller. The question to be answered by the next sections is why the low-draft platforms show an improved performance compared to the ones of deeper draft and which indicators help to predict such favorable overall dynamics.

6.4.4 Indicators for the goodness of a design

In LIFES50+ Deliverable 7.4 [3], the variety of different existing standards and design guidelines for FOWTs was analyzed, compared and a new design process was developed. In the first design stage, as defined in [3, p. 13], it is crucial to arrive quickly and efficiently at a reasonable design, which is able to meet the specifications.

In this section, the RAO will be analyzed in order to find out how well the amplifications of the wave height on the platform DoFs reflects the results obtained with the simplified FOWT model shown in the previous section. Thereafter, two additional indicators are presented with an improved significance.

Response amplitude operator and wave cancellation

It is common to use the RAO as a means to quickly estimate the principle dynamics of a floating body. The RAO is the transfer function from the wave height at the CF to the six DoFs of the floating body, as introduced in Section 2.5.3. With the developed linear FOWT model it is possible to derive the transfer functions also to other states. On the other hand, the transfer functions to the same DoFs, as calculated by the panel code, can be calculated with the developed coupled model, resulting in a refined result due to the additional physics included.

In Figure 6.13, the RAO in pitch-direction is shown for the three different geometries. It is compared to the equivalent RAO, calculated with the linearized SLOW model, including the linearized Morison drag, the flexible tower and aerodynamics. Additional to this, the closed-loop RAO is shown for the SISO PI-controller and the LQR. It can be observed that the Morison drag damps significantly the pitch-resonance. The PI-controller reduces the eigenfrequency, which was also found from the experiments in Chapter 4. The LQR can introduce additional damping for the pitch motion, which confirms the results of Figure 6.9. In the wave frequency range, above the pitch-mode, the amplification is equal for all configurations, which confirms the difficulty of damping the wave response through position or velocity feedback control.
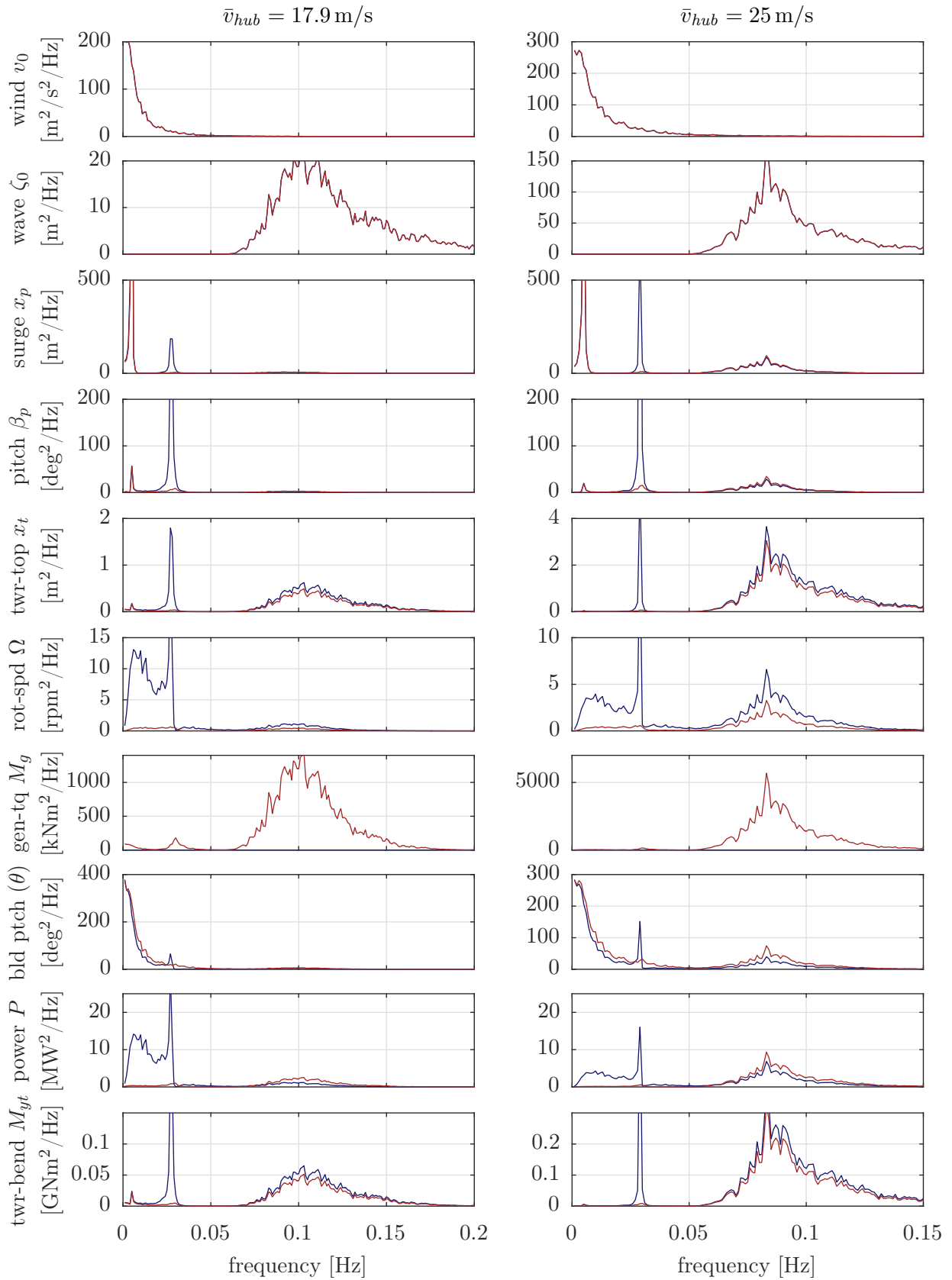
Figure 6.12: Comparison of PI-controller (blue) and LQR (red) for $\bar{v}_{hub} = 17.9\,\mathrm{m/s}$ (left) and $\bar{v}_{hub} = 25.0\,\mathrm{m/s}$ (right) for deep-draft $d = 15\,\mathrm{m}$.
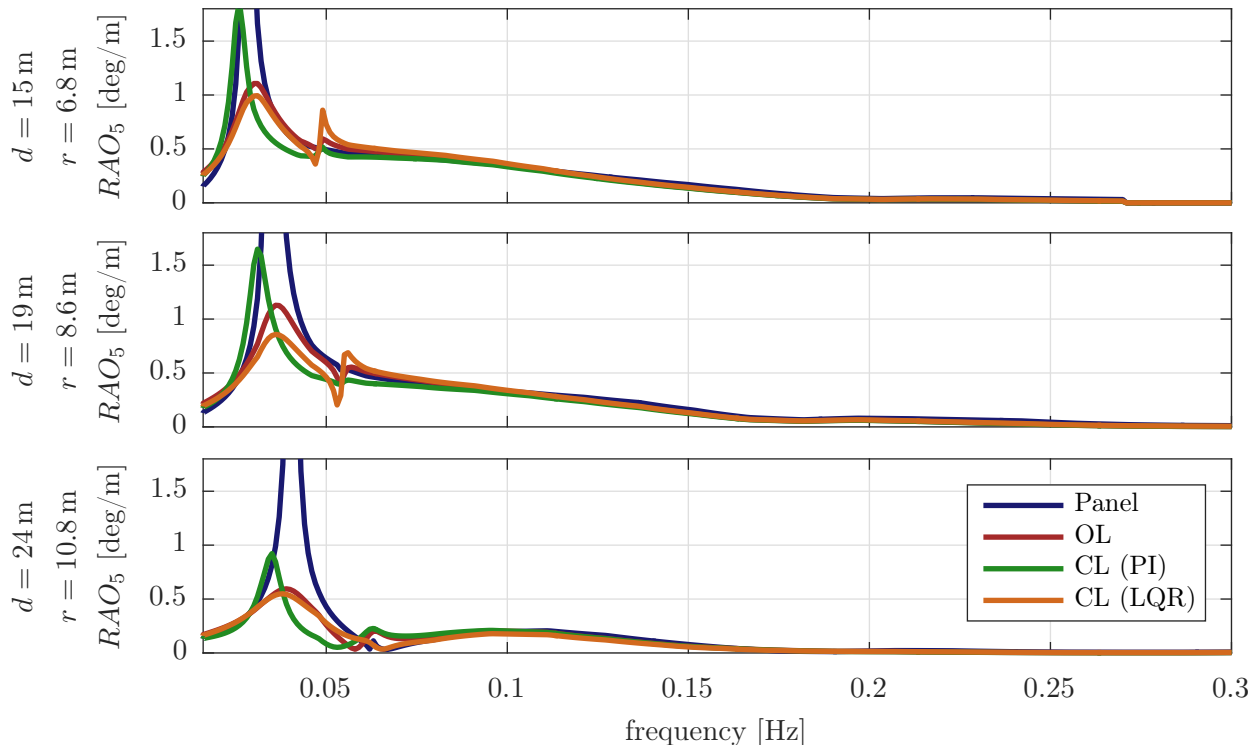
Figure 6.13: RAO, transfer function from wave height ζ_0 to platform pitch angle β_p for three different designs. Calculated with panel code (Ansys Aqwa) for a rigid body and mooring system stiffness and with linearized FOWT model of Chapter 3 including flexible tower, aerodynamic drag and viscous Morison drag without controller (OL) and PI and LQR-controller of Chapter 5.

Figure 6.14 shows the RAO in surge and pitch-direction for different column spacings d. It can be seen that there is a clear difference of the amplification of wave loads in the typical wave frequency range around 0.1 Hz, especially in pitch-direction. This is due to the above-mentioned wave cancellation effect, which happens because the wave excitation forces on a submerged hull cancel themselves if summed for a certain DoF (e.g. platform pitch). This effect depends on the ratio of column spacing to the wave length but also on the hull shape geometry, especially heave plates, which introduce vertical Froude-Krylov forces and confirms the previous results of DLC 1.2.

For this reason it is also useful to look at the force-RAO, the transfer function from wave height to the six forces on the body. If it does not show a large amplification for the wave frequency range it is likely that the forces cancel themselves, e.g. in the pitch-direction. This effect can be observed in Figure 6.15 for the platform of $d = 23$ m (second darkest), whereas the platform of largest column spacing $d = 24$ m (darkest) amplifies the waves around 0.1 Hz, as it happens for the other shapes of deeper draft. This is surprising because the best dynamics, predicted by the simplified FOWT model of Figure 6.9, are those of the platform with lowest draft ($d = 24$ m).
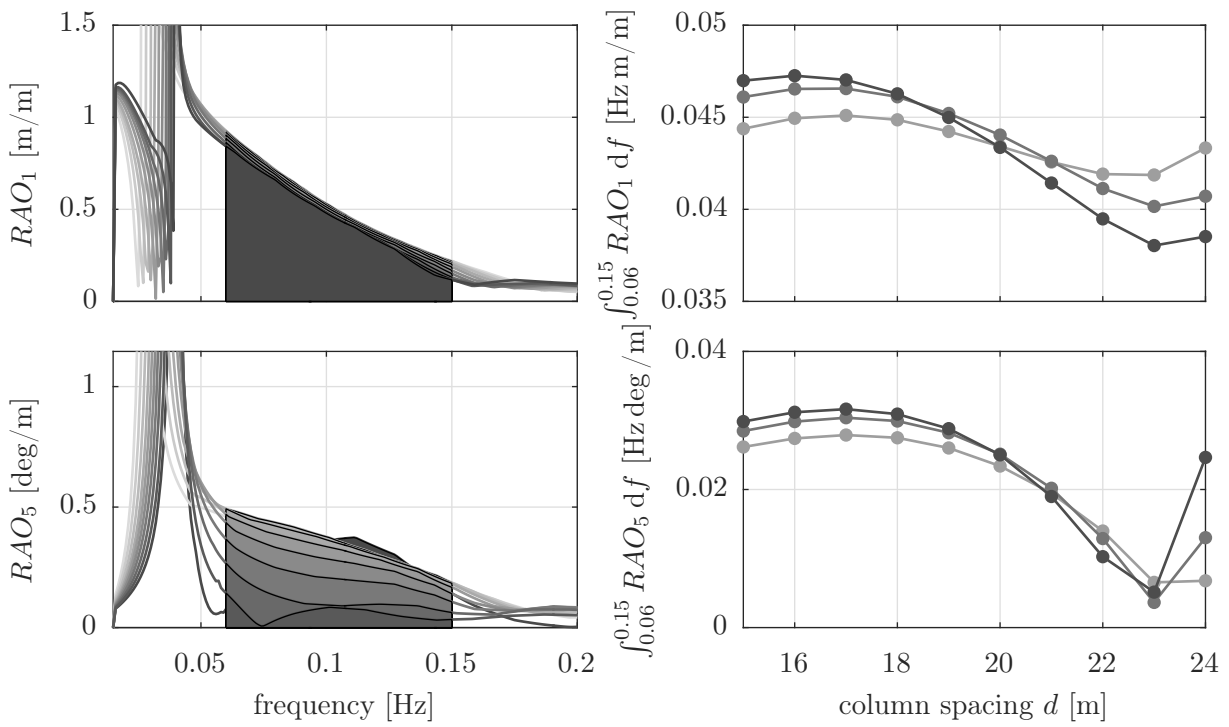
Figure 6.14: RAO in surge and pitch-directions (left) for $d = [15(1)24]$ m (increasing darkness). Integral over $f = 0.06 \ldots 0.15$ Hz, shown on the left is visualized for all designs over column spacing d for all heave plate heights $h_{hp} = [1.0, 4.5, 8.0]$ m (increasing darkness).
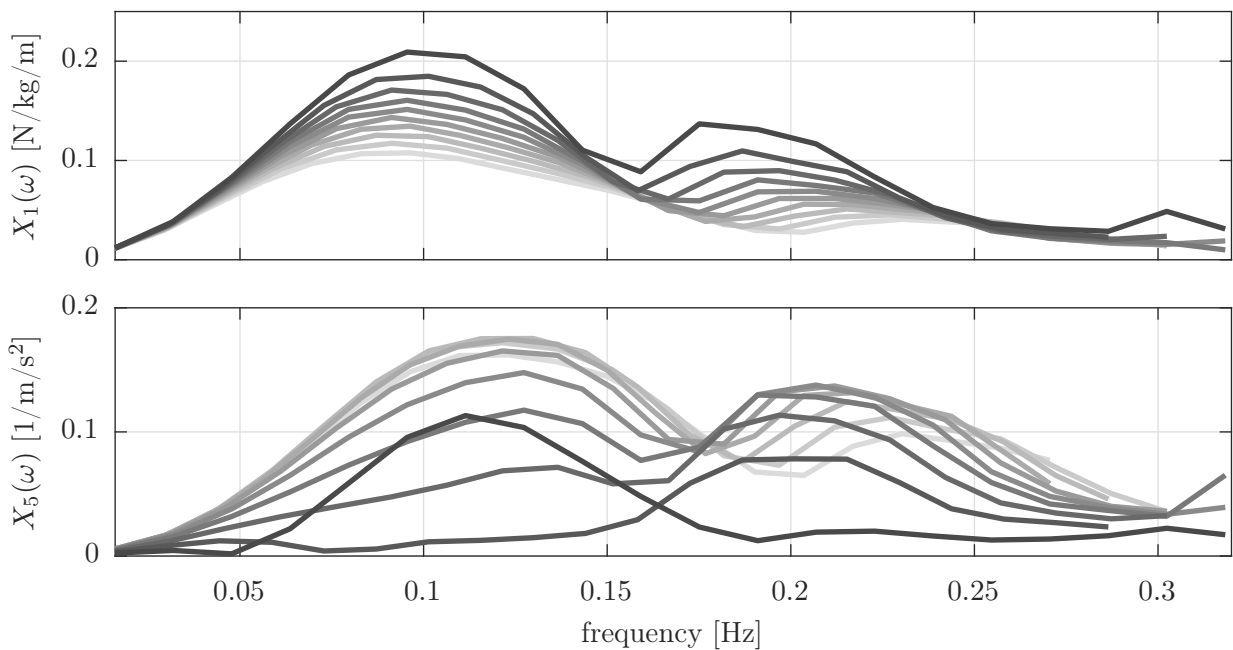
Figure 6.15: Wave excitation force vector $X(\omega)$ in surge-direction (top) and pitch-direction (bottom) normalized by the respective FOWT mass matrix entry including zero-frequency added mass for column spacings $d = [15(1)24]$ m (increasing darkness) and $h_{hp} = 4.5$ m.

As an indicator of goodness of the design, the RAO is integrated over $f = 0.06\dots0.15\,\mathrm{Hz}$ in Figure 6.14. The results agree well with those of the simplified model, Figure 6.9, as the integral decreases for larger spacings d. However, the RAO of Figure 6.14 increases again significantly for the largest spacing of $d = 24\,\mathrm{m}$ in the same way as the force-RAO of Figure 6.15. The reason why the largest spacing ($d = 24\,\mathrm{m}$) is underestimated by the RAO, as opposed to the DLC results, is discussed in the next section.

Harmonic response

A key to understanding the underlying effect for the disturbance rejection of the low-draft platform ($d = 24\,\mathrm{m}$) is the harmonic response to wind and wave loads. Figure 6.16 shows lines representing the FOWT centerline. The horizontal displacement and orientation of each line stands for the amplitude of the body response at all elevations along the centerline to sinusoidal wind (top) and wave excitations (bottom) of different frequencies. The analysis is made with the reduced order linearized model with first-order hydrodynamics in closed-loop with the PI-controller at $\bar{v}_{hub} = 13.9\,\mathrm{m/s}$. It is noted that the controller does not significantly affect the harmonic response, especially for the wave response, which cannot be damped through control. The solid horizontal lines indicate the overall CM of the FOWT and the dashed line indicates the center of buoyancy. For ships, the instantaneous center of roll motions is usually the metacenter [218, p. 62]. Here, the instantaneous center of rotation in pitch is the vertical location on the platform with zero amplitude. The response to harmonic wind excitations shows a center of rotation equal to the CM. The same behavior is generally visible for all platforms.

Looking at the response to waves in the lower part of Figure 6.16 shows that the instantaneous center of rotation is now below the CM for the deep drafted platforms. A remarkable effect can be seen for the platform of the lowest draft ($d = 24\,\mathrm{m}$): Here, the instantaneous center of rotation is at higher locations, close to the hub. This is remarkable as it means that the hub does not move horizontally due to wave excitations. Consequently, the wind turbine power production is only minimally affected by the waves for this geometry. The harmonic response is such that the motion in surge is positive, when it is negative in pitch. Thus, both DoFs are out-of-phase, as opposed to the platforms of deeper drafts, which have an in-phase response of surge and pitch to waves. For a better understanding of the behavior of the designs in-between, the medium and low-draft is shown in Appendix B.3.

The result of Figure 6.16 is important for the design as the observed "counter-phase pitch response" is favorable for both, the stability and the rejection of disturbances: With a small motion response at the hub, the power fluctuation is minimized and the controller coupling is also reduced. The controller usually feeds back the rotor speed deviation from the set point. If the rotor responds less to the wave forces, the wave response will be amplified less by the controller than with an instantaneous center of rotation at lower levels. The observation of
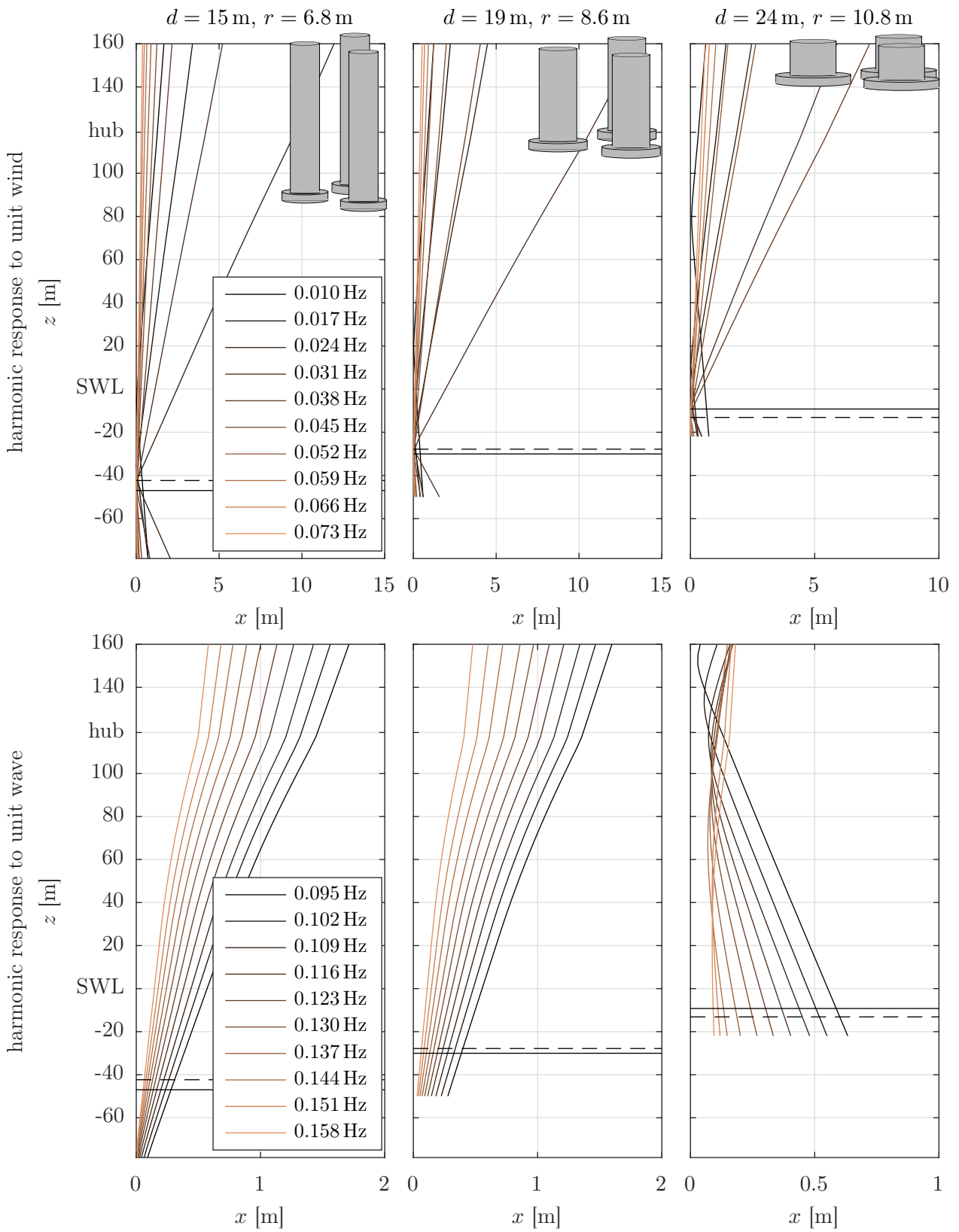
Figure 6.16: Harmonic response of FOWT system in closed-loop with PI-controller over typical wind frequencies (top) and wave frequencies (bottom) at $v_0 = 13.9\,\mathrm{m/s}$ with heave plate height $h_{hp} = 4.5\,\mathrm{m}$. Solid black line: FOWT overall center of mass, dashed black line: center of buoyancy.

Figure 6.16 is also of importance for the design of more advanced controllers as it reveals that feeding back the platform pitch angle for motion damping might not be harmful for the designs of deeper drafts, but it would even increase the response of the hub for the low-drafted platform.

In summary, the good performance of the low-draft platform in terms of the DLC 1.2 results can be explained by the "counter-phase pitch response". As the standard RAO to the platform DoFs predicts only the response magnitude in the individual DoFs, it cannot reproduce this coupled system response behavior, as opposed to the SLOW model used to generate the harmonic response of Figure 6.16.

Minimum required actuation with perfect control

It has been shown that the harmonic response to waves is a suitable design criterion to predict the good dynamics of the low-draft shape. In this section, a new design indicator will be introduced. It quantifies the necessary controller activity to reject the external forcing from wind and waves. The smaller the controller activity, the better the capability of the design to reject disturbances itself. Figure 6.17 shows the FOWT system $\boldsymbol{G}(j\omega)$ with additive disturbance transfer functions for the same inputs $\boldsymbol{u} = [M_g, \theta]^T$ and outputs $\boldsymbol{y} = [\Omega, x_t]^T$ as in Section 3.8. The disturbance transfer function for wind $G_{d,v_0}(j\omega)$ and for waves $G_{d,\zeta}(j\omega)$, collected in $\boldsymbol{G}_d$, are again scaled according to Eq. (5.2) as well as the plant $\boldsymbol{G}(j\omega)$ and the maximum input magnitude exceeds its limit if $u_i \geq 1$. According to [259], the minimum required control input magnitude U^*_{min} for perfect control (perfectly rejecting the disturbances) can be calculated by solving

$$U^*_{min} = \max_d(\min_u \|\boldsymbol{u}\|) \qquad \text{s.t.} \qquad \boldsymbol{G}\boldsymbol{u} + \boldsymbol{G}_d\boldsymbol{d} = \boldsymbol{0}; \quad \|\boldsymbol{d}\| \leq 1. \qquad (6.2)$$

with the 2-norm of the inputs $\|\boldsymbol{u}\|_2 = \sqrt{u_1^2 + u_2^2 + \ldots + u_n^2}$. Thus, the outputs $\boldsymbol{y}$ as responses to $|\boldsymbol{d}\| \leq 1$ shall be exactly zero. The required control input $\boldsymbol{u}$ can be obtained given a disturbance $\boldsymbol{d}$ through system inversion as

$$\boldsymbol{u} = -\boldsymbol{G}^{-1}\boldsymbol{G}_d\boldsymbol{d}. \qquad (6.3)$$

In order to simplify the problem set of Eq. (6.2), only one disturbance at a time will be considered in the following: Using the singular values of Eq. (5.3), we can obtain the "strongest" and "weakest" combination of the inputs $\boldsymbol{u}$. Then, the required control input can be calculated to cancel the disturbances for both, the strongest and weakest singular values resulting in a range of the 2-norm of the input signal $\|\boldsymbol{u}\|$ in-between these two boundaries according to [259] as

$$\frac{\|\boldsymbol{G}_d\|_2}{\overline{\sigma}(\boldsymbol{G})} \leq \|\boldsymbol{u}\|_2 \leq \frac{\|\boldsymbol{G}_d\|_2}{\underline{\sigma}(\boldsymbol{G})}. \qquad (6.4)$$

The resulting system inputs $\boldsymbol{u}$ (the outputs of the inverted system) are the ones necessary to
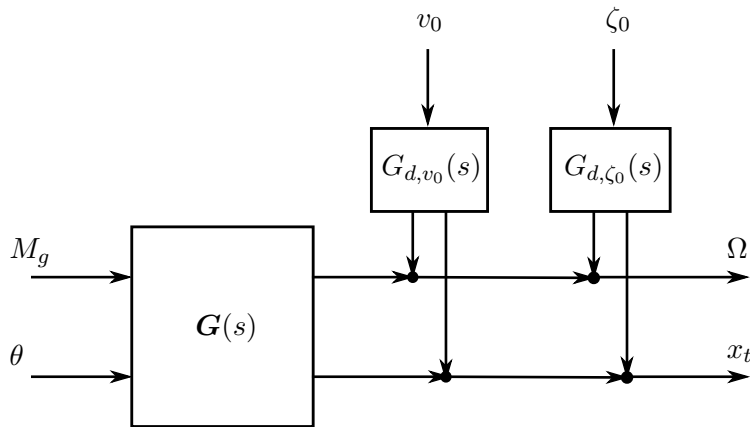
**Figure 6.17:** FOWT square plant with additive disturbances.

perfectly cancel the disturbances. The strongest actuation "direction" given by the SVD, see Section 5.1, will be used in the following. Thus, a scalar value of $U^*_{min} = \|\boldsymbol{G}_d\|_2 / \overline{\sigma}(\boldsymbol{G})$ results, representative of both control inputs.

The minimum required actuation $U^*_{min}(\omega)$ has been calculated for the different platforms, for wind excitation $d = v_0 = 1$ and wave excitation $d = \zeta_0 = 1$, separately in Figure 6.18. The part from wind excitation (upper part of Figure 6.18) does not show a large variation over the design space, except for the variation of the eigenfrequencies. For the part from wave excitation it is different: The best performance (equal to the least required actuation U^*_{min}) results here for the largest column spacing $d = 24\,\text{m}$. This is opposite to the RAO of Figure 6.14, which showed a larger response in pitch for the low-draft platform ($d = 24\,\text{m}$) than the narrower ($d = 23\,\text{m}$) design.

Thus, the assessment of the minimum required control input makes it possible to identify the optimality of the semi-submersibles seen in the harmonic response of Figure 6.16 and the weighted results of DLC 1.2, Figure 6.9. As opposed to the RAO, U^*_{min} is a design indicator able to predict the optimal behavior through the "counter-phase pitch response".

In summary, this section provided insight into the physical reasons of the low-draft platform better performing than the ones of deeper draft. The coupled response behavior to waves, with the surge and pitch-DoF being out of phase giving an almost stationary hub, yields the least variation of the rotor speed and power and also the smallest tower-base bending. Although this optimality cannot be seen from the RAO, the new design indicator of the minimum required control input proves to be better suited here.

The next section will analyze the fidelity of the reduced-order models compared to FAST for the three selected designs.
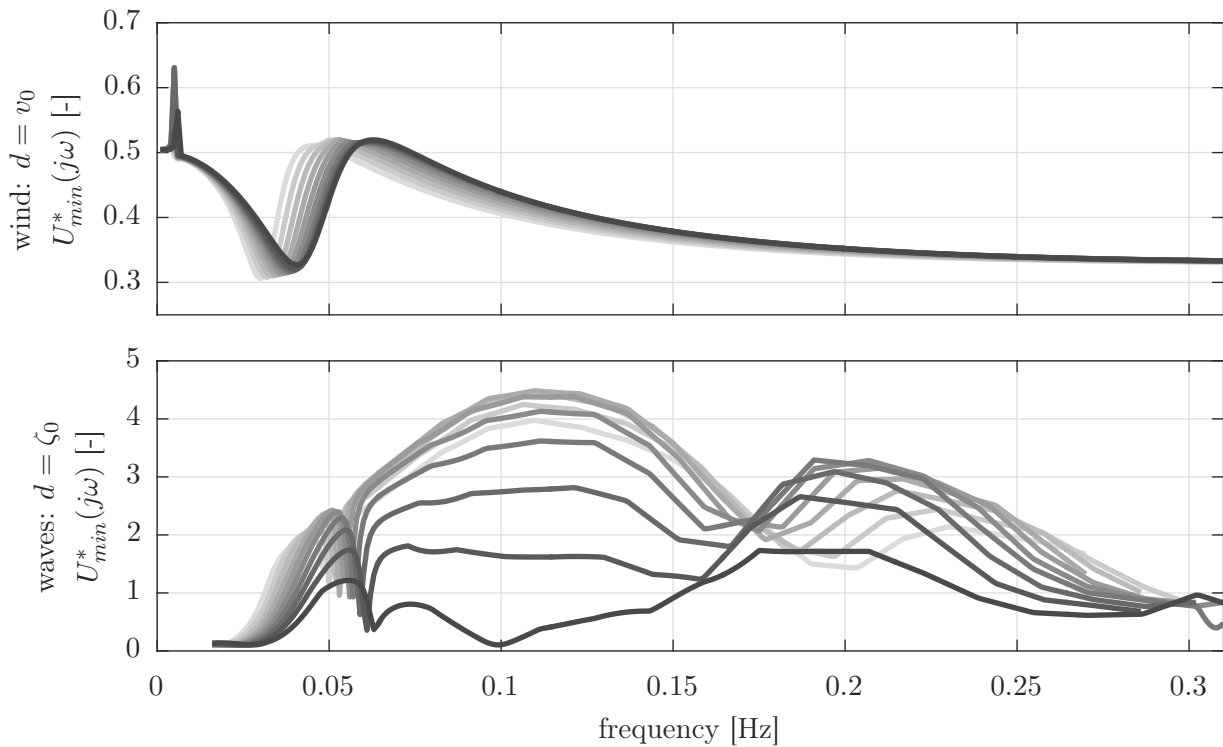
Figure 6.18: Minimum required control input magnitude U^*_{min} to perfectly reject wind (top) and wave (bottom) disturbances assuming the strongest combination of control inputs $\boldsymbol{u} = [M_g, \theta]$ for platforms of different column spacings $d = [15(1)24]\,\mathrm{m}$ (increasing darkness) and $h_{hp} = 4.5\,\mathrm{m}$.

6.4.5 Assessment of numerical models for three concepts

The agreement of the reduced-order SLOW models against FAST was shown in Section 3.9 for the TripleSpar concept at the wind speed bin of $\bar{v}_{hub} = 17.9\,\mathrm{m/s}$. In this section, the code-to-code comparison will be made for the three different designs of the integrated optimization. The previous analysis showed that the motion response characteristics depend significantly on the hull shape of the designs of Figure 6.3. Therefore, the comparison will show if the optimization results are valid for the entire range of platforms. The following Figures 6.19–6.23 compare the response PSD of various signals to the wind and wave excitations, shown on top, between the reduced-order linearized frequency-domain model, the reduced-order nonlinear time-domain model and the FAST model.

Model settings

The FAST model has all 25 DoFs enabled, while the SLOW models have 6 DoFs and the motion is only allowed in the vertical xz-plane, see Section 3.2. Radiation damping is neglected for the reduced-order models, following the argumentation of Sections 3.5.1 and 3.10. The importance of radiation damping over the design space will be discussed in Section 6.4.6. The hydrodynamic forces include for all models first and second-order excitations using Newman's

approximation, see Section 2.5.3, and additionally the drag-induced damping and excitation from Morison's equation, see Section 3.5.4. All models use the PI-controller with the gains of Figure 6.4. The below-rated controllers are the same for all models, see Chapter 5, with a linearized representation of the nonlinear state-feedback in the frequency-domain model.

The results are shown for operational conditions at three wind speeds of Table 2.1 below rated, above rated and at cut-out: $\bar{v}_{hub} = [7.1, 17.9, 25]\,\text{m/s}$. The severity of the sea state does significantly increase with the wind speed and thus, the validity of the linearized model is clearly challenged for the higher waves as nonlinear effects become important. All time-domain simulations are run over $T = 3600\,\text{s}$. A convergence study has been performed with simulation lengths up to 3 hours, showing that the selected simulation length is enough to obtain reliable responses in the low-frequency range.

Response spectra to stochastic loads during operation

Figures 6.19–6.21 show the results for the deep-draft design at the three wind speeds. The rotor-effective wind speed on top with rotational sampling of turbulence shows a peak at the 3p-frequency, which has the purpose of introducing the nodding forces through vertical wind shear. Generally, a good agreement between the reduced-order models and FAST can be observed. Differences to FAST are the surge-response at the platform pitch-eigenfrequency at around 0.03 Hz. The closed loop eigenfrequencies for all platforms were shown in Figure 6.8. Simulations without aerodynamic forcing have shown that this is due to the aerodynamic model, while the difference-frequency forcing is equal between FAST and the reduced model. This difference will be discussed more in detail in Section 6.4.6.

The heave response agrees well and is very small compared to the low-draft designs, which have larger vertical Froude-Krylov forces due to the vertical surfaces closer to SWL. The pitch-response agrees also well with differences to FAST again at the pitch-eigenfrequency. For the small wave height there is no visible response of pitch to waves. This is different for the tower-top displacement x_t, which is underpredicted in the wave frequency-range by the reduced-order models. This is the effect of the neglected radiation damping. It will be seen in Figure 6.25 (lower left), discussed in Section 6.4.6, for the same platform and same loads that the simplified constant matrix approach (Section 3.5.1) can result in a larger x_t-response with the radiation model than without.

The response of the rotor speed Ω to low-frequency wind-excitations and to the wave excitations agrees well among the models, in the same way as the electrical power P. The section forces at the tower-base have the most energy at the wind frequencies for the small sea state here. The agreement is very well. Here, no notable difference occurs between the linearized and the nonlinear reduced model.
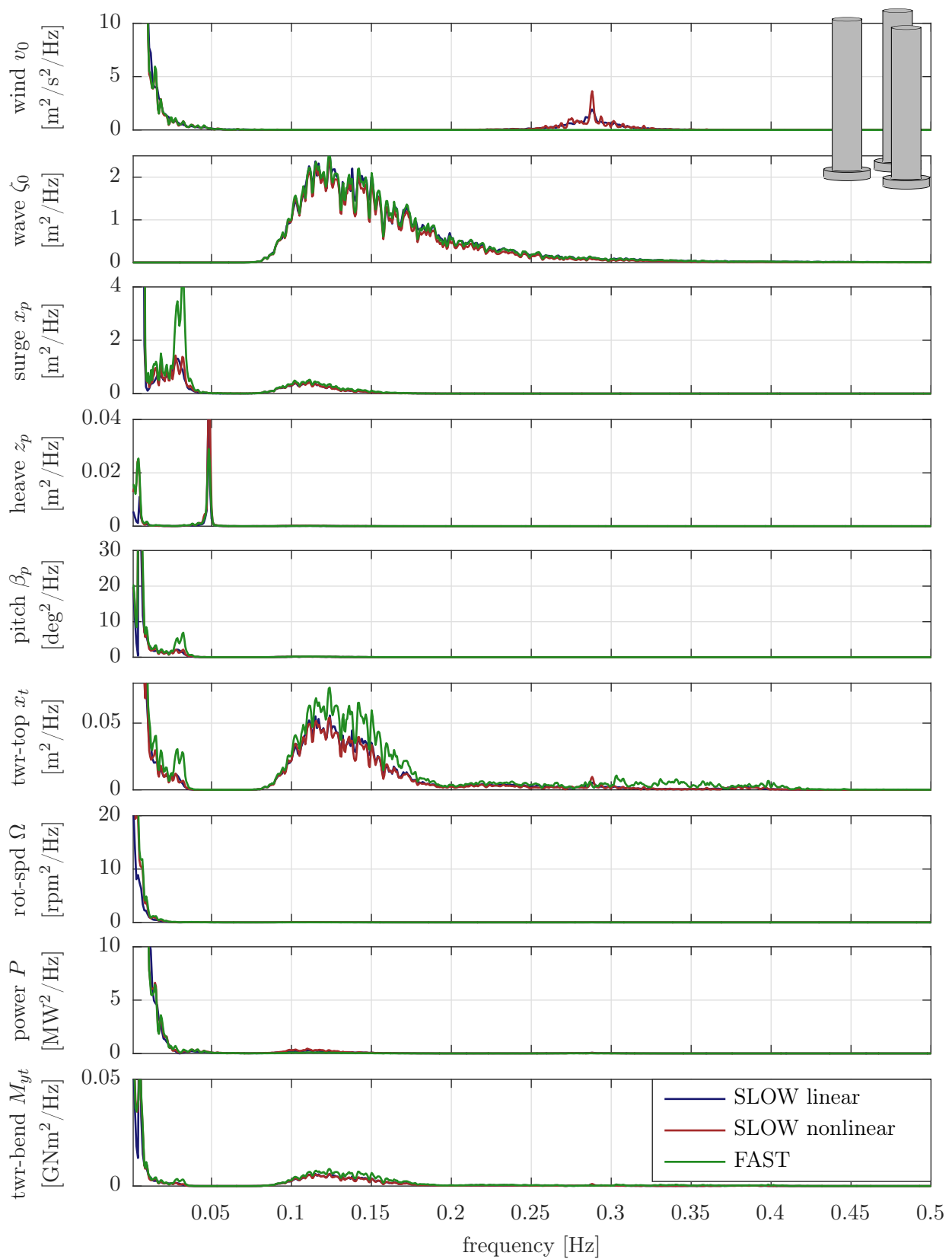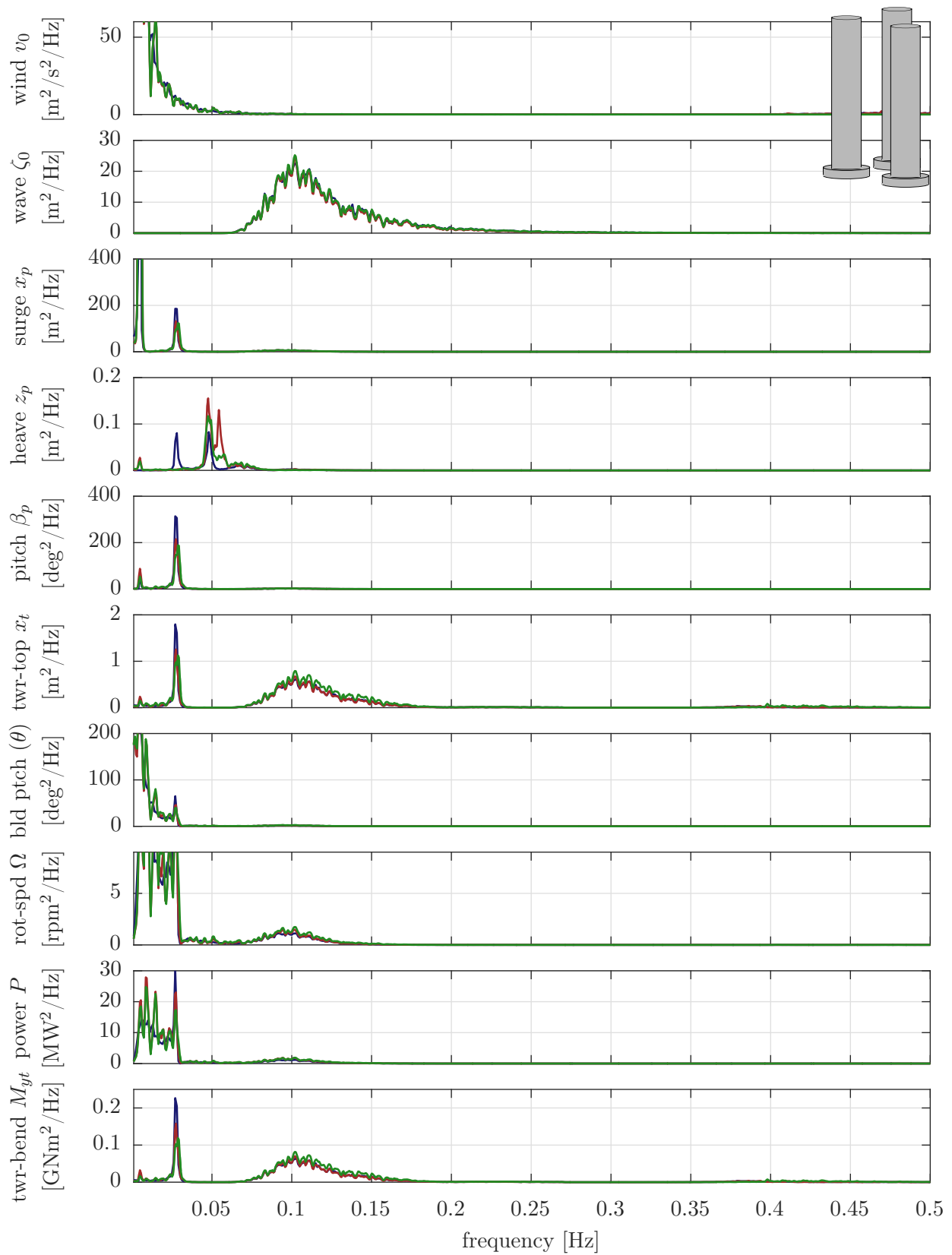
Figure 6.19: Model comparison $\bar{v}_{hub} = 7.1\,\text{m/s}$, $H_s = 1.7\,\text{m}$, $T_p = 8.0\,\text{s}$ for deep draft $d = 15\,\text{m}$: linear model, frequency-domain (blue), nonlinear model, time-domain (red), FAST, time-domain (green).

For the wind speed $\bar{v}_{hub} = 17.9\,\mathrm{m/s}$ above rated, Figure 6.20 shows for the deep-draft platform generally better agreements between the reduced-order models and FAST. The responses to waves are now clearly larger than for the below-rated case. However, the energy contained in the low-frequency response of the platform-DoFs (x_p, z_p, β_p) to wind and difference-frequency forces is still significant, compared to the one of first-order waves. For z_p, some scatter of the heave response magnitude and frequency is visible, which can be due to numerics, considering the small overall response magnitude in heave. The difference of x_t in the wave frequency range, due to the neglected radiation damping, is here not as pronounced anymore as in the smaller sea state. This is because the viscous Morison damping becomes more important than the linear radiation damping for larger response magnitudes.

Figure 6.21 shows the highest wind speed and the largest sea state with the deep-draft platform. Here, a large response to first-order wave forces and a pronounced peak for the platform pitch eigenfrequency is visible. The agreement of the models is here surprisingly good as the environmental conditions might suggest that the assumptions for the linearized model do not hold anymore. The wave response of the rotor speed Ω and the electrical power P is underpredicted by the linearized model, equally to the following cases. This was discussed already in Section 3.2.7. A likely reason is the neglect of the cross-correlation between the rotor-effective wind v_0 and the wave height ζ_0.

In summary, the code-to-code comparison for the deep-draft platform shows that the SLOW models can well represent the main resonances at the eigenfrequencies but also the forced responses to wind, including the 3p-forcing from the wind shear and the response to first-order and second-order wave forces. For this deep-draft platform, the hydrodynamic drag at the columns is more important than for the ones of larger diameter as shown in Figure 2.4. Its linearization is successful, which is proven by the agreement of the first-order wave response and the platform low-frequency resonances.

For the medium-draft and the low-draft designs only the largest sea state is shown here, while the other two conditions are shown in Appendix B.4. Figure 6.22 shows the medium-draft design response with $t = 50\,\mathrm{m}$ at the cut-out wind speed of $\bar{v}_{hub} = 25\,\mathrm{m/s}$. It has generally a comparable level of agreement among the models as the low-draft design. The only difference of the linearized model is the response at the platform pitch mode, which is larger for the frequency-domain model. As the response for the time-domain models is equal, it is likely that the linearization is the origin of this difference. A simple explanation is the different resolution of the frequency-axis for the frequency-domain calculation, which better resolves this narrow-banded resonance. Another explanation is the linearization technique of the viscous drag of Section 3.5.4: The selected linearization technique of the Morison damping neglects the wave kinematics. This does, however, not explain why the agreement is better for the low-draft platform. The underpredicted rotor speed and power by the linearized model is, again, attributed to the neglected cross-correlation between the wind and the wave response.

Figure 6.20: Model comparison $\bar{v}_{hub} = 17.9\,\text{m/s}$, $H_s = 4.3\,\text{m}$, $T_p = 10.0\,\text{s}$ for deep draft $d = 15\,\text{m}$: linear model, frequency-domain (blue), nonlinear model, time-domain (red), FAST, time-domain (green).
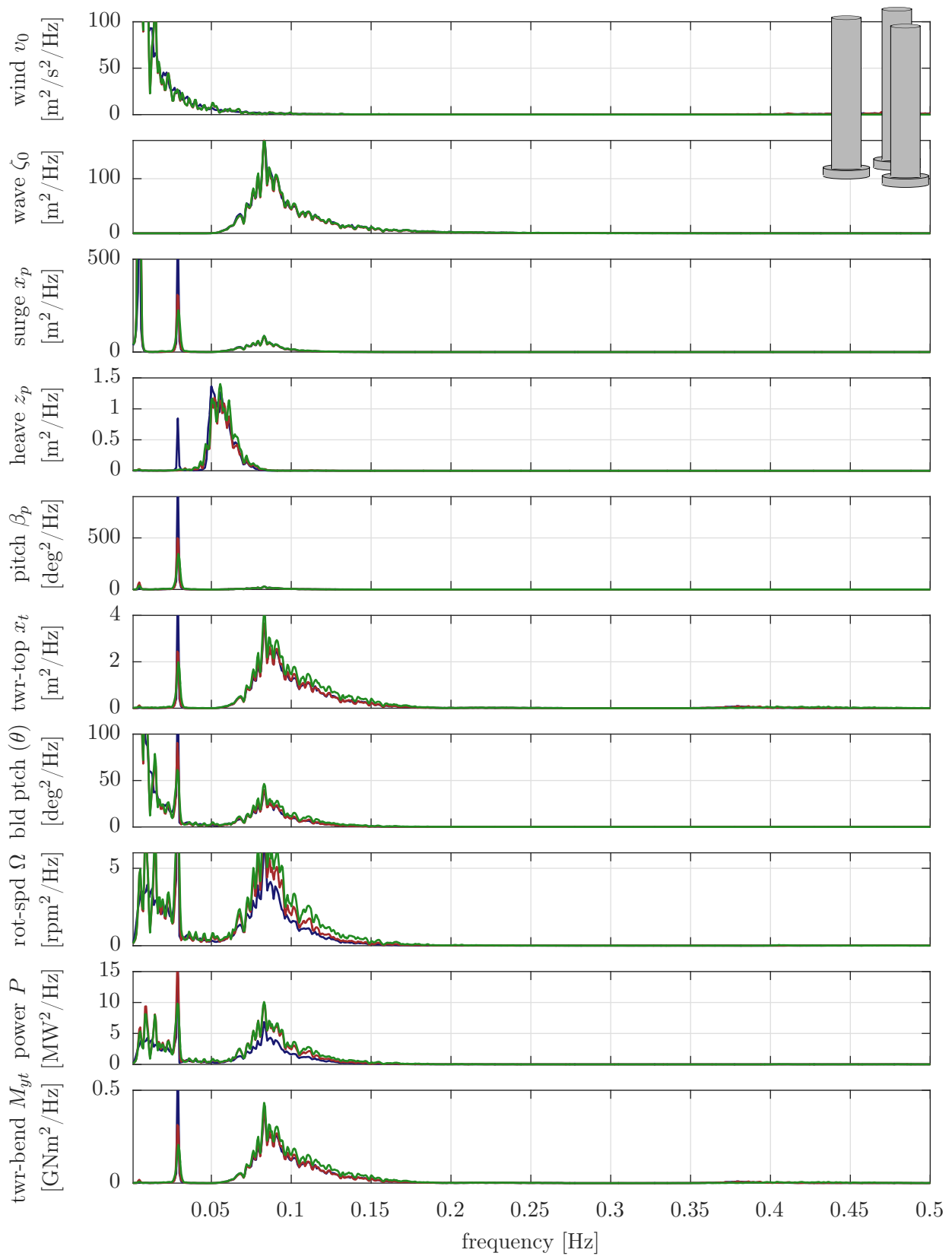
Figure 6.21: Model comparison $\bar{v}_{hub} = 25.0\,\text{m/s}$, $H_s = 8.3\,\text{m}$, $T_p = 12.0\,\text{s}$ for deep draft $d = 15\,\text{m}$: linear model, frequency-domain (blue), nonlinear model, time-domain (red), FAST, time-domain (green).
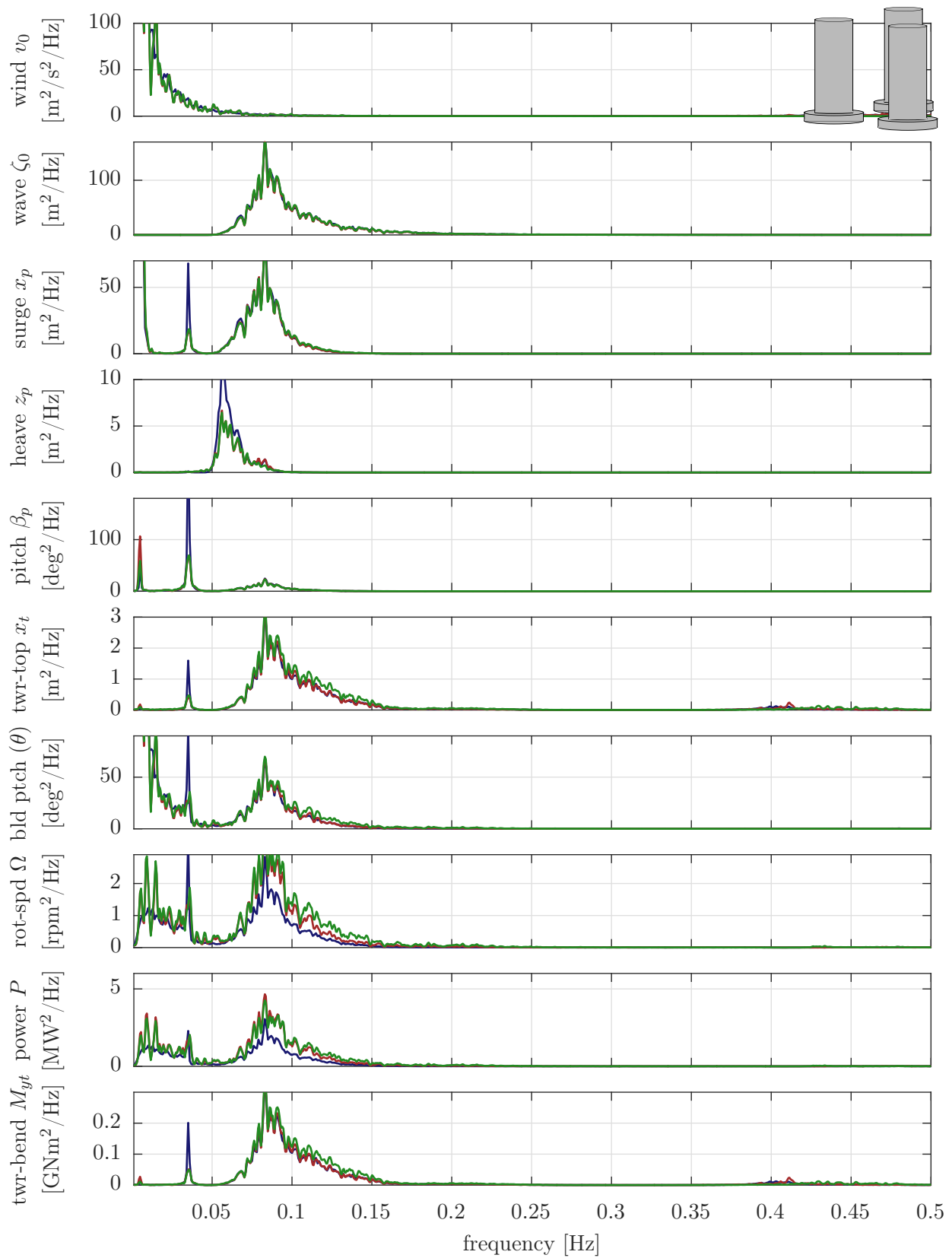
Figure 6.22: Model comparison $\bar{v}_{hub} = 25.0\,\mathrm{m/s}$, $H_s = 8.3\,\mathrm{m}$, $T_p = 12.0\,\mathrm{s}$, medium draft $d = 19\,\mathrm{m}$: linear model, frequency-domain (blue), nonlinear model, time-domain (red), FAST, time-domain (green).

Figure 6.23 shows the low-draft platform response to the largest wind and sea state. The largest difference between the models can be seen for this platform: Due to the severity of the sea state, large drag-excitation forces are present, induced by the large-diameter heave plates. This effect represents a clear difference between the linearized and the nonlinear models. Interestingly, the tower-top displacement x_t predicted by the nonlinear SLOW model, deviates more from FAST than the frequency-domain SLOW model. The same effect can be seen for the tower-base fore-aft bending moment M_{yt}. As opposed to the tower-top displacement x_t, the platform pitch angle β_p is larger for the reduced-order models than for the FAST model.

Figures B.6–B.7 of the appendix show the lower wind speeds $\bar{v}_{hub} = [7.1, 17.9]\,\mathrm{m/s}$ for the medium-draft and low-draft designs. No notable, additional model deviations are visible for these less sever conditions, compared to the previous results.

In order to obtain this agreement over the entire design space, an iteration of the model fidelity was necessary: Especially, the viscous heave plate drag turned out to be of importance for the low-draft platforms. Thus, a computation of the wave particle kinematics at the exact location of the members is necessary and for the linear model a good linearization technique for the Morison drag is required. For all models and the considered signals, the aerodynamic model is sufficiently accurate and the neglected radiation damping (constant-matrix approach) does not yield significant modeling errors at a highly improved computational efficiency. The difference of the number of DoFs in FAST and in SLOW, especially the fact that the SLOW model moves only in the 2D xz-plane does not yield noticeable deviations of the response. After this comparison of the PSDs, the weighted STDs and the DEL over the entire lifetime will be compared in the next section.

Weighted lifetime results

Figure 6.24 shows the weighted DEL of the tower-base bending moment M_{yt}, the STD of the platform pitch angle β_p, the rotor speed Ω and the blade pitch angle θ. The first observation is that the qualitative optimum towards large d (low drafts) is predicted equally by the three models. There is a constant concept-independent offset of the DEL between the simplified models and FAST. This is due to the approximate inclusion of the 3p-excitation through rotational sampling of turbulence in the simplified nonlinear and the linearized aerodynamic/wind model, see Section 3.3. Although the previous PSDs showed a comparable 3p-response, the resulting fatigue damage at the tower-base is underpredicted by SLOW. The other noticeable offset is related to the linearized SLOW model for the rotor signals Ω and θ: This model underpredicts the fluctuation of these signals, which is due to the influence of the switching in region 2.5, see Chapter 5. The switching becomes here important through the weighting with the Weibull distribution of Figure 2.6 because the wind speeds slightly below rated are weighted higher than the others. This is a nonlinear effect, which cannot be represented in the
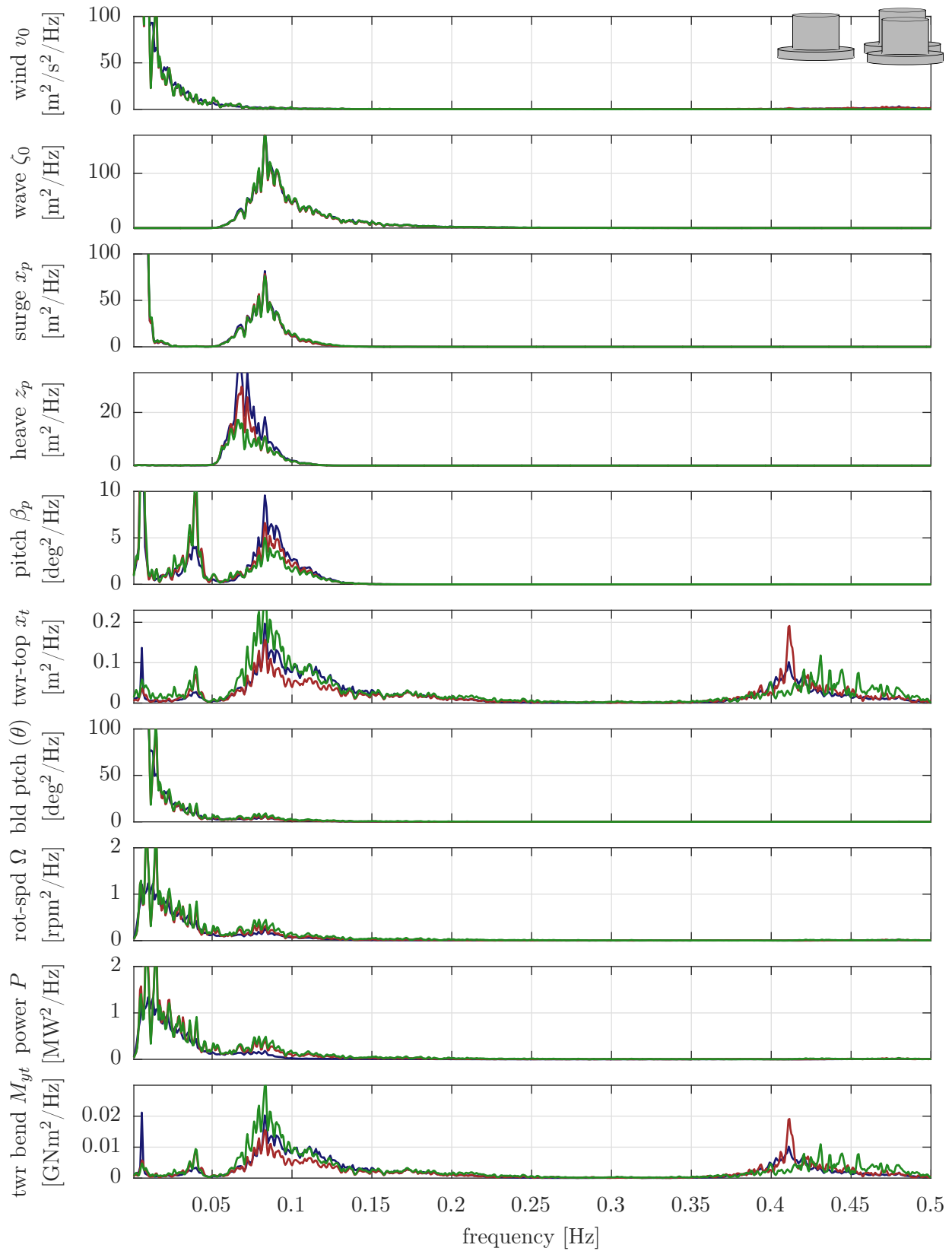
Figure 6.23: Model comparison $\bar{v}_{hub} = 25.0\,\text{m/s}$, $H_s = 8.3\,\text{m}$, $T_p = 12.0\,\text{s}$ for low-draft $d = 24\,\text{m}$: linear model, frequency-domain (blue), nonlinear model, time-domain (red), FAST, time-domain (green).

frequency-domain model. It is, however, included in the time-domain model, which shows a notably good agreement with FAST for both rotor signals. The platform pitch angle agrees well among the time-domain models with a slight underprediction of SLOW for the deep-drafted platforms. The linearized model underpredicts the pitch-STD for the low-draft platforms.
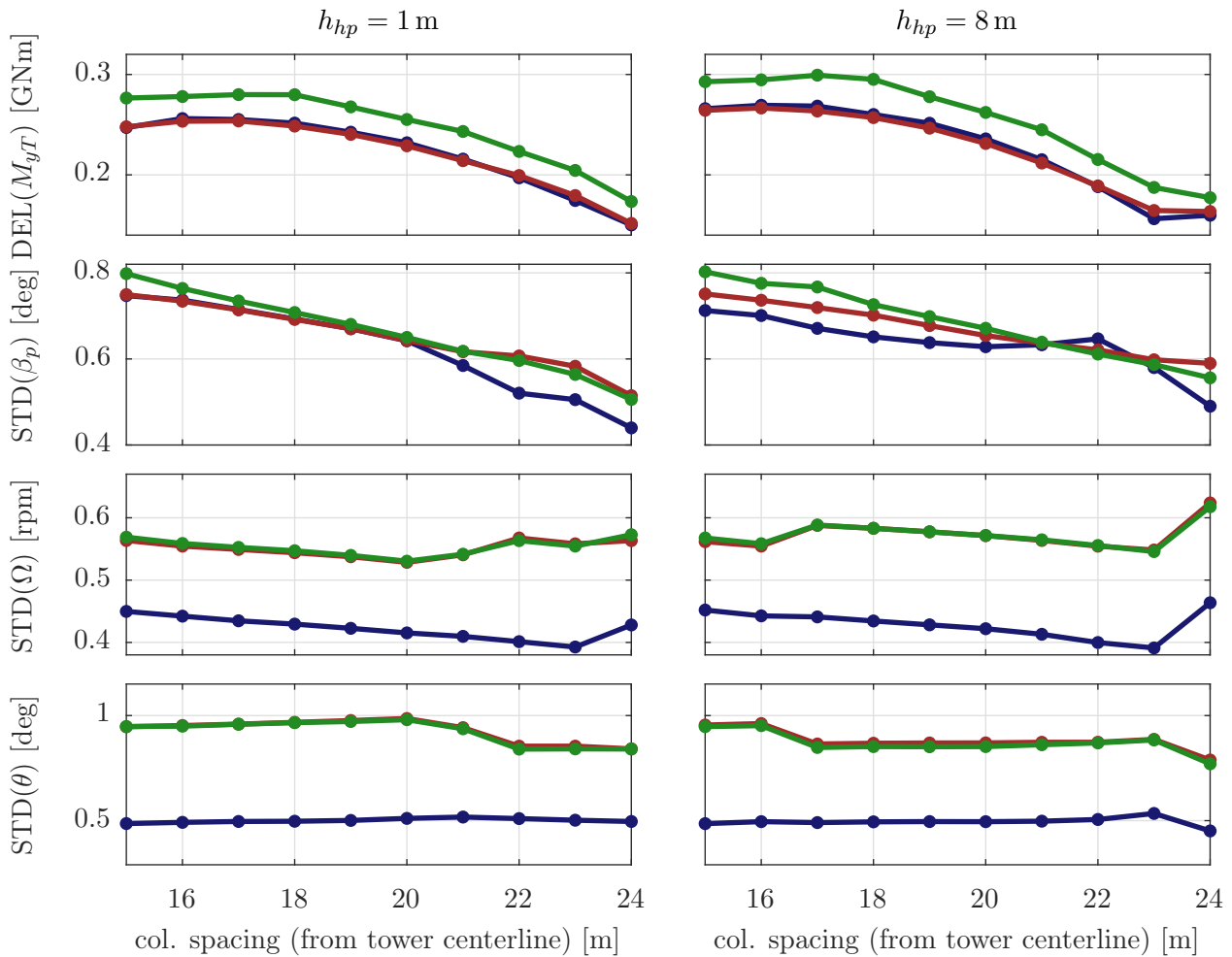
Figure 6.24: Response statistics of operational DLC1.2 with PI-controller, Tab 2.1, weighted for all wind speeds with distribution of Figure 2.6. Linear model (blue), nonlinear model (red), FAST (green).

Summary

As a result of this code-to-code comparison, it can be said that the agreement between the simplified models and FAST is surprisingly good, given that the simulated conditions (Table 2.1) are rather severe. The model fidelity of SLOW, i.e. the number of DoFs and its physical modeling assumptions (see Table 3.1) are suitable for the representation of the overall system dynamics throughout the present design space of semi-submersibles.

6.4.6 Model fidelity

In this section, specific phenomena found in the previous section are analyzed more in detail. The first assessment addresses the significant simplification of SLOW, neglecting the radiation damping and modeling the radiation memory effect with a constant added mass as introduced in Section 3.5.1. Also the importance of drag-induced Morison excitation and the effect of difference-frequency wave forces is assessed. Finally, the impact of the aerodynamic model on the pitch-mode below rated is addressed.

Radiation model

The constant-matrix approach is used throughout the analyses of this chapter because it has clear advantages in terms of computational speed as shown in Table 3.2. However, the simplified frequency-domain model has the capability to model the radiation memory effect and therefore simulations have been performed with this model and FAST with the full radiation model and with the simplified constant matrix approach for both models. It is noted that this approach does not only impact the damping properties but also the added mass. Consequently, the constant-matrix approach can have an effect on the system eigenfrequencies.

In order to implement this approximation in FAST, modified Wamit files (.1-file) were generated with a constant added mass, interpolated at the respective eigenfrequencies, see Figure 3.3. The radiation damping coefficients were set to zero and the flag to compute the radiation memory effect convolution was switched off. Figure 6.25 shows the comparison between the linearized SLOW and the FAST model for the deep-draft platform and Figure 6.26 shows the results for the low-draft platform, both for the below-rated and the cut-out wind speed. All figures are zoomed in at the frequencies where radiation is important, roughly at the frequencies of the wave spectra, see Figure 3.4. It is noted that the absolute response magnitude is small in some cases, especially for the below-rated wind speed. In Figure 6.25, it can be seen for the below-rated wind at $\bar{v}_{hub} = 7.1\,\mathrm{m/s}$ that generally, the difference between the models is larger than the difference induced by the radiation effect and the response to first-order wave forces is very small. For the cut-out wind at $\bar{v}_{hub} = 25\,\mathrm{m/s}$, FAST does not show any difference between the radiation modeling approaches whereas the reduced model shows a slightly smaller platform response. For the tower-top displacement x_t the same holds, whereas the reduced frequency-domain model gives a smaller response with radiation damping.

Looking now at the same analysis for the low-draft platform in Figure 6.26, the platform responses for x_p and β_p for the below-rated wind speed are comparable. For the higher wind speed (right column), there is a general difference between SLOW and FAST, with SLOW predicting a larger response. However, both show a reduced β_p response with radiation damping. This is not the case for the tower-top displacement x_t. It shows an even larger response at the higher wind speed for the low-draft platform with radiation damping enabled compared to the
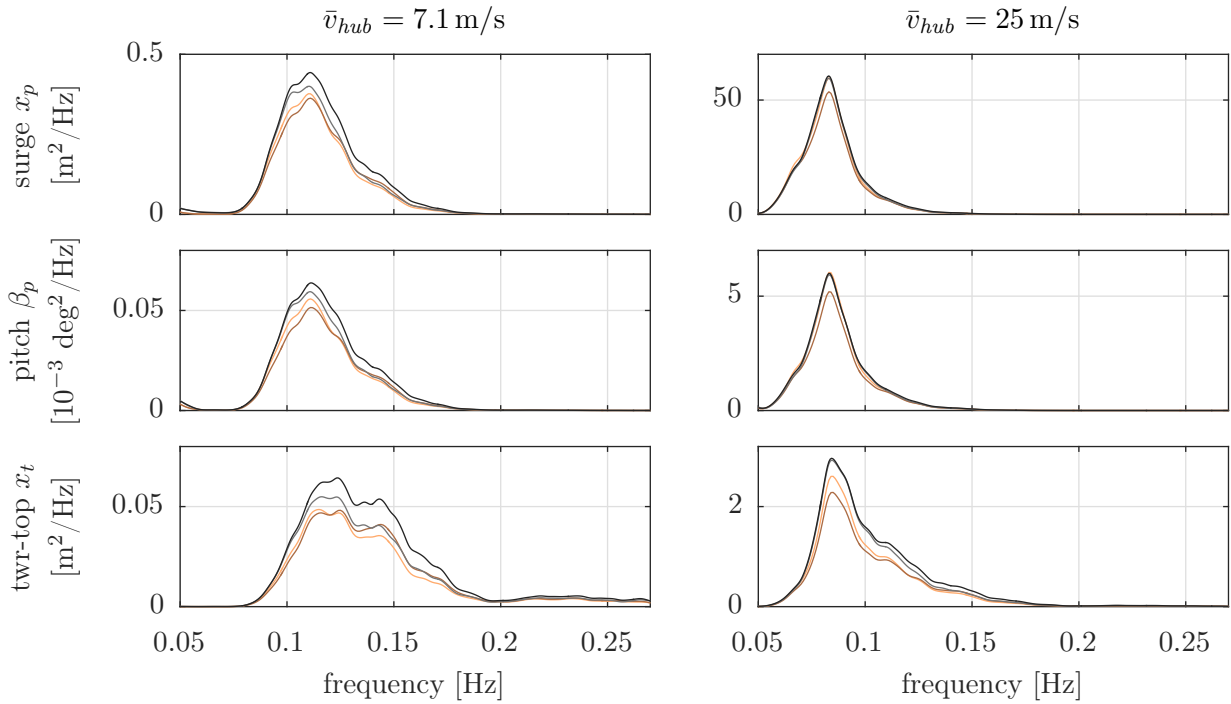
Figure 6.25: Comparison of constant added mass approach without radiation damping (light color) against radiation model (dark color). Nonlinear time-domain model FAST (gray) and linear frequency-domain model (red), deep draft ($d = 15\,\mathrm{m}$).
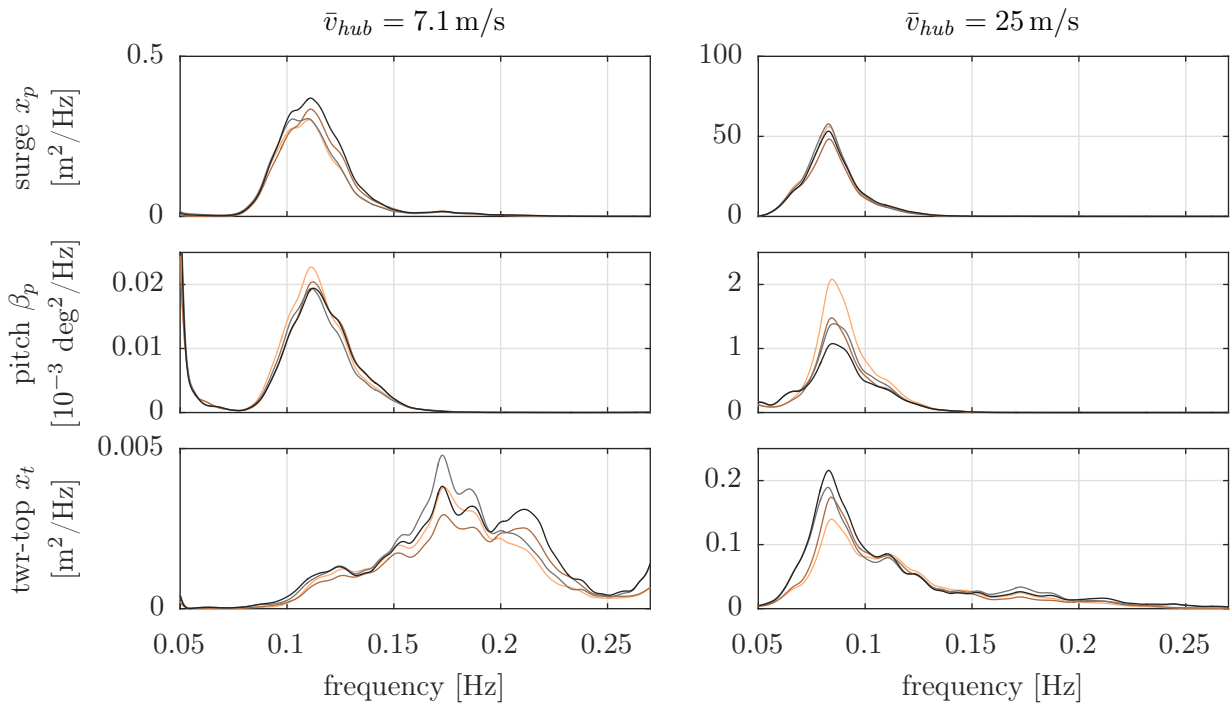
Figure 6.26: Comparison of constant added mass approach without radiation damping (light color) against radiation model (dark color). Nonlinear time-domain model FAST (gray) and linear frequency-domain model (red), low-draft ($d = 24\,\mathrm{m}$).

constant matrix approach. This might be due to the effect of the constant matrix approach on the added mass magnitude and the resulting change of eigenfrequencies. Thus, it might not be due to the damping effect, alone.

In general, the analysis shows that the effect of radiation damping is small in most cases. Due to the linear nature of the damping, it can be dominant over quadratic damping for small motion responses. In the analysis for the given design space, the most significant difference is present for the largest sea state for the low-draft platform. No visible change in the platform eigenfrequencies between the models is present in the results. This can be also observed in the previous Section 6.4.5, where FAST always includes radiation damping with the convolution integral while the simplified models neglect radiation damping.

Wave forces from Morison drag and first-order potential forces

Figure 6.27 shows the three components of the wave force spectra of the xz-plane for the deep-draft and the low-draft concept. While the ratio of first-order potential forces to Morison-drag forces is equal for both designs in the first direction (x) there is a clear difference between these ratios for the forces in heave- and pitch-direction. With large heave plates, the Morison drag-excitation becomes more important such that their correct modeling is of importance. This means, in addition, that the drag linearization leads to errors in the simulation of large waves.
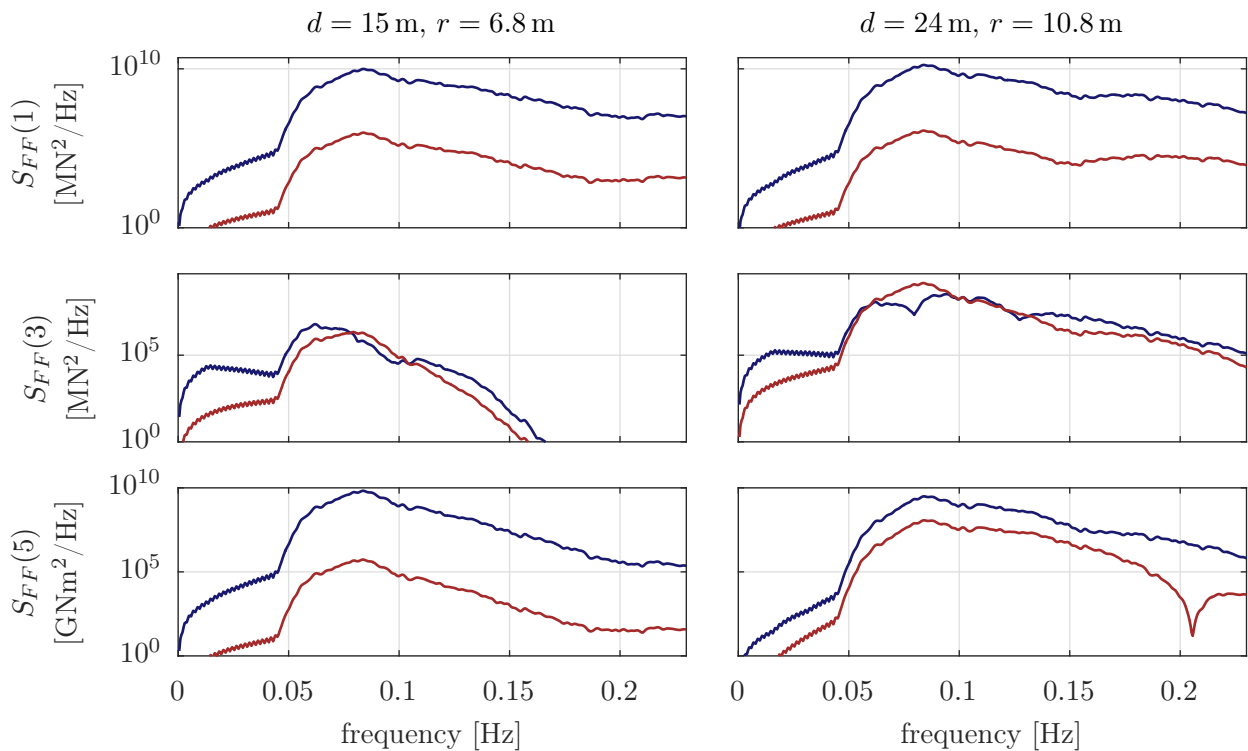
Figure 6.27: First-order wave force spectrum (blue) and Morison drag-excitation force spectrum (red) in surge, heave and pitch-direction for deep-draft (left) and low-draft (right) at $\bar{v}_{hub} = 25\,\text{m/s}$.

This confirms the results of Section 6.4.5, where the largest differences between the linear and the nonlinear SLOW model were present for the platform with the largest heave plates at the largest wind and sea state.

Second-order slow-drift forces

Figure 6.28 and Figure 6.29 show the response with and without difference-frequency excitation for the two wind speeds of the previous analyses. While there is almost no difference for the small sea state at $\bar{v}_{hub} = 7.1\,\mathrm{m/s}$ in both figures, differences are visible for the deep-draft platform for the above-rated wind speed of $\bar{v}_{hub} = 25.0\,\mathrm{m/s}$. Especially at the low surge-frequency, the response is higher if the second-order forcing is included.
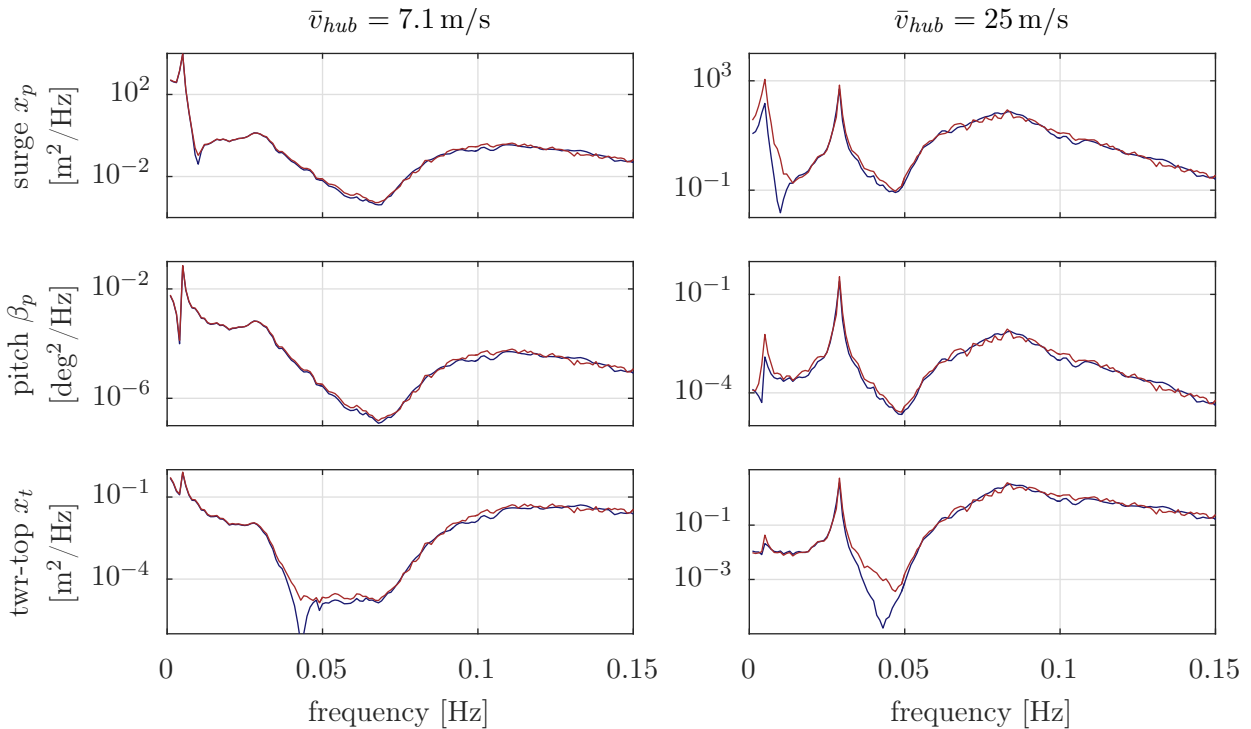
Figure 6.28: Comparison of response without (blue) and with (red) difference-frequency excitation, deep-draft $(d = 15\,\mathrm{m})$.

For the low-draft platform, Figure 6.29 shows for the high sea state (right column) that the response to drift forces at the eigenfrequencies at $0.008\,\mathrm{Hz}$ and $0.035\,\mathrm{Hz}$ is significant. Consequently, it is more important to include the second-order force models for the low-draft platform than for the deep-draft platform.

Aerodynamics

In this section, the simplified rigid disk model of SLOW is compared to the two aerodynamic models of FAST. Simulations were run with SLOW and FAST in still water at a wind speed
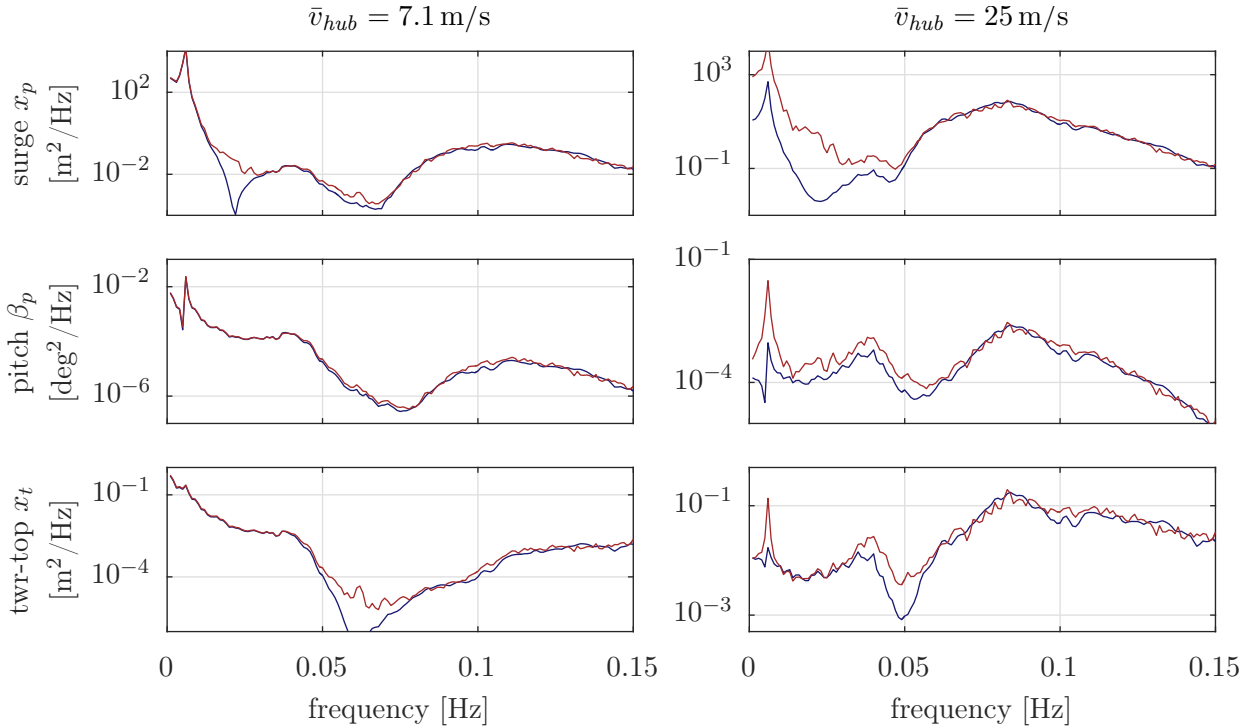
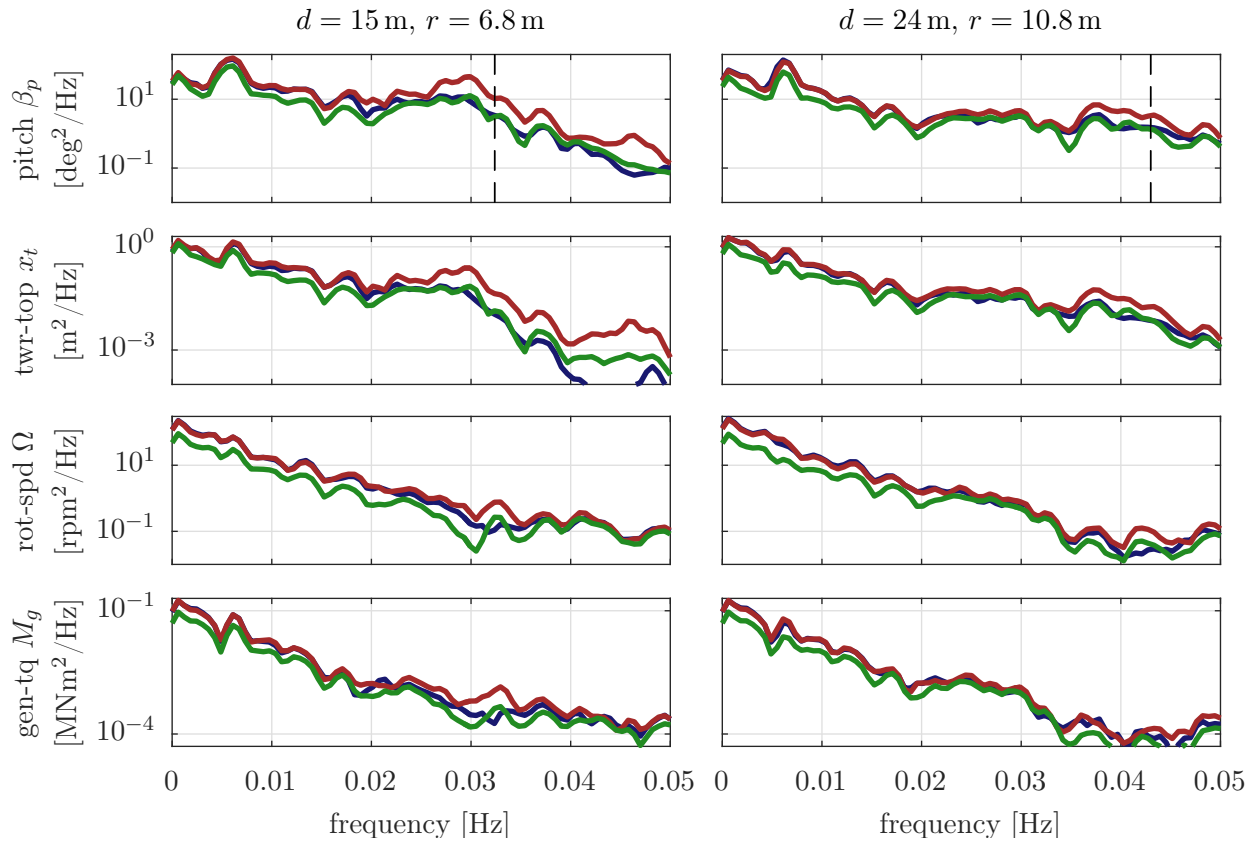**Figure 6.29:** Comparison of response without (blue) and with (red) difference-frequency excitation, low-draft ($d = 24\,\mathrm{m}$).

of $\bar{v}_{hub} = 10.3\,\mathrm{m/s}$. Next to the previously used BEM-model of FAST, simulation were performed with the Generalized Dynamic Wake (GDW) model, which includes dynamic inflow effects. The same was done in the recent publication [74], in which scaled model experiments for the unsteady aerodynamics of a FOWT were compared to the GDW model. In that paper the "reduced wake velocity" was introduced as

$$V_W^* = \frac{\bar{v}_{hub}T}{D}, \tag{6.5}$$

which represents the ratio of the distance of the wind traveling with the velocity $\bar{v}_{hub}$ within one period T of the platform motion to the rotor diameter D. This value is for the deep-draft platform $V_W^* \approx 1.9$ and for the low-draft platform $V_W^* \approx 1.4$. The authors of the publication [74] state that unsteady aerodynamic effects are of importance for $V_W^* < 5$, which confirms the importance of the unsteady aerodynamic model in the present case.

Figure 6.30 shows the response in pitch β_p, tower-top displacement x_t, rotor speed Ω and generator torque M_g for the two platforms. The platform pitch eigenfrequency is highlighted for both designs. Interesting is the fact that the response at the pitch-mode of FAST with GDW is closer to the simplified SLOW model than to the FAST model with a steady BEM model. For lower frequencies, the GDW-model predicts generally smaller responses of the signals shown here. This is the same for the low-draft and the deep-draft platform.

Figure 6.30: Comparison of response to wind only (still water) at $\bar{v}_{hub} = 10.3 \, \text{m/s}$ for simplified non-linear model (blue), for FAST model using steady inflow model (red) and for FAST model with GDW model (green). Deep-draft (left) and low-draft (right). Pitch eigenfrequency $f_{d,pitch}$ marked for both geometries.

These results show that the aerodynamic modeling is especially important at these resonance frequencies, in spite of the general dominance of the wave forcing, and even more for lower wind speeds than for high wind speeds, where V_W^* takes larger values. In conclusion, the further investigation of unsteady aerodynamic effects needs to be assessed in more detail, refining the state-of-the-art BEM model. Although it is not expected that a more detailed model would change the findings of the present platform optimization, the unsteady aerodynamics can be important for model-based controller design as discussed in Section 2.5.2.

7 Conclusions and Outlook

The goal of this work was to improve the understanding of how wind and waves impact the dynamic behavior of the floating systems and how their shape can be optimized for floating wind turbines showing the same stable dynamics as bottom-fixed ones with a rather lightweight, and resource-efficient foundation. In order to pursue this goal, a dedicated simulation model was developed with a simplified representation of the structure, the aerodynamics and hydrodynamics. The developed model was verified with the open-source code FAST for a public baseline design of a 10 MW turbine on a concrete deep-draft semi-submersible. It was also validated against scaled experiments of the same concept in a combined wind and wave tank including blade pitch control. Finally, a brute-force optimization of a three-column semi-submersible with adapted wind turbine controllers revealed that an optimization of the hull shape can yield a reduction of the tower-base bending moment of more than 30 %, yielding comparable fatigue to onshore turbines.

7.1 Reduced-Order Simulation Model

A flexible multibody system has been developed with a general formulation that is not specific to wind turbines. It has been set up with only six degrees of freedom, allowing a motion in two dimensions. A symbolic linearization method yields a linear representation, which was used for load calculations in the frequency-domain and linear system analyses. Through a comparison of the simulation results with the higher-fidelity FAST code and experimental data, the relevance of the physical effects could be estimated.

A rather high level of detail was selected for the hydrodynamic model because the loads and motion response of floating wind turbines is dominated by the wave forcing and the hydrodynamic viscous drag is important for the overall system dynamics. In addition to the first-order panel code coefficients, a flexible node-based implementation of Morison's equation was realized. The Morison drag forces include the horizontal and vertical components of damping, as well as wave excitation. The magnitude of the Morison drag-excitation depends strongly on the semi-submersible heave plates and requires a proper linearization procedure or a nonlinear modeling for large sea-states. The radiation memory effect, however, has shown to have a minor impact on the main system dynamics for the considered platform shapes. Its proposed

simplification yields a substantially decreased simulation time. For an identification of the hydrodynamic drag coefficients, especially the inclusion of the second-order difference-frequency forces was important. The results of the model validation led to a parametric definition of the heave plate drag, which, using the linearized frequency-domain model, allowed for an iterative solution. These load case-dependent drag coefficients were used for the simplified nonlinear model and the FAST model. Both results show that the parametric heave plate drag results mainly in larger global damping coefficients for larger sea-states. It will be important to take such a parameterization into account for a realistic estimation of the hydrodynamic damping in load simulations.

The aerodynamics could be well represented through an efficient force model for the integral rotor. The quasi-static model provides the rotor forces as function of the tip speed ratio and the blade pitch angle, the actuated variable of the above-rated controller. For a representation of the blade excitation from wind shear, rotational sampling of turbulence showed to be an efficient and suitable method.

In a comparison with FAST, the model has proven to be able to represent the dominant system dynamics, the main eigenfrequencies but also the magnitude of the frequency response to rather severe met-ocean conditions. In a comparison against scaled experiments, the eigenfrequencies and the magnitude of the response to wind and wave forces was well predicted.

The computational performance of the time-domain model is such that a simulation runs about 120 times faster than real-time. The linear frequency-domain model requires only matrix algebraic operations and is therefore even faster. Common state-of-the-art simulation models are usually not faster than twice the real-time, which might limit large conceptual design studies.

The model was successfully applied for linear model-based controller design. The resulting PI-controller proved to be suitable also for the FAST model, which includes dynamics, neglected in the controller design model. The integrated platform optimization over a large design space of semi-submersible platforms made use of the tailored properties of the model. Although the hydrodynamic properties of the analyzed platforms show a large variation with different characteristics of the hydrodynamic forcing, the developed model was able to reliably predict the dynamic behavior for all designs. A verification of the optimization results with FAST showed the same optimum.

Although the model description, adapted to the problem, is highly efficient for this work, there are clear limitations, related to the simplifications of the above mentioned involved sub-models. Especially the motion, constrained to the vertical plane in wind and wave direction prohibits the modeling of yawed inflow and misaligned waves. The structural dynamics neglect the elasticity of the floating platform, the higher tower modes and the blade elasticity. The simplified representation of the aerodynamics does not allow for the simulation of extreme aerodynamic situation with strong shears, transient events or stalled flow conditions. The hy-

drodynamic model resembles more the one of the FAST model but there is also a restriction to linear waves and the second-order slow drift forces are approximated. Hence, the model is well suited for operational conditions without failures or extreme events. Operational load cases are the important ones in the concept design stage and for a general system optimization. Extreme cases are subject of the detailed design stage, which requires high-fidelity models, adapted to the complexity of the simulated conditions.

In summary, the developed reduced-order simulation model could successfully fill the gap between spreadsheet calculations on one side and simulation tools for certification on the other side. It is hence a well-suited model for the conceptual design phase of floating wind systems. Even though it includes all main system dynamic effects, it can be used for large parameter studies. It was shown in the integrated optimization that such a coupled description is necessary to find the optimum for the herein selected design space of semi-submersible platforms, as opposed to simpler, de-coupled approaches.

7.2 Controller Design

A Single-Input-Single-Output (SISO)-design procedure was developed, satisfying a predefined stability margin at all operating points. With this new procedure of a gain scheduling controller for floating wind turbines, the entire system is considered for the controller design. Commonly, the gain scheduling function maintains the closed loop rotor dynamics over the entire operating range.

In the proposed method, not only the rotor dynamics but the entire FOWT dynamic system stability is a design criterion for all operating points. The developed SISO design procedure yields a gain scheduling for above-rated wind speeds, which differs from the common gain scheduling of onshore turbines. This is because the stability issue of floating wind turbines is more critical for lower wind speeds than for higher wind speeds. As a result, the proportional gain decreases for increasing wind speeds above rated, before it increases again towards cut-out wind speeds. A rather high time constant of the SISO-Proportional-Integral (PI)-controller showed to give better results for floating turbines, which is another difference to common on-shore controllers. The advantages of this controller are the robustness properties and therefore the high independence from the simulation model in terms of unmodeled dynamics of the design model. The developed design algorithm can be automated using the linearized model in each operating point.

Additionally to this controller, an optimal Multi-Input-Multi-Output (MIMO) controller was designed, in order to show its advantages over the previous one. The determination of the controller weights was successful with a good performance over the design space. While the controller showed to improve significantly the damping of the system resonances, its robustness

is limited. Therefore, the controller is useful as an indicator of the upper performance bound, showing the theoretical potential to damp low-frequency platform resonances and improving rotor speed tracking.

7.3 Integrated Optimization

The optimum platform shape of a concrete semi-submersible was found through an integrated design approach. The primary goal of this optimization was to improve the overall system dynamics of the FOWT, such that the response of the system to stochastic wind and wave loads in fore-aft direction but also in terms of the power fluctuation is reduced. To meet this goal, a small design space of a three-column semi-submersible with heave plates was set up, ranging from a slender deep-draft geometry to a low-draft one with large column diameter. As a result of the optimization, the low-drafted design gave a promising improvement of the response of the tower-base bending, at only slightly higher levels than onshore wind turbines (which are not subject to wave forcing).

Subsequent analyses using the linear dynamic model revealed the reasons of the variation of the performance among the different designs. The optimum design was found to be not the one with the smallest wave load amplification in pitch-direction as predicted by the Response Amplitude Operator (RAO), the commonly used performance indicator in the conceptual design phase. With the harmonic response function, derived from the developed linearized low-order model, the dynamic characteristics of the optimum shape could be identified: The FOWT response amplitudes to unit waves along the tower centerline were visualized. The optimal design shows almost no fore-aft motion at the rotor hub, which means that the entire system, subject to wave loads, rotates about this point. As a result, the hub is almost stationary and the fluctuations of the power, the rotor speed, generator torque and blade pitch angle can be significantly reduced. An interpretation of this is that the surge and pitch response are out-of-phase, yielding a positive surge displacement when the pitch angle is negative.

In order to generally rate the suitability of a floating platform to support a wind turbine, a new performance indicator was developed: From control engineering, controllability measures are known, quantifying the necessary actuator performance for perfectly rejecting a given disturbance. A plot of this "least required actuator action" to reject the wave loads showed that the actuator action magnitude, especially at the wave frequencies, is proportional to the fatigue loads over the design space. Consequently, this indicator is one which is able to predict the platform design optimum obtained from the conducted optimization.

7.4 Outlook

The reduced-order simulation model SLOW, the parametric control routines, as well as the integrated optimization approach can be employed in further studies. Tailored designs, grown into the ocean environment, rejecting wind and wave loads with the help of advanced sensors and actuators, shall help to make floating wind more sustainable in the future. The following works, based on the presented thesis, are conceivable:

- Structural model: The blade elasticity was not included in the present work. However, works started on including modally reduced bodies for the blades and need to be continued in order to be able to compute the blade loads and represent azimuth-dependent loading on the rotor.

- Aerodynamic model: A more detailed model including azimuth dependency, aerodynamic states and sheared inflow should be implemented while keeping the efficiency. In certain conditions, unsteady aerodynamic effects can be of importance for model-based controller design and should be represented.

- Hydrodynamic model: Only one possible way of implementing the linearized Morison equation was realized. The influence of the cross-correlation between body motion and wave motion is to be analyzed as well as other, improved, formulations for the drag linearization.

- Experiments: The tool validation with scaled experiments showed that the magnitude of the response to wind and waves and the system dynamic properties are well predicted by the developed simulation model. However, the uncertainty related to all of the involved components, measurement devices and testing procedures needs to be assessed. This will go in line with the further improvement of the testing methodologies themselves, mitigating the issues related to the simultaneous scaling of aerodynamics and hydrodynamics.

- Control: A standard and an optimal controller were developed. A frequency-domain optimal controller should be tested, especially for a further reduction of the response to first-order wave loads.

- Optimization: The developed methodology can be applied to other concepts of floating wind turbines. Closed-loop optimization algorithms were tested in this work but not shown here in order to allow a better interpretation and visualization. The development of suitable cost functions and the selection of appropriate optimizers should be addressed using Systems Engineering approaches.

A Model Parameters

All parameters of the FOWT designs used in this work are listed in the following Sections A.1–A.3. Platform parameters always refer to the structural properties of the platform from keel to the tower base, without mooring lines.

A.1 Full-Scale TripleSpar Parameters

Table A.1 lists the parameters of the scaled simulation model used for the simulations of Chapter 6.

Table A.1: Model parameters of the full-scale TripleSpar concept with the DTU 10 MW RWT.

Parameter	Unit	Value
Platform mass (incl. ballast)	[kg]	2.82682×10^7
Tower mass	[kg]	4.36451×10^5
Nacelle mass	[kg]	4.46036×10^5
Rotor mass	[kg]	2.30598×10^5
Platform inertia about y w.r.t. its CM	[kgm^2]	1.8674×10^{10}
Nacelle inertia about y w.r.t. its CM	[kgm^2]	7.32634×10^6
Column spacing (to tower centerline)	[m]	26.0
Column diameter	[m]	15.0
Heave plate thickness	[m]	0.5
Heave plate diameter	[m]	22.5
Draft	[m]	54.464
Platform CM below SWL	[m]	36.018
Tower-base above SWL	[m]	25.0
Tower CM above SWL	[m]	63.72
Nacelle CM above SWL	[m]	118.08

Nacelle CM downwind of tower centerline	[m]	2.687
Shaft tilt	[deg]	5.0
Hub overhang (yaw axis to hub)	[m]	7.1
Vert. dist. from tower-top to shaft	[m]	2.75
Generator efficiency	[-]	0.94
Blade pitch actuator eigenfrequency	[Hz]	1.6
Blade pitch actuator damping ratio	[-]	0.8
Rotor max. power coefficient c_p	[-]	0.48
Gen. torque control k_Ω	[Nms^2/rad^2]	112.34
Rated rotor speed	[rpm]	9.6
Rated wind speed	[m/s]	11.4
Rotor opt. TSR	[-]	7.2
Rotor radius	[m]	89.17
Rotor inertia about shaft	[kgm^2]	1.59993×10^8
Gearbox ratio	[-]	0.02
Hub height	[m]	119.0
Tower outer radius @ tower-base	[m]	3.85
Tower inner radius @ tower-base	[m]	3.816
Tower outer radius @ tower-top	[m]	2.76
Tower inner radius @ tower-top	[m]	2.74
Tower length (elastic)	[m]	90.63
Tower Young's Modulus	[N/m^2]	2.1×10^{11}
Tower steel density	[kg/m^3]	8.5×10^3
Tower fore-aft (1st) modal stiffness	[N/m]	3.497×10^6
Tower fore-aft (1st) modal damping	[Ns/m]	1.8204×10^4
Platform displaced volume	[m^3]	2.9205×10^4
Hydrostatic stiffness in z	[N/m]	5.328×10^6
Hydrostatic stiffness about y (buoyancy + waterplane area) w.r.t. SWL	[Nm/rad]	-6.199×10^9
Added mass A_{11} @ surge eigenfrequency	[kg]	2.75×10^7
Added mass A_{33} @ heave eigenfrequency	[kg]	9.0×10^6

Added mass A_{55} @ pitch eigenfrequency w.r.t. SWL	[kgm^2]	1.085×10^{10}
Added mass A_{51} @ surge eigenfrequency w.r.t. SWL	[kgm]	2.605×10^8
Added mass A_{15} @ pitch eigenfrequency	[kgm]	2.455×10^8
Morison drag coefficient C_D for columns	[-]	0.4
Morison drag coefficient $C_{D,hp}$ for heave plates (vert.)	[-]	see Figure 3.16
Mooring line length	[m]	610.0
Mooring line mass per length in air	[kg/m]	594.0
Mooring line weight per length in water	[N/m]	5066.0
Number of mooring lines	[-]	3
Angle of first line towards downwind direction	[deg]	0.0
Fairleads radius	[m]	54.48
Fairleads above SWL	[m]	8.7
Anchor radius	[m]	600.0
Water depth	[m]	180.0

A.2 Model-Scale TripleSpar Parameters

Table A.2 shows the parameters of the scaled simulation model used for the simulations of Chapter 4.

Table A.2: Model parameters of scaled 1/60 TripleSpar simulation model.

Parameter	Unit	Value
Platform mass (incl. ballast)	[kg]	127.4
Tower mass	[kg]	2.25
RNA mass	[kg]	3.495
Platform inertia about y w.r.t. its CM	[kgm^2]	32.25
Tower inertia about y w.r.t. its CM	[kgm^2]	0.53
RNA inertia about y w.r.t. its CM	[kgm^2]	0.782
Column spacing (to tower centerline)	[m]	0.43
Column diameter	[m]	0.25
Heave plate thickness	[m]	0.003

Heave plate diameter	[m]	0.375
Draft	[m]	0.918
Platform CM below SWL	[m]	0.639
Tower-base above SWL	[m]	0.333
Tower CM above SWL	[m]	1.173
RNA CM above SWL	[m]	2.07
RNA CM downwind of tower centerlinex	[m]	0.0007
Rotor overall efficiency (elec.+mech.)	[-]	0.65
Rotor max. power coefficient	[-]	0.36
Minimum blade pitch angle	[deg]	1.5
Rated rotor speed	[rpm]	71.0
Rated wind speed	[m/s]	1.47
Rotor design-TSR	[-]	7.516
Rotor radius	[m]	1.486
Rotor inertia about shaft	[kgm^2]	0.2259
Gearbox ratio	[-]	1/5
Hub height	[m]	2.07
Tower fore-aft stiffness	[N/m]	1050.0
Tower fore-aft structural damping	[Ns/m]	8.04
Displaced volume	[m^3]	0.1362
Hydrostatic stiffness in z	[N/m]	1441.549
Hydrostatic stiffness about y (buoyancy + waterplane area) w.r.t. SWL	[Nm/rad]	-476.6247
Added mass A_{11} @ surge eigenfrequency	[kg]	126.2
Added mass A_{33} @ heave eigenfrequency	[kg]	36.85
Added mass A_{55} @ pitch eigenfrequency w.r.t. SWL	[kgm^2]	16.29
Added mass A_{51} @ surge eigenfrequency w.r.t. SWL	[kgm]	25.15
Added mass A_{15} @ pitch eigenfrequency	[kgm]	25.15
Additional stiffness in x @ SWL representing power cables	[N/m]	8.0
Additional stiffness about y representing power cables	[Nm/rad]	-25.0

Mooring line length	[m]	9.95
Mooring line mass per length in air	[kg/m]	0.1650
Mooring line weight per length in water	[N/m]	1.4072
Number of mooring lines	[-]	3
Angle of first line towards downwind direction	[deg]	0.0
Fairleads radius	[m]	0.908
Fairleads above SWL	[m]	0.145
Anchor radius	[m]	9.74
Water depth	[m]	3.0

A.3 Deep-Draft, Medium-Draft and Low-Draft Parameters

Table A.3 shows the parameters of the three selected platforms of the design space of Chapter 6. All values not included in Table A.3 are equal to the ones of Table A.1.

Table A.3: Model parameters of deep-draft, medium-draft and low-draft platforms.

Parameter	Deep-draft	Medium-draft	Low-draft
Platform mass (incl. ballast) [kg]	36.051×10^6	38.691×10^6	31.149×10^6
Platform inertia about y w.r.t. CM [kgm^2]	28.38×10^9	17.0×10^9	87.97×10^8
Column spacing (to tower centerline) [m]	15.0	19.0	24.0
Column radius [m]	6.76	8.56	10.81
Heave plate thickness [m]	4.5	4.5	4.5
Heave plate radius [m]	10.9	13.8	17.4
Draft [m]	78.48	49.95	21.94
Platform CM below SWL [m]	52.34	34.28	13.36
Displaced volume [m^3]	3.6837×10^4	3.9412×10^4	3.2055×10^4
Fairleads radius [m]		26.0	
Fairleads above SWL [m]		8.7	
Anchor radius [m]		571.5	

B Additional Results

The results, presented in the following, complete the results of Chapter 6. For the cases, where not all of the three selected platforms of Table 6.2, or not all of the three wind speeds could be shown, results can be found in the following sections. An additional sensitivity study, assessing the effect of the peak spectral wave period is subject of Section B.2.

B.1 Comparison of Controllers for Low-Draft Platform

Figure B.1 shows the PSD for the low-draft platform. It can be seen that the LQR performs better than the PI-controller also for this platform, as it does for the deep-draft platform, Figure 6.12. This confirms the validity of the selected LQR gains of Table 5.2.
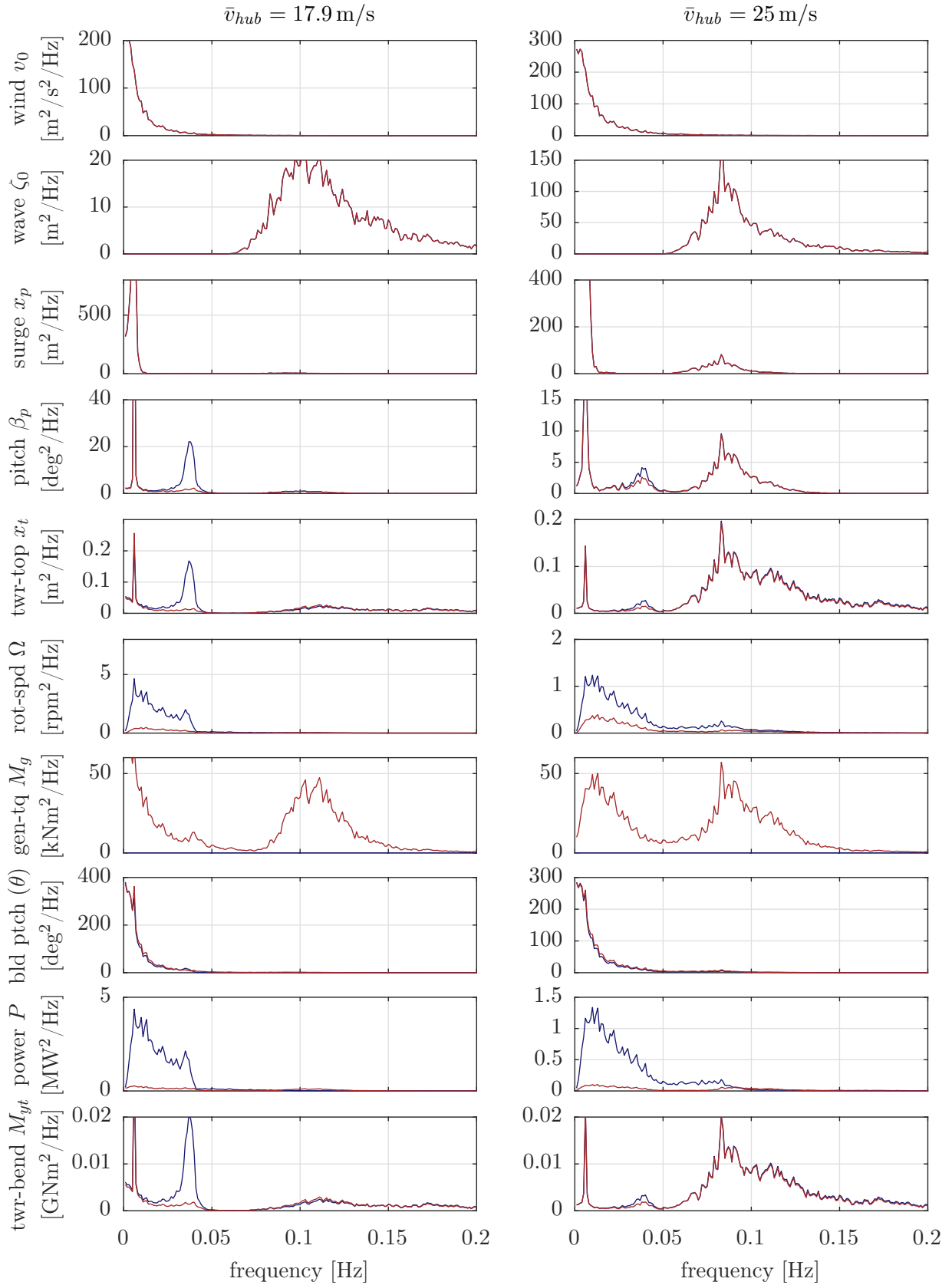
Figure B.1: Comparison of PI-controller (blue) and LQR (red) for $\bar{v}_{hub} = 17.9\,\mathrm{m/s}$ (left) and $\bar{v}_{hub} = 25.0\,\mathrm{m/s}$ (right) for low-draft $d = 24\,\mathrm{m}$.

B.2 Sensitivity to Wave Period

This analysis indicates whether the reason for the low-draft better rejecting the wave loads is due to the magnitude of its eigenfrequencies, only. This refers to a hypothetical claim that the low-draft performs better only because its eigenfrequencies are located more favorable than those of the other designs. Figure B.2 shows the response statistics for a single wind speed ($\bar{v}_{hub} = 13.9\,\text{m/s}$) for various wave peak spectral periods T_p as given in [143, Chapter 7]. It can be seen that a dependency on the wave period exists, mainly reflected on the platform pitch signal for platforms of larger column spacing. Larger wave periods tend to yield smaller responses. The fact that the low-draft platforms have a larger eigenfrequency in pitch (see Figure 6.7) does not explain why these platforms should give a smaller response for excitations closer to the eigenfrequencies. Eventually, this analysis shows that the platform eigenfrequencies are likely not the reason for the performance difference among the designs.
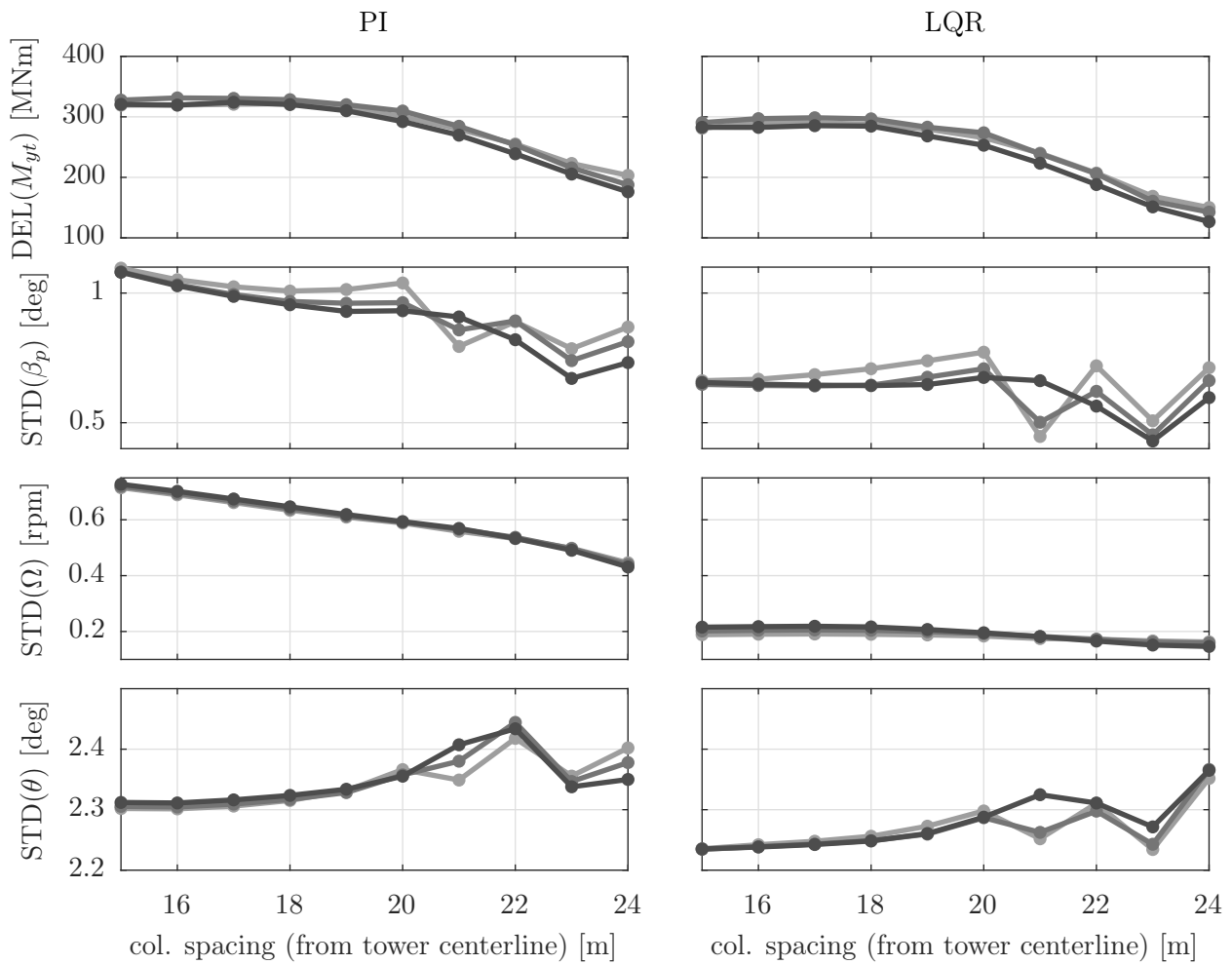
Figure B.2: Response statistics operational DLC1.2, Tab 2.1, for PI-controller (left) and LQR-controller (right) for three wave periods $\bar{v}_{hub} = 13.9\,\text{m/s}$ (darker colors for higher wave period).

B.3 Harmonic Response

Figure B.3 shows the harmonic response for the column spacings $d \leq 24\,\mathrm{m}$. In Figure 6.16 it could be observed that the instantaneous center of rotation due to sinusoidal wave excitations moves from positions far below SWL to the hub for the low-draft platform. In Figure B.3 it can be seen that the transition of the center of rotation happens only for the largest considered spacing of $d = 24\,\mathrm{m}$. For platforms of smaller breadth, the pitch motion is almost completely suppressed yielding to a surge-motion, only. In fact, this behavior can also yield a good performance in terms of tower-sectional loads since no moments due to gravity are present.
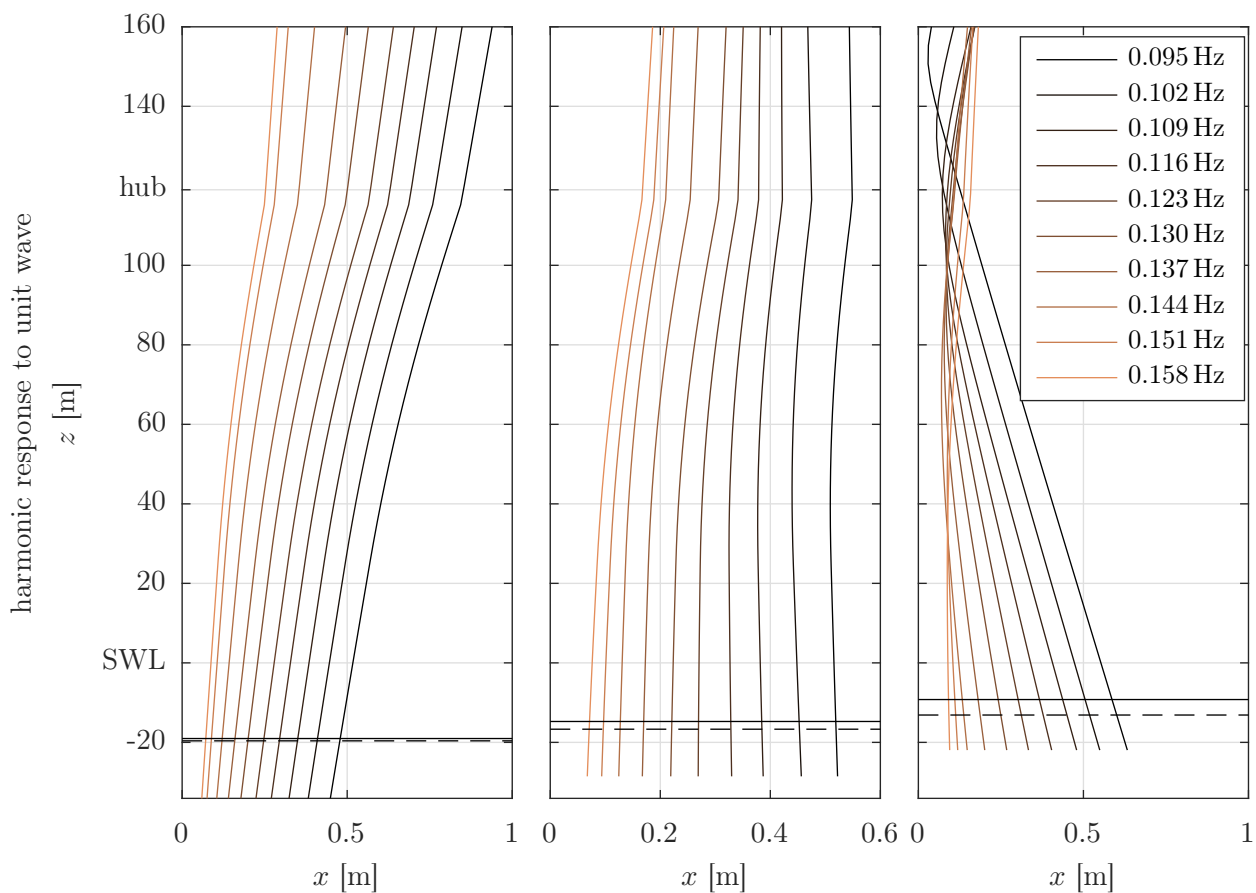
Figure B.3: Harmonic response for upper range of column spacings ($d = [22, 23, 24]\,\mathrm{m}$) of FOWT system in closed loop with PI-controller over typical wind frequencies (top) and wave frequencies (bottom) at $v_0 = 13.9\,\mathrm{m/s}$ with heave plate height $h_{hp} = 4.5\,\mathrm{m}$. Solid black line: FOWT overall center of mass, dashed black line: center of buoyancy. Compare to Figure 6.16.

B.4 Assessment of Numerical Models for Three Concepts

In Section 6.4.5, the code-to-code comparison was shown for three wind speeds for the deep-draft platform. For the medium-draft and the low-draft only the highest wind speed was shown. The others are included in this section. Figure B.4 shows modeling differences between FAST and SLOW, comparable to the deep-draft design. Here, however, the coupled surge, pitch and rotor speed resonance at the pitch-eigenfrequency is smaller than for the deep-draft.

At the above-rated wind speed of $\bar{v}_{hub} = 17.9\,\mathrm{m/s}$, Figure B.5 shows a remarkably good agreement between the models with only a small underprediction of the first-order wave response by the SLOW models.

The low-draft shape at the below-rated wind speed, shown in Figure B.6, does not have the coupled resonance of β_p and Ω at the platform-pitch mode anymore for FAST. Above rated, Figure B.7 the agreement is still good, with FAST showing slightly more energy at the lower part of the wave spectrum. The reason for this is not clear. The aerodynamic forcing seems to be of higher relative importance as the differences between the rotational sampling for SLOW and the fully turbulent FAST model is more visible here.
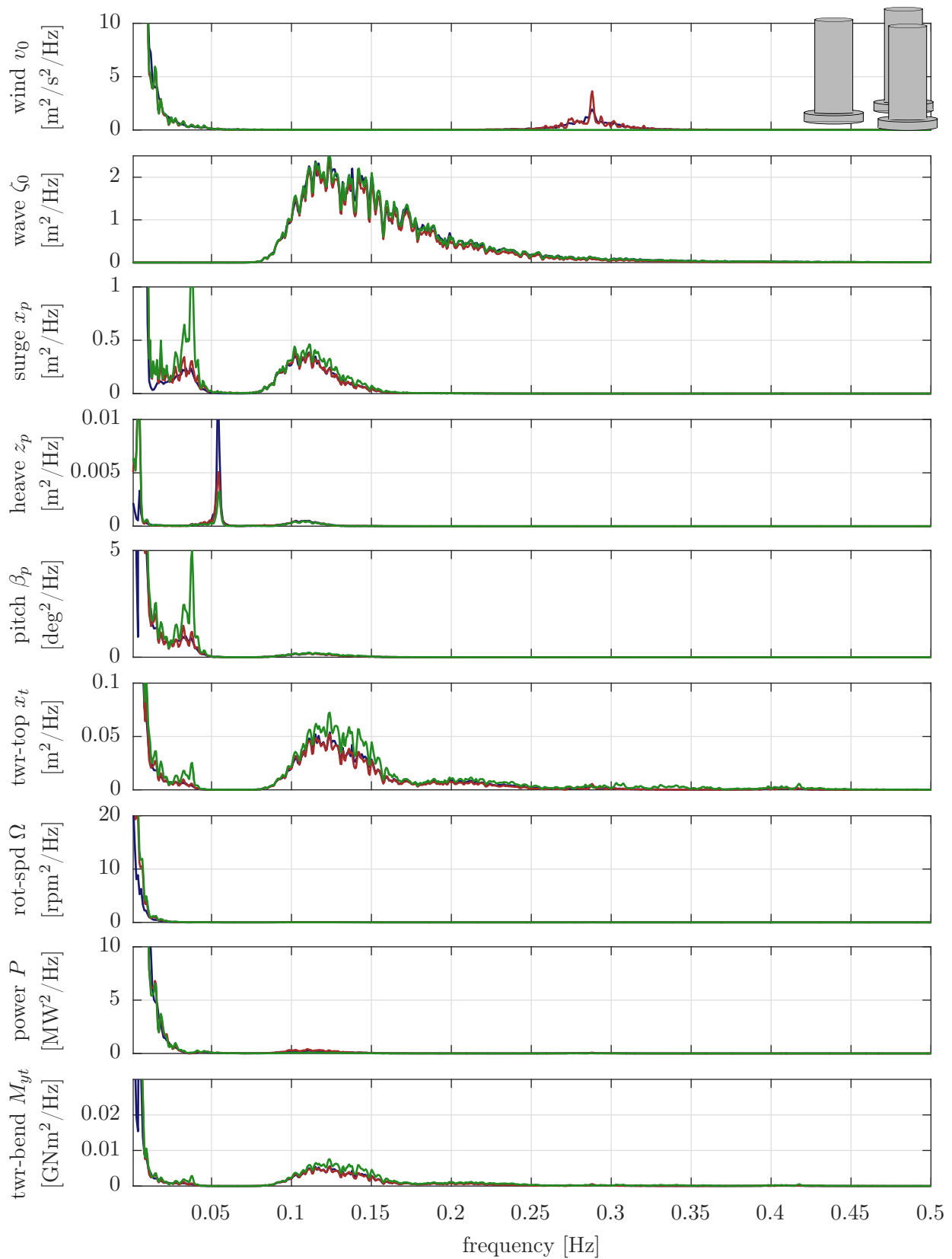
Figure B.4: Model comparison $\bar{v}_{hub} = 7.1\,\mathrm{m/s}$, $H_s = 1.7\,\mathrm{m}$, $T_p = 8.0\,\mathrm{s}$ for medium draft $d = 19\,\mathrm{m}$: linear model, frequency-domain (blue), nonlinear model, time-domain (red), FAST, time-domain (green).
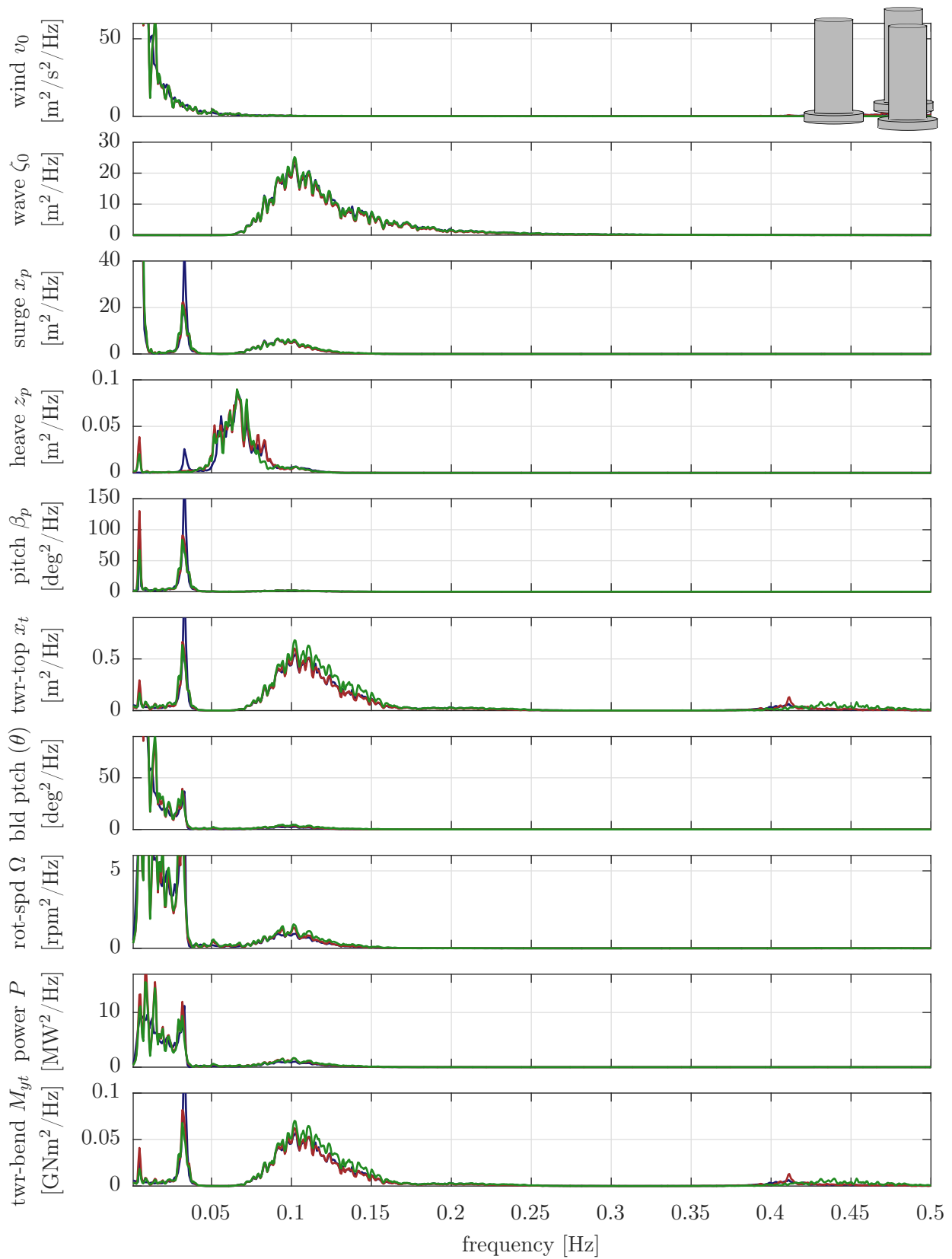
Figure B.5: Model comparison $\bar{v}_{hub} = 17.9\,\text{m/s}$, $H_s = 4.3\,\text{m}$, $T_p = 10.0\,\text{s}$, medium draft $d = 19\,\text{m}$: linear model, frequency-domain (blue), nonlinear model, time-domain (red), FAST, time-domain (green).
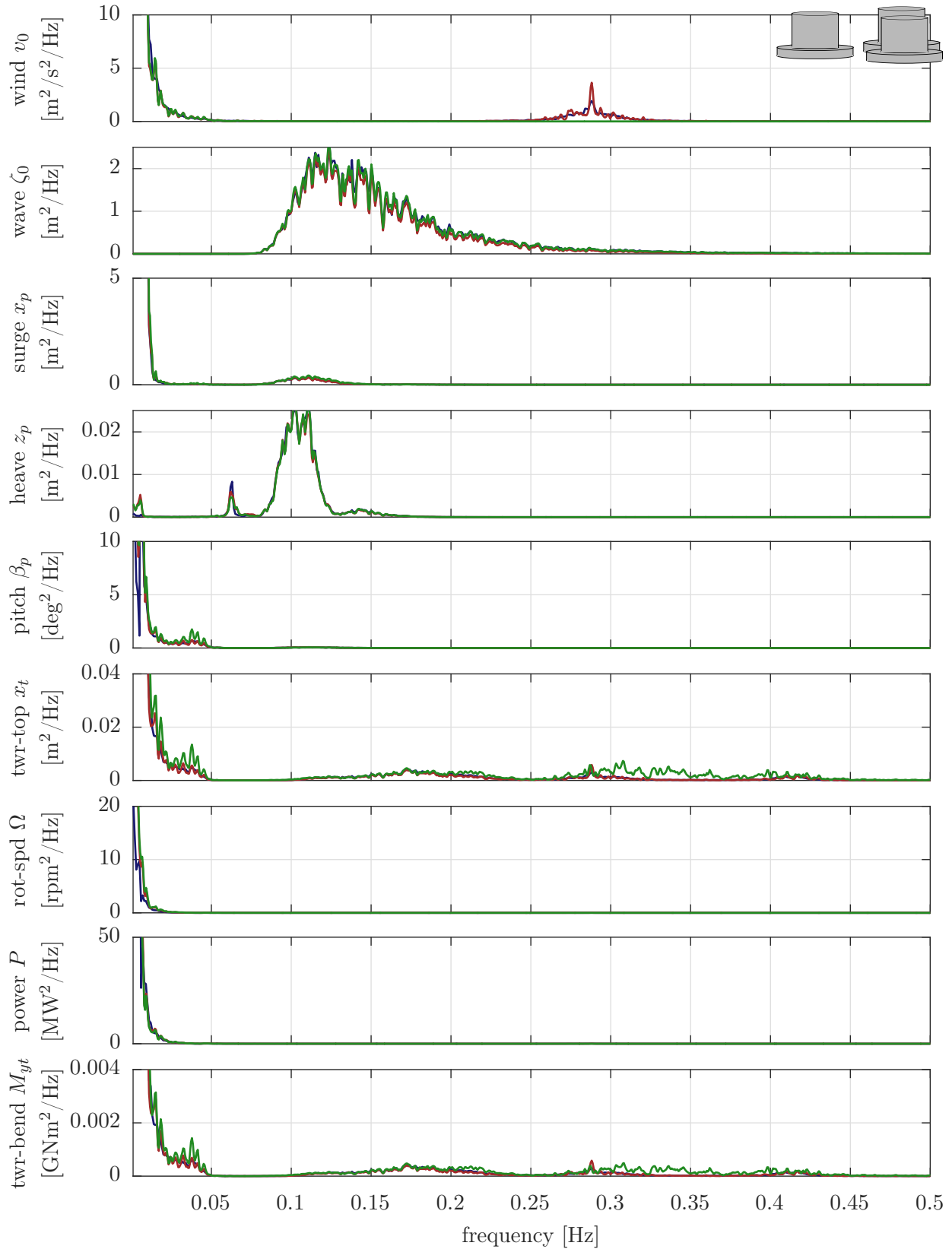
Figure B.6: Model comparison $\bar{v}_{hub} = 7.1\,\mathrm{m/s}$, $H_s = 1.7\,\mathrm{m}$, $T_p = 8.0\,\mathrm{s}$ for low-draft $d = 24\,\mathrm{m}$: linear model, frequency-domain (blue), nonlinear model, time-domain (red), FAST, time-domain (green).
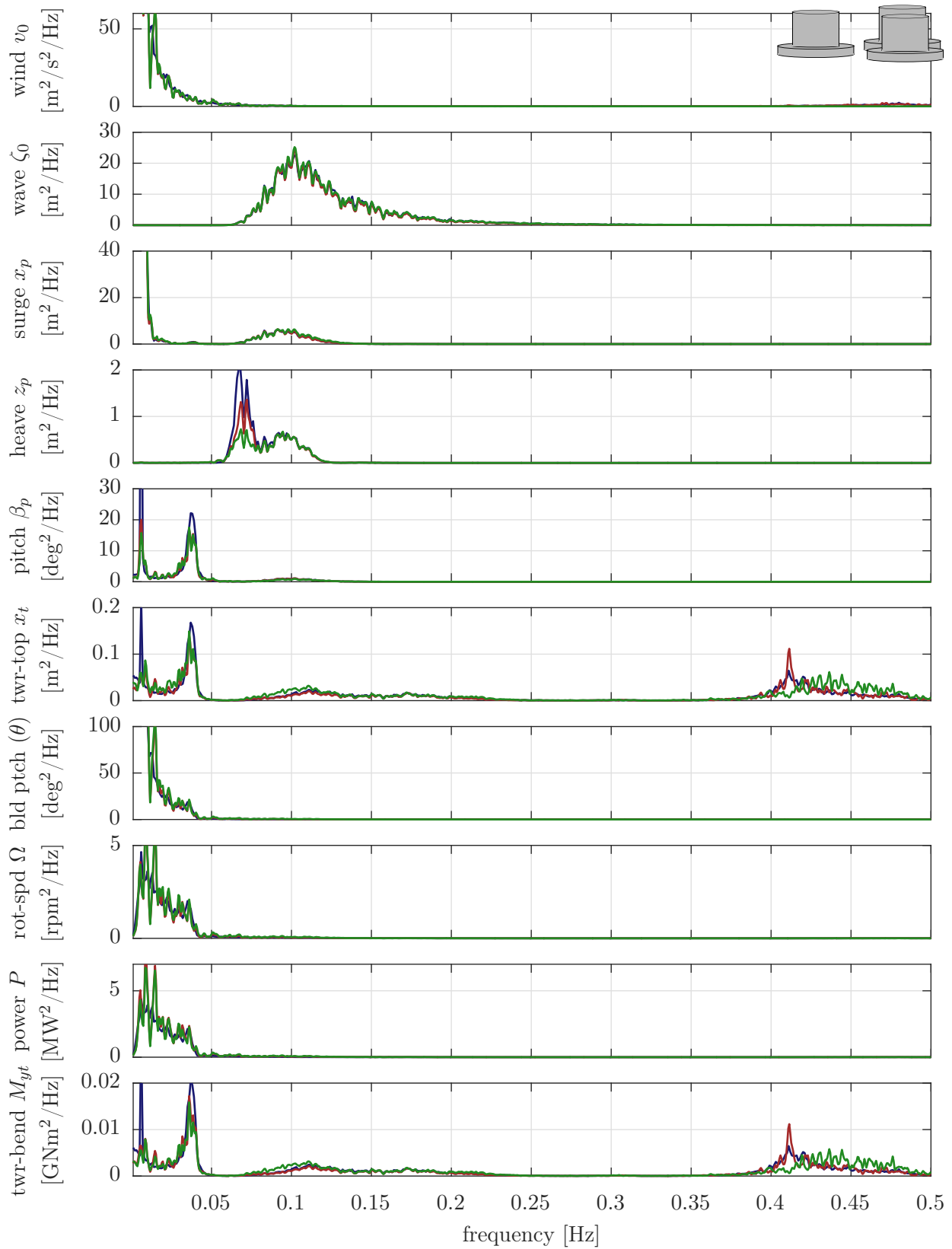
Figure B.7: Model comparison $\bar{v}_{hub} = 17.9\,\text{m/s}$, $H_s = 4.3\,\text{m}$, $T_p = 10.0\,\text{s}$ for low-draft $d = 24\,\text{m}$: linear model, frequency-domain (blue), nonlinear model, time-domain (red), FAST, time-domain (green).

Bibliography

[1] James, R. and Costa Ros, M. Floating offshore wind: Market and technology review. Tech. rep., The Carbon Trust, 2015. URL `http://www.carbontrust.com/media/670664/floating-offshore-wind-market-technology-review.pdf`.

[2] Matha, D., Pérez Moran, G., Müller, K., and Lemmer, F. Comparative analysis of industrial design methodologies for fixed-bottom and floating wind turbines. In: *Proceedings of the ASME 35th International Conference on Ocean, Offshore and Arctic Engineering*. Busan, Korea, 2016. doi:10.1115/OMAE2016-54920.

[3] Müller, K., Lemmer, F., Borisade, F., Kretschmer, M., Gruber, J., Hagemann, L., Nguyen, N.-D., and Vita, L. LIFES50+ D7.4 State-of-the-art FOWT design practice and guidelines. Tech. rep., University of Stuttgart, 2015. URL `http://lifes50plus.eu/wp-content/uploads/2015/11/GA_640741_LIFES50_D7.4.pdf`.

[4] Henderson, A. *Analysis tools for large floating offshore wind farms*. Ph.D. thesis, University College London, 2000.

[5] Sclavounos, P. D., Tracy, C., and Lee, S. Floating offshore wind turbines: Responses in a seastate, pareto optimal designs and economic assessment. In: *Proceedings of the ASME 27th International Conference on Offshore Mechanics and Arctic Engineering*. 2007. doi:10.1115/OMAE2008-57056.

[6] Jonkman, J. and Matha, D. Dynamics of offshore floating wind turbines–Analysis of three concepts. *Wind Energy*, vol. 14(4):pp. 557–569, 2011. doi:10.1002/we.442.

[7] Fylling, I. and Berthelsen, P. A. Windopt – An optimization tool for floating support structures for deep water wind turbines. In: *Proceedings of the ASME 30th International Conference on Ocean, Offshore and Arctic Engineering*. ASME, Rotterdam, Netherlands, 2011. doi:10.1115/OMAE2011-49985.

[8] Bachynski, E. *Design and dynamic analysis of tension leg platform wind turbines*. Ph.D. thesis, NTNU, 2014. ISBN 978-82-326-0096-0.

[9] Hall, M., Buckham, B., and Crawford, C. Evolving offshore wind: A genetic algorithm-based support structure optimization framework for floating wind turbines. In: *Proceedings of the OCEANS MTS/IEEE*. IEEE, Bergen, Norway, 2013. doi:10.1109/OCEANS-Bergen.2013.6608173.

[10] Larsen, T. J. and Hanson, T. D. A method to avoid negative damped low frequent tower

vibrations for a floating, pitch controlled wind turbine. *Journal of Physics: Conference Series*, vol. 75, 2007. doi:10.1088/1742-6596/75/1/012073.

[11] Jonkman, J. Influence of control on the pitch damping of a floating wind turbine. In: *Proceedings of the 46th AIAA Aerospace Sciences Meeting and Exhibit*. Reno, USA, 2008. doi:10.2514/6.2008-1306.

[12] Fischer, B. Reducing rotor speed variations of floating wind turbines by compensation of non-minimum phase zeros. *IET Renewable Power Generation*, vol. 7(4):pp. 413–419, 2013. doi:0.1049/iet-rpg.2012.0263.

[13] Karimirad, M. and Moan, T. A simplified method for coupled analysis of floating offshore wind turbines. *Marine Structures*, vol. 27(1):pp. 45–63, 2012. doi:10.1016/j.marstruc.2012.03.003.

[14] Betti, G., Farina, M., Marzorati, A., and Scattolini, R. Modeling and control of a floating wind turbine with spar buoy platform. In: *Proceedings of the Energy Conference and Exhibition (ENERGYCON), IEEE International*, pp. 189–194. Florence, Italy, 2012. ISBN 9781467314541.

[15] Jonkman, J. *Dynamics modeling and loads analysis of an offshore floating wind turbine*. Ph.D. thesis, University of Colorado, 2007, URL `http://www.nrel.gov/docs/fy08osti/41958.pdf`.

[16] Lupton, R. *Frequency-domain modelling of floating wind turbines*. Ph.D. thesis, University of Cambridge, 2014, URL `https://www.repository.cam.ac.uk/bitstream/handle/1810/252880/thesis.pdf`.

[17] Pineda, I. and Tardieu, P. Wind in power - 2016 European statistics. Tech. rep., WindEurope, 2017. URL `https://windeurope.org/wp-content/uploads/files/about-wind/statistics/WindEurope-Annual-Statistics-2016.pdf`.

[18] EWEA. Wind energy scenarios for 2030. Tech. rep., European Wind Energy Association, 2015. URL `http://www.ewea.org/fileadmin/files/library/publications/reports/EWEA-Wind-energy-scenarios-2030.pdf`.

[19] International Energy Agency. World energy outlook 2017. Tech. rep., 2017. URL `http://www.iea.org/Textbase/npsum/weo2017SUM.pdf`.

[20] Arapogianni, A., Genachte, A.-B., Manzanas Ochagavia, R., Pascual Vergara, J., Castell, D., Rodriguez Tsouroukdissian, A., Korbijn, J., Bolleman, N. C. F., Huera-Huarte, F., Schuon, F., Ugarte, A., Sandberg, J., de Laleu, V., Maciel, J., Tunbjer, A., Roth, R., de la Gueriviere, P., Coulombeau, P., Jedrec, S., Philippe, C., Voutsinas, S., Weinstein, A., Vita, L., Byklum, E., Hurley, W. L., and Grubel, H. Deep water - The next step for offshore wind energy. Tech. rep., European Wind Energy Association, 2013. ISBN 9782930670041.

[21] Hanson, T. D., Skaare, B., Yttervik, R., Nielsen, F. G., and Havmøller, O. Comparison of measured and simulated responses at the first full scale floating wind turbine Hywind. In:

Proceedings of the European Wind Energy Association Annual Event. Brussels, Belgium, 2011. ISBN 9781618399915.

[22] Roddier, D., Cermelli, C., Aubault, A., and Peiffer, A. Summary and conclusions of the full life-cycle of the WindFloat FOWT prototype project. In: *Proceedings of the ASME 36th International Conference on Ocean, Offshore and Arctic Engineering*. Trondheim, Norway, 2017. doi:10.1115/OMAE2017-62561.

[23] Wang, C. M., Utsunomiya, T., Wee, S. C., and Choo, Y. S. Research on floating wind turbines: A literature survey. *The IES Journal Part A: Civil & Structural Engineering*, vol. 3(4):pp. 267–277, 2010. doi:10.1080/19373260.2010.517395.

[24] Tande, J. O. G., Merz, K., Paulsen, U. S., and Svendsen, H. G. Floating offshore turbines. *Wiley Interdisciplinary Reviews: Energy and Environment*, vol. 4(3):pp. 213–228, 2015. doi:10.1002/wene.130.

[25] Roddier, D., Cermelli, C., Weinstein, J., Byklum, E., Atcheson, M., Utsunomiya, T., Jorde, J., and Borgen, E. State-of-the-art. In: M. Atcheson and J. Cruz, eds., *Floating Offshore Wind Energy*, pp. 271–332. Springer, 2016. ISBN 978-3-319-29398-1. doi:10.1007/978-3-319-29398-1.

[26] Matha, D. *Impact of aerodynamics and mooring system on dynamic response of floating wind turbines*. Ph.D. thesis, University of Stuttgart, 2016. ISBN 978-3-8439-3113-7.

[27] Liu, Y., Li, S., Yi, Q., and Chen, D. Developments in semi-submersible floating foundations supporting wind turbines: A comprehensive review. *Renewable and Sustainable Energy Reviews*, vol. 60:pp. 433–449, 2016. doi:10.1016/j.rser.2016.01.109.

[28] DNV. DNV-OS-J103: Design of floating wind turbine structures. 2013.

[29] Robertson, A. and Jonkman, J. Loads analysis of several offshore floating wind turbine concepts. In: *Proceedings of the 21st International Ocean and Polar Engineering Conference*, pp. 443–450. Maui, USA, 2011. ISBN 9781880653968.

[30] Bottasso, C. L., Bortolotti, P., Croce, A., and Gualdoni, F. Integrated aero-structural optimization of wind turbines. *Multibody System Dynamics*, vol. 38(4):pp. 317–344, 2016. doi:10.1007/s11044-015-9488-1.

[31] Pavese, C., Tibaldi, C., Zahle, F., and Kim, T. Aeroelastic multidisciplinary design optimization of a swept wind turbine blade. *Wind Energy*, vol. 20(12):pp. 1941–1953, 2017. doi:10.1002/we.2131.

[32] Birk, L., Clauss, G. F., and Lee, J. Y. Practical application of global optimization to the design of offshore structures. In: *Proceedings of the ASME 23rd International Conference on Offshore Mechanics and Arctic Engineering*. Vancouver, Canada, 2004. doi:10.1115/OMAE2004-51225.

[33] Kühn, M. *Dynamics and design optimization of offshore wind energy conversion systems*. Ph.D. thesis, Delft University of Technology, 2003. ISBN 9076468079.

[34] Häfele, J. and Rolfes, R. Approaching the ideal design of jacket substructures for offshore

wind turbines with a Particle Swarm Optimization algorithm. In: *Proceedings of the 26th International Ocean and Polar Engineering Conference*, pp. 156–163. Rhodes, Greece, 2016. ISBN 9781880653883.

[35] Schafhirt, S., Zwick, D., and Muskulus, M. Reanalysis of Jacket support structure for computer-aided optimization of offshore wind turbines with a Genetic Algorithm. *Journal of Ocean and Wind Energy*, vol. 1(4):pp. 209–216, 2014. doi:10.17736/23103604.

[36] Chew, K.-h., Tai, K., and Muskulus, M. Optimization of offshore wind turbine support structures using analytical gradient-based method. *Energy Procedia*, vol. 80:pp. 100–107, 2015. doi:10.1016/j.egypro.2015.11.412.

[37] Yeter, B., Garbatov, Y., and Soares, C. G. Risk-based multi-objective optimisation of a monopile offshore wind turbine support structure. In: *Proceedings of the ASME 36th International Conference on Ocean, Offshore and Arctic Engineering*. Trondheim, Norway, 2017. doi:10.1115/OMAE2017-617565.

[38] Kurz, T. *Symbolic modeling and optimization of elastic multibody systems*. Ph.D. thesis, University of Stuttgart, 2013. ISBN 9783844020465.

[39] Jonkman, J. and Buhl, M. FAST user's guide. Tech. rep., National Renewable Energy Laboratory, Boulder, USA, 2005.

[40] Sandner, F., Schlipf, D., Matha, D., and Cheng, P. W. Integrated optimization of floating wind turbine systems. In: *Proceedings of the ASME 33rd International Conference on Ocean, Offshore and Arctic Engineering*. San Francisco, USA, 2014. doi: 10.1115/OMAE2014-24244.

[41] DNV. DNV-OS-C103: Structural design of column stabilised units. 2012.

[42] Bak, C., Zahle, F., Bitsche, R., Kim, T., Yde, A., Henriksen, L., Natarajan, A., and Hansen, M. Description of the DTU 10MW reference wind turbine. Tech. rep., Technical University of Denmark, Roskilde, Denmark, 2013.

[43] NWTC. NWTC information portal (FAST v8). 2016. URL `https://nwtc.nrel.gov/FAST8`.

[44] Burton, T., Sharpe, D., Jenkins, N., and Bossanyi, E. *Wind Energy Handbook*. John Wiley and Sons, Oxford, 2nd edn., 2011. ISBN 978-0-470-69975-1.

[45] Dirlik, T. *Application of computers in fatigue analysis*. Ph.D. thesis, University of Warwick, 1985, URL `http://go.warwick.ac.uk/wrap/2949`.

[46] Borgman, L. E. The spectral density for ocean wave forces. In: *Proceedings of the Santa Barbara Coastal Engineering Conference*, pp. 147–182. Santa Barbara, USA, 1965.

[47] Argyriadis, K. and Klose, M. Interaction of load analysis and structural design of offshore wind turbines. In: *Proceedings of the ASME 25th International Conference on Offshore Mechanics and Arctic Engineering*. Hamburg, Germany, 2006. doi: 10.1115/OMAE2006-92081.

[48] Muskulus, M. Why design load calculations for offshore wind turbine support structures

cannot use load time series from moving rotors. In: *Proceedings of the 25th International Ocean and Polar Engineering Conference*, pp. 525–529. Kona, USA, 2015. ISBN 9781880653890.

[49] van der Tempel, J. *Design of support structures for offshore wind turbines*. Ph.D. thesis, Delft University of Technology, 2006. ISBN 9076468117.

[50] Matha, D., Cruz, J., Masciola, M., Bachynski, E. E., Atcheson, M., Goupee, A. J., Gueydon, S., and Robertson, A. N. Modelling of Floating Offshore Wind Technologies. In: M. Atcheson and J. Cruz, eds., *Floating Offshore Wind Energy*, pp. 133–240. Springer, 2016. ISBN 978-3-319-29398-1. doi:10.1007/978-3-319-29398-1.

[51] Jonkman, J. and Musial, W. Offshore Code Comparison Collaboration (OC3) for IEA Task 23 Offshore Wind Technology and Deployment. Tech. rep., National Renewable Energy Laboratory, Boulder, USA, 2010.

[52] Robertson, A., Jonkman, J., and Musial, W. Offshore Code Comparison Collaboration, Continuation: Phase II results of a floating semisubmersible wind system. In: *Proceedings of the European Wind Energy Association Offshore Wind Conference and Exhibition*. Frankfurt, Germany, 2013.

[53] Robertson, A., Jonkman, J., Vorpahl, F., Popko, W., Qvist, J., Frøyd, L., Chen, X., Azcona, J., Uzunoglu, E., Guedes Soares, C., Luan, C., Yutong, H., Pencheng, F., Yde, A., Larsen, T., Nichols, J., Buils Urbano, R., Lei, L., Nygaard, T. A., Manolas, D., Heege, A., Ringdalen Vatne, S., Ormberg, H., Duarte, T., Godreau, C., Fabricius Hansen, H., Wedel Nielsen, A., Riber, H., Le Cunff, C., Beyer, F., Yamaguchi, A., Jin Jung, K., Shin, H., Shi, W., Park, H., Alves, M., and Guérinel, M. Offshore Code Comparison Collaboration Continuation within IEA Wind Task 30: Phase II results regarding a floating semisubmersible wind system. In: *Proceedings of the ASME 33rd International Conference on Ocean, Offshore and Arctic Engineering*. San Francisco, USA, 2014. doi:10.1115/OMAE2014-24040.

[54] Robertson, A., Wendt, F., Jonkman, J. M., Popko, W., Dagher, H. J., Gueydon, S., Qvist, J., Vittori, F., Azcona, J., Uzunoglu, E., Soares, C. G., Harries, R., Yde, A., Galinos, C., Hermans, K., de Vaal, B. J., Bozonnet, P., Bouy, L., Bayati, I., Bergua, R., Galvan, J., Mendikoa, I., Barrera, C., Shin, H., Oh, S., Molins, C., and Debruyne, Y. OC5 project phase II: Validation of global loads of the DeepCwind floating semisubmersible wind turbine. *Energy Procedia*, vol. 137:pp. 38–57, 2017. doi:10.1016/j.egypro.2017.10.333.

[55] Cordle, A. and Jonkman, J. State of the art in floating wind turbine design tools. In: *Proceedings of the 21st International Ocean and Polar Engineering Conference*. Maui, USA, 2011. ISBN 9781880653968.

[56] Matha, D., Schlipf, M., Pereira, R., and Jonkman, J. Challenges in simulation of aerodynamics, hydrodynamics, and mooring-line dynamics of floating offshore wind turbines. In: *Proceedings of the 21st International Ocean and Polar Engineering Conference*. Maui, USA, 2011. ISBN 9781880653968.

[57] Bae, Y. H., Kim, M. H., Im, S. W., and Chang, I. H. Aero-elastic-control-floater-mooring coupled dynamic analysis of floating offshore wind turbines. In: *Proceedings of the 21st International Ocean and Polar Engineering Conference*, pp. 429–435. Maui, USA, 2011. ISBN 9781880653968.

[58] Lemmer, F., Müller, K., Pegalajar-Jurado, A., Borg, M., and Bredmose, H. LIFES50+ D4.1: Simple numerical models for upscaled design. Tech. rep., University of Stuttgart, 2016.

[59] Schwertassek, R. and Wallrapp, O. *Dynamik flexibler Mehrkörpersysteme: Methoden der Mechanik zum rechnergestützten Entwurf und zur Analyse mechatronischer Systeme*. Grundlagen und Fortschritte der Ingenieurwissenschaften. Friedr. Vieweg und Sohn, 1999. ISBN 978-3-322-93976-0.

[60] Hansen, M. O. L. *Aerodynamics of Wind Turbines*. Earthscan, 2nd edn., 2000. ISBN 978-1-84407-438-9.

[61] Hansen, M. O. L., Sørensen, J. N., Voutsinas, S., Sørensen, N., and Madsen, H. A. State of the art in wind turbine aerodynamics and aeroelasticity. *Progress in Aerospace Sciences*, vol. 42(4):pp. 285–330, 2006. doi:10.1016/j.paerosci.2006.10.002.

[62] Guntur, S., Jonkman, J., Jonkman, B., Wang, Q., Sprague, M. A., Hind, M., Sievers, R., and Schreck, S. J. A validation and code-to-code verification of FAST for a megawatt-scale wind turbine with aeroelastically tailored blades. *Wind Energy Science*, vol. 2:pp. 443–468, 2017. doi:10.5194/wes-2-443-2017.

[63] Buils Urbano, R., Nichols, J., Livingstone, M., Cruz, J., Alexandre, A., and Mccowen, D. Advancing numerical modelling of floating offshore wind turbines to enable efficient structural design. In: *Proceedings of the European Wind Energy Association Offshore Wind Conference and Exhibition*. Frankfurt, Germany, 2013.

[64] Luan, C., Gao, Z., and Moan, T. Development and verification of a time-domain approach for determining forces and moments in structural components of floaters with an application to floating wind turbines. *Marine Structures*, vol. 51:pp. 87–109, 2017. doi:10.1016/j.marstruc.2016.10.002.

[65] Borg, M., Hansen, A. M., and Bredmose, H. Floating substructure flexibility of large-volume 10MW offshore wind turbine platforms in dynamic calculations. *Journal of Physics: Conference Series*, vol. 753, 2016. doi:10.1088/1742-6596/753/8/082024.

[66] Borg, M., Bredmose, H., and Hansen, A. M. Elastic deformations of floaters for offshore wind turbines: dynamic modelling and sectional load calculations. In: *Proceedings of the ASME 36th International Conference on Ocean, Offshore and Arctic Engineering*. Trondheim, Norway, 2017. doi:10.1115/OMAE2017-61466.

[67] Knudsen, T. and Bak, T. Simple model for describing and estimating wind turbine dynamic inflow. *Proceedings of the American Control Conference*, pp. 640–646, 2013. doi:10.1109/ACC.2013.6579909.

[68] Snel, H. and Schepers, J. Joint investigation of dynamic inflow effects and implementation of an engineering method. Tech. rep., ECN, 1995. URL `https://www.ecn.nl/publications/E/1995/ECN-C--94-107`.

[69] Merz, K., Muskulus, M., and Moe, G. A simple frequency-domain method for stress analysis of stall-regulated wind turbines. *Wind Energy*, vol. 15:pp. 773–798, 2012. doi:10.1002/we.504.

[70] NWTC. NWTC information portal (AirfoilPrep). 2014. URL `https://nwtc.nrel.gov/AirFoilPrep`.

[71] Snel, H. Review of the present status of rotor aerodynamics. *Wind Energy*, vol. 1:pp. 46–69, 1998.

[72] Sant, T. *Improving BEM-based aerodynamic models in wind turbine design codes*. Ph.D. thesis, Delft University of Technology, 2007. ISBN 9789993204831.

[73] Vaal, J. B. D., Hansen, M. O. L., and Moan, T. Effect of wind turbine surge motion on rotor thrust. *Wind Energy*, vol. 17(1):pp. 105–121, 2014. doi:10.1002/we.1562.

[74] Bayati, I., Belloli, M., Bernini, L., and Zasso, A. A formulation for the unsteady aerodynamics of floating wind turbines, with focus on the global system dynamics. In: *Proceedings of the ASME 36th International Conference on Ocean, Offshore and Arctic Engineering*. Trondheim, Norway, 2017. doi:10.1115/OMAE2017-61925.

[75] Suzuki, A. and Hansen, A. Generalized dynamic wake model for Yawdyn. In: *Proceedings of the AIAA18th Wind Energy Symposium*, pp. 186–191. Reno, USA, 1999. doi:10.2514/6.1999-41.

[76] Moriarty, P. J. and Hansen, C. AeroDyn theory manual. Tech. rep., National Renewable Energy Laboratory, Golden, USA, 2005. URL `https://nwtc.nrel.gov/system/files/AD_Theory.pdf`.

[77] Sebastian, T. *The aerodynamic and near wake of an offshore floating horizontal axis wind turbine*. Ph.D. thesis, University of Massachussetts, Amherst, USA, 2012, URL `https://scholarworks.umass.edu/open_access_dissertations/516/`.

[78] Manolas, D. *Hydro-aero-elastic analysis of offshore wind turbines*. Ph.D. thesis, National Technical University of Athens, 2015, URL `https://dspace.lib.ntua.gr/dspace2/bitstream/handle/123456789/42037/PhD_Manolas_DI_2015_Hydro-Aero-Elastic_Analysis_of_Offshore_WTs.pdf`.

[79] Lennie, M., Marten, D., Pechlivanoglou, G., Nayeri, C. N., and Paschereit, C. O. Modern methods for investigating the stability of a pitching floating platform wind turbine. *Journal of Physics: Conference Series*, vol. 753, 2016. doi:10.1088/1742-6596/753/8/082012.

[80] Bekiropoulos, D., Rieß, R. M., Lutz, T., and Krämer, E. Simulation of unsteady aerodynamic effects on floating offshore wind turbines. In: *Proceedings of the German Wind Energy Conference DEWEK*. Bremen, Germany, 2012.

[81] Tran, T. T. and Kim, D. H. The platform pitching motion of floating offshore wind

turbine: A preliminary unsteady aerodynamic analysis. *Journal of Wind Engineering and Industrial Aerodynamics*, vol. 142:pp. 65–81, 2015. doi:10.1016/j.jweia.2015.03.009.

[82] Sant, T., Bonnici, D., Farrugia, R., and Micallef, D. Measurements and modelling of the power performance of a model floating wind turbine under controlled conditions. *Wind Energy*, vol. 18:pp. 811–834, 2015. doi:10.1002/we.1730.

[83] Lin, L., Vassalos, D., and Dai, S. CFD simulation of aerodynamic performance of floating offshore wind turbine compared with BEM method. In: *Proceedings of the 26th International Ocean and Polar Engineering Conference*, pp. 568–575. Kona, USA, 2016. ISBN 978-1-880653-88-3.

[84] Wu, C.-H. K. and Nguyen, V.-T. Aerodynamic simulations of offshore floating wind turbine in platform-induced pitching motion. *Wind Energy*, vol. 20(5):pp. 835–858, 2017. doi:10.1002/we.2066.

[85] Matha, D., Wendt, F., Werner, M., Cheng, P. W., and Lutz, T. Aerodynamic inflow conditions on floating offshore wind turbine blades for airfoil design purposes. In: *Proceedings of the 22nd International Ocean and Polar Engineering Conference*, pp. 480–488. Rhodes, Greece, 2012. ISBN 9781880653944.

[86] Pedersen, M. and Fossen, T. Efficient nonlinear wind-turbine modeling for control applications. In: *Proceedings of the 7th International Conference on Mathematical Modelling*. Vienna, Austria, 2012. doi:10.3182/20120215-3-AT-3016.00046.

[87] Sønderby, I. B. *Low-order aeroelastic models of wind turbines for controller design*. Ph.D. thesis, Technical University of Denmark, 2013, URL `http://orbit.dtu.dk/files/74567482/thesis..PDF`.

[88] Matha, D., Lemmer, F., and Muskulus, M. Hydrodynamics of Offshore Wind Turbines (in production). In: P. Veers, ed., *Wind Power Modelling: Turbines and Systems*, vol. 2. The IET, 2019.

[89] McCormick, M. E. *Ocean Engineering Mechanics*. Cambridge University Press, 2010. ISBN 978-0-521-85952-3.

[90] Journée, J. and Massie, W. W. *Offshore Hydromechanics*. Delft University of Technology, 1st edn., 2001. URL `https://ocw.tudelft.nl/wp-content/uploads/OffshoreHydromechanics_Journee_Massie.pdf`.

[91] Newman, J. N. *Marine Hydrodynamics*. MIT Press, Cambridge, USA, 1977. ISBN 978-0-262-14026-3.

[92] Sarpkaya, T. *Wave Forces on Offshore Structures*. Cambridge University Press, 1st edn., 2010. ISBN 978-0-521-89625-2.

[93] Cummins, W. The impulse response function and ship motion. In: *Proceedings of the Symposium on Ship Theory*. Hamburg, Germany, 1962.

[94] Ogilvie, T. F. Recent progress toward the understanding and prediction of ship motions. In: *Proceedings of the Fifth Symposium on Naval Hydrodynamics*. Bergen, Norway, 1964.

[95] Jonkman, J., Robertson, A., and Hayman, G. HydroDyn user's guide and theory manual. Tech. rep., National Renewable Energy Laboratory, Boulder, USA, 2014. URL `https://nwtc.nrel.gov/system/files/HydroDyn_Manual_0.pdf`.

[96] Pegalajar-Jurado, A., Borg, M., and Bredmose, H. An efficient frequency-domain model for quick load analysis of floating offshore wind turbines. *Wind Energy Science*, vol. 3:pp. 693–712, 2018. doi:10.5194/wes-3-693-2018.

[97] Yu, Z. and Falnes, J. State-space modelling of a vertical cylinder in heave. *Applied Ocean Research*, vol. 17(5):pp. 265–275, 1995. doi:10.1016/0141-1187(96)00002-8.

[98] Yu, Z. and Falnes, J. State-space modeling of dynamic systems in ocean engineering. *Journal of Hydrodynamics*, vol. 24(1):pp. 1–17, 1998.

[99] Pérez, T. and Fossen, T. Time- vs. frequency-domain identification of parametric radiation force models for marine structures at zero speed. *Modeling, Identification and Control*, vol. 29(1):pp. 1–19, 2008. doi:10.4173/mic.2008.1.1.

[100] Kristiansen, E., Hjulstad, Å., and Egeland, O. State-space representation of radiation forces in time-domain vessel models. *Modeling, Identification and Control*, vol. 27(1):pp. 23–41, 2006. doi:10.1016/j.oceaneng.2005.02.009.

[101] Pérez, T. and Fossen, T. A matlab toolbox for parametric identification of radiation-force models of ships and offshore structures. *Journal of Modeling, Identification and Control*, vol. 30(1):pp. 1–15, 2009. doi:10.4173/mic.2009.1.1.

[102] Duarte, T., Sarmento, A., Alves, M., and Jonkman, J. State-space realization of the wave-radiation force within FAST. In: *Proceedings of the ASME 32nd International Conference on Ocean, Offshore and Arctic Engineering*. Nantes, France, 2013. doi:10.1115/OMAE2013-10375.

[103] Lemmer, F., Raach, S., Schlipf, D., and Cheng, P. W. Parametric wave excitation model for floating wind turbines. *Energy Procedia*, vol. 94:pp. 290–305, 2016. doi:10.1016/j.egypro.2016.09.186.

[104] Sørensen, A., Sagatun, S., and Fossen, T. Design of a dynamic positioning system using model-based control. *Control Engineering Practice*, vol. 4(3):pp. 359–368, 1996. doi:10.1016/0967-0661(96)00013-5.

[105] Lackner, M. and Rotea, M. Structural control of floating wind turbines. *Mechatronics*, vol. 21(4):pp. 704–719, 2011. doi:10.1016/j.mechatronics.2010.11.007.

[106] Schlipf, D., Sandner, F., Raach, S., Matha, D., and Cheng, P. W. Nonlinear model predictive control of floating wind turbines. In: *Proceedings of the 23rd International Ocean and Polar Engineering Conference*, pp. 440–447. Anchorage, USA, 2013. doi:10.18419/opus-3908.

[107] Lemmer, F., Raach, S., Schlipf, D., and Cheng, P. W. Prospects of linear model predictive control on a 10MW floating wind turbine. In: *Proceedings of the ASME 34th International*

Conference on Ocean, Offshore and Arctic Engineering. St. John's, Canada, 2015. doi: 10.1115/OMAE2015-42267.

[108] Schlipf, D., Simley, E., Lemmer, F., Pao, L., and Cheng, P. W. Collective pitch feedforward control of floating wind turbines using Lidar. *Journal of Ocean and Wind Energy*, vol. 2(4):pp. 223–230, 2015. doi:10.17736/jowe.2015.arr04.

[109] Morison, J. R. The force distribution exerted by surface waves on piles. Tech. rep., University of California, Institute of Engineering Research, Berkeley, USA, 1953.

[110] Sarpkaya, T. and Isaacson, M. *Mechanics of Wave Forces on Offshore Structures.* Van Nostrand Reinhold Co., 1981. ISBN 9780442254025.

[111] Jonkman, J. Definition of the floating system for phase IV of OC3. Tech. rep., National Renewable Energy Laboratory, 2010.

[112] Robertson, A., Jonkman, J., Masciola, M., Song, H., Goupee, A., Coulling, A., and Luan, C. Definition of the semisubmersible floating system for phase II of OC4. Tech. rep., National Renewable Energy Laboratory, Boulder, USA, 2014. URL `http://www.nrel.gov/docs/fy14osti/60601.pdf`.

[113] Östergaard, C. and Schellin, T. E. Comparison of experimental and theoretical wave actions on floating and compliant offshore structures. *Applied Ocean Research*, vol. 9(4), 1987. doi:10.1016/0141-1187(87)90002-2.

[114] Brorsen, M. Slowly-varying 2nd order wave forces on large structures. Aalborg University, 2006. URL `http://vbn.aau.dk/files/6771919/Slowly-varying_2._order_Wave_Forces_on_Large_Structures`.

[115] Faltinsen, O. M. *Sea Loads On Ships And Offshore Structures.* Cambridge University Press, 1993. ISBN 0-521-45870-6.

[116] Gueydon, S., Duarte, T., and Jonkman, J. Comparison of second-order loads on a semisubmersible floating wind turbine. In: *Proceedings of the ASME 33rd International Conference on Ocean, Offshore and Arctic Engineering.* San Francisco, USA, 2014. doi: 10.1115/OMAE2014-23398.

[117] Duarte, T., Sarmento, A., and Jonkman, J. Effects of second-order hydrodynamic forces on floating offshore wind turbines. In: *Proceedings of the AIAA SciTech.* National Harbor, USA, 2014. doi:10.2514/6.2014-0361.

[118] Roald, L., Jonkman, J., Robertson, A., and Chokani, N. The effect of second-order hydrodynamics on floating offshore wind turbines. *Energy Procedia*, vol. 35:pp. 253–264, 2013. doi:10.1016/j.egypro.2013.07.178.

[119] Lupton, R. and Langley, R. S. Assessing the importance of the slow drift motion of floating wind turbine platforms. In: *Proceedings of the ASME 33rd International Conference on Ocean, Offshore and Arctic Engineering.* San Francisco, USA, 2014. doi:10.1115/OMAE2014-23859.

[120] Gueydon, S. and Jonkman, J. Update on the comparison of second-order loads on a ten-

sion leg platform for wind turbines. In: *Proceedings of the 26th International Ocean and Polar Engineering Conference*, pp. 323–332. Rhodes, Greece, 2016. ISBN 9781880653883.

[121] Bachynski, E. and Moan, T. Second order wave force effects on tension leg platform wind turbines in misaligned wind and waves. In: *Proceedings of the ASME 33rd International Conference on Ocean, Offshore and Arctic Engineering.* San Francisco, USA, 2014. doi: 10.1115/OMAE2014-23131.

[122] Azcona, J. *Computational and experimental modelling of mooring line dynamics for offshore floating wind turbines.* Ph.D. thesis, Universidad Politécnica de Madrid, 2016, URL `http://oa.upm.es/44708/1/JOSE_AZCONA_ARMENDARIZ_2.pdf`.

[123] Azcona, J., Palacio, D., Munduate, X., González, L., and Nygaard, T. A. Impact of mooring lines dynamics on the fatigue and ultimate loads of three offshore floating wind turbines computed with IEC 61400-3 guideline. *Wind Energy*, vol. 20(5):pp. 797–813, 2016. doi:10.1002/we.2064.

[124] Masciola, M., Robertson, A., Jonkman, J., Coulling, A., and Goupee, A. Assessment of the importance of mooring dynamics on the global response of the DeepCwind floating semisubmersible offshore wind turbine. In: *Proceedings of the 23rd International Ocean and Polar Engineering Conference.* Anchorage, USA, 2013. ISBN 978-1 880653 99-9.

[125] Masciola, M. Instructional and theory guide to the mooring analysis program. Tech. rep., National Renewable Energy Laboratory, 2014. URL `http://wind.nrel.gov/designcodes/simulators/map/MAP.pdf`.

[126] Hall, M. MoorDyn user's guide. Tech. rep., University of Maine, Orono, USA, 2015. URL `https://nwtc.nrel.gov/MoorDyn`.

[127] Matha, D., Fechter, U., Kühn, M., and Cheng, P. W. Non-linear multi-body mooring system model for floating offshore wind turbines. In: *Proceedings of the European Wind Energy Association Offshore Wind Conference and Exhibition.* Amsterdam, Netherlands, 2011.

[128] Azcona, J., Munduate, X., González, L., and Nygaard, T. Experimental validation of a dynamic mooring lines code with tension and motion measurements of a submerged chain. *Ocean Engineering*, vol. 129:pp. 415–427, 2017. doi:10.1016/j.oceaneng.2016.10.051.

[129] Masciola, M., Jonkman, J., and Robertson, A. Extending the capabilities of the mooring analysis program: A survey of dynamic mooring line theories for integration into FAST. In: *Proceedings of the ASME 33rd International Conference on Ocean, Offshore and Arctic Engineering.* San Francisco, USA, 2014. doi:10.1115/OMAE2014-23508.

[130] Hsu, W.-t., Thiagarajan, K. P., MacNicoll, M., and Akers, R. Prediction of extreme tensions in mooring lines of a floating offshore wind turbine in a 100-year storm. In: *Proceedings of the ASME 34th International Conference on Ocean, Offshore and Arctic Engineering.* Saint John's, Canada, 2015. doi:10.1115/OMAE2015-42015.

[131] IEC. 61400-1 Wind turbines - Part 1: Design requirements. 2005.

[132] Sutherland, H. J. On the fatigue analysis of wind turbines. Tech. rep., Sandia National Laboratories, Albuquerque, USA, 1999.

[133] Philippe, M., Babarit, A., and Ferrant, P. Comparison of time and frequency domain simulations of an offshore floating wind turbine. In: *Proceedings of the ASME 30th International Conference on Ocean, Offshore and Arctic Engineering.* Rotterdam, Netherlands, 2011. doi:10.1115/OMAE2011-49722.

[134] Kvittem, M. and Moan, T. Frequency versus time domain fatigue analysis of a semi-submersible wind turbine tower. In: *Proceedings of the ASME 33rd International Conference on Ocean, Offshore and Arctic Engineering.* San Francisco, USA, 2014. doi: 10.1115/OMAE2014-23385.

[135] Savenije, F. and Peeringa, J. Aero-elastic simulation of offshore wind turbines in the frequency domain. Tech. rep., ECN, Petten, Netherlands, 2009. URL `http://www.ecn.nl/docs/library/report/2009/e09060.pdf`.

[136] Larsen, T. J. and Hansen, A. M. How 2 HAWC2, the user's manual. Tech. rep., Technical University of Denmark, Roskilde, Denmark, 2007. ISBN 9788755035836.

[137] IEC. 61400-3 Wind turbines - Part 3: Design requirements for offshore wind turbines. 2007.

[138] Veers, P. Three-dimensional wind simulation. Tech. rep., Sandia National Laboratories, Albuquerque, USA, 1988. URL `http://prod.sandia.gov/techlib/access-control.cgi/1988/880152.pdf`.

[139] Jonkman, B. and Kilcher, L. TurbSim user's guide. Tech. rep., National Renewable Energy Laboratory, Boulder, USA, 2009. URL `https://nwtc.nrel.gov/system/files/TurbSim.pdf`.

[140] IEC. 61400-3-2 TS Ed. 1 Wind turbines - Part 3-2: Design requirements for floating offshore wind turbines (under preparation). 2018.

[141] DNV. DNV-OS-J101: Design of offshore wind turbine structures. 2014.

[142] Cheng, P. W. *A reliability based design methodology for extreme response of offshore wind turbines.* Ph.D. thesis, Delft University of Technology, 2002. ISBN 90-79468-08-7.

[143] Krieger, A., Ramachandran, G. K. V., Vita, L., Gómez Alonso, P., Berque, J., and Aguirre-Suso, G. LIFES50+ D7.2 Design basis. Tech. rep., DNV-GL, 2016. URL `http://lifes50plus.eu/wp-content/uploads/2015/11/D72_Design_Basis_Retyped-v1.1.pdf`.

[144] DIN. Eurocode 3: Design of steel structures - Part 1-9: Fatigue (DIN EN 1993-1-9). 2010.

[145] DNV. DNV-RP-C203: Fatigue design of offshore steel structures. 2011.

[146] Lotsberg, I. *Fatigue Design of Marine Structures.* Cambridge University Press, Cambridge, 2016. doi:10.1017/CBO9781316343982.

[147] Halfpenny, A. A frequency domain approach for fatigue life estimation from Finite Ele-

ment Analysis. In: *Proceedings of the International Conference on Damage Assessment of Structures*, pp. 401–410. Dublin, Ireland, 1999. ISBN 0878498397.

[148] Naess, A. and Moan, T. *Stochastic Dynamics of Marine Structures*. Cambridge University Press, 2012. doi:10.1017/CBO9781139021364.

[149] Bredmose, H., Larsen, S. E., Matha, D., Rettenmeier, A., Marino, E., and Saettran, L. MARINET D2.4: Collation of offshore wind-wave dynamics. Tech. rep., Technical University of Denmark, 2012. URL `http://orbit.dtu.dk/files/60086212/Collation_of_offshore.pdf`.

[150] Goupee, A. J., Koo, B. J., Kimball, R. W., Lambrakos, K. F., and Dagher, H. J. Experimental comparison of three floating wind turbine concepts. In: *Proceedings of the ASME 31st International Conference on Ocean, Offshore and Arctic Engineering*. Rio de Janeiro, Brazil, 2012. doi:10.1115/OMAE2012-83645.

[151] Robertson, A., Goupee, A., Jonkman, J., Prowell, I., Molta, P., Coulling, A., and Masciola, M. Summary of conclusions and recommendations drawn from the DeepCwind scaled floating offshore wind system test campaign. In: *Proceedings of the ASME 32nd International Conference on Ocean, Offshore and Arctic Engineering*. 2013. doi:10.1115/OMAE2013-10817.

[152] Vittori, F., Bouchotrouch, F., Lemmer, F., and Azcona, J. Hybrid scaled testing of a 5MW floating wind turbine using the SIL method compared with numerical models. In: *Proceedings of the ASME 37th International Conference on Ocean, Offshore and Arctic Engineering*. Madrid, Spain, 2018. doi:10.1115/OMAE2018-77853.

[153] Kanner, S., Koukina, E., and Yeung, R. W. Power optimization of model-scale floating wind turbines using real-time hybrid testing with autonomous actuation and control. In: *Proceedings of the ASME 36th International Conference on Ocean, Offshore and Arctic Engineering*. Trondheim, Norway, 2017. doi:10.1115/OMAE2017-62175.

[154] Karimirad, M., Bachynski, E., Berthelsen, P. A., and Ormberg, H. Comparison of real-time hybrid model testing of a braceless semi- submersible wind turbine and numerical simulations. In: *Proceedings of the ASME 36th International Conference on Ocean, Offshore and Arctic Engineering*. ASME, Trondheim, Norway, 2017. doi:10.1115/OMAE2017-61121.

[155] Bayati, I., Belloli, M., Bernini, L., and Zasso, A. Wind tunnel validation of AeroDyn within LIFES50+ project: Imposed surge and pitch tests. *Journal of Physics: Conference Series*, vol. 753, 2016. doi:10.1088/1742-6596/753/9/092001.

[156] Müller, K., Sandner, F., Bredmose, H., Azcona, J., Manjock, A., and Pereira, R. Improved tank test procedures for scaled floating offshore wind turbines. In: *International Wind Engineering Conference IWEC*. Hannover, Germany, 2014. doi:10.18419/opus-8261.

[157] Matha, D., Sandner, F., Molins, C., Campos, A., and Cheng, P. W. Efficient preliminary floating offshore wind turbine design and testing methodologies and application to a

concrete spar design. *Philosophical Transactions of the Royal Society A*, vol. 373(2035), 2015. doi:10.1098/rsta.2014.0350.

[158] Borisade, F., Koch, C., Lemmer, F., Cheng, P. W., and Matha, D. Validation of INNWIND.EU scaled model tests of a semisubmersible floating wind turbine. *International Journal of Offshore and Polar Engineering*, vol. 28(1):pp. 54–64, 2017. doi: 10.17736/ijope.2018.fv04.

[159] Klein, L., Schulz, C., Lutz, T., and Krämer, E. Influence of jet flow on the Aerodynamics of a floating model wind turbine. In: *Proceedings of the 26th International Ocean and Polar Engineering Conference*, pp. 403–410. Rhodes, Greece, 2016. ISBN 9781880653883.

[160] Bredmose, H., Lemmer, F., Borg, M., Pegalajar-Jurado, A., Mikkelsen, R. F., Stoklund Larsen, T., Fjelstrup, T., Yu, W., Lomholt, A. K., Boehm, L., and Azcona, J. The TripleSpar campaign: Model tests of a 10MW floating wind turbine with waves, wind and pitch control. *Energy Procedia*, vol. 137:pp. 58–76, 2017. doi:10.1016/j.egypro.2017. 10.334.

[161] Yu, W., Lemmer, F., Bredmose, H., Borg, M., Pegalajar-Jurado, A., Mikkelsen, R. F., Stoklund Larsen, T., Fjelstrup, T., Lomholt, A., Boehm, L., Schlipf, D., and Azcona, J. The TripleSpar Campaign: Implementation and test of a blade pitch controller on a scaled floating wind turbine model. In: *Energy Procedia*, vol. 137, pp. 323–338. Elsevier, Trondheim, Norway, 2017. doi:10.1016/j.egypro.2017.10.357.

[162] Schlipf, D. *Lidar-assisted control concepts for wind turbines*. Ph.D. thesis, University of Stuttgart, 2015. ISBN 978-3-8439-2518-1.

[163] Gasch, R. and Twele, J. *Windkraftanlagen - Grundlagen, Entwurf, Planung und Betrieb*. B.G. Teubner, Wiesbaden, 4th edn., 2005. ISBN 978-3-519-36334-7.

[164] Skaare, B., Hanson, T. D., and Nielsen, F. G. Importance of control strategies on fatigue life of floating wind turbines. In: *Proceedings of the ASME 26th International Conference on Offshore Mechanics and Arctic Engineering*. San Diego, USA, 2007. doi:10.1115/ OMAE2007-29277.

[165] Veen, G. V. D., Couchman, Y., and Bowyer, R. Control of floating wind turbines. In: *Proceedings of the American Control Conference*, pp. 3148–3153. Montreal, Canada, 2012. doi:10.1109/ACC.2012.6315120.

[166] Skogestad, S. and Postlethwaite, I. *Multivariable Feedback Control: Analysis and Design*. John Wiley and Sons, Chichester, 2nd edn., 2007. ISBN 978-0470011683. ISSN 1049-8923.

[167] Fleming, P., Pineda, I., Rossetti, M., Wright, A., and Arora, D. Evaluating methods for control of an offshore floating turbine. In: *Proceedings of the ASME 33rd International Conference on Ocean, Offshore and Arctic Engineering*. 2014. doi:10.1115/ OMAE2014-24107.

[168] Savenije, F. and Peeringa, J. Control development for floating wind. *Journal of Physics: Conference Series*, vol. 524, 2014. doi:10.1088/1742-6596/524/1/012090.

[169] Vanni, F., Rainey, P., and Bossanyi, E. A comparison of control-based platform stabilisation strategies for floating wind turbines. In: *Proceedings of the European Wind Energy Association Offshore Wind Conference and Exhibition*. Copenhagen, Denmark, 2015.

[170] Ritter, B. and Konigorski, U. Advanced multivariable control design for modern multi-MW wind turbines. In: *Proceedings of the EAWE 11th Phd Seminar on Wind Energy in Europe*. Stuttgart, Germany, 2015.

[171] Horowitz, I. M. *Synthesis of Feedback Systems*. Acad. Press, New York, USA, 1963. ISBN 978-1-4832-3282-9. URL `http://www.sciencedirect.com/science/book/9781483232829`.

[172] Lindeberg, E., Svendsen, H. G., and Uhlen, K. Smooth transition between controllers for floating wind turbines. *Energy Procedia*, vol. 24:pp. 83–98, 2012. doi:10.1016/j.egypro.2012.06.090.

[173] Ramos, R. Optimal vibration control of floating wind turbines in the presence of nonlinearities. In: *Proceedings of the ASME 32nd International Conference on Ocean, Offshore and Arctic Engineering*. Nantes, France, 2013. doi:10.1115/OMAE2013-10242.

[174] Schuler, S., Schlipf, D., Cheng, P. W., and Allgöwer, F. ℓ1-optimal control of large wind turbines. *IEEE Transactions on Control Systems Technology*, vol. 21(4):pp. 1079–1089, 2013. doi:10.1109/tcst.2013.2261068.

[175] de Corcuera, A. D., Pujana-Arrese, A., Ezquerra, J. M., Segurola, E., and Landaluze, J. H_∞-based control for load mitigation in wind turbines. *Energies*, vol. 5(4):pp. 938–967, 2012. doi:10.3390/en5040938.

[176] Si, Y. and Karimi, H. R. Gain scheduling H_2/H_∞ structural control of a floating wind turbine. *IFAC Proceedings Volumes*, vol. 47(3):pp. 6788–6793, 2014. doi:10.3182/20140824-6-ZA-1003.02775.

[177] Christiansen, S. *Model-based control of a ballast-stabilized floating wind turbine exposed to wind and waves*. Ph.D. thesis, Aalborg University, 2013, URL `vbn.aau.dk/files/77466696/thesis.pdf`.

[178] Christiansen, S., Tabatabaeipour, S. M., Bak, T., and Knudsen, T. Wave disturbance reduction of a floating wind turbine using a reference model-based predictive control. In: *Proceedings of the American Control Conference*, pp. 2214–2219. Washington, USA, 2013. doi:10.1109/ACC.2013.6580164.

[179] Lio, W. H., Rossiter, J. A., and Jones, B. L. A review on applications of model predictive control to wind turbines. In: *Proceedings of the UKACC 10th International Conference on Control*, pp. 680–685. Loughborough, UK, 2014.

[180] Wright, A. *Modern control design for flexible wind turbines*. Ph.D. thesis, University of Colorado, 2004. ISBN 9780496444748.

[181] Stol, K. A. and Balas, M. J. Periodic disturbance accommodating control for blade

load mitigation in wind turbines. *Journal of Solar Energy Engineering*, vol. 125(4):pp. 379–385, 2003. doi:10.1115/1.1621672.

[182] Namik, H. *Individual blade pitch and disturbance accommodating control of floating offshore wind turbines*. Ph.D. thesis, University of Auckland, 2012, URL `http://hdl.handle.net/2292/11198%0A`.

[183] Fleming, P., Peiffer, A., and Schlipf, D. Wind turbine controller to mitigate structural loads on a floating wind turbine platform. In: *Proceedings of the ASME 35th International Conference on Ocean, Offshore and Arctic Engineering*. Busan, Korea, 2016. doi:10.1115/OMAE2016-54536.

[184] Stewart, G. Load reduction of floating wind turbines using tuned mass dampers. Master's thesis, University of Massachusetts, 2012. URL `https://scholarworks.umass.edu/theses/781/`.

[185] Jalili, K., Li, Y., and Rotea, M. Pitch and roll motion control of a floating wind turbine with hybrid actuation. In: *Proceedings of the ASME Dynamic Systems and Control of Wind Energy Systems Conference*. San Antonio, USA, 2014. doi:10.1115/DSCC2014-6064.

[186] Luo, N., Bottasso, C., Karimi, H. R., and Zapateiro, M. Semiactive control for floating offshore wind turbines subject to aero-hydro dynamic loads. In: *Proceedings of the International Conference on Renewable Energies and Power Quality*. Las Palmas, Spain, 2011. ISBN 978-84-614-7527-8.

[187] Pérez-Collazo, C., Greaves, D., and Iglesias, G. A review of combined wave and offshore wind energy. *Renewable and Sustainable Energy Reviews*, vol. 42:pp. 141–153, 2015. doi:10.1016/j.rser.2014.09.032.

[188] Pascu, V., Kanev, S., and van Wingerden, J.-W. Adaptive tower damping control for offshore wind turbines. *Wind Energy*, vol. 20:pp. 765–781, 2017. doi:10.1002/we.2058.

[189] Fischer, B. and Shan, M. A survey on control methods for the mitigation of tower loads. Tech. rep., Fraunhofer-Institut für Windenergiesysteme, Kassel, Germany, 2013. URL `http://publica.fraunhofer.de/eprints/urn_nbn_de_0011-n-2721917.pdf`.

[190] Fischer, T. *Mitigation of aerodynamic and hydrodynamic induced loads of offshore wind turbines*. Ph.D. thesis, University of Stuttgart, 2012. ISBN 978-3844015010.

[191] Jost, E., Fischer, A., Lutz, T., and Krämer, E. An investigation of unsteady 3D effects on trailing edge flaps. *Wind Energy Science*, vol. 2:pp. 241–256, 2017. doi:10.5194/wes-2-241-201.

[192] Bossanyi, E. A. Individual blade pitch control for load reduction. *Wind Energy*, vol. 6(2):pp. 119–128, 2003. doi:10.1002/we.76.

[193] Yang, F., Song, Q.-w., Wang, L., Zuo, S., and Li, S.-s. Wind and wave disturbances compensation to floating offshore wind turbine using improved individual pitch control

based on fuzzy control strategy. *Abstract and Applied Analysis*, 2014. doi:10.1155/2014/968384.

[194] Lackner, M. Controlling platform motions and reducing blade loads for floating wind turbines. *Wind Engineering*, vol. 33(6):pp. 541–553, 2009. doi:10.1260/0309-524X.33.6.541.

[195] Navalkar, S., van Wingerden, J.-W., Fleming, P., and van Kuik, G. A. M. Integrating robust Lidar-based feedforward with feedback control to enhance speed regulation of floating wind turbines. In: *Proceedings of the American Control Conference*. Chicago, USA, 2015. doi:10.1109/ACC.2015.7171804.

[196] Raach, S., Schlipf, D., Sandner, F., Matha, D., and Cheng, P. W. Nonlinear model predictive control of floating wind turbines with individual pitch control. In: *Proceedings of the American Control Conference*. Portland, Oregon, USA, 2014.

[197] Skaare, B., Hanson, T. D., Nielsen, F. G., Yttervik, R., Hansen, A. M., Thomsen, K., and Larsen, T. J. Integrated dynamic analysis of floating offshore wind turbines. In: *Proceedings of the European Wind Energy Conference*. Milan, Italy, 2007.

[198] Henriksen, L. C., Hansen, M. O. L., and Poulsen, N. K. Beyond the cp-curve in model-based control of wind turbines. In: *Proceedings of the European Wind Energy Association Annual Event*. Copenhagen, Denmark, 2012.

[199] Leithead, W., Dominguez, S., and Spruce, C. Analysis of tower/blade interaction in the cancellation of the tower fore-aft mode via control. In: *Proceedings of the European Wind Energy Conference*. London, UK, 2004.

[200] Sandner, F., Yu, W., Matha, D., Azcona, J., Munduate, X., Grela, E., Voutsinas, S., and Natarajan, A. INNWIND.EU D4.33: Innovative concepts for floating structures. Tech. rep., University of Stuttgart, 2014. URL `http://www.innwind.eu/-/media/Sites/innwind/Publications/Deliverables/DeliverableD4-33_Innovative-Concepts-for-Floating-Structures_INNWIND-EU`.

[201] Skaare, B. Development of the Hywind concept. In: *Proceedings of the ASME 36th International Conference on Ocean, Offshore and Arctic Engineering*. Trondheim, Norway, 2017. doi:10.1115/OMAE2017-62710.

[202] Molins, C., Campos, A., Sandner, F., and Matha, D. Monolithic concrete off-shore floating structure for wind turbines. In: *Proceedings of the European Wind Energy Association Annual Event*. Barcelona, Spain, 2014.

[203] Lemmer, F., Amann, F., Raach, S., and Schlipf, D. Definition of the SWE-TripleSpar platform for the DTU10MW reference turbine. 2016. URL `http://www.ifb.uni-stuttgart.de/windenergie/downloads`.

[204] Lemmer, F., Yu, W., Schlipf, D., and Cheng, P. W. Multibody modeling for concept-level floating offshore wind turbine design (submitted and under review). *Multibody System Dynamics*, 2019.

[205] Lemmer, F., Schlipf, D., and Cheng, P. W. Control design methods for floating wind turbines for optimal disturbance rejection. *Journal of Physics: Conference Series*, vol. 753, 2016. doi:10.18419/opus-8906.

[206] Schiehlen, W. and Eberhard, P. *Applied Dynamics*. Springer International Publishing, 1st edn., 2014. doi:10.1007/978-3-319-07335-4.

[207] Seifried, R. *Dynamics of Underactuated Multibody Systems: Modeling, Control and Optimal Design*. Springer International Publishing, 2014. doi:10.1007/978-3-319-01228-5.

[208] Kane, T. R. and Levinson D. A. *Dynamics: Theory and Applications*. McGraw-Hill Inc., New York, 1985. ISBN 0-07-037846-0.

[209] Woernle, C. *Mehrkörpersysteme: Eine Einführung in die Kinematik und Dynamik von Systemen starrer Körper*. Springer Vieweg, 2nd edn., 2011. doi:10.1007/978-3-662-46687-2.

[210] Bauchau, O. *Flexible Multibody Dynamics*, vol. 176 of *Solid Mechanics and its Applications*. Springer Netherlands, Dordrecht, 1st edn., 2011. ISBN 978-94-007-0334-6.

[211] Dresig, H. and Holzweißig, F. *Maschinendynamik*. Springer, Berlin, Heidelberg, 11th edn., 2012. doi:10.1007/978-3-642-29571-3.

[212] Nygaard, T. A., De Vaal, J., Pierella, F., Oggiano, L., and Stenbro, R. Development, verification and validation of 3DFloat; Aero-servo-hydro-elastic computations of offshore structures. *Energy Procedia*, vol. 94:pp. 425–433, 2016. doi:10.1016/j.egypro.2016.09.210.

[213] Wang, Q., Sprague, M. A., Jonkman, J., Johnson, N., and Jonkman, B. BeamDyn: A high-fidelity wind turbine blade solver in the FAST modular framework. *Wind Energy*, vol. 20:pp. 1439–1462, 2017. doi:10.1002/we.2101.

[214] Shabana, A. A. *Dynamics of Multibody Systems*. Cambridge University Press, 3rd edn., 2005. ISBN 0-521-85011-8.

[215] Holzwarth, P. *Modellordnungsreduktion für substrukturierte mechanische Systeme*. Ph.D. thesis, University of Stuttgart, 2017. ISBN 978-3-8440-5234-3.

[216] Holm-Jørgensen, K. and Nielsen, S. R. System reduction in multibody dynamics of wind turbines. *Multibody System Dynamics*, vol. 21(2):pp. 147–165, 2009. doi:10.1007/s11044-008-9132-4.

[217] Bir, G. S. User's guide to BModes. Tech. rep., NREL, 2007. URL `https://nwtc.nrel.gov/system/files/BModes.pdf`.

[218] Fossen, T. *Handbook of Marine Craft Hydrodynamics and Motion Control*. John Wiley and Sons, 1st edn., 2011. doi:10.1002/9781119994138.

[219] Wallrapp, O. Standardization of flexible body modeling in multibody system codes, part I: Definition of standard input data. *Mechanics of Structures and Machines*, vol. 22(3):pp. 283–304, 1994. doi:10.1080/08905459408905214.

[220] Taghipour, R., Pérez, T., and Moan, T. Hybrid frequency-time domain models for dy-

namic response analysis of marine structures. *Ocean Engineering*, vol. 35(7):pp. 685–705, 2008. doi:10.1016/j.oceaneng.2007.11.002.

[221] Falnes, J. On non-causal impulse response functions related to propagating water waves. *Applied Ocean Research*, vol. 17(6):pp. 379–389, 1995. doi:10.1016/S0141-1187(96)00007-7.

[222] Ljung, L. *System Identification - Theory for the User*. Prentice-Hall, Upper Saddle River, USA, 2nd edn., 2009. ISBN 0-13-656695-2.

[223] NWTC. NWTC Information Portal (OpenFAST). URL `https://nwtc.nrel.gov/OpenFAST`.

[224] Jonkman, J., Wright, A. D., Hayman, G. J., and Robertson, A. N. Full-system linearization for floating offshore wind turbines in OpenFAST (pre-print). In: *Proceedings of the ASME 2018 1st International Offshore Wind Technical Conference*. ASME, San Francisco, USA, 2018.

[225] Fossen, T. Nonlinear unified state-space model for ship maneuvering and control in a seaway. *International Journal of Bifurcation and Chaos*, vol. 15(9):pp. 2717–2746, 2005. doi:10.1142/S0218127405013691.

[226] Lemmer, F., Yu, W., and Cheng, P. W. Iterative frequency-domain response of floating wind turbines with parametric drag. *Journal of Marine Science and Engineering*, vol. 6(4), 2018. doi:10.3390/jmse6040118.

[227] Sumer, B. M. and Fredsøe, J. *Hydrodynamics Around Cylindrical Structures*. World Scientific, Singapore, 1st edn., 1997. ISBN 978-981-270-039-1.

[228] Wolfram, J. On alternative approaches to linearization and Morison's equation for wave forces. *Proceedings of the Royal Society A: Mathematical, Physical and Engineering Sciences*, vol. 455(1988):pp. 2957–2974, 1999. doi:10.1098/rspa.1999.0434.

[229] Langley, R. On the time domain simulation of second order wave forces and induced responses. *Applied Ocean Research*, vol. 8(3):pp. 134–143, 1986. doi:10.1016/S0141-1187(86)80012-8.

[230] Tao, L. and Dray, D. Hydrodynamic performance of solid and porous heave plates. *Ocean Engineering*, vol. 35(10):pp. 1006–1014, 2008. doi:10.1016/j.oceaneng.2008.03.003.

[231] Newman, J. N. Second-order, slowly-varying forces on vessels in irregular waves. In: *Proceedings of International Symposium on Dynamics of Marine Vehicles and Structures in Waves*. London, UK, 1974.

[232] Standing, R., Brendling, W., and Wilson, D. Recent developments in the analysis of wave drift forces, low-frequency damping and response. In: *Proceedings of the Offshore Technology Conference*. Houston, USA, 1987. doi:10.4043/5456-MS.

[233] Azcona, J., Vittori, F., Schmidt Paulsen, U., Savenije, F., Kapogiannis, G., Karvelas, X., Manolas, D., Voutsinas, S., Amann, F., Faerron-Guzmán, R., and Lemmer, F. IN-

NWIND.EU D4.37: Design solutions for 10MW floating offshore wind turbines. Tech. rep., CENER, 2017.

[234] Matha, D., Sandner, F., and Schlipf, D. Efficient critical design load case identification for floating offshore wind turbines with a reduced nonlinear model. *Journal of Physics: Conference Series*, vol. 555, 2014. doi:10.1088/1742-6596/555/1/012069.

[235] Sandner, F., Schlipf, D., Matha, D., Seifried, R., and Cheng, P. W. Reduced nonlinear model of a spar-mounted floating wind turbine. In: *Proceedings of the German Wind Energy Conference DEWEK*. Bremen, Germany, 2012. doi:10.18419/opus-4528.

[236] Olondriz, J., Yu, W., Jugo, J., Lemmer, F., Elorza, I., Alonso-Quesada, S., and Pujana-Arrese, A. Using multiple fidelity numerical models for floating offshore wind turbine advanced control design. *Energies*, vol. 11(9), 2018. doi:10.3390/en11092484.

[237] Lemmer, F., Müller, K., Yu, W., Schlipf, D., and Cheng, P. W. Optimization of floating offshore wind turbine platforms with a self-tuning controller. In: *Proceedings of the ASME 36th International Conference on Ocean, Offshore and Arctic Engineering*. Trondheim, Norway, 2017. doi:10.1115/OMAE2017-62038.

[238] Yu, W., Lemmer, F., Schlipf, D., Cheng, P. W., Visser, B., Links, H., Gupta, N., Dankemann, S., Couñago, B., and Serna, J. Evaluation of control methods for floating offshore wind turbines. *Journal of Physics: Conference Series*, vol. 1104:p. 012033, 2018. doi: 10.1088/1742-6596/1104/1/012033.

[239] Luhmann, B., Seyedin, H., and Cheng, P. W. Numerical investigation of the load reduction potential of a flexible hub connection on two-bladed wind turbines. *Journal of Physics: Conference Series*, vol. 753, 2015. doi:10.1088/1742-6596/753/8/082013.

[240] Lemmer, F., Yu, W., Cheng, P. W., Pegalajar-Jurado, A., Borg, M., Mikkelsen, R., and Bredmose, H. The TripleSpar campaign: Validation of a reduced-order simulation model for floating wind turbines. In: *Proceedings of the ASME 37th International Conference on Ocean, Offshore and Arctic Engineering*. ASME, Madrid, Spain, 2018. doi:10.1115/OMAE2018-78119.

[241] Yu, W. Modeling, control design and testing of a scaled floating offshore wind turbine. Master's thesis, University of Stuttgart, 2016.

[242] Fjelstrup, T. and Larsen, T. S. Experimental study of a triple spar floating wind turbine in wind and wave forcing. Master's thesis, Technical University of Denmark, 2016.

[243] Chujo, T., Minami, Y., Nimura, T., and Ishida, S. Experimental study for spar type floating offshore wind turbine with blade-pitch control. In: *Proceedings of the ASME 32nd International Conference on Ocean, Offshore and Arctic Engineering*. Nantes, France, 2013. doi:10.1115/OMAE2013-10649.

[244] Goupee, A. J., Kimball, R. W., and Dagher, H. J. Experimental observations of active blade pitch and generator control influence on floating wind turbine response. *Renewable Energy*, vol. 104:pp. 9–19, 2017. doi:10.1016/j.renene.2016.11.062.

[245] Savenije, F. Model testing of a floating wind turbine including control. In: *EERA Deepwind*. Trondheim, Norway, 2017.

[246] Hara, N., Tsujimoto, S., Nihei, Y., Iijima, K., and Konishi, K. Experimental validation of model-based blade pitch controller design for floating wind turbines: System identification approach. *Wind Energy*, vol. 20(7):pp. 1187–1206, 2017. doi:10.1002/we.2089.

[247] Pegalajar-Jurado, A., Hansen, A. M., Laugesen, R., Mikkelsen, R. F., Borg, M., Kim, T., Heilskov, N. F., and Bredmose, H. Experimental and numerical study of a 10MW TLP wind turbine in waves and wind. *Journal of Physics: Conference Series*, vol. 753, 2016. doi:10.1088/1742-6596/753/9/092007.

[248] Berthelsen, P. A., Bachynski, E., Karimirad, M., and Thys, M. Real-time hybrid model tests of a braceless semi-submersible wind turbine. part III: Calibration of a numerical model. In: *Proceedings of the ASME 35th International Conference on Ocean, Offshore and Arctic Engineering*. ASME, Busan, Korea, 2016. doi:10.1115/OMAE2016-54640.

[249] Lemmer, F., Schlipf, D., and Cheng, P. W. Robust gain scheduling control of floating offshore wind turbines (submitted and under review). *Wind Energy*, 2019.

[250] Åström, K. J. and Murray, R. M. *Feedback Systems*. Princeton University Press, 2nd edn., 2016. ISBN 9781400828739.

[251] Lemmer, F., Müller, K., Yu, W., Faerron-Guzmán, R., and Kretschmer, M. LIFES50+ D4.3: Optimization framework and methodology for optimized floater design. Tech. rep., University of Stuttgart, 2016. URL `http://lifes50plus.eu/wp-content/uploads/2015/11/GA_640741_LIFES50_D4.3-web.pdf`.

[252] Lemmer, F., Müller, K., Yu, W., and Cheng, P. W. Semi-submersible wind turbine hull shape design for a favorable system response behavior (submitted, revised version under preparation). *Marine Structures*, 2019.

[253] Hanna, S. Y. Wave cancellation effects and extreme wave dynamics. In: *Proceedings of the Offshore Technology Conference*. Houston, USA, 1986.

[254] Manolas, D., Karvelas, C., Kapogiannis, I., Riziotis, V., Spiliopoulos, K., and Voutsinas, S. A comprehensive method for the structural design and verification of the INNWIND 10MW tri-spar floater. *Journal of Physics: Conference Series*, vol. 1104:p. 012025, 2018. doi:10.1088/1742-6596/1104/1/012025.

[255] Benveniste, G., Lerch, M., de Prada, M., Kretschmer, M., Berque, J., López, A., and Pérez-Morán, G. LIFES50+ D2.2 LCOE tool description, technical and environmental impact evaluation procedure. Tech. rep., Catalonia Institute for Energy Research, Barcelona, Spain, 2015. URL `http://lifes50plus.eu/wp-content/uploads/2016/10/GA_640741_D2.2-internal.pdf`.

[256] DNV-GL. DNVGL-RP-C205: Environmental conditions and environmental loads. Tech. rep., DNV-GL, 2017. URL `https://rules.dnvgl.com/docs/pdf/DNV/codes/docs/2014-04/RP-C205.pdf`.

[257] Yu, W., Müller, K., Lemmer, F., Schlipf, D., Bredmose, H., Borg, M., Landbø, T., and Andersen, H. LIFES50+ D4.2 Public definition of the two LIFES50+ 10MW floater concepts. Tech. rep., University of Stuttgart, 2017.

[258] Pegalajar-Jurado, A., Bredmose, H., Borg, M., Straume, J., Landbø, T., Andersen, H., Yu, W., Müller, K., and Lemmer, F. State-of-the-art model for the LIFES50+ OO-Star Wind Floater Semi 10MW floating wind turbine. *Journal of Physics: Conference Series*, vol. 1104:p. 012024, 2018. doi:10.1088/1742-6596/1104/1/012024.

[259] Skogestad, S. and Wolff, E. Controllability measures for disturbance rejection. *Journal of Modeling, Identification and Control*, vol. 17(3):pp. 167–182, 1996. doi:10.4173/mic. 1996.3.1.

Curriculum Vitae

Frank Lemmer (né Sandner) was born on September, 29, 1985 in Ostfildern-Ruit, Germany.

He received his Diplomingenieur's degree (Dipl.-Ing.) in mechanical engineering in 2012 from the University of Stuttgart with specializations in dynamic systems and hydraulic machinery. Through a scholarship offered by the German-American Fulbright Commission he was able to spend two semesters (2009–2010) at the University of Michigan, Ann Arbor, USA, studying electromechanical systems and ocean energy converters. In December 2010 he completed an internship at Alstom S.A. in the field of gas turbine structural analysis. An additional, voluntary internship in 2011 with the German development cooperation GIZ in Bénin gave him valuable insight into the field of agricultural transformation and engineering works in West Africa. After his return to Stuttgart he completed his studies and graduated with the thesis entitled "Reduced Model Design of a Floating Wind Turbine".

He has worked as researcher at the University of Stuttgart at Stuttgart Wind Energy (SWE) since then. His project work focused on integrated conceptual design of floating wind turbine systems with a focus on coupled dynamic modeling and controls. The involvement in the EU-funded projects AFOSP, INNWIND.EU and LIFES50+ helped him to gain valuable experience in the field of floating offshore wind.

He has chaired different sessions at the ASME International Conference on Ocean, Offshore and Arctic Engineering and was invited as a lecturer to the International Summer School on Stochastic Dynamics of Wind Turbines and Wave Energy Absorbers in Aalborg, Denmark. During the time as researcher at SWE, he has supervised more than 15 Bachelor's and Master's theses. He has authored and co-authored more than 20 papers in proceedings of international conferences and one book section, which is currently under production. Four papers on the present work have been submitted to international scientific journals, of which one is already published at the time of publication of this thesis.